Natural Resources Canada | Ressources naturelles Canada

GEOLOGICAL SURVEY OF CANADA
OPEN FILE 9170

Time-domain electromagnetic soundings for talik investigations, Rankin Inlet, Nunavut

G.A. Oldenborger

2024

Canada

GEOLOGICAL SURVEY OF CANADA
OPEN FILE 9170

Time-domain electromagnetic soundings for talik investigations, Rankin Inlet, Nunavut

G.A. Oldenborger

2024

Permanent link: https://doi.org/10.4095/p60hysa40q

This publication is available for free download through the NRCan Open Science and Technology Repository (https://ostrnrcan-dostrncan.canada.ca/).

Recommended citation
Oldenborger, G.A., 2024. Time-domain electromagnetic soundings for talik investigations, Rankin Inlet, Nunavut; Geological Survey of Canada, Open File 9170, 113 p. https://doi.org/10.4095/p60hysa40q

Publications in this series have not been edited; they are released as submitted by the author.

ISSN 2816-7155
ISBN 978-0-660-70483-8
Catalogue No. M183-2/9170E-PDF

SUMMARY

Knowledge of the occurrence of taliks or unfrozen ground beneath lakes in permafrost terrain is critical for understanding the interaction between surface and groundwater. Due to the contrast in electrical properties between frozen and unfrozen ground, time-domain electromagnetic (TEM) surveys may be useful for talik detection and mapping. TEM soundings were acquired over nine lakes in the vicinity of Rankin Inlet, Nunavut for talik studies. Soundings were also acquired over shallow lake terraces and onshore. One-dimensional modelling and inversion of the data show marked variability in the data and the recovered resistivity models between lakes of different sizes and different bedrock geology. The survey results are not easily interpreted in terms of a simple permafrost paradigm of frozen (high resistivity) and unfrozen (low resistivity) ground. The recovered electrical resistivity models generally exhibit highly resistive ground under lakes, moderately resistive ground onshore, and a conductive zone at 50 to 240 m depth.

TABLE OF CONTENTS

INTRODUCTION

In continuous permafrost, lake taliks are areas of ground below lakes that remain unfrozen due to the heat storage of the lake water (van Everdingen, 2005). Open or through taliks, where the unfrozen region completely penetrates permafrost, are of particular concern in that they allow for a connected system of surface and groundwater, and may allow for lake-to-lake flow paths. Such physical conditions are relevant and important when considering drinking water supply and infrastructure development. Open and connected taliks represent both significant groundwater resource potential and potential pathways for contaminant transport.

The presence of a talik beneath a lake or small group of lakes can be predicted using equations describing the thermal disturbance of lakes on permafrost (Lachenbruch, 1957; Burn, 2002) or by heat transfer models (Golder Associated Ltd., 2021a). Alternatively, proxy measures of lake depth (LeBlanc et al., 2021) or the presence of bottom-fast ice (Sladen et al., 2024) can be used for talik assessment (LeBlanc et al., 2022). Given the contrast in electrical properties between frozen and unfrozen ground, electrical and electromagnetic geophysical surveys may be useful for talik detection and mapping, or interpretation of permafrost conditions. In particular, time-domain electromagnetic (TEM) soundings can be well-suited to talik investigations due to the large depth of exploration obtained with a relatively small surface offset or footprint. In resistive polar environments, penetration depths of hundreds of meters are possible (i.e., Madsen et al., 2022). TEM soundings were used by Todd and Dalimore (1998) to investigate depths of permafrost exceeding 500 m and associated intra-permafrost taliks. TEM soundings were also used by Creighton et al. (2018) to study closed talik geometry beneath a thermokarst lake.

This Open File reports on TEM soundings collected over nines lakes, over shallow lake terraces, and onshore in the vicinity of Rankin Inlet, Nunavut. TEM soundings were designed to achieve a depth of investigation on the order of hundreds of metres, subject to ground resistivity. The TEM data were processed and inverted to generate one-dimensional (1D) resistivity models at the sounding sites. The resistivity models can be used to interpret permafrost depth and talik occurrence in relation to lake features such as area, depth, or terrace morphology.

STUDY AREA

The Hamlet of Rankin Inlet is located on the western coast of Hudson Bay in the Kivalliq Region of Nunavut, Canada (Figure 1). The surficial geology in the vicinity of Rankin Inlet consists of relatively thin glacial, glaciofluvial, marine, alluvial, and organic deposits (McMartin, 2002).

Regional bedrock is comprised of various units of the Archean Rankin Inlet Greenstone Belt including poly-metamorphosed mafic volcanic, felsic pyroclastic, and sedimentary rocks with abundant faults (Figure 2; Golder Associates Ltd., 2021b).

Rankin Inlet is within the continuous permafrost zone where 90%–100% of the land area is underlain by permafrost (Heginbottom et al., 1995). Mean annual ground temperature at the top of permafrost varies from −9.5 to −5.5°C and active layer thickness ranges from 50 to 160 cm (LeBlanc and Oldenborger, 2021). The base of permafrost (0°C isotherm) is expected to be variable between 285 to 430 m depth with shallower depths occurring near lakes both with and without open taliks (Golder Associates Ltd., 2021b). Bottom-fast ice (BFI) is expected for lakes with depths less than 1.7 m (Sladen et al., 2024) and permafrost is expected below lakes with depths less than 1 m (LeBlanc et al., 2024). In contrast, unfrozen water and open taliks are expected beneath lakes having a half-width or radius greater than approximately 160 to 485 m depending on lake shape and lake terraces (Golder Associates Ltd., 2014). Furthermore, permafrost in the region may be saline due to deep brines and postglacial inundation of the land surface (Hivon, 1991; Dyke, 2004). High salinity may contribute to freezing point depression such that the transition between frozen to unfrozen water may occur above the base of permafrost resulting in a basal cryopeg. Golder Associates Ltd. (2021b) report the salinity of deep groundwater to be approximately 61 g/L with a basal cryopeg depth of approximately 280 to 290 m away from lakes. The salinity of groundwater under lakes with open taliks is expected to be less due to connection with overlying fresh water (Golder Associates Ltd., 2021b).

The upper lithospheric crust along the western coast of Hudson Bay near Rankin Inlet and Baker Lake is generally resistive with km-scale electrical resistivity values on the order of 10^3–10^4 Ωm (Jones et al., 2014). Significant uncertainty may arise in the discrimination of high resistivity bedrock versus high resistivity permafrost which may exhibit electrical resistivity values up to 10^3–10^5 Ωm (e.g., Palacky, 1988). Natural ice near 0°C is expected to have electrical resistivity in the range of 10^3–10^5 Ωm (Reynolds and Paren, 1984; Mikucki et al., 2015). Heterogeneity of electrical resistivity is to be expected at the scale of TEM surveys due to local geology and the occurrence of conductive features such as saline groundwater. For the cryopeg salinity of 61 g/L reported by Golder Associates Ltd. (2021b), fluid resistivity may be as low as 0.2 Ωm at 0°C (e.g., Oldenborger, 2021). For the lower talik salinity of approximately 1 g/L reported by Golder Associates Ltd. (2021b), fluid resistivity may be as high as 10 Ωm at 0°C. Fractures, faults, graphitic fault gauge, and sulphide minerals may also contribute to low electrical resistivity. Variations in resistivity will also arise from the geothermal gradient of approximately 0.015°C/m (Golder Associates Ltd., 2014) that will result in several degrees of temperature variation with

depth for the TEM soundings. No temperature compensation is considered herein, but it may be warranted in some cases (i.e., Oldenborger, 2021).

METHODS

Data Acquisition

Acquisition of the Rankin Inlet TEM data occurred from April 21–29, 2023. The study area and sounding sites are shown in Figure 1. TEM sounding sites were selected to represent lakes of a variety of sizes and terrace morphologies (e.g., LeBlanc et al., 2022). Sounding sites were chosen without consideration of bedrock geology (Figure 2). Site conditions were lake ice or snow-covered tundra shorelines, both with approximately 30 cm of snow cover. Data were collected over nine lakes and shorelines for a total of 22 soundings. At each site, ice thickness, lake depth (from top of ice), and water conductivity were measured by weighted-line sounding unless bottom-fast ice was suspected (Table 1).

TEM data were collected with a digital 20-gate ProTEM-D receiver (SN 959704), a TEM47 transmitter (SN 031892), a TEM57-MK2 transmitter (SN 10057) and a high-frequency (HF) receiver coil (SN 0301, 31.4 m^2) all manufactured by Geonics Ltd. In all cases, the transmitter utilized a 100 m × 100 m single-coil square loop of AWG 12 stranded copper wire with a measured resistance of 2 Ω at −4°C. Dual transmitters were utilized to take advantage of both the higher frequency, better time resolution, and early-time measurements of the TEM47, and the higher current and later-time measurements of the TEM57. Transmitter current was 3.0 A for the TEM47 and 8.5 to 9.0 A for the TEM57 depending on base frequency.

All soundings were acquired in a central-loop configuration using base frequencies of 285 Hz, 75 Hz, and 30 Hz with the TEM47, and 30 Hz, 7.5 Hz, and 3 Hz with the TEM57. Schematic survey layout and an example field site and are illustrated in Figure 3. There is significant overlap in the measurement intervals and gate times for the base frequencies used, but the multiple acquisitions allow for redundancy checks, and for flexible data selection and processing. Data were collected as three separate successive records per base frequency and each record was stacked for integration times of 8 s (u), 15 s (v), 30 s (H), and 60 s (M, L) such that the number of stacks and signal-to-noise ratio decreased for lower base frequency. Gain was set variably in order to keep ambient noise below ±5 nV/m^2 in the last 5 time gates at any base frequency, and to avoid any early-time saturation of the signal (e.g., Geonics Ltd., 2011). Ambient noise records (data acquired

in the absence of a transmitter signal) were collected at every site for each base frequency of acquisition using the same stacking and gain parameters as the data.

Processing and Inversion

For each base frequency, a single data record of induced receiver coil voltage was computed on a gate-by-gate basis as the mean signed value for each of the three records. Given the variable gain, moment, and gate times for each base frequency, the mean voltage measurements were next adjusted for nonlinear gain and then normalized to a transmitter of unit area and current (mV/Am^2) so that records for each base frequency could be combined as a single sounding. Such a normalization is equivalent to transformation of the loop voltage to the time rate of change of the magnetic field (T/s). Variations between frequencies and sites are highlighted by an additional nonlinear transformation to late-time apparent resistivity which further compensates for measurement time (Spies and Eggers, 1986). Figure 4 illustrates the full range of gain-adjusted and normalized sounding data for all base frequencies, and the transformation to apparent resistivity for Site 1.

TEM sounding data can be contaminated by natural electromagnetic noise, or by anthropogenic noise associated with cultural features such as radio transmitters or power lines (Macnae et al., 1984; Danielsen et al., 2003). Cultural features are few in the survey area, but a radio tower for mine site communication is present on a nearby bedrock ridge (Figure 1). Stacking over each record and averaging independent records are effective for removing random noise, spikes, or oscillations. Stacking should also be effective for removing correlated noise associated with radio signals (McLachlan et al., 2022). The magnitude of the data noise can be established using a combination of record repeatability and measured background ambient noise. The noise at each time gate for each base frequency was computed as the maximum of the ambient induced voltage and the repeatability given by the standard deviation of the three stacked voltage records. The data are generally less repeatable at later times and for lower frequency with the same transmitter, and repeatability errors are usually less than the ambient voltage but of the same order of magnitude. Danielsen et al. (2003) give a time of 1–2 ms at which the measurable signal falls below the ambient noise levels for the ProTEM 47. Figure 4 illustrates a gain-adjusted and normalized noise level of approximately 10^{-7} mV/Am^2 at approximately 1.3 ms for Site 1 which is consistent across most soundings.

Interpretation of TEM data can also be confounded by systematic noise: measurable, repeatable signal that is only present after transmitter on time, that is not present in the ambient noise records,

and is not removed by stacking. Examples are geometry errors, signal run-on, and coupling with power lines or grounded metallic infrastructure (Danielsen et al., 2003). Neither conductive ground nor coupling to cultural features are expected for the Rankin Inlet TEM data. However, induced polarization (IP) effects may be present in permafrost terrain, and are a source of systematic noise if not explicitly accounted for. IP effects are most influenced by the near surface and typically result in negative transients, or sign reversals of the TEM decay curve at late times (Smith and West, 1989; Macnae, 2016). Although sign reversals are observed in the Rankin Inlet TEM data, the offending data are never of a magnitude in excess of the ambient noise and cannot be reliably attributed to IP effects. All reverse-polarity measurements were removed from the sounding data.

After normalization of each sounding and establishment of the noise levels, the data were edited in preparation for inversion. There is typically some offset between the last several time gates at any particular base frequency and the first gates of the next lower frequency that may be due to transmitter run-on effects, or the different ramp times used by the two transmitters (Figure 4). It is also sometimes the case that the records for different base frequencies may diverge at late time (not shown). Such offsets and divergence can result in convergence problems during inversion due to data inconsistency. On a site-by-site basis, data were selected from the combined suite of decay curves according to the following general principles consistent with lower noise, better time resolution, and smooth decays: the last several gates at each frequency were removed in preference of the first gates at the next frequency; higher frequencies were preferentially retained over lower frequencies; TEM47 data were preferentially retained over TEM57 data; the first few gates at each frequency were removed to achieve consistency with the last gates of the next higher frequency; and data with noise levels in excess of 25% were removed. The result is a single edited decay curve for each site (Figure 4) that was inverted to yield a corresponding layered resistivity model. In all cases, the edited decay curves consist predominantly or entirely of data collected using the TEM47 transmitter.

The soundings were inverted individually using EM1DTM (Farquharson and Oldenburg, 1993). EM1DTM is based on an over-determined, least-squares one-dimensional inversion algorithm that operates on a layered-Earth parameterization. The data were fit using both L^2 (least-squares or "smooth") and L^1 (minimum length or "blocky") constraints on the model structure (Farquharson and Oldenburg, 1998). The model was over-parameterized with 35 layers increasing in thickness by a factor of 1.1 from a surface thickness equal to the measured lake ice thickness at each site (Table 1). The initial and reference models were homogeneous with a resistivity equal to that of the most representative halfspace for the data. If the L^2 solution did not return to the reference resistivity at depth, the number of layers was increased to 40.

The inversion incorporates variable noise weighting and attempts to fit the data to a level commensurate with the noise according to the discrepancy principle and the chi-squared statistic χ^2. In most cases, the inversions converged to χ^2 values greater than unity indicating that the data cannot be fit (overall) to the assigned level of noise. In some cases, L^2 or L^1 inversions were initialized with the L^1 or L^2 solution, or an overly conductive reference model was used to improve convergence or obtain a lower χ^2 value (e.g., Oldenborger and Oldenburg, 2008). The root-mean-square (RMS) misfit was typically comparable to the RMS noise level, with most of the discrepancy attributable to late times. A χ^2 value greater than unity is acceptable (with reasonable RMS misfit) knowing that the data from the different base frequencies are not always consistent and that noise levels are likely underestimated, especially for high frequencies and early times for which the data are highly repeatable, but likely suffer from systematic errors. Model reliability was assessed by considering the data noise, the data misfit, and the model stability for different inversion scenarios, including the persistence of specific model features and the depth of investigation index (DOI, Oldenburg and Li 1999).

RESULTS

The models resulting from TEM sounding are summarized in Figure 5. The data for each site, the recovered models, the data misfit, and the DOI are given in the Appendix. The inversion solutions exhibit strong heterogeneity of several orders of magnitude both more resistive and less resistive than the reference halfspace. Moreover, the models exhibit significant variability between the different sounding sites, despite similar lake sizes and site conditions. Pseudo cross-sections of electrical resistivity are shown for Little Meliadine Lake (Figures 6 and 7), for Ming Major Lake (Figure 8), and for Second and First Landing Lakes (Figure 9). Several general observations can be made from the pseudo cross-sections.

Most of the lakes sites (shallow, terrace and deep) exhibit a moderate to strong conductor at approximately 50 to 240 m depth with resistivity of <1–100 Ωm. The conductor is interpreted as present only if it is consistently required by the L^2, L^1, and DOI models with similar misfit. Depth to the conductor is interpreted as uncertain if the L^2, L^1, or DOI models recover significantly different conductor depths (Appendix). Even if required by all models, existence of the conductor and its depth are both uncertain if the conductor occurs below the depth of model reliability (e.g., Sites 5, 19, and 6). In most cases, the conductor is strong enough to prevent any reliable interpretation at depths beyond the conductor. For the onshore sites, a comparable deep conductor is only observed for Site 14 between Second and First Landing Lakes (Figure 9). Onshore Site 22

exhibits no conductor (Figure 9) and onshore Site 4 exhibits a shallow weak conductor that is not convincingly correlated to the deep conductor (Figure 6). The strongest deep conductors are observed at sites over known faults or shear zones (Figure 8, Site 21 and Figure 9, Sites 12–17), but onshore Site 22 has no reliable deep conductor, despite the mapped fault (Figure 9).

All of the lake sites exhibit either a conductive surface or a shallow conductive layer with resistivity of 1–100 Ωm with layer thickness that is somewhat correlated to measured lake depth (Table 1). For Little Meliadine Lake, this surface conductor occurs at greater depth for deeper water and is absent onshore (Figure 6). Across the shallower Ming Major Lake, no distinct conductive layer is recovered, but the model surfaces are conductive (Sites 7, 8, 9, and 20) and a conductive layer is recovered at Site 21 (Figure 8). Across Second and First Landing Lakes, there are both distinct consecutive shallow conductive layers (Sites 10–13) and conductive model surfaces (Sites 15–17). Onshore Site 14 between Second and First Landing Lakes also exhibits a distinct near-surface conductor, and onshore Site 22 exhibits a weak near-surface conductor (Figure 9).

The electrical resistivity under the deep lakes is relatively high in comparison to the observed conductors and the onshore sites. For Little Meliadine Lake, the recovered resistivity above the deep conductor is 2,500–500,000 Ωm (Figure 6), whereas the recovered resistivity at onshore Site 4 is approximately 50–200 Ωm (above the depth of reliable model interpretation). Across the Ming Major Lake cross-section, recovered resistivity above the deep conductor is also consistently greater than 3,000 Ωm and often much higher (Figure 8). For the smaller Ming Minor Lake, recovered resistivity above the depth of reliable model interpretation is approximately 100–500 Ωm (Figure 7, Site 6). However, for the even smaller lake at Site 5, resistivity is approximately 35,000 Ωm (Figure 7) and for the smallest lake surveyed at Site 9, resistivity is approximately 5,000 Ωm (Figure 7). Across Second and First Landing Lakes, resistivity is more variable ranging from 350 Ωm at Site 13 to 55,000 Ωm at Site 10 (Figure 9). The onshore sites are also variable with 1,100 Ωm observed at Site 22 versus 250,000 Ωm observed at Site 14.

DISCUSSION

A simple conceptual paradigm for the electrical properties of taliks in permafrost terrain would involve low electrical resistivity in the presence of unfrozen water, moderate resistivity in the presence of poorly ice-bonded permafrost, and high resistivity in the presence of ice-bonded permafrost. According to this paradigm, taliks would be detected in field survey data as low resistivity anomalies with some transition to high resistivity permafrost (e.g., Todd and Dallimore,

1998; Creightion et al., 2018). The presence of saline water adds complexity and prevents interpretation in terms of the 0°C isotherm, but does not alter the fundamental concept of unfrozen and frozen water being the primary phenomena responsible for differences in electrical properties.

The Rankin Inlet TEM data are not readily interpretable in terms of this simple paradigm. Low resistivity is recovered for some soundings over deep water (Site 16) and very high resistivity is recovered for one of the onshore soundings (Site 14). However, more generally, resistive to highly resistive ground is observed under large lakes such as Little Meliadine Lake that most likely support through taliks. In contrast, less resistive ground is observed for onshore Sites 4 and 22 that are expected to be representative of ice-bonded permafrost in bedrock. Furthermore, soundings over (presumed) bottom-fast ice do not appear consistently more (or less) resistive than soundings over deep-water sites.

Variable salinity and variable geology will both act to confound interpretation of TEM soundings in terms of talik occurrence and permafrost conditions. It is suspected that both of these factors contribute to the inconsistencey observed in the Rankin Inlet TEM data. High salinity permafrost has been interpreted from shallow electrical data in the Rankin Inlet area (Oldenborger et al., 2020) and saline permafrost can be expected at all depths in addition to deep brines that may be responsible for a basal cryopeg (e.g., Golder Associates Ltd., 2021b). In addition to salinity, geological conditions are heterogeneous with many soundings falling on or near geological contacts, major faults, or shear zones. Variability of 2D or 3D geology (or salinity) is not accounted for in the 1D TEM inversion procedure and will result in erroneous models. This is of particular concern for soundings conducted over contacts and faults, but also soundings collected on lake terraces or the near-onshore region where the adjacent deep water and shore may both influence the data. Current “smoke rings” are often used to visualize TEM soundings (Nabighian, 1979). At 100 m depth, induced currents may be 140 to 200 m laterally distant from the edge of the transmitter loop resulting in significant heterogeneity being encountered.

The presence of polarizable ground will also introduce systematic noise that may result in erroneous models if unaccounted for. Although IP effects in the data are not present as polarity reversals, Lorentzen et al. (2024) classify other atypical decay curves such as non-monotonic and “flat” decay curves that they attribute to polarizable ground in permafrost terrain. These atypical decays are manifest in some of the Rankin Inlet soundings (Appendix). However, for large-loop TEM configurations, non-monotonic, flat, and other atypical decay curves can result from purely resistive ground and interaction of the large loop with strong one-dimensional conductivity contrasts. Furthermore, significant IP effects are not expected for taliks or unfrozen ground.

Despite the departure form the conceptual paradigm, the Rankin Inlet TEM soundings do support some general interpretations. The shallow conductor (or conductive model surface) is interpreted

to result from a layer of unfrozen saturated or super-saturated sediments that appears to persist beneath most (or all) lakes regardless of bottom-fast ice or permafrost conditions. Recovered resistivity for this near-surface conductor is comparable to the measured lake water resistivity (Table 1). In some cases, the shallow conductive layer is overlain by a distinct resistive surface (e.g., Figure 6, Site 2). This may be a combined effect of the snow, ice, and water column being separable from the lake-bottom sediments that are highly conductive due to higher total dissolved and suspended solids within the sediments. In the case of a conductive model surface (e.g., Figure 9, Site 16), this may be the effect of the snow, ice, and water column being lumped with the lake-bottom sediments resulting in a higher bulk resistivity than for the distinct layer case. The differences in resolution of these two cases may be attributed to differences in the most early-time data for the soundings and the particularities of each site and each inversion. The depth of the near-surface conductor is not always consistent with the measured lake depth due to its likely extent beyond the actual water column as measured (and due to resolution limitations). However, the relative depth of this layer is consistent with the lake depth profile from shallow (Site 3) to deep (Site 18) as shown in Figure 6.

The lake-bottom sediments are interpreted to be underlain by bedrock with significantly lower (unfrozen) water content. It is hypothesized that the lake sites are flushed by relatively fresh surface water (with little to no suspended solids) such that resistivity is relatively high, but is comparable to expected values (e.g., Palacky, 1988; Jones et al., 2014). Using a simple Archie-type petrophysical model, resistivity in excess of 300,000 Ωm is entirely plausible for bedrock with an effective porosity of 0.001 and salinity of 1 g/L (e.g., Golder Associates Ltd. 2021b).

The deep conductor is interpreted to result from a transition from fresh surface water to more saline groundwater. However, using the same petrophysical model as above, a reduction in recovered resistivity by 3–4 orders of magnitude requires the same reduction in fluid resistivity or approximately the same increase in salinity (e.g., Oldenborger, 2021), which is not possible given the solubility of typical salts in water. An increase in salinity from 1 g/L to 100 g/L can only account for a 2 order of magnitude decrease in resistivity. Furthermore, cryopeg depth is reported as 280 to 290 m away from lakes (Golder Associates Ltd. 2021b), whereas the interpreted fresh-saline water transition is much shallower for the TEM data, and is not observed at all for two of the three onshore sites (although the cryopeg may be deeper than the sounding depth at these sites). Lower resistivity can also result from increased effective porosity, which has a much greater effect than salinity alone. Sedimentary rocks, faults, or shear zones may serve to increase the effective porosity and significantly decrease the recovered resistivity. Similarly, variations in the interpreted depth to the deep conductor may result from 3D effects of geology and faults, rather than depth variation of the fresh-saline water transition. Hydraulic testing suggests that the sedimentary bedrock has an order of magnitude higher hydraulic conductivity than the mafic volcanic bedrock (Golder Associates Ltd., 2021b). A similar relationship may be expected for electrical resistivity.

The above interpretation does not readily explain the differences (or lack thereof) observed between the lake sites, terrace sites, and the onshore sites, or between the onshore sites themselves. It is hypothesized that the onshore Sites 4 and 22 are saline permafrost resulting from post-glacial inundation and are thus less resistive than the flushed lake sites. Occurrence of a crypog cannot be observed due to the moderately conductive ground that results in limited penetration of the TEM signal. In contrast, it is hypothesized that onshore Site 14 is flushed by the drainage system connecting Second and First Landing lakes and may be partly unfrozen due the thermal influence of the adjacent lakes (in addition to the surrounding lakes influencing the sounding). The conductive shallow layer at Site 14 may represent unfrozen glacial sediments over flushed resistive bedrock, or a layer of saline permafrost.

CONCLUSION

TEM soundings were performed over nine lakes and shorelines in the vicinity of Rankin Inlet, Nunavut. The sounding data were inverted for 1D models of electrical resistivity to be interpreted in terms of permafrost conditions and talik occurrence. The recovered electrical resistivity models exhibit highly resistive ground under lakes, moderately resistive ground onshore, and a conductive zone at 50 to 240 m depth. The survey results are not easily interpreted in terms of lake morphology or a simple permafrost paradigm with frozen and unfrozen ground. Salinity alone cannot easily explain the observed contrast in electrical properties.

Despite generally good data quality, recovered resistivity models may lack precision in interpretation due to insensitivity of results to highly restive ground, and due to complexity and 3D effects introduced by geology and variable salinity. Better understanding of the survey results might be achieved via more in-depth investigation of the relationships between resistivity and geology, or resistivity and lake morphology including lake depth and lake terraces. Models and interpretation might be improved by consideration of additional model constraints if sufficient and reliable supporting information could be obtained on a case-by-case basis. Any future work should involve data collection that better allows for 2D or 3D contextual interpretation.

ACKNOWLEDGEMENTS

Part of the Natural Resources Canada GEM-GeoNorth Program. Data collected with assistance from K. Brewer and A.-M. LeBlanc. Internal review by A.-M. LeBlanc. Data are available from the author under the Open Government Licence – Canada (https://open.canada.ca).

REFERENCES

Burn, C.R., 2002. Tundra lakes and permafrost, Richards Island, western Arctic coast, Canada. Canadian Journal of Earth Sciences 39, 1281–1298. https://doi.org/10.1139/e02-035

Creighton, A.L., Parsekian, A.D., Angelopoulos, M., Jones, B.M., Bondurant, A., Engram, M., Lenz, J., Overduin, P.P., Grosse, G., Babcock, E., Arp, C.D., 2018. Transient electromagnetic surveys for the determination of talik depth and geometry beneath thermokarst lakes. Journal of Geophysical Research: Solid Earth 123, 9310–9323. https://doi.org/10.1029/2018JB016121

Danielsen, J.E., Auken, E., Jorgensen, F., Sondergaard, V., Sorensen, K.I., 2003. The application of the transient electromagnetic method in hydrogeophysical surveys. Journal of Applied Geophysics 53, 181–198. https://doi.org/10.1016/j.jappgeo.2003.08.004

Dyke, A.S., 2004. An outline of North American deglaciation with emphasis on central and northern Canada. Developments in Quaternary Sciences 2, 373–424. https://doi.org/10.1016/s1571-0866(04)80209-4

Farquharson, C.G., Oldenburg, D.W., 1993. Inversion of time-domain electromagnetic data for a horizontally layered Earth. Geophysical Journal International 114, 433–442. https://doi.org/10.1111/j.1365-246X.1993.tb06977.x

Farquharson, C.G., Oldenburg, D.W., 1998. Non-linear inversion using general measures of data misfit and model structure. Geophysical Journal International 134, 213–227. https://doi.org/10.1046/j.1365-246x.1998.00555.x

Geonics Ltd., 2011. PROTEM 47D Operating Manual for 20/30 Gate Model.

Golder Associates Ltd., 2014. SD 6-1 Permafrost thermal regime baseline studies - Meliadine gold project. Report No. Doc 225-1314280007 Ver. 0, submitted to Agnico Eagle Mines Limited.

Golder Associates Ltd., 2021a. Meliadine Extension, 2020 Thermal Assessment. Report No. 20136436-815-R-Rev2-2200, submitted to Agnico Eagle Mines Limited.

Golder Associates Ltd., 2021b. Summary of Hydrogeology Existing Conditions, Meliadine Extension. Report No. 20136436-855-R-ExistingConditionsReport-Rev3, submitted to Agnico Eagle Mines Limited.

Heginbottom, J.A., Dubreuil, M.H., Harker, P.T., 1995. Canada, Permafrost. National Atlas of Canada, 5th ed., Plate 2.1, MCR 4177.

Hivon, E.G., 1991. Behaviour of Saline Frozen Soils. Ph.D. Dissertation. University of Alberta.

Jones, A.G., Ledo, J., Ferguson, I., Craven, J.A., Unsworth, M.J., Chouteau, M., Spratt, J.E., 2014. The electrical resistivity of Canada's lithosphere and correlation with other parameters: contributions from Lithoprobe and other programmes. Canadian Journal of Earth Sciences 51, 573–617. https://doi.org/10.1139/cjes-2013-0151

Lachenbruch, A.H. 1957b. Three-dimensional heat conduction beneath heated buildings. U.S. Geological Survey, Bulletin 1052-B, 51–69.

LeBlanc, A.-M., Chartrand, J., Smith, S.L., 2021. Estimation of maximum lake depth from the surrounding topography: Towards a regional assessment of the occurrence of taliks below Arctic lakes. Geological Survey of Canada, Scientific Presentation 122. https://doi.org/10.4095/328242

LeBlanc, A.-M., Chartrand, J., Smith, S.L., 2022. Regional assessment of the presence of taliks below Arctic lakes, Nunavut. Geological Survey of Canada, Scientific Presentation 138. https://doi.org/10.4095/330205

LeBlanc, A.-M., Oldenborger, G.A., 2021. Ground temperature, active layer thickness and ground ice conditions in the vicinity of Rankin Inlet, Nunavut. Canada-Nunavut Geoscience Office, Summary of Activities 2020, 63–72.

LeBlanc, A-M, Sladen, W.E, Faucher, B., 2024. Lake-bottom temperature on shallow and deep terraces for sublacustrine open talik assessment near Rankin Inlet, Nunavut, Canada. International Conference on Permafrost, Whitehorse.

Lorentzen, T.H., Kass, M.A., Scheer, J., Tomaškovičová, S., Christiansen, A.V., Maury, P.K., Ingeman-Nielsen, T., 2024. Exploring the challenges of interpreting near-surface towed TEM data on saline permafrost. Geophysics, in press. https://doi.org/10.1190/geo2023-0221.1

McMartin, I. 2002. Surficial geology, Rankin Inlet, Nunavut. Geological Survey of Canada, Open File 4116. https://doi.org/10.4095/299616

Macnae, J., 2016. Quantifying airborne induced polarization effects in helicopter time domain electromagnetics. Journal of Applied Geophysics 135, 495–502. https://doi.org/10.1016/j.jappgeo.2015.10.016

McLachlan, P., Christiensen, N.B., Grombacher, D., Christiansen, A.V., 2023. Evaluating the impact of correlated noise for time-lapse transient electromagnetic (TEM) monitoring studies. Near Surface Geophysics 21, 333–342. https://doi.org/10.1002/nsg.12262

Mikucki, J., Auken, E., Tulaczyk, S., Virginia, R.A., Schamper, C., Sørensen, K.I., Doran, P.T., Dugan, H., Foley, N., 2015. Deep groundwater and potential subsurface habitats beneath an Antarctic dry valley. Nature Communications 6, 6831. https://doi.org/10.1038/ncomms7831

Nabighian, M.N., 1979. Quasi-static transient response of a conducting half-space - An approximate representation. Geophysics 44, 1700–1705. https://doi.org/10.1190/1.1440931

Oldenborger, G.A., 2021. Subzero temperature dependence of electrical conductivity for permafrost geophysics. Cold Regions Science and Technology 182, 103214. https://doi.org/10.1016/j.coldregions.2020.103214

Oldenborger, G.A., Oldenburg, D.W., 2008. Inversion of 3D time-domain EM data for high conductivity contrasts. SEG Expanded Abstracts 27. https://doi.org/10.1190/1.3063727

Oldenborger, G.A., Routh, P.S., Knoll, M.D., 2007. Model reliability for 3D electrical resistivity tomography: Application of the volume of investigation index to a time-lapse monitoring experiment. Geophysics 72, F167–F175. https://doi.org/10.1190/1.2732550

Oldenborger, G.A., Short, N., LeBlanc, A.-M., 2020. Electrical conductivity and ground displacement in permafrost terrain. Journal of Applied Geophysics 181, 104148. https://doi.org/10.1016/j.jappgeo.2020.104148

Oldenburg, D., Li, Y., 1999. Estimating depth of investigation in dc resistivity and IP surveys. Geophysics 64, 403–416. https://doi.org/10.1190/1.1444545

Palacky, G.J., 1988. Resistivity characteristics of geologic targets, in: Nabighian, M.N. (Ed.), Electromagnetic Methods in Applied Geophysics, Investigations in Geophysics. Society of Exploration Geophysicists, pp. 53–129.

Reynolds, J., Paren, J., 1984. Electrical resistivity of ice from the Antarctic Peninsula, Antarctica. Journal of Glaciology 30, 289–295. https://doi.org/10.3189/S0022143000006110

Sladen, W.E., LeBlanc, A.-M., Chartrand, J., van der Sanden, J., 2024. Using RADARSAT Constellation Mission Imagery to Support Talik Mapping, Rankin Inlet, Nunavut, Canada. International Conference on Permafrost, Whitehorse.

Smith, R.S., West, G.F., 1989. Field examples of negative coincident-loop transient electromagnetic responses modeled with polarizable half-planes. Geophysics 54, 1491–1498. https://doi.org/10.1190/1.1442613

Spies, B.R., Eggers, D.E., 1986. The use and misuse of apparent resistivity in electromagnetic methods. Geophysics 51, 1462–1471. https://doi.org/10.1190/1.1442194

Todd, B.J., Dallimore, S.R., 1998. Electromagnetic and geological transect across permafrost terrain, Mackenzie River delta, Canada. Geophysics 63, 1914–1924. https://doi.org/10.1190/1.1444484

van Everdingen, R.O., 2005. Multi-language glossary of permafrost and related ground-ice terms. International Permafrost Association.

Table 1. Site locations (receiver coil) with measured ice thickness and lake depth. Sites without ice thickness measurements were either onshore or assumed to be bottom-fast-ice (BFI) conditions (unverified). Water conductivity is reported at in-situ temperature and is a representative value for the entire water column. Conductivity was observed to increase near the lake bottom.

Site	Easting (m)	Northing (m)	Ice Thickness (m)	Water Depth (m)	Water Conductivity (mS/m, Ωm)
1	538,490	6,978,028	1.7	9.4	8, 125
2	537,138	6,978,249	1.8	12.8	8, 125
3	536,815	6,978,011	1.5	1.9	34, 29
4	536,714	6,977,846	Onshore	NA	NA
5	536,891	6,977,419	BFI	BFI	-
6	538,865	6,976,569	BFI	BFI	-
7	538,392	6,975,961	BFI	BFI	-
8	539,120	6,975,419	1.6	1.8	35, 29
9	539,827	6,974,558	BFI	BFI	-
10	542,768	6,971,136	BFI	BFI	-
11	542,737	6,970,929	1.8	3.1	16, 62
12	542,307	6,970,745	1.7	16.6	25, 40
13	541,939	6,970,815	1.8	6.7	15, 67
14	541,445	6,970,989	Onshore	NA	NA
15	540,903	6,970,835	1.7	6.7	17, 59
16	540,101	6,970,945	1.5	4.8	17, 59
17	539,757	6,971,255	BFI	BFI	-
18	537,941	6,978,501	1.8	17.3	18, 56
19	538,060	6,977,336	1.8	7.1	9, 111
20	540,030	6,974,019	1.7	3.1	30, 33
21	540,886	6,971,888	BFI	BFI	-
22	542,769	6,971,318	Onshore	NA	NA

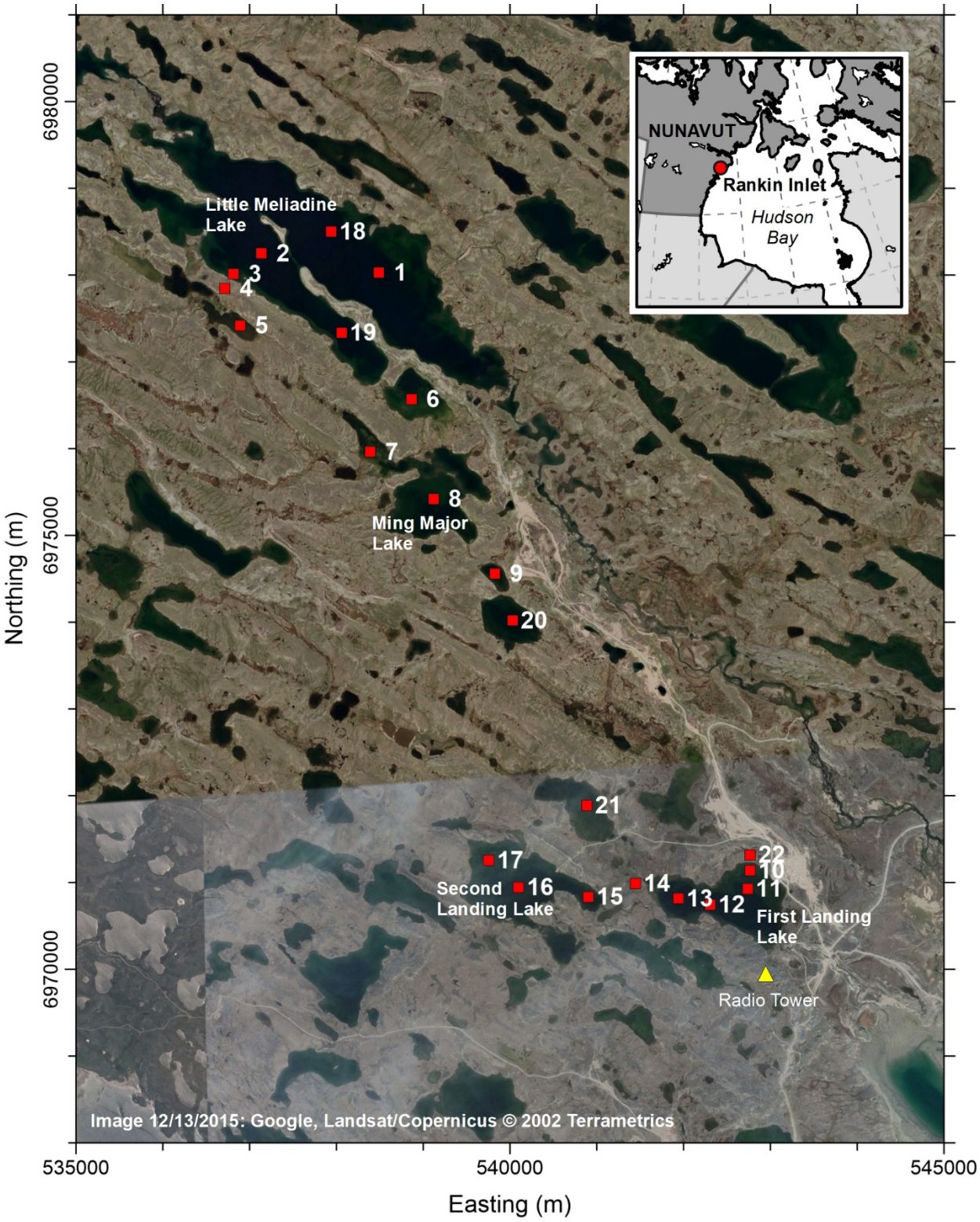

Figure 1. TEM sounding locations near Rankin Inlet, Nunavut (62°48′38″N, 92°06′53″W). Coordinates are Easting and Northing, NAD83 UTM Zone 15N.

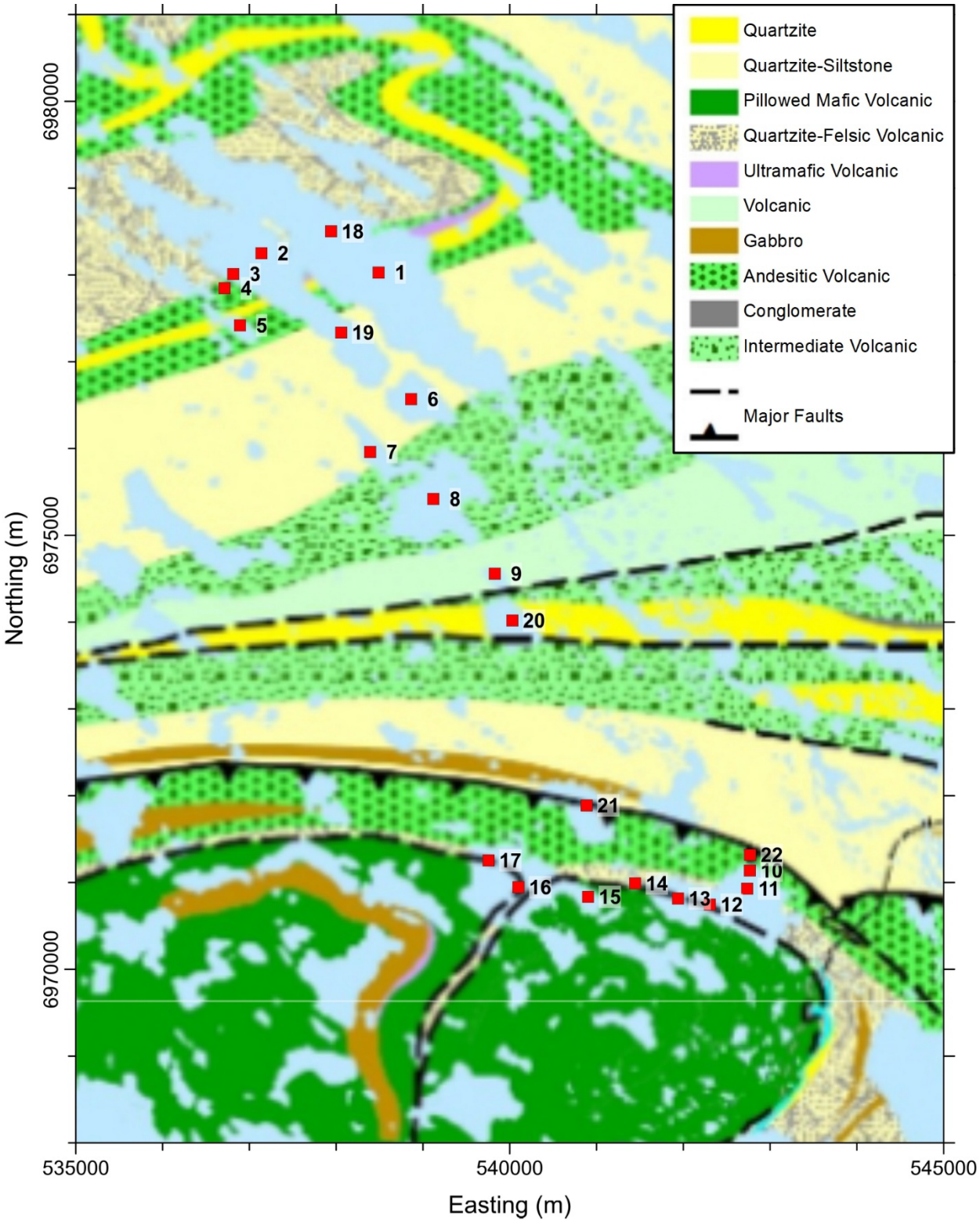

Figure 2. Bedrock geology near Rankin Inlet, Nunavut (Golder Associates Ltd., 2021). Coordinates are Easting and Northing, NAD83 UTM Zone 15N.

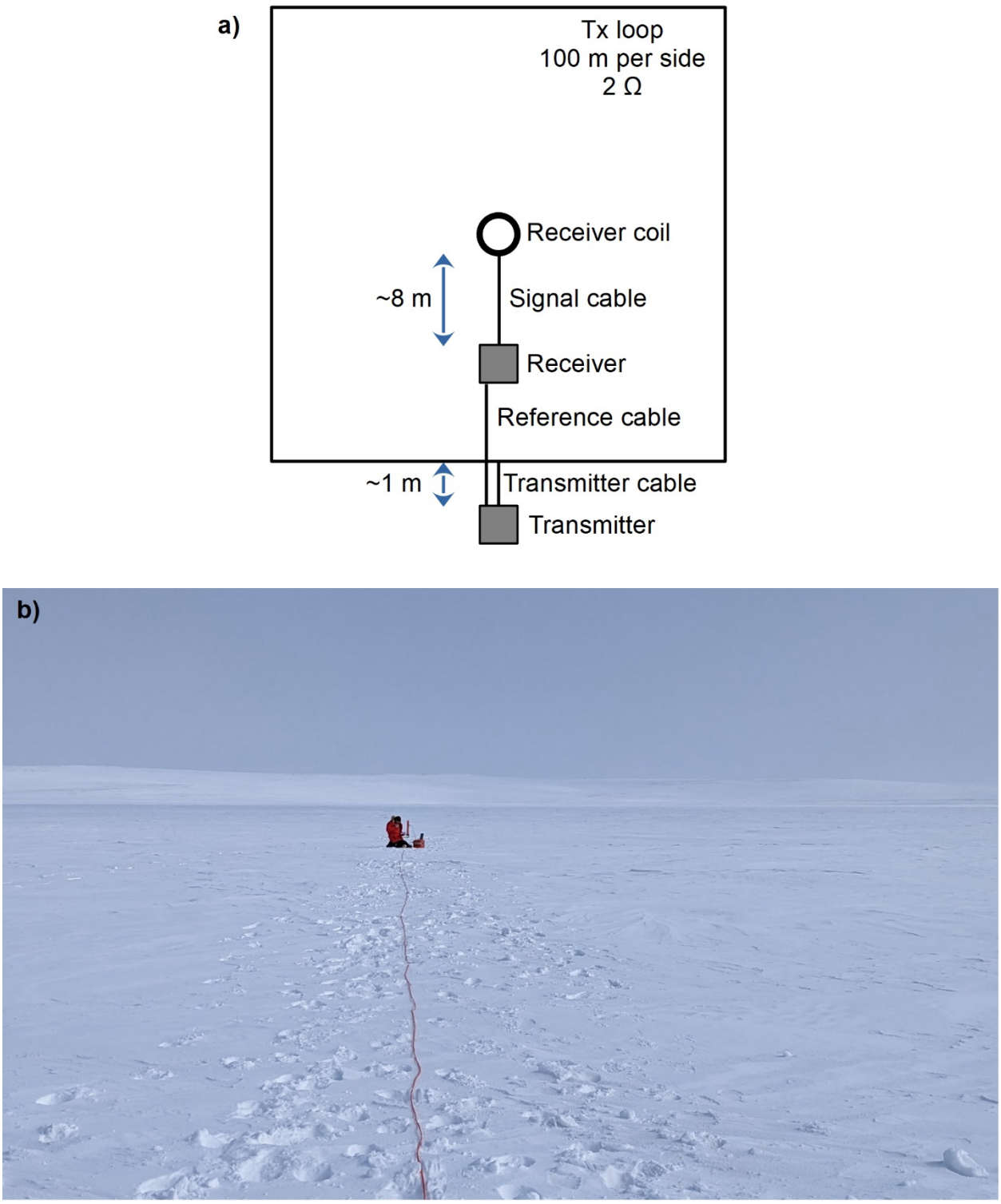

Figure 3. a) Schematic of TEM sounding survey layout (not to scale). b) View looking northeast towards the TEM receiver coil and operator at Site 1, Little Meliadine Lake, Nunavut. Photograph by K. Brewer. NRCan photo 2023-421.

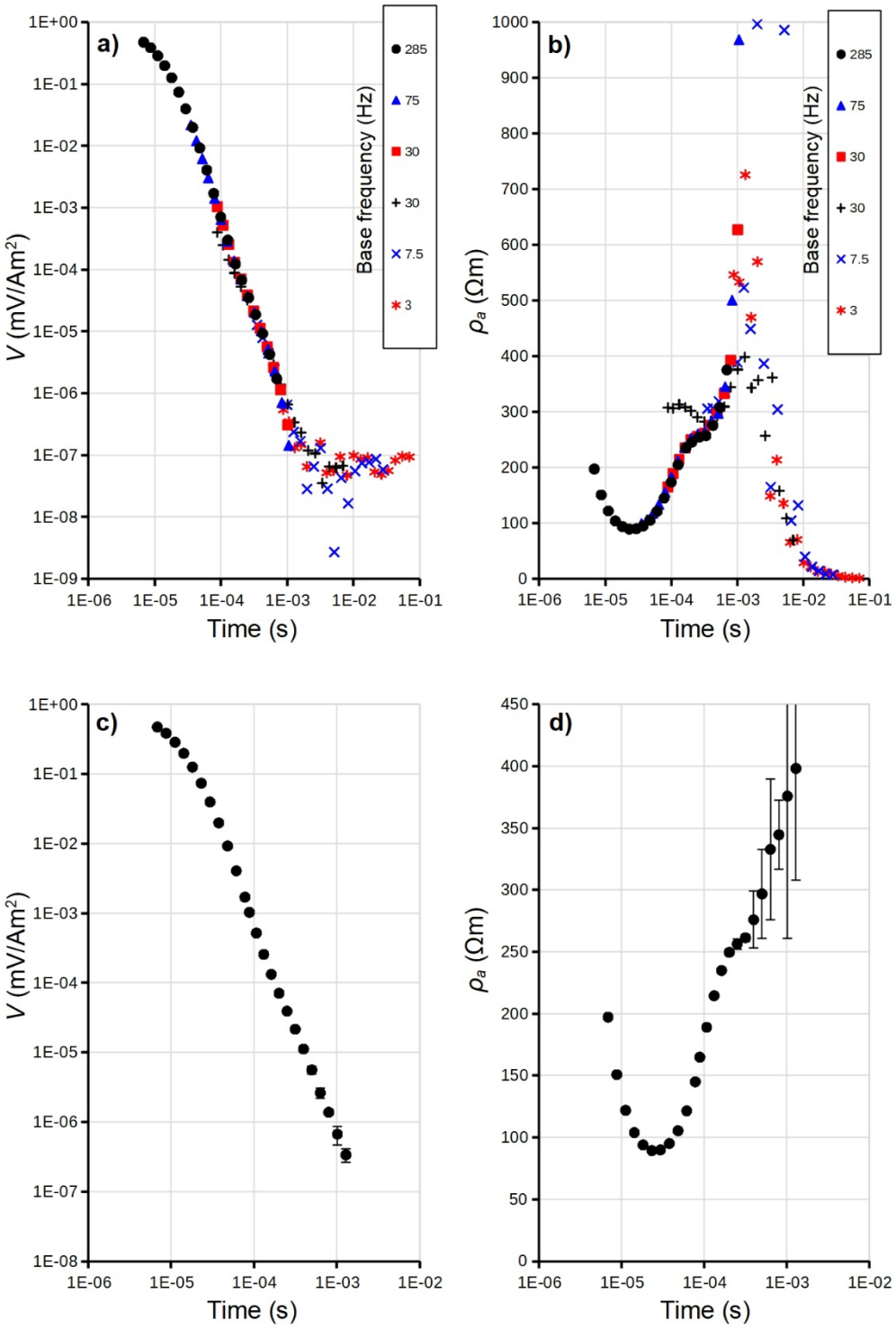

Figure 4. a) TEM sounding data gain-adjusted and normalized for all base frequencies at Site 1. The noise level is approximately 10^{-7} mV/Am^2 at approximately 1.3 ms. b) Transformation to apparent resistivity accentuates offsets between different base frequencies. c) Edited TEM sounding data for Site 1 (used for inversion). d) Transformation to apparent resistivity.

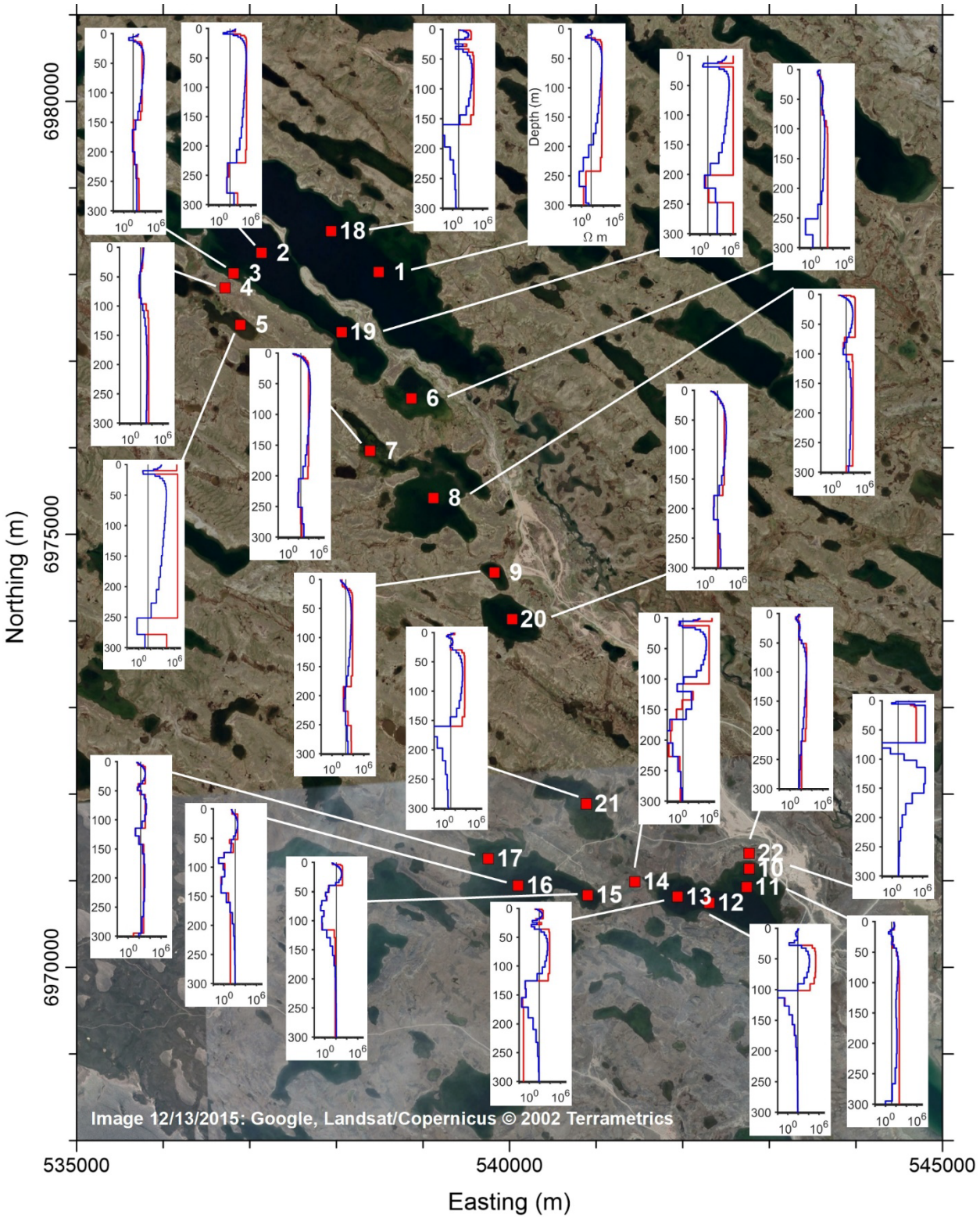

Figure 5. Summary of TEM models for L^2 (blue) and L^1 (red) model constraints. Models are displayed with a uniform resistivity of 10^{-2} to 10^{7} Ωm to a uniform depth of 300 m. Data misfit is variable across models and not all models are reliable to the displayed depth (Appendix)

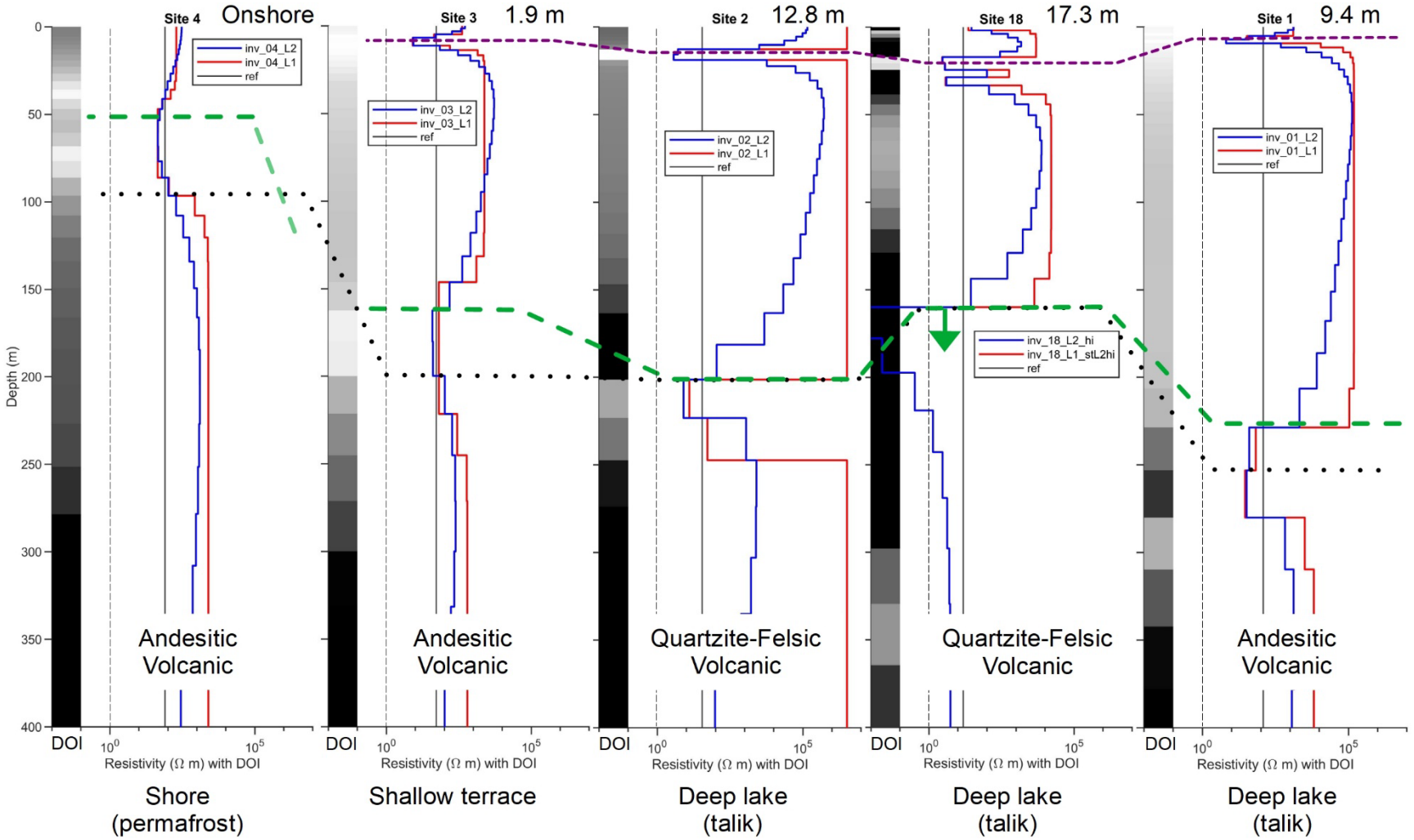

Figure 6. Cross section of TEM sounding models across Little Meliadine Lake from west (left) to east (right): Sites 4, 3, 2, 18, 1 (Figure 1). Lake depth or BFI is indicated above each model. Shallow and deep conductors (purple and green dashed lines) are observed for all soundings over Little Meliadine Lake, but not onshore. Uncertainty of depth is indicated by arrows. DOI values are given from 0 (white) to 1 (black). The approximate depth of reliable model interpretation is given by the black dotted line.

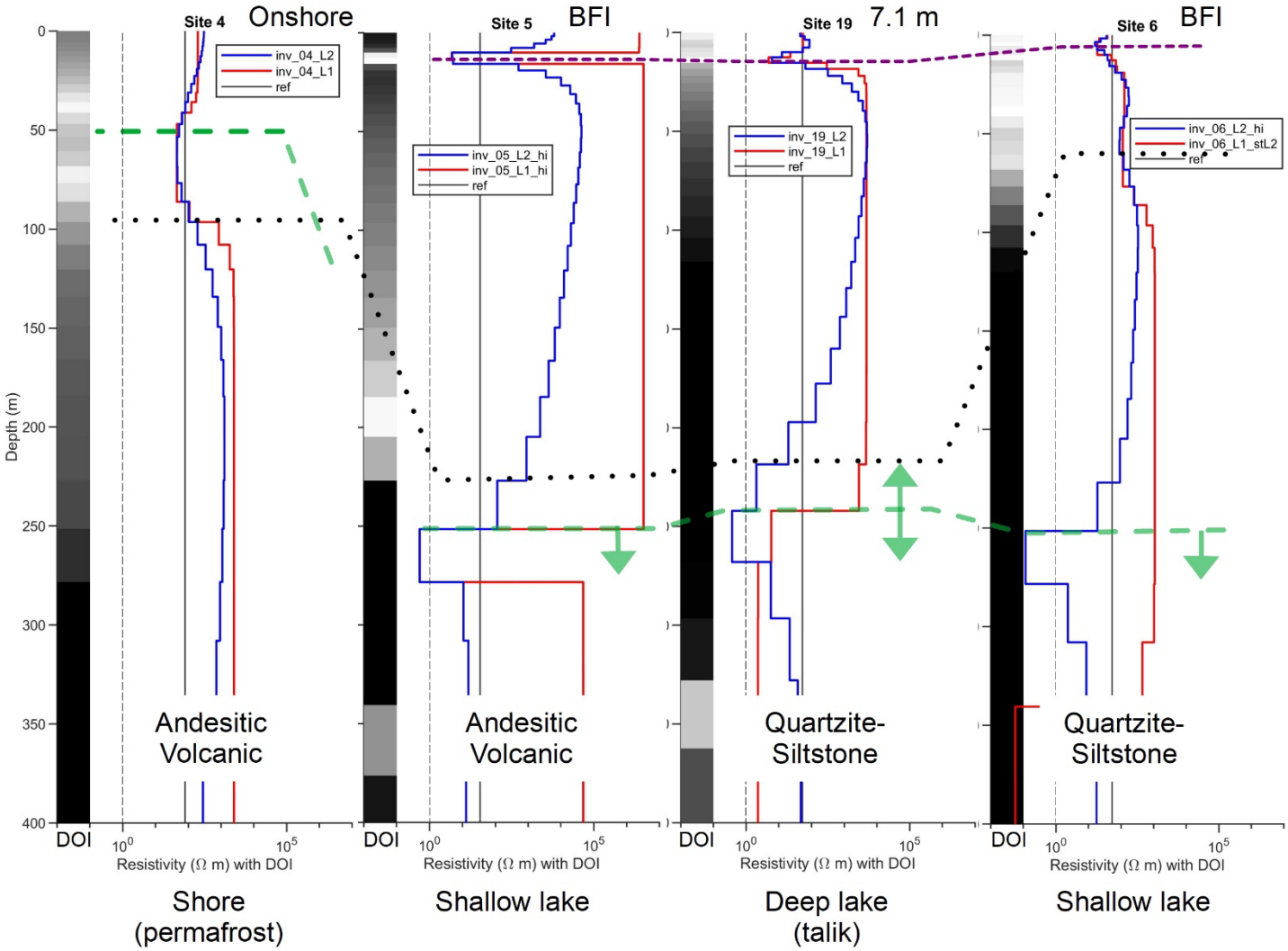

Figure 7. Cross section of TEM sounding models across Little Meliadine Lake from northwest (left) to southeast (right): Sites 4, 5, 19, 6 (Figure 1). Lake depth or BFI is indicated above each model. A shallow conductor (purple dashed line) is observed for all lakes. Presence of a deep conductor is interpreted, but uncertain (green dashed line). Uncertainty of depth is indicated by arrows. DOI values are given from 0 (white) to 1 (black). The approximate depth of reliable model interpretation is given by the black dotted line.

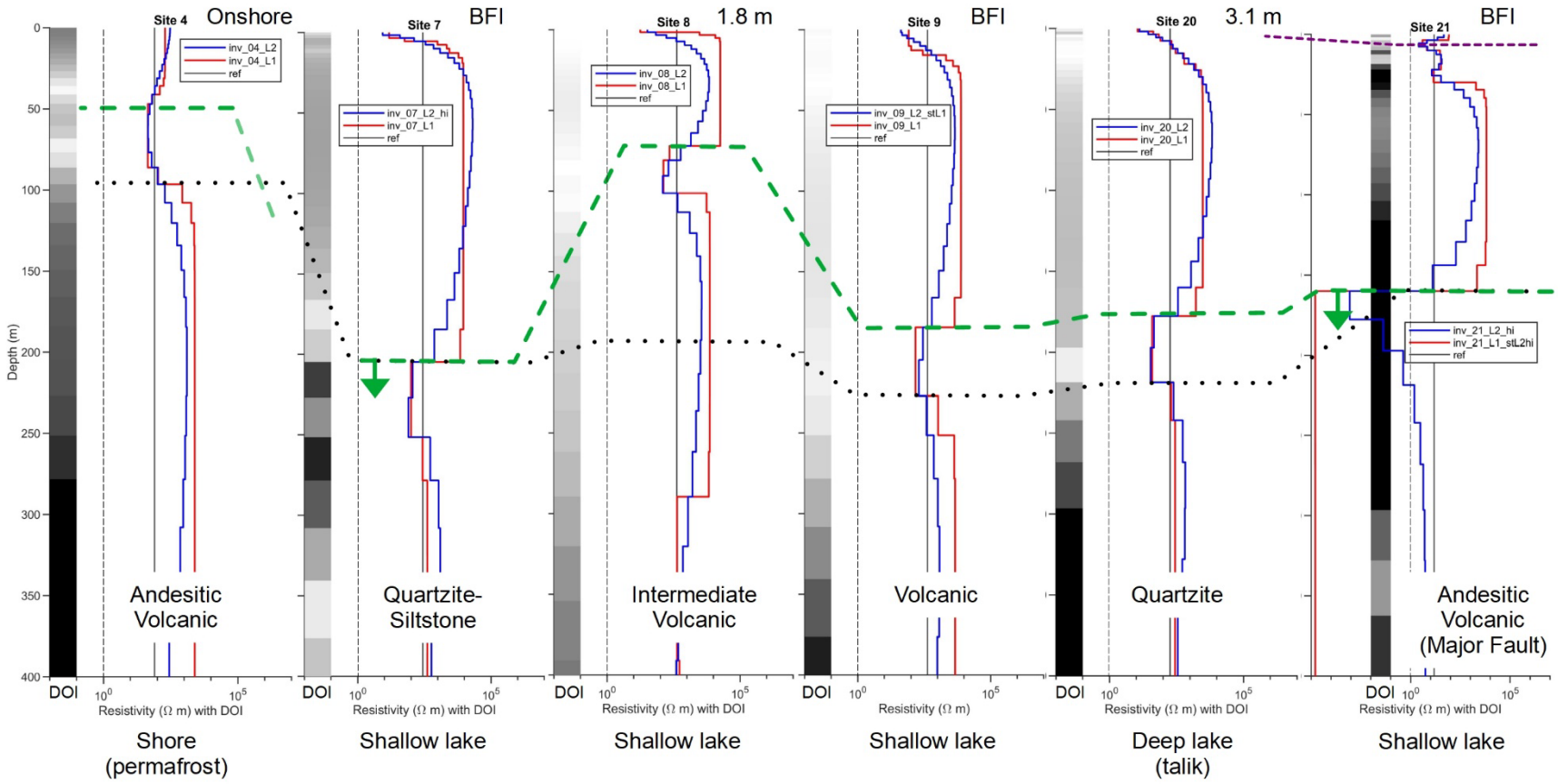

Figure 8. Cross section of TEM sounding models across Ming Major Lake from northwest (left) to southeast (right): Sites 4, 7, 8, 9, 20, 21 (Figure 1). Lake depth or BFI is indicated above each model. Shallow conductors (purple dashed line) or a conductive surface, and a deep conductor (green dashed line) are observed for all lakes. Uncertainty of depth is indicated by arrows. DOI values are given from 0 (white) to 1 (black). The approximate depth of reliable model interpretation is given by the black dotted line.

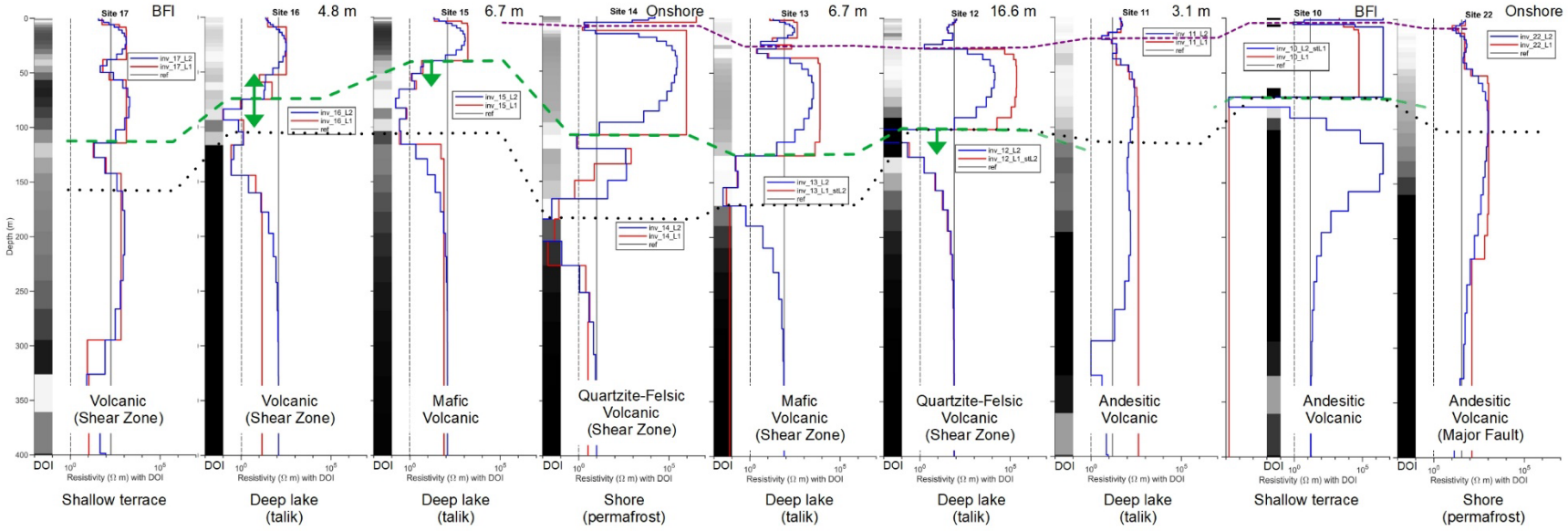

Figure 9. Cross section of TEM sounding models from Second Landing Lake to First Landing Lake from west (left) to east (right): Sites 17, 16, 15, 14, 13, 12, 11, 10, 22. Lake depth or BFI is indicated above each model. A deep conductor (green dashed line) is observed across Second Landing Lake and between the lakes, but not continuously across First Landing lake. Uncertainty of depth is indicated by arrows. DOI values are given from 0 (white) to 1 (black). The approximate depth of reliable model interpretation is given by the black dotted line.

APPENDIX

TEM data and inversion results are presented on a site-by-site basis. The data used for inversion are a result of iterative editing of the gain-adjusted and normalized sounding data according to the following general principles consistent with lower noise, better time resolution, and smooth sounding curves: the last several gates at each frequency were removed in preference of the first gates at the next frequency; higher frequencies were preferentially retained over lower frequencies; TEM47 data were preferentially retained over TEM57 data; the first few gates at each frequency were removed to achieve consistency with the last gates of the next higher frequency; and data with noise levels in excess of 25% were removed.

Inversion results are shown for each site using both L^2 (blue) and L^1 (red) model constraints. Solution convergence and the best possible data fit were typically achieved using the most representative halfspace ("ref") as the initial and reference resistivity. For some sites, improved convergence and/or better data fit were achieved using an L^2 or L^1 model constraint initialized with the L^1 or L^2 solution ("stL1" or "stL2"), or by using an overly conductive reference model (e.g., Oldenborger and Oldenburg, 2008) given by the most representative halfspace scaled by e ("hi"). For each model, predicted voltage is compared to the measured voltage for which several measures of data misfit were calculated. The L^2 and L^1 solutions do not always converge to the same level of misfit. Similarly, the inverse solutions for different sites typically exhibit different levels of misfit. In general, a model with lower misfit can be considered the better model in the absence of overfitting or unrealistic model structure.

Attempts were made to initialize and/or reference the inversions with models representing the lake ice and water depth. In almost all cases, these attempts at initialization and referencing failed. The lake ice is a difficult target to resolve given its nature as a very thin resistor. Inversion results will tend to lump the ice layer with the overall conductance of the lake, especially for inversions that involve a homogeneous reference model (L^2 or L^1). Furthermore, there is no information to assign the initial or reference resistivity below the lake bottom.

The L^2 and L^1 solutions result from optimization of different objective functions and their similarity can be considered as a measure of model reliability (if similar levels of data misfit are acheived). Model reliability was also assessed using the depth of investigation index (Oldenburg and Li, 1999). The depth of investigation index (DOI) was computed using the natural logarithm of electrical conductivity with high- and low-sided reference models ("hi" and "lo") given by the most representative halfspace scaled by e. The DOI is a measure of the data influence and increases

as the model resolution decreases and the influence of non-uniqueness increases (Oldenborger et al., 2007). The TEM models are displayed to a uniform depth of 400 m, but the DOI shows that model reliability varies with depth, and that not all models are reliable to the same depth (results are shown with DOI = 0 as white and DOI ≥ 1 as black).

Although the DOI is useful for assessing model reliability, it is most valid when the high- and low-sided solutions converge to the same level of data misfit. Otherwise, the DOI may be comparing models that are too far from the final solution and the DOI may not be an accurate measure of model resolution (Oldenborger et al., 2007). Furthermore, the DOI was developed for galvanic resistivity surveys for which the sensitivity is linearly proportional to resistivity. For TEM surveys, the sensitivity decreases nonlinearly with resistivity and the data are insensitive to very high resistivity. As such, the DOI can be overly-restrictive for resistive ground where the model resistivity is high and stable, but the resistivity may be increased without significantly altering the predicted data. In these cases, a resistive layer may be reliably interpreted despite high DOI values, but the value of the resistivity may be uncertain. Resistivity greater than 10^6 Ωm is considered to be an inversion artefact due to loss of sensitivity. Conversely, non-uniqueness may be observed for low resistivity despite higher sensitivity. In this case, a conductive layer may be reliably interpreted despite high DOI values, but the exact layer depth or value of the resistivity may be uncertain. Resistivity less than 10^{-2} Ωm is considered physically unreasonable (e.g., Palacky, 1988) and is considered an inversion artefact. Overall model uncertainty or reliability should be assessed using a combination of factors including data noise, data misfit, model stability, and the DOI.

Measures of Data Misfit

MN: mean (%) noise for measured voltage
RMSN: root-mean-square (%) noise for measured voltage
MPE: mean percent error (data misfit)
MAPE: mean absolute percent error (data misfit)
RMSPE: root-mean-square percent error (data misfit)
ϕ_d: data objective function at convergence
χ^2: chi-squared statistic (equal to unity for overall data misfit commensurate with noise)
ARE: absolute relative error (datum misfit)
NE: normalized error (equal to unity for datum misfit commensurate with noise)

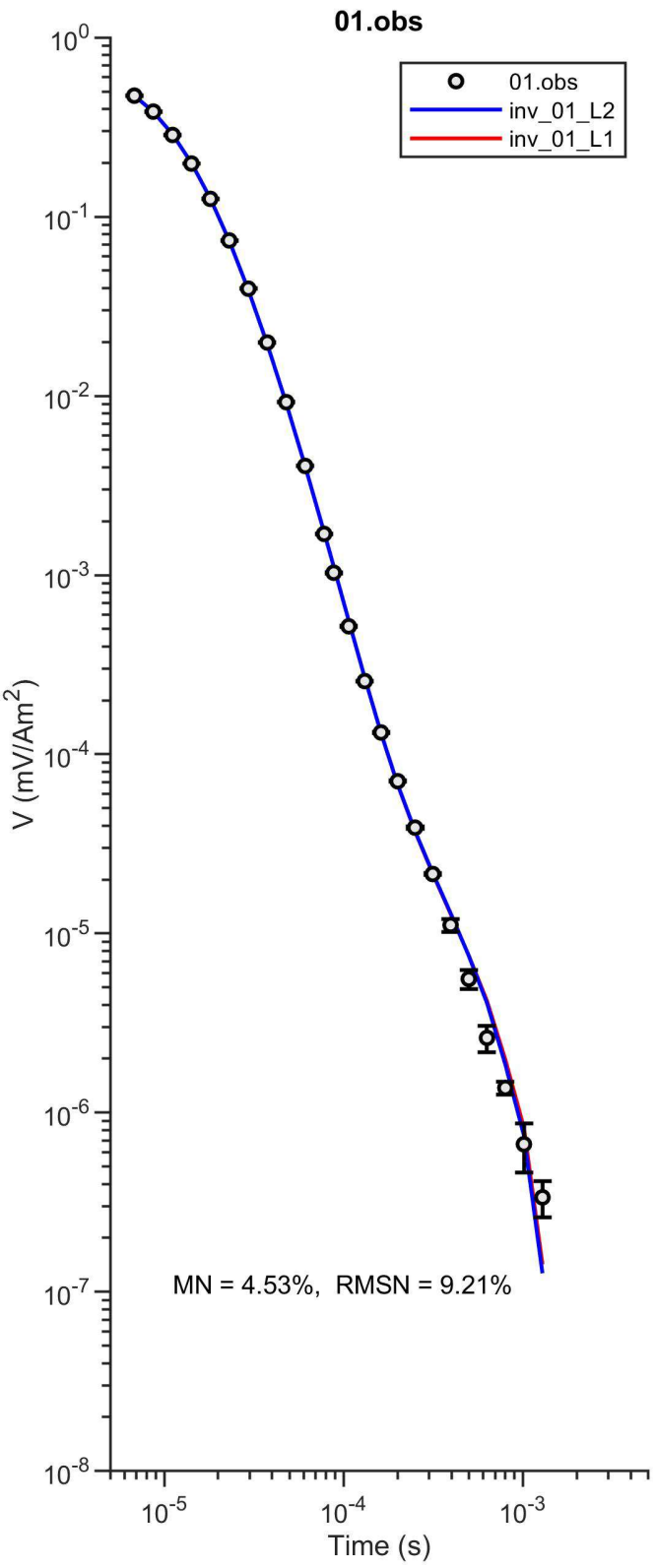
01.obs
01.obs
inv_01_L2
inv_01_L1
V (mV/Am^2)
Time (s)
MN = 4.53%, RMSN = 9.21%

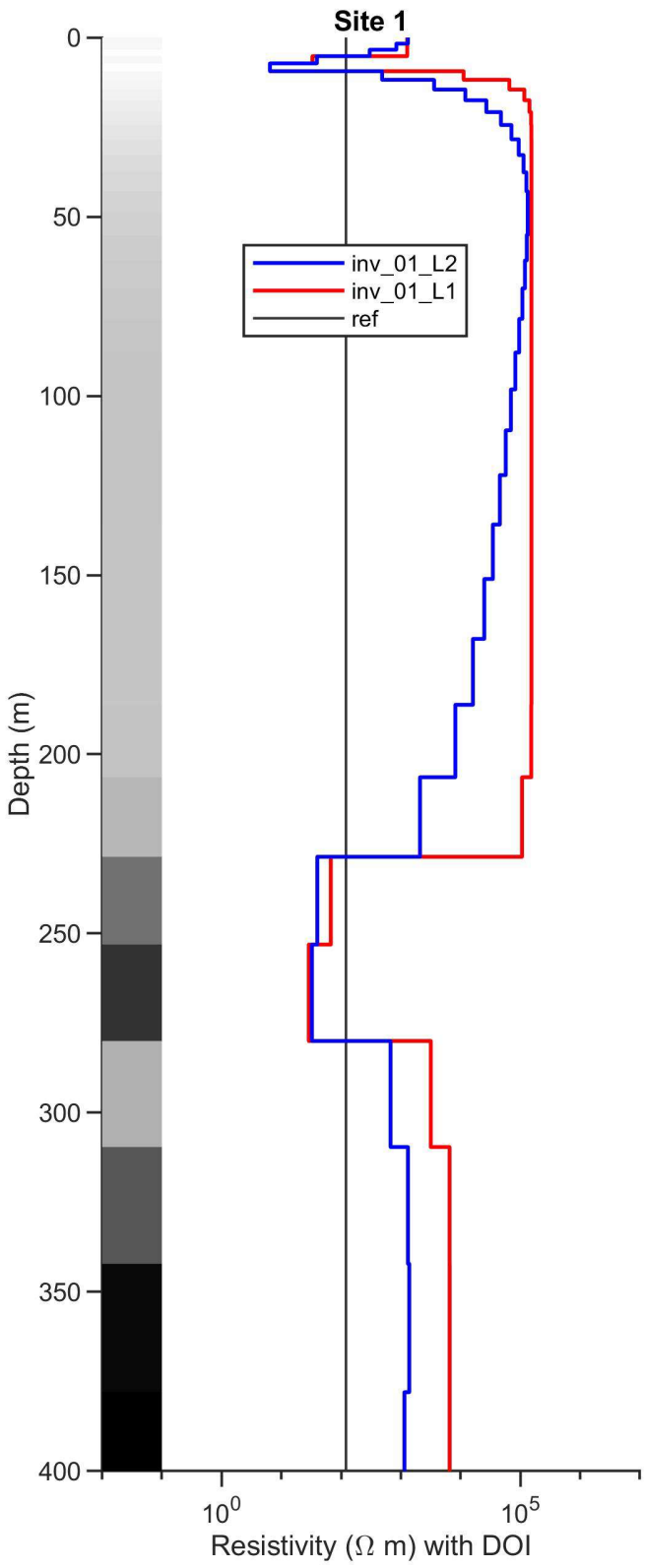
Site 1
inv_01_L2
inv_01_L1
ref
Depth (m)
Resistivity (Ω m) with DOI

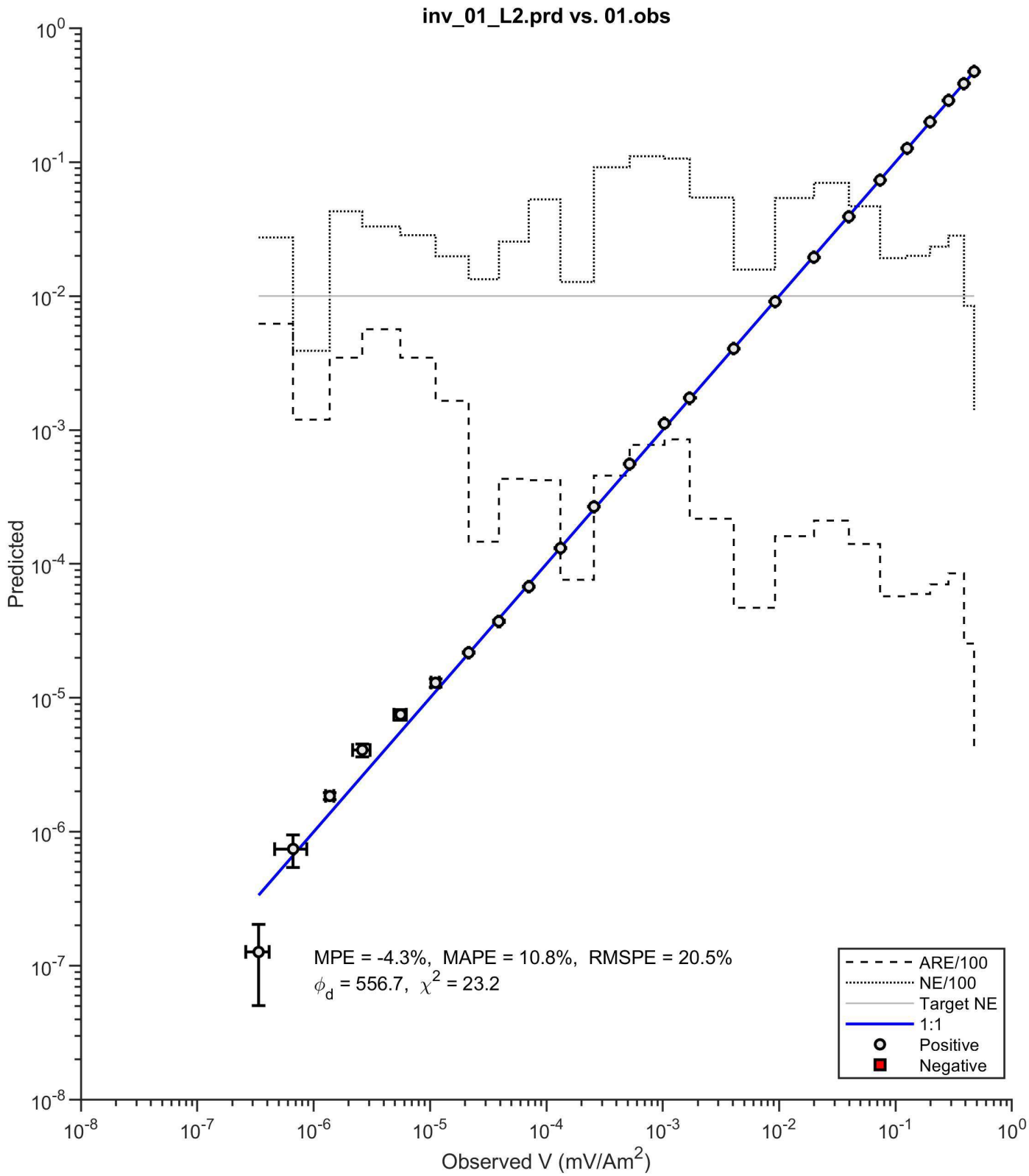
inv_01_L2.prd vs. 01.obs
Predicted
Observed V (mV/Am^2)
10^{0}
10^{-1}
10^{-2}
10^{-3}
10^{-4}
10^{-5}
10^{-6}
10^{-7}
10^{-8}
MPE = -4.3%, MAPE = 10.8%, RMSPE = 20.5%
ϕ_d = 556.7, χ^2 = 23.2
ARE/100
NE/100
Target NE
1:1
Positive
Negative

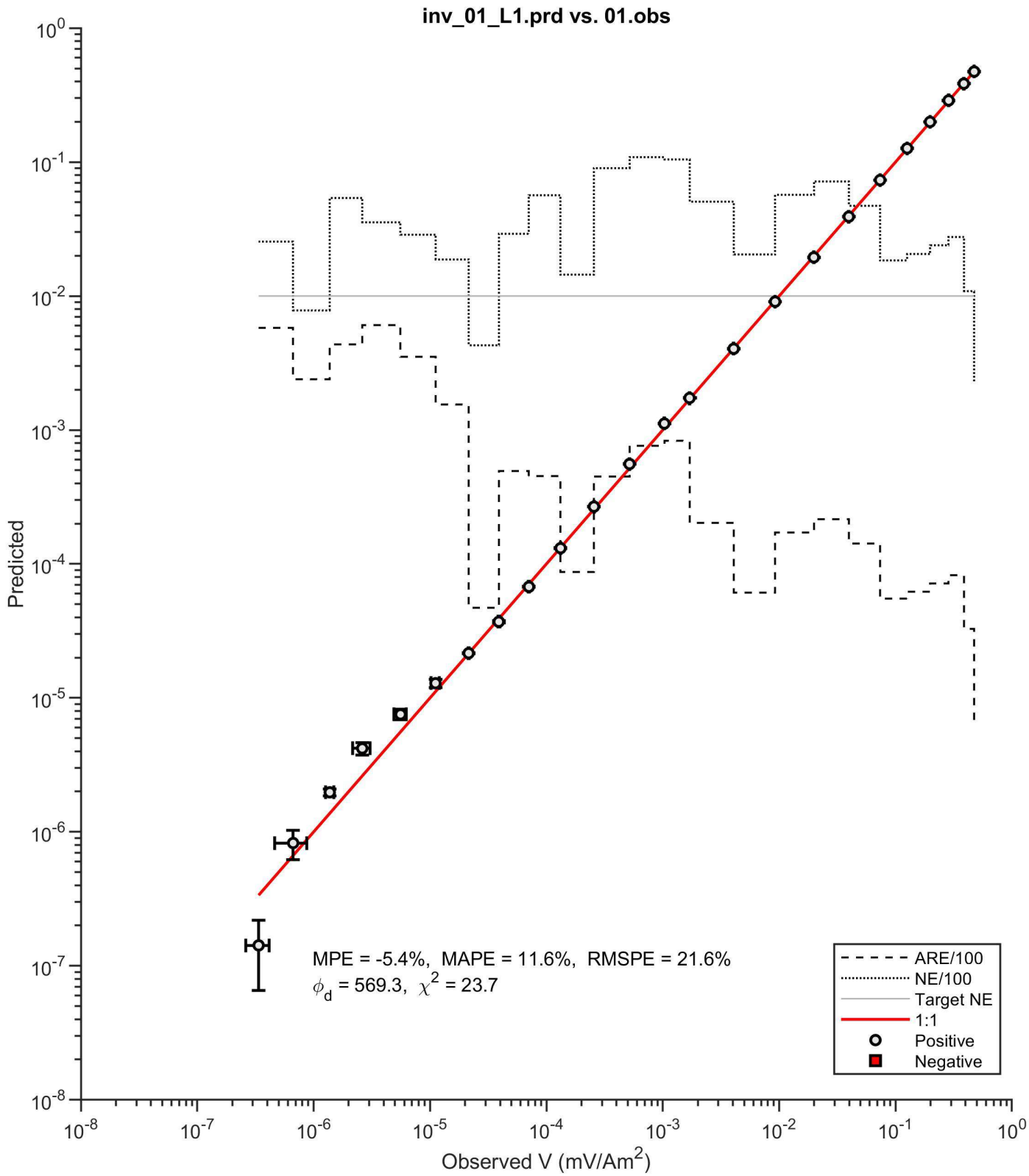
inv_01_L1.prd vs. 01.obs
Predicted
Observed V (mV/Am^2)
MPE = -5.4%, MAPE = 11.6%, RMSPE = 21.6%
ϕ_d = 569.3, χ^2 = 23.7
ARE/100
NE/100
Target NE
1:1
Positive
Negative

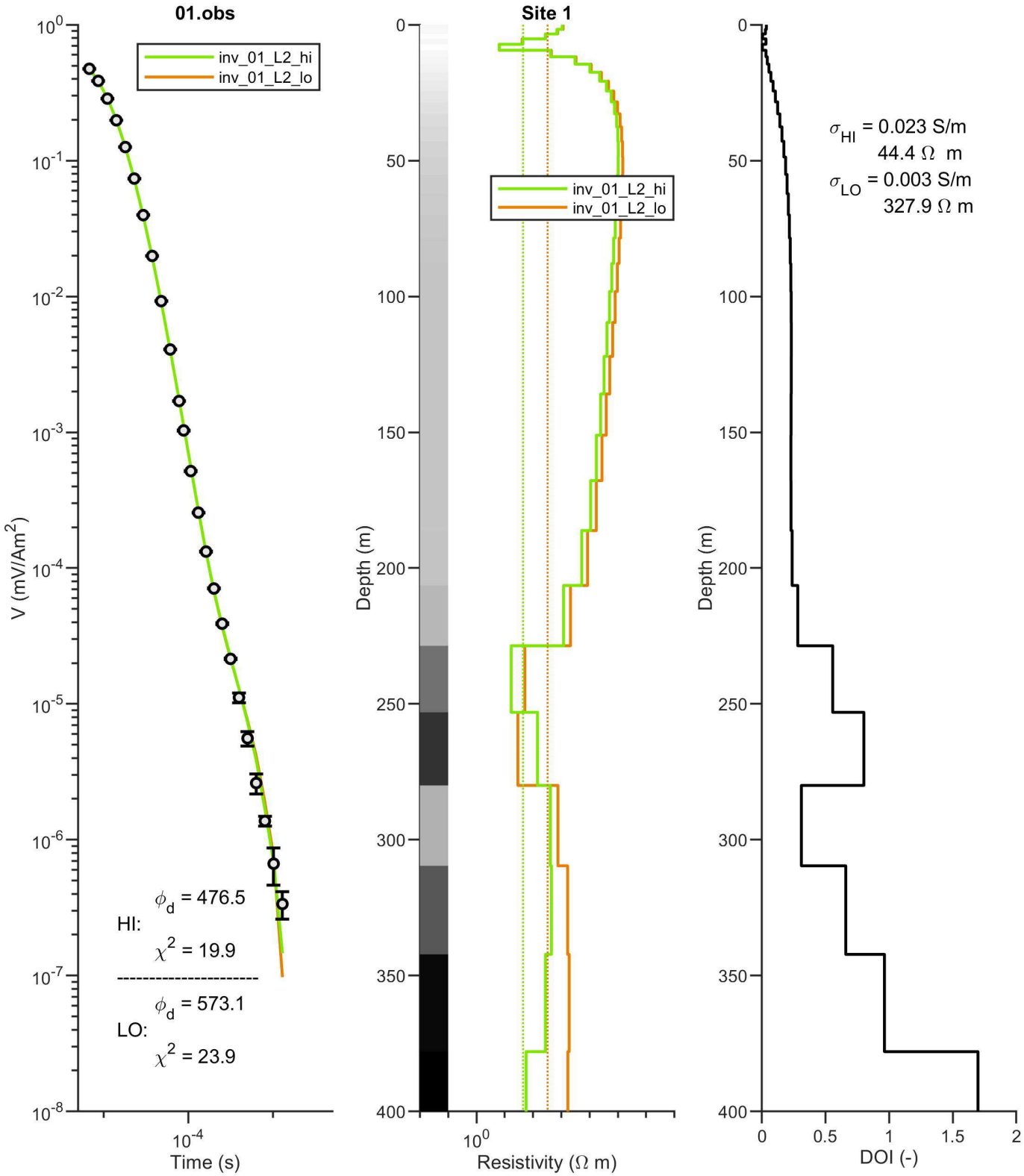
01.obs
inv_01_L2_hi
inv_01_L2_lo
V (mV/Am^2)
Time (s)
ϕ_d = 476.5
HI:
χ^2 = 19.9
ϕ_d = 573.1
LO:
χ^2 = 23.9
Site 1
inv_01_L2_hi
inv_01_L2_lo
Depth (m)
Resistivity (Ω m)
σ_{HI} = 0.023 S/m
44.4 Ω m
σ_{LO} = 0.003 S/m
327.9 Ω m
Depth (m)
DOI (-)

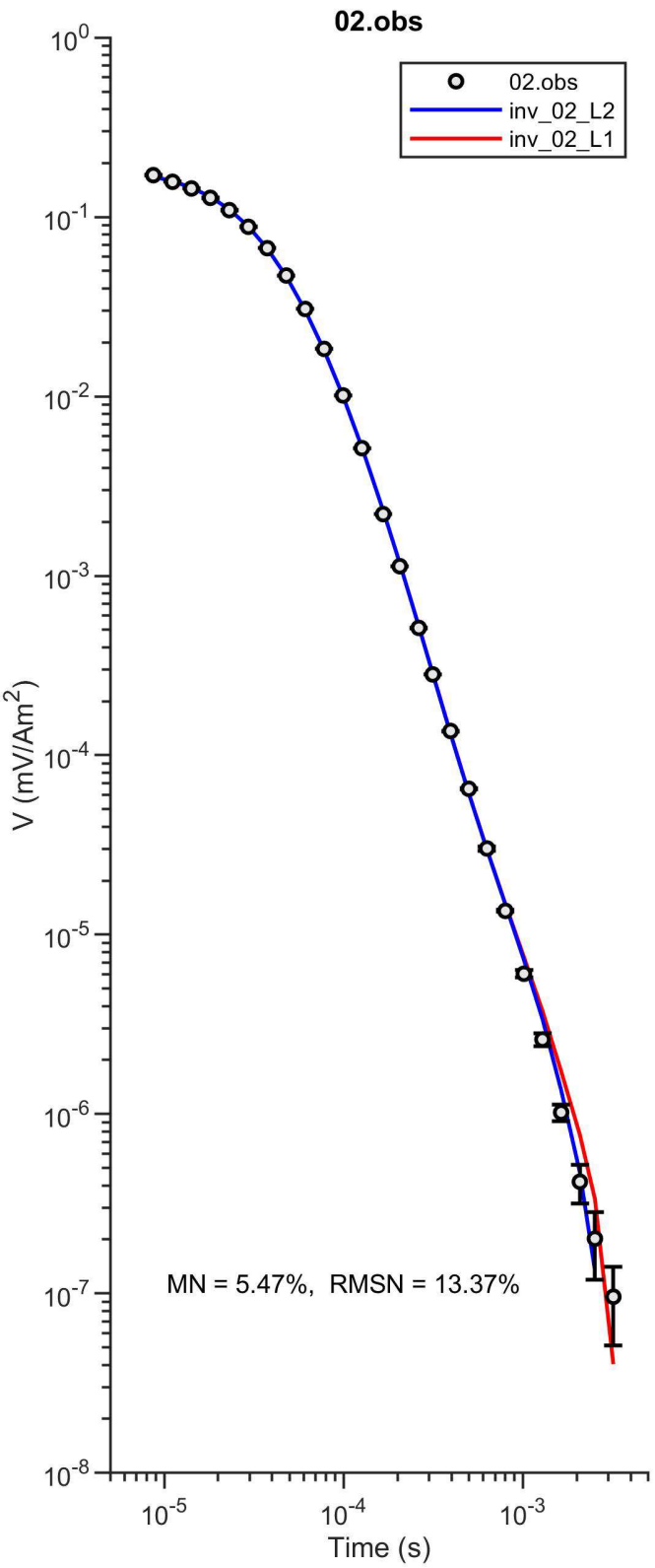
02.obs
02.obs
inv_02_L2
inv_02_L1
V (mV/Am^2)
Time (s)
MN = 5.47%, RMSN = 13.37%

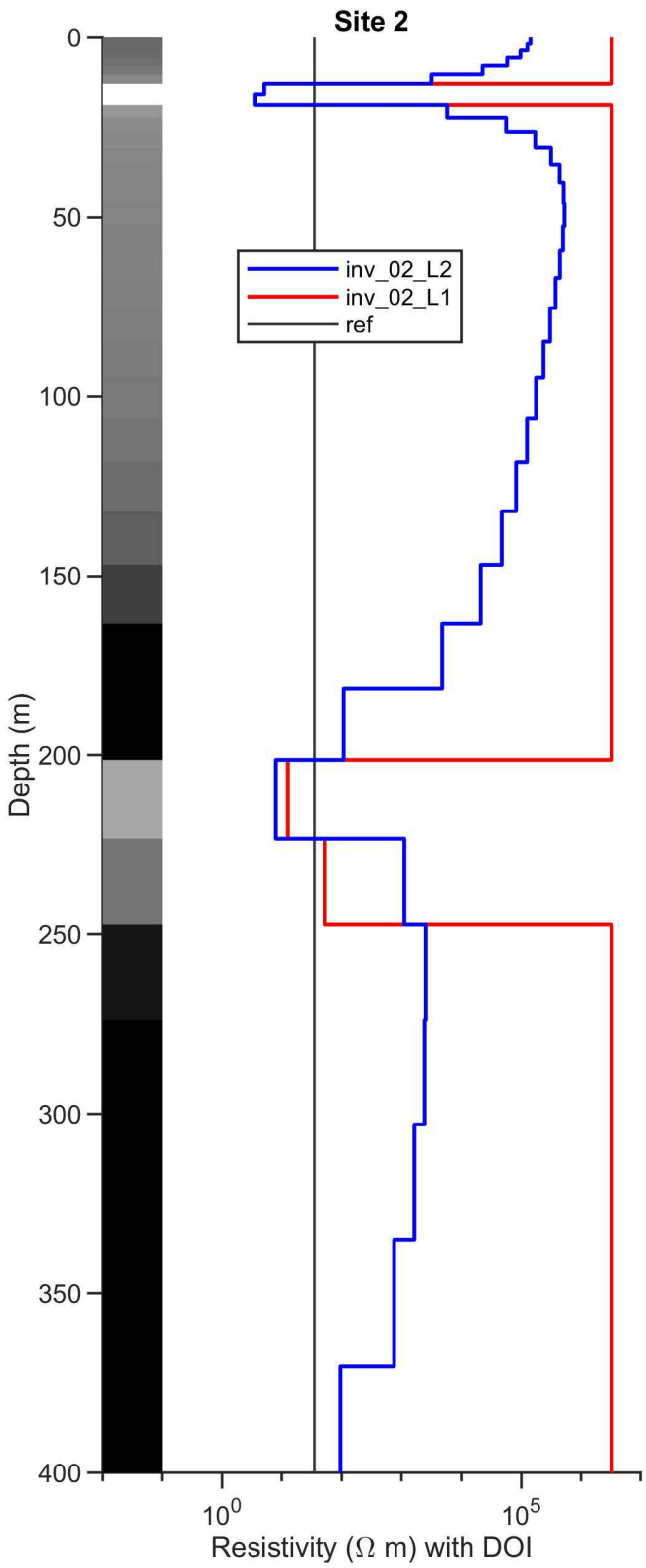
Site 2
inv_02_L2
inv_02_L1
ref
Depth (m)
Resistivity (Ω m) with DOI

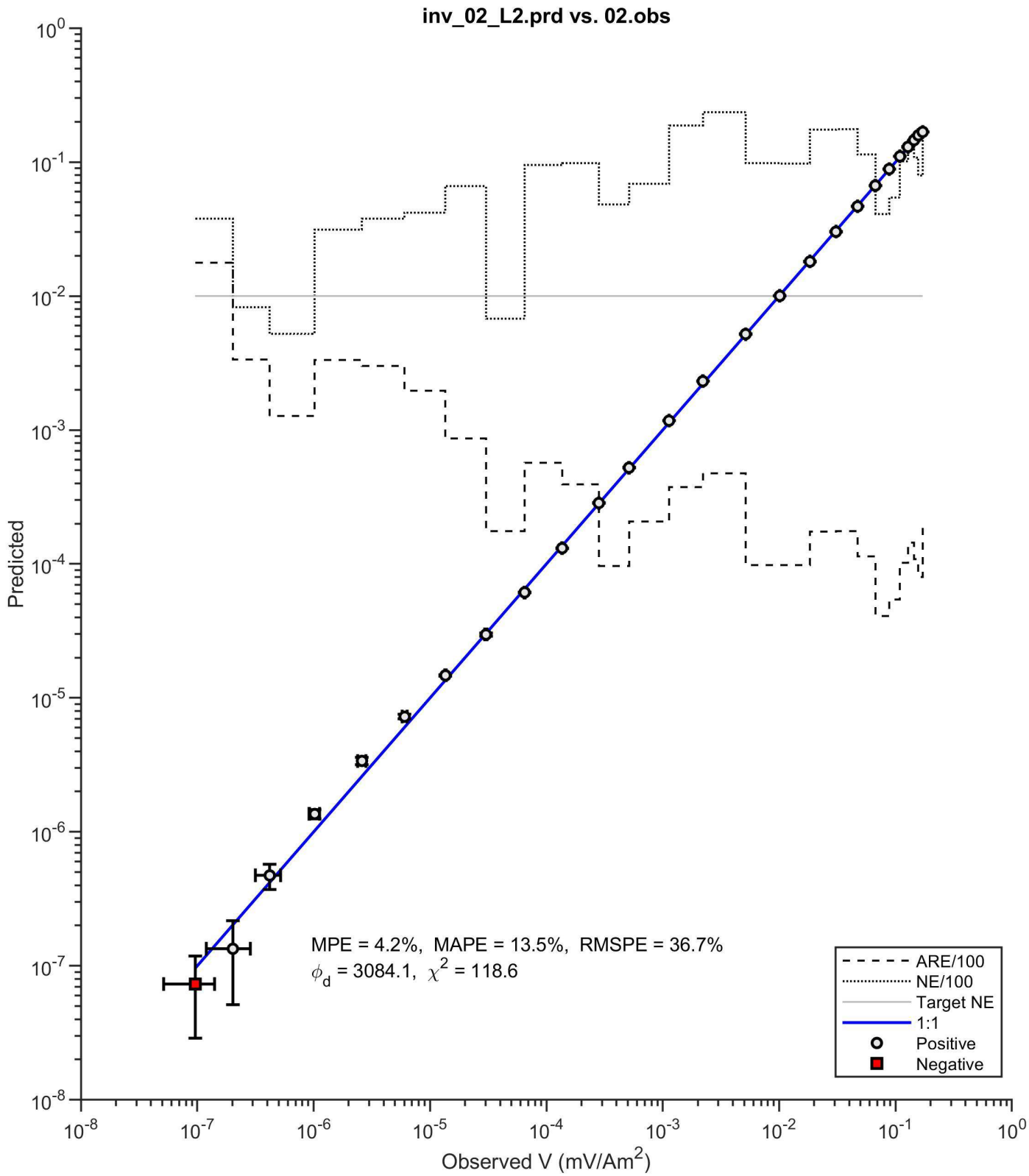
inv_02_L2.prd vs. 02.obs
Predicted
Observed V (mV/Am^2)
MPE = 4.2%, MAPE = 13.5%, RMSPE = 36.7%
ϕ_d = 3084.1, χ^2 = 118.6
ARE/100
NE/100
Target NE
1:1
Positive
Negative

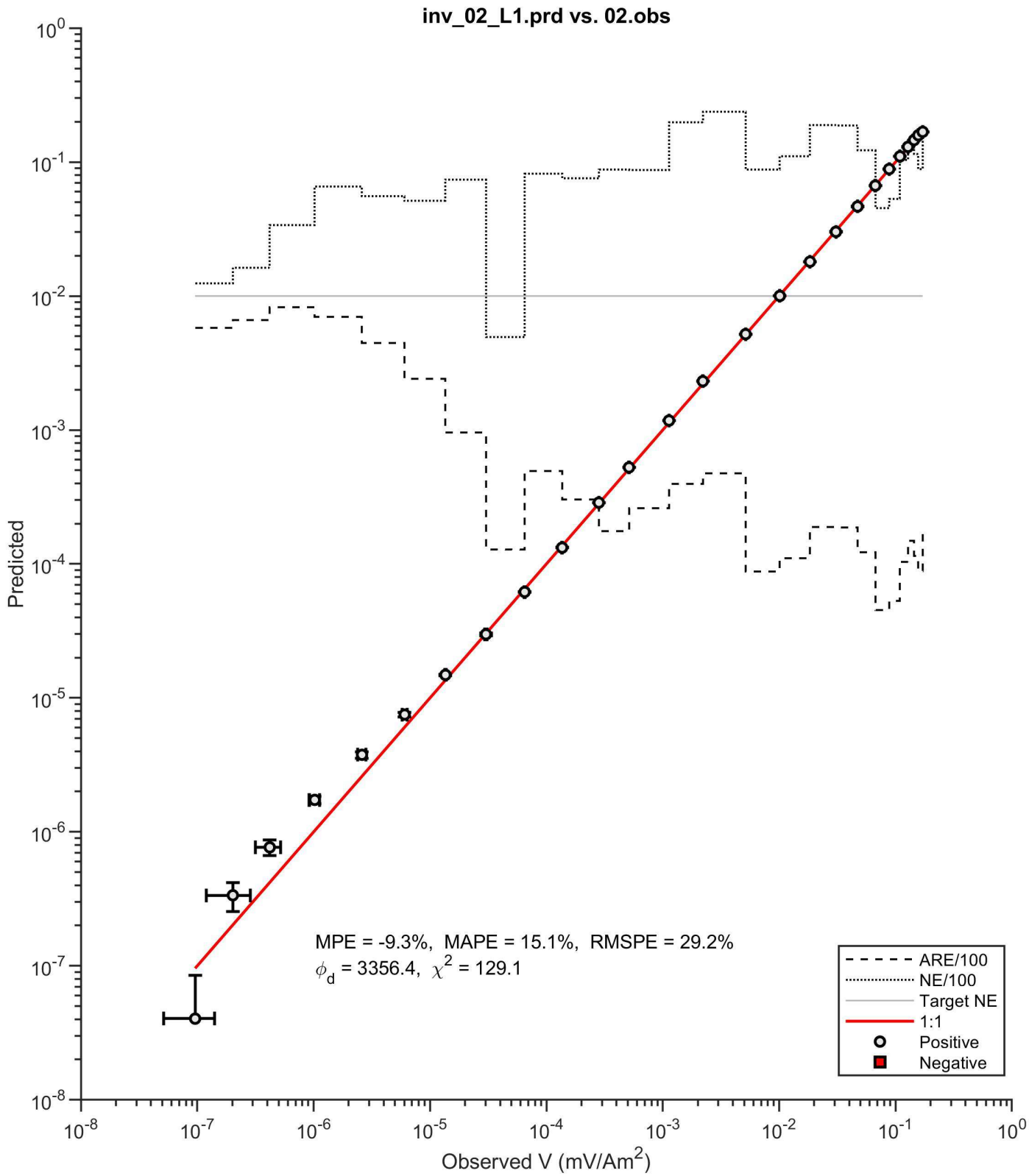
inv_02_L1.prd vs. 02.obs
Predicted
Observed V (mV/Am^2)
MPE = -9.3%, MAPE = 15.1%, RMSPE = 29.2%
ϕ_d = 3356.4, χ^2 = 129.1
ARE/100
NE/100
Target NE
1:1
Positive
Negative

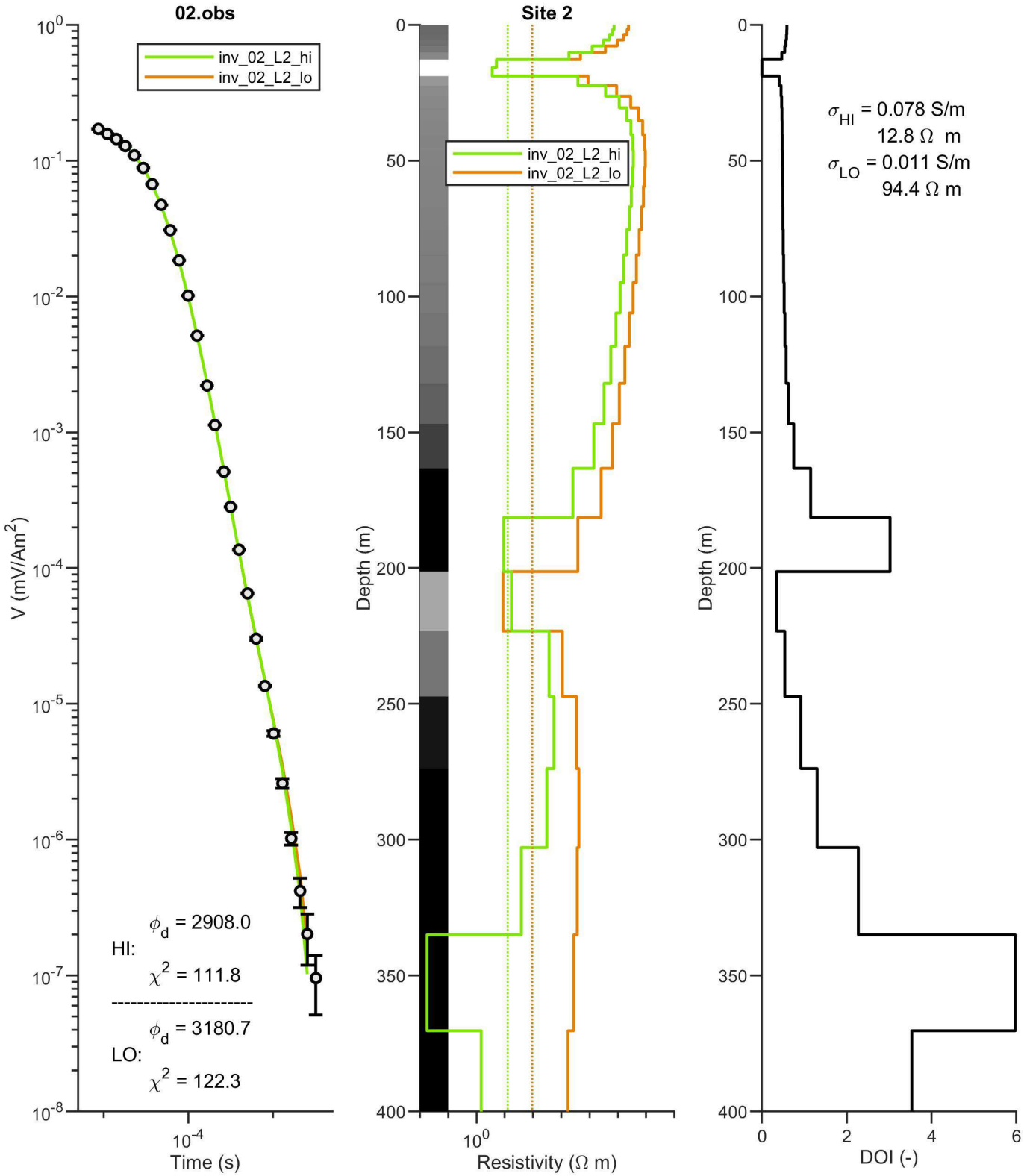
02.obs
inv_02_L2_hi
inv_02_L2_lo
V (mV/Am^2)
Time (s)
ϕ_d = 2908.0
HI:
χ^2 = 111.8
ϕ_d = 3180.7
LO:
χ^2 = 122.3
Site 2
inv_02_L2_hi
inv_02_L2_lo
Depth (m)
Resistivity (Ω m)
σ_{HI} = 0.078 S/m
12.8 Ω m
σ_{LO} = 0.011 S/m
94.4 Ω m
Depth (m)
DOI (-)

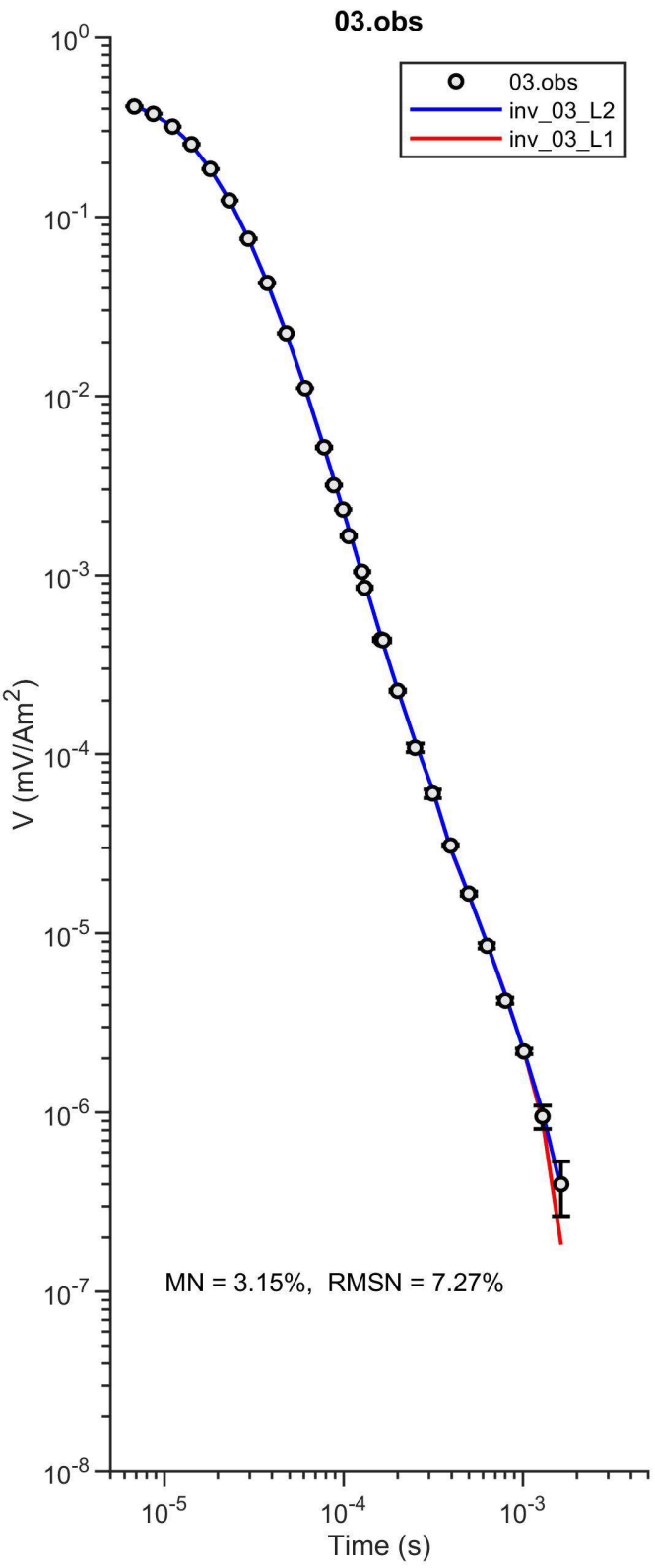
03.obs
03.obs
inv_03_L2
inv_03_L1
V (mV/Am^2)
Time (s)
MN = 3.15%, RMSN = 7.27%

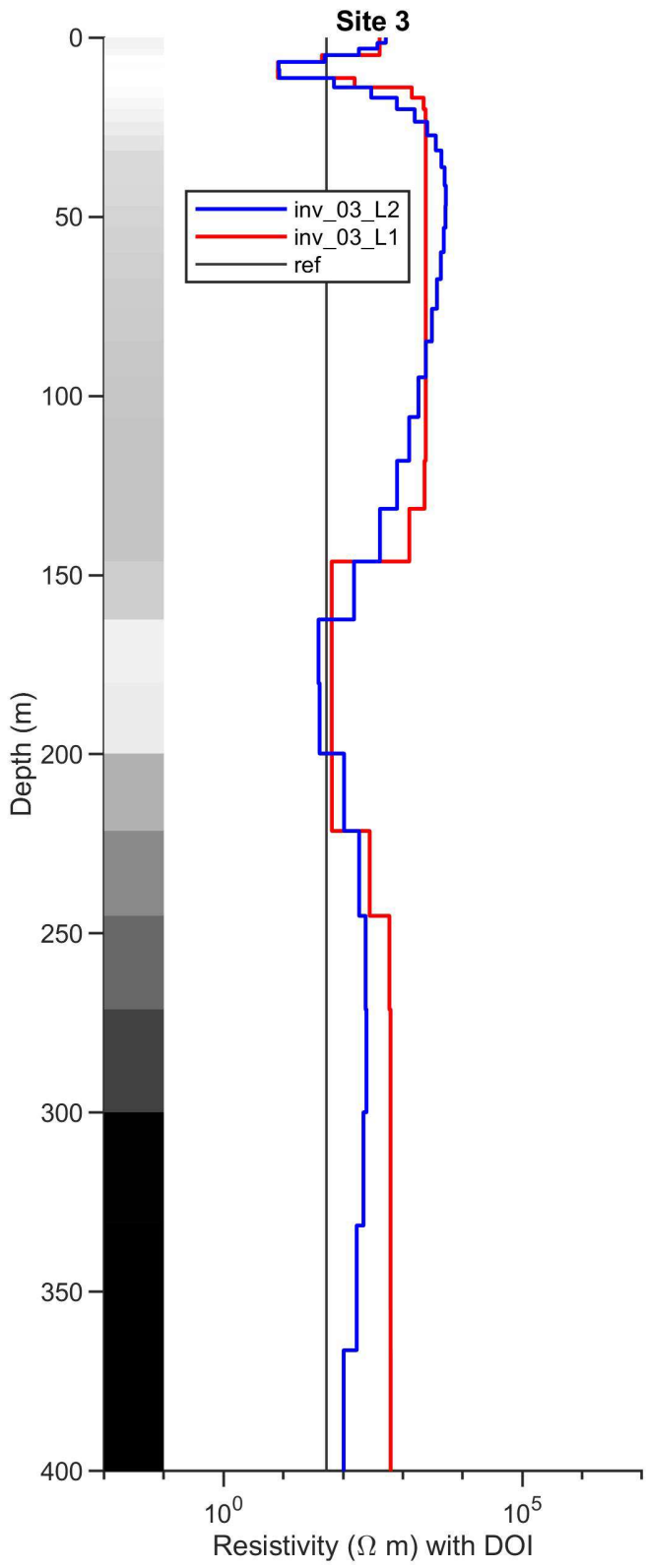
Site 3
inv_03_L2
inv_03_L1
ref
Depth (m)
Resistivity (Ω m) with DOI

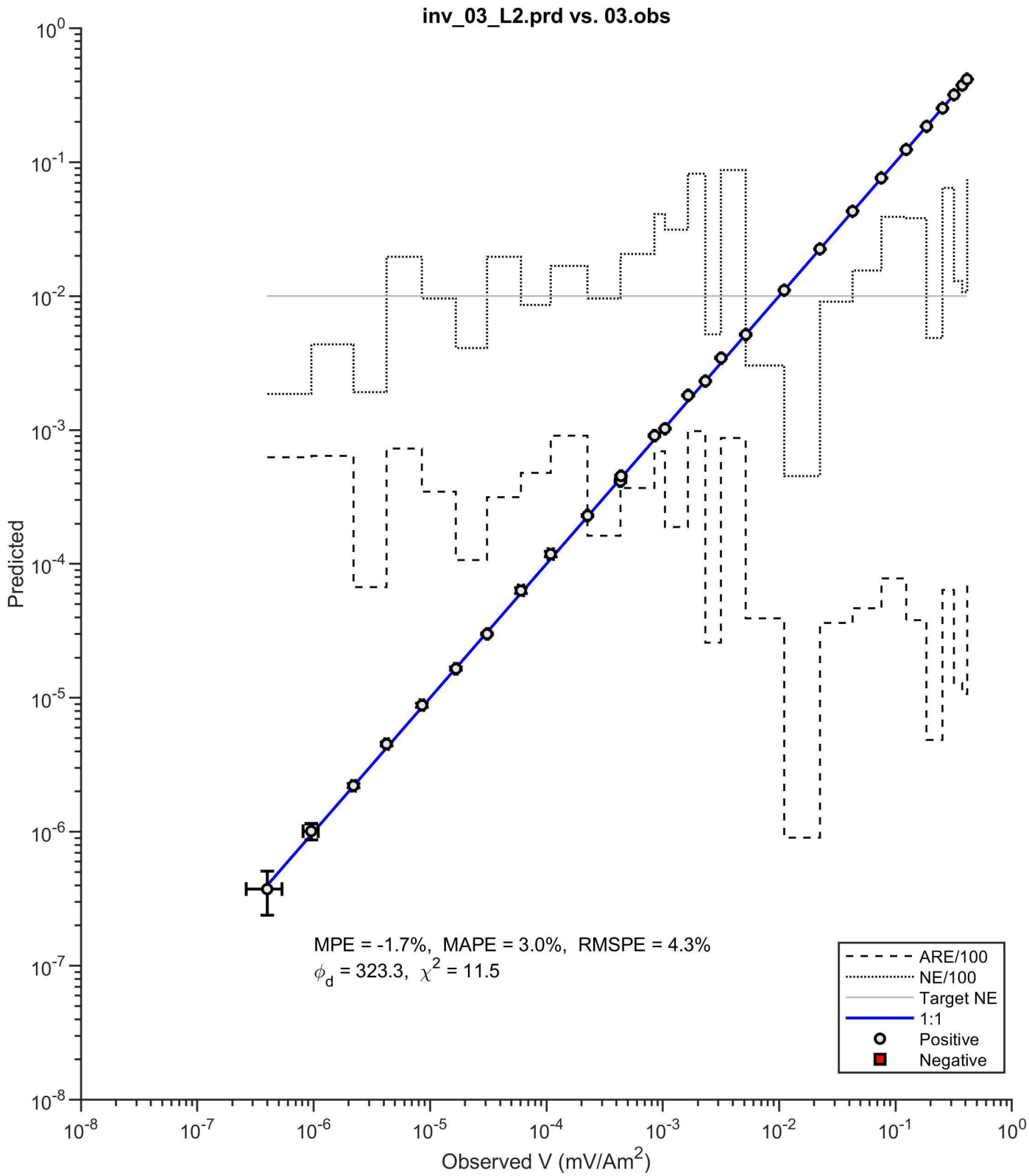
inv_03_L2.prd vs. 03.obs
Predicted
Observed V (mV/Am^2)
10^{0}
10^{-1}
10^{-2}
10^{-3}
10^{-4}
10^{-5}
10^{-6}
10^{-7}
10^{-8}
MPE = -1.7%, MAPE = 3.0%, RMSPE = 4.3%
ϕ_d = 323.3, χ^2 = 11.5
ARE/100
NE/100
Target NE
1:1
Positive
Negative

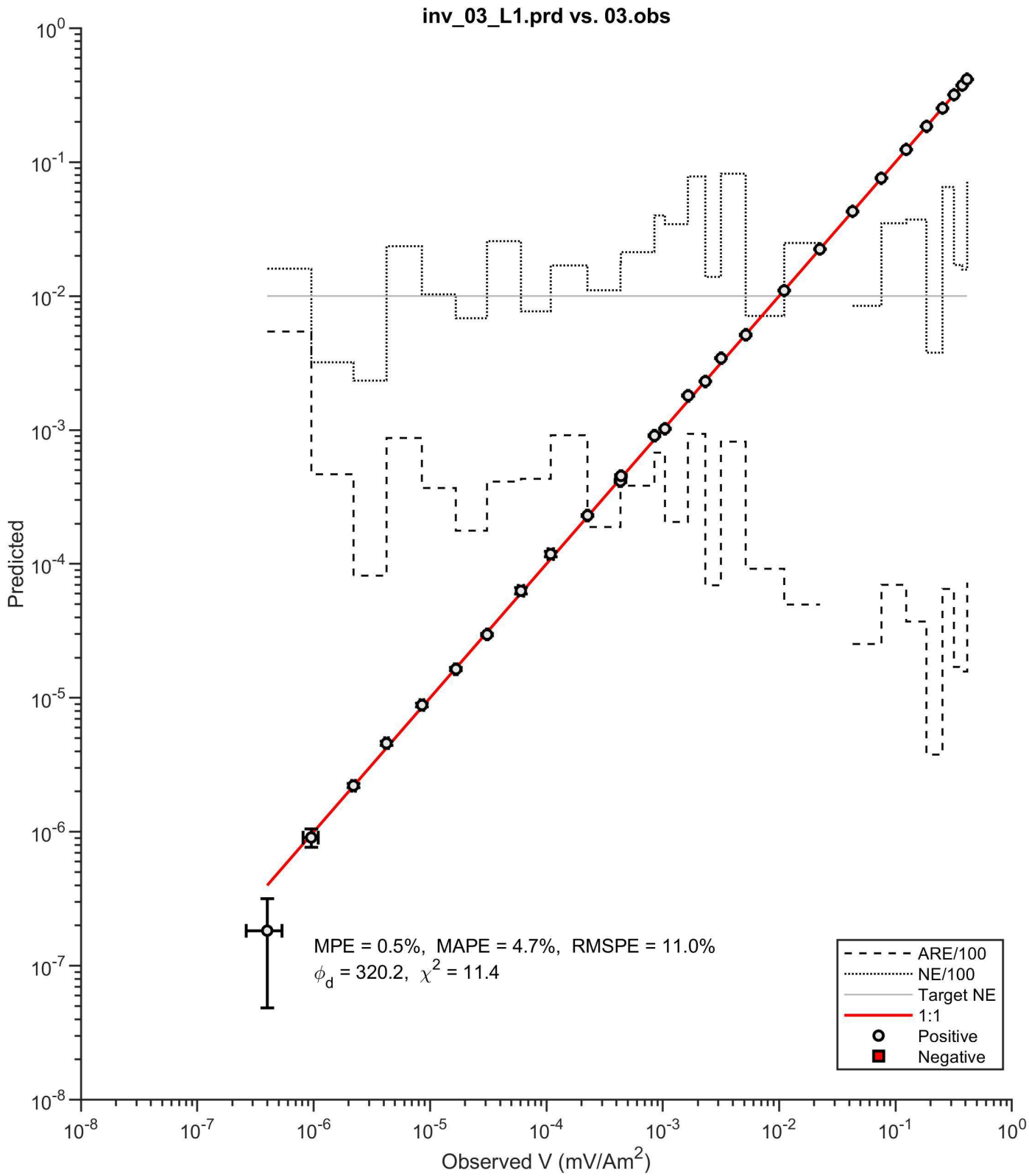
inv_03_L1.prd vs. 03.obs
Predicted
Observed V (mV/Am^2)
10^{0}
10^{-1}
10^{-2}
10^{-3}
10^{-4}
10^{-5}
10^{-6}
10^{-7}
10^{-8}
MPE = 0.5%, MAPE = 4.7%, RMSPE = 11.0%
ϕ_d = 320.2, χ^2 = 11.4
ARE/100
NE/100
Target NE
1:1
Positive
Negative

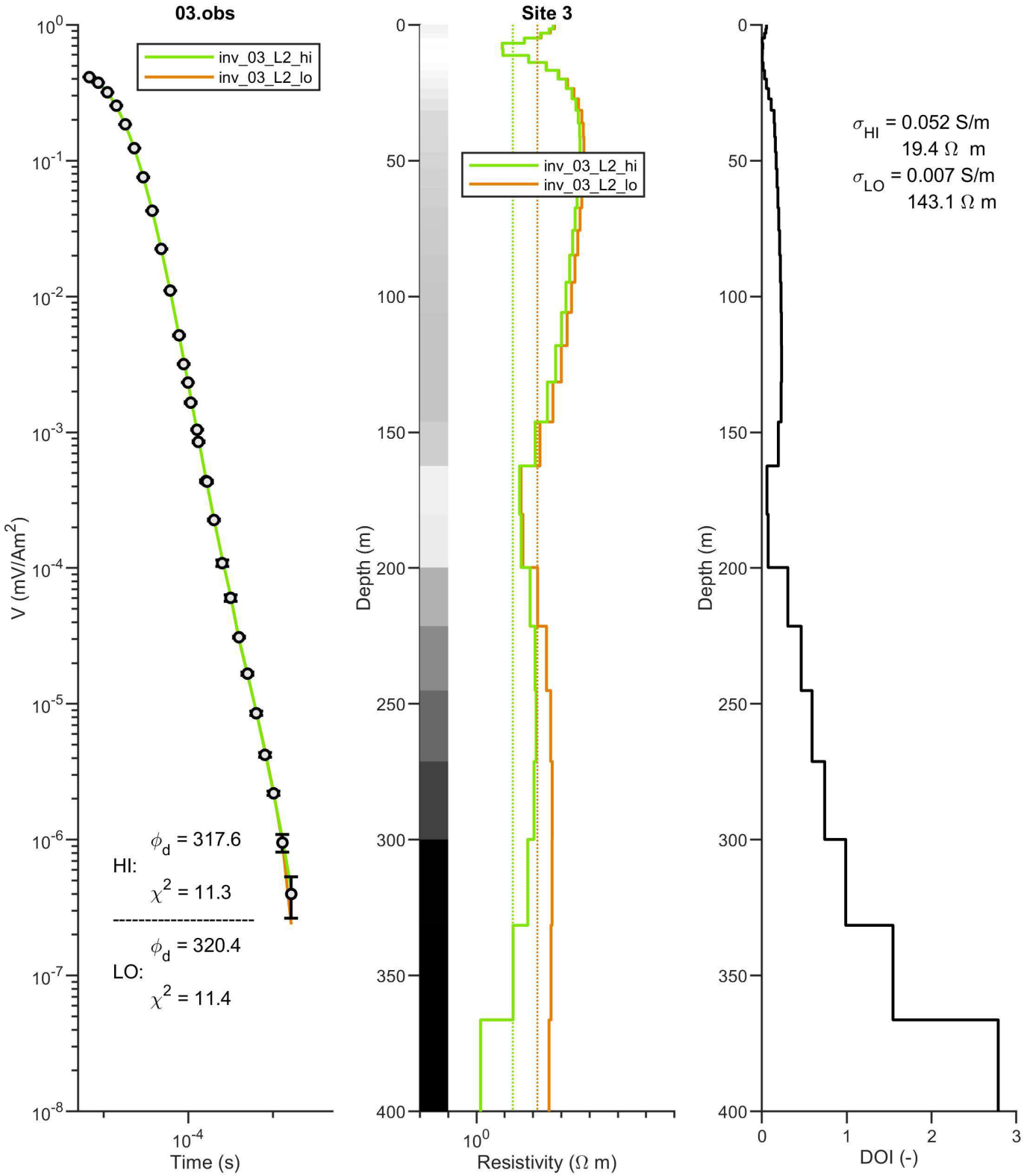
03.obs
inv_03_L2_hi
inv_03_L2_lo
V (mV/Am^2)
Time (s)
ϕ_d = 317.6
HI:
χ^2 = 11.3
ϕ_d = 320.4
LO:
χ^2 = 11.4
Site 3
inv_03_L2_hi
inv_03_L2_lo
Depth (m)
Resistivity (Ω m)
σ_{HI} = 0.052 S/m
19.4 Ω m
σ_{LO} = 0.007 S/m
143.1 Ω m
Depth (m)
DOI (-)

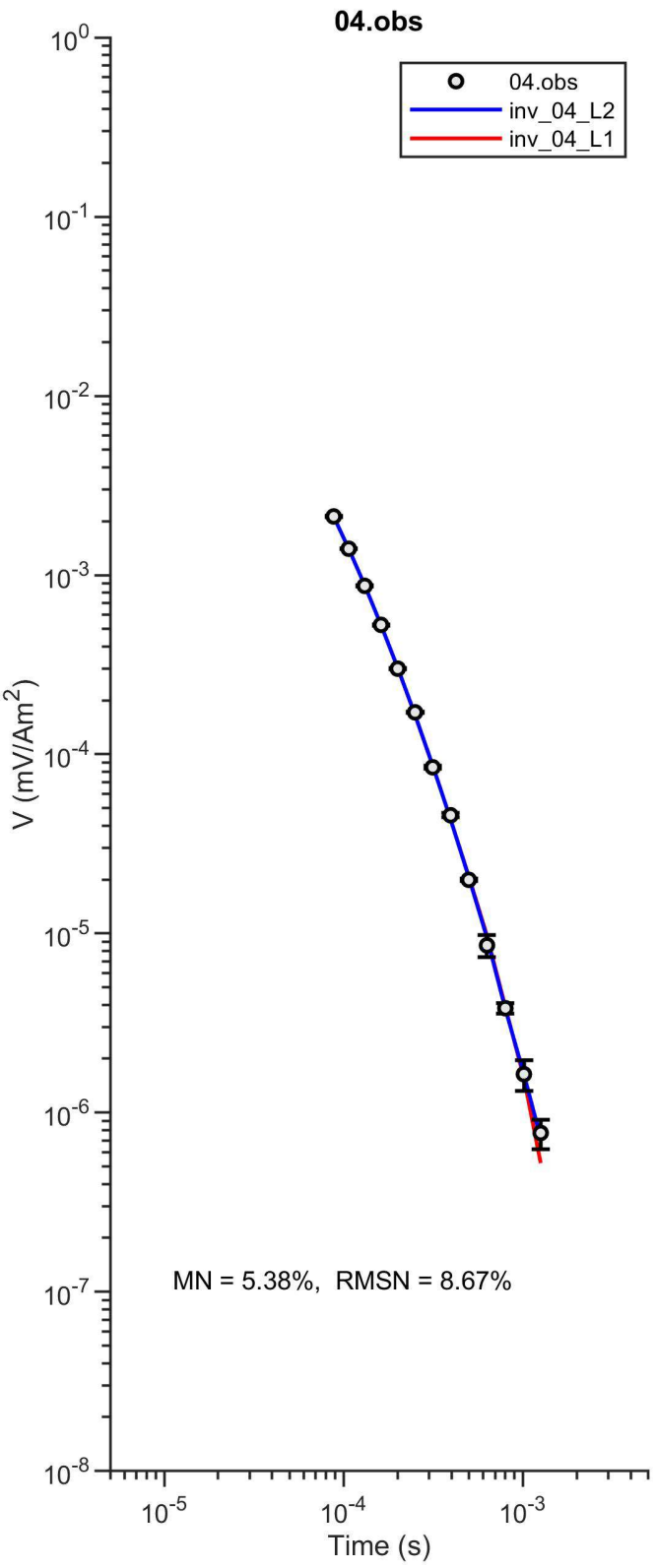
04.obs
04.obs
inv_04_L2
inv_04_L1
V (mV/Am^2)
Time (s)
MN = 5.38%, RMSN = 8.67%

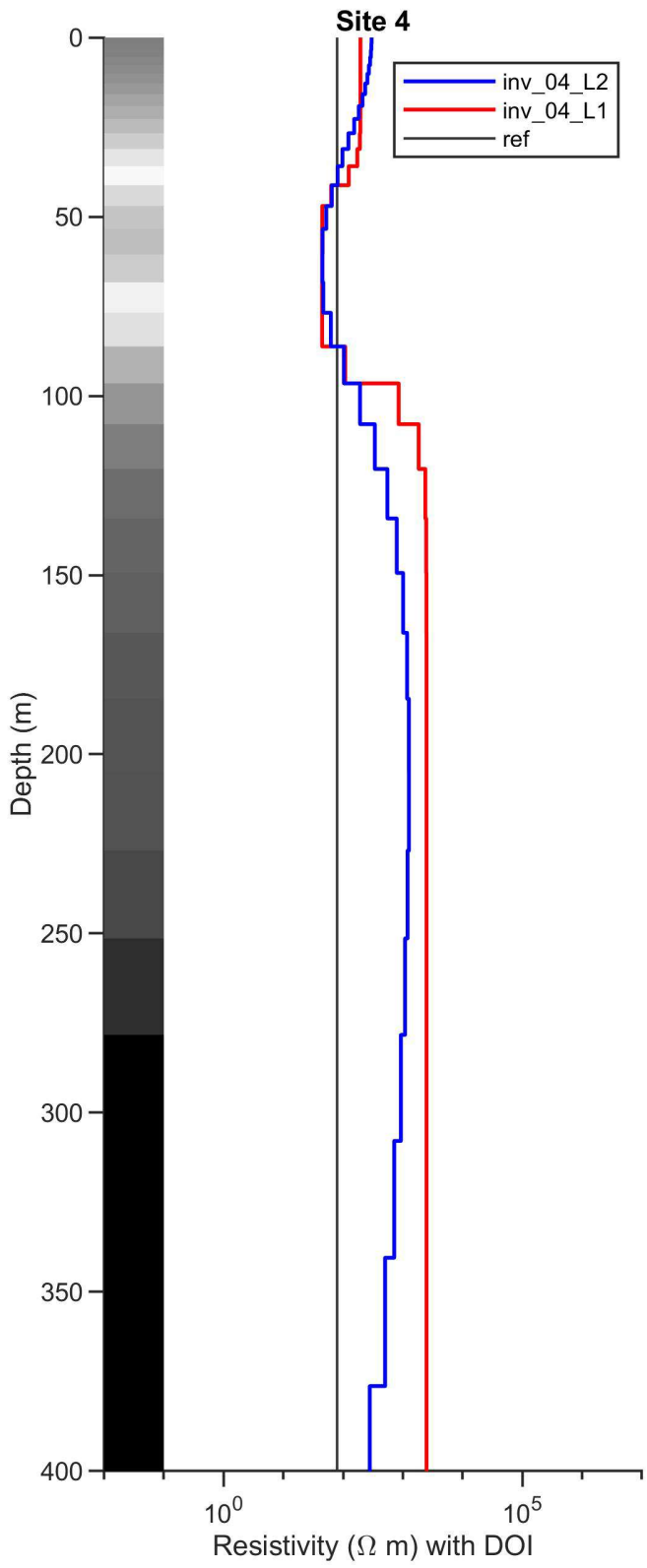
Site 4
inv_04_L2
inv_04_L1
ref
Depth (m)
Resistivity (Ω m) with DOI

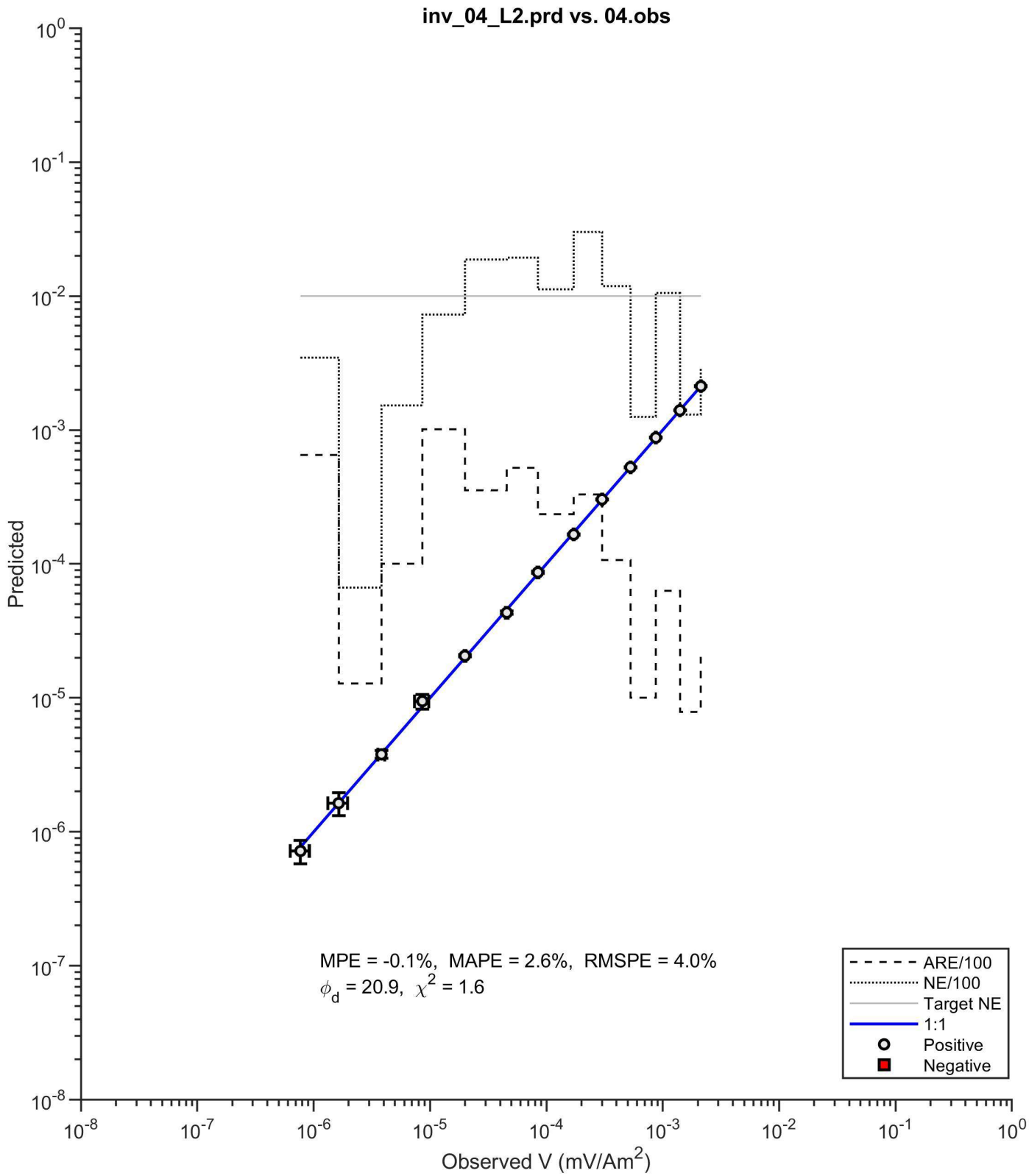
inv_04_L2.prd vs. 04.obs
Predicted
Observed V (mV/Am^2)
MPE = -0.1%, MAPE = 2.6%, RMSPE = 4.0%
ϕ_d = 20.9, χ^2 = 1.6
ARE/100
NE/100
Target NE
1:1
Positive
Negative

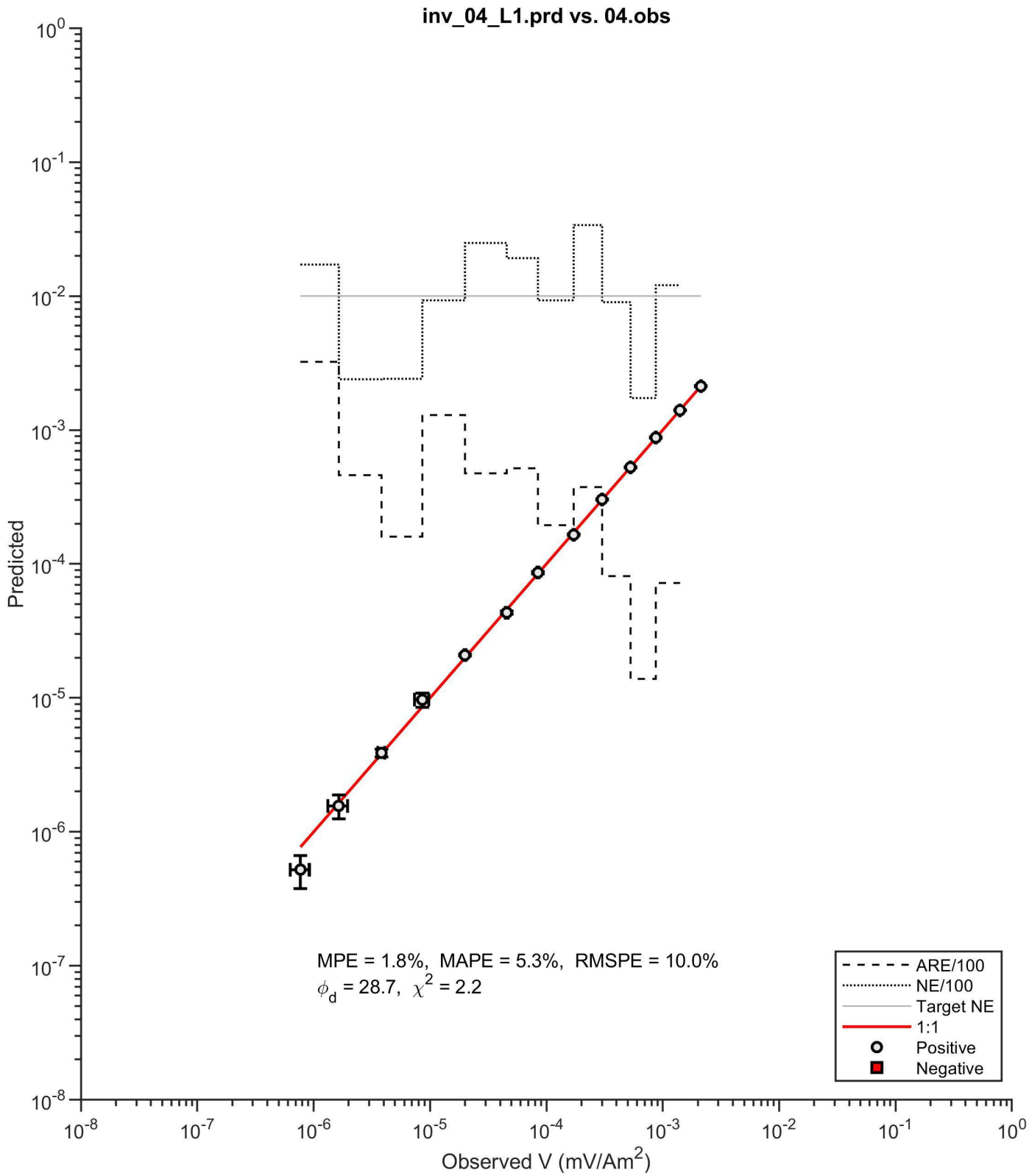
inv_04_L1.prd vs. 04.obs
Predicted
Observed V (mV/Am^2)
10^{0}
10^{-1}
10^{-2}
10^{-3}
10^{-4}
10^{-5}
10^{-6}
10^{-7}
10^{-8}
MPE = 1.8%, MAPE = 5.3%, RMSPE = 10.0%
ϕ_d = 28.7, χ^2 = 2.2
ARE/100
NE/100
Target NE
1:1
Positive
Negative

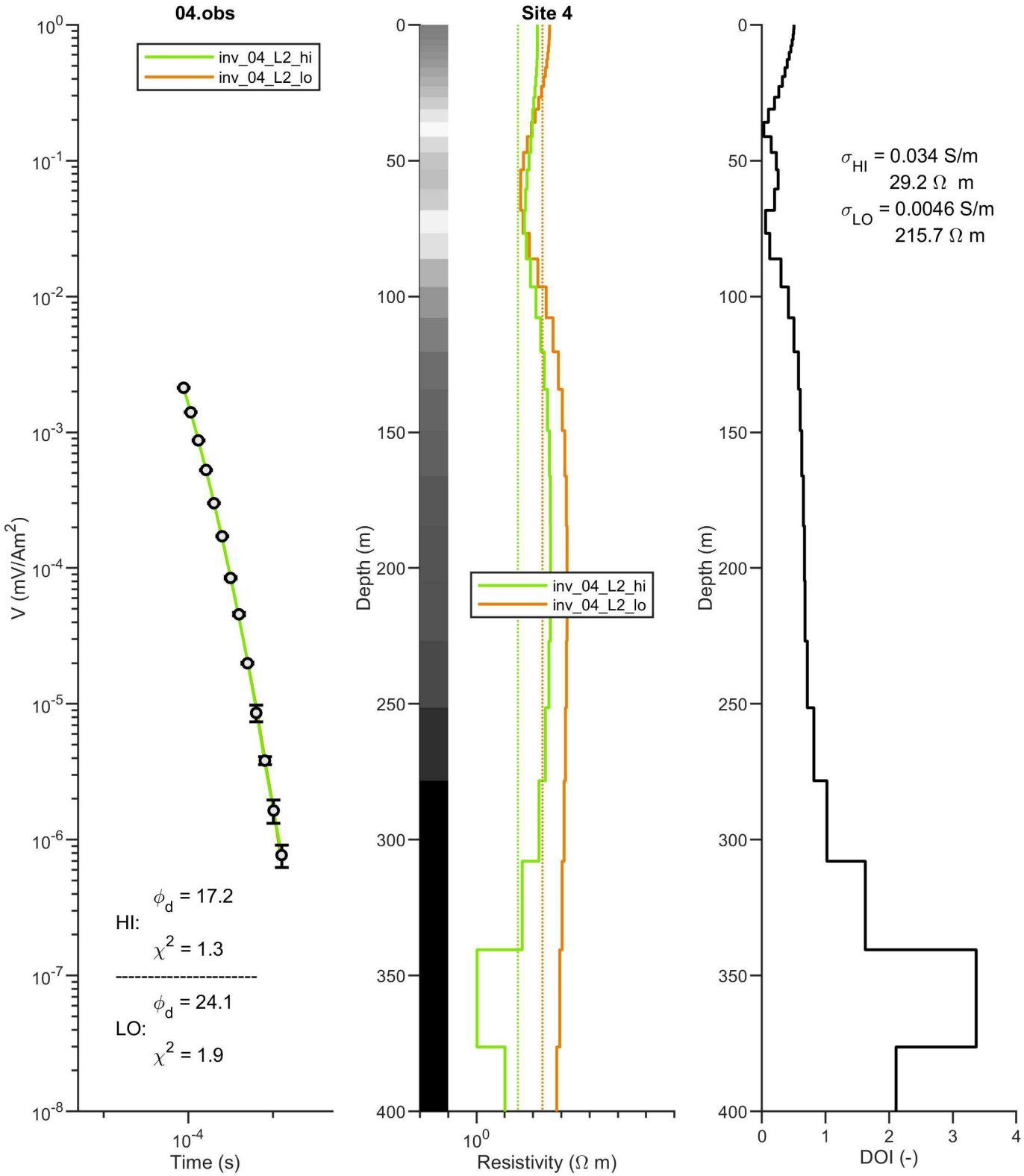
04.obs
inv_04_L2_hi
inv_04_L2_lo
V (mV/Am^2)
Time (s)
ϕ_d = 17.2
HI:
χ^2 = 1.3
ϕ_d = 24.1
LO:
χ^2 = 1.9
Site 4
Depth (m)
Resistivity (Ω m)
σ_{HI} = 0.034 S/m
29.2 Ω m
σ_{LO} = 0.0046 S/m
215.7 Ω m
DOI (-)

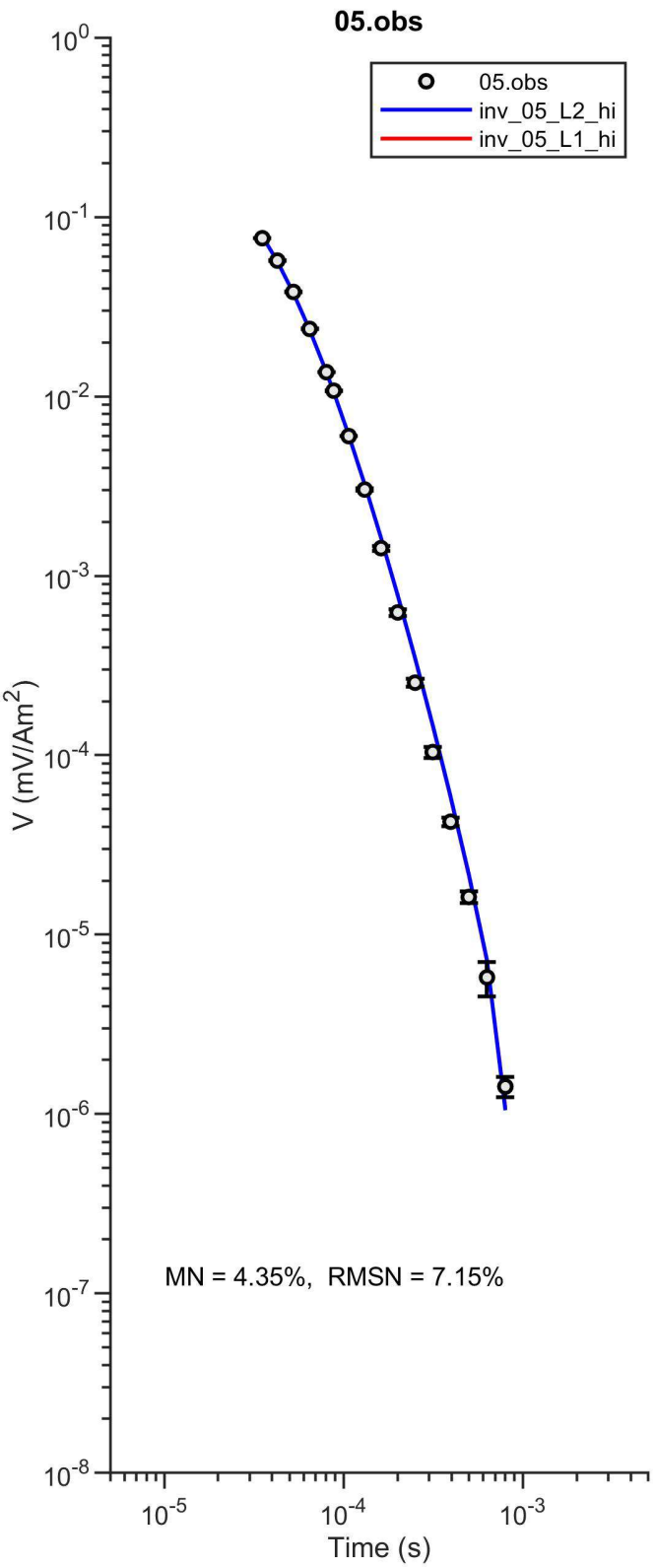
05.obs
05.obs
inv_05_L2_hi
inv_05_L1_hi
V (mV/Am^2)
Time (s)
MN = 4.35%, RMSN = 7.15%

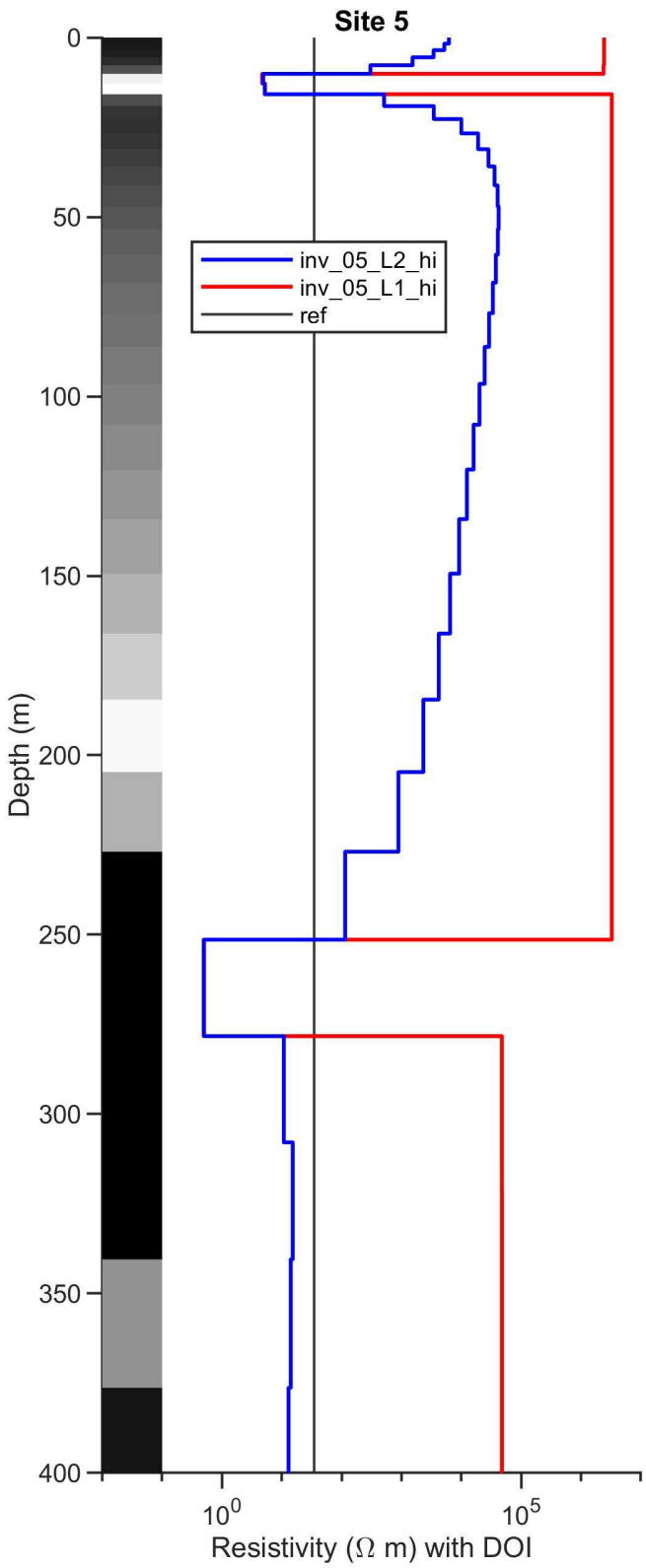
Site 5
inv_05_L2_hi
inv_05_L1_hi
ref
Depth (m)
Resistivity (Ω m) with DOI

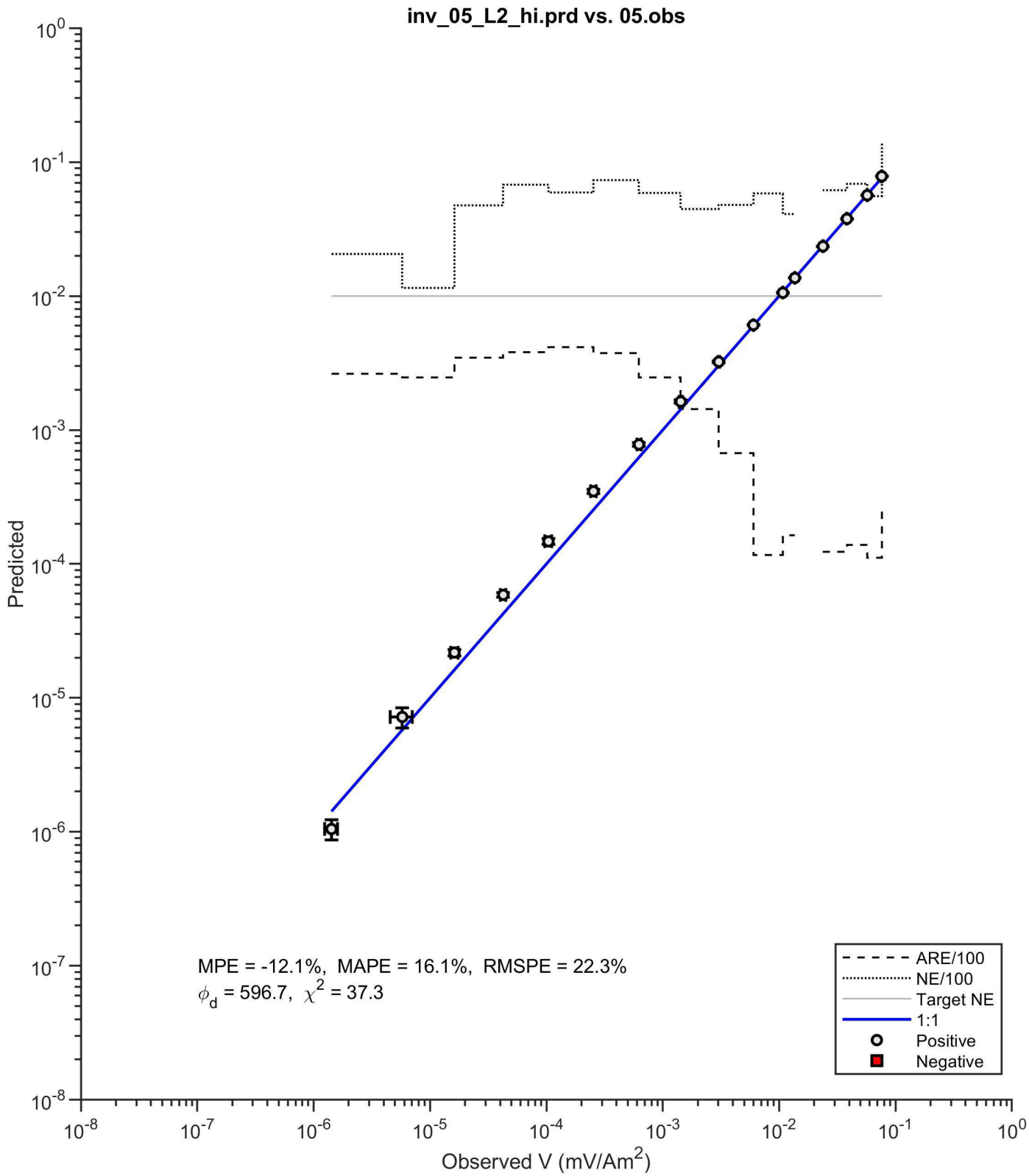
inv_05_L2_hi.prd vs. 05.obs
Predicted
Observed V (mV/Am^2)
10^{0}
10^{-1}
10^{-2}
10^{-3}
10^{-4}
10^{-5}
10^{-6}
10^{-7}
10^{-8}
MPE = -12.1%, MAPE = 16.1%, RMSPE = 22.3%
ϕ_d = 596.7, χ^2 = 37.3
ARE/100
NE/100
Target NE
1:1
Positive
Negative

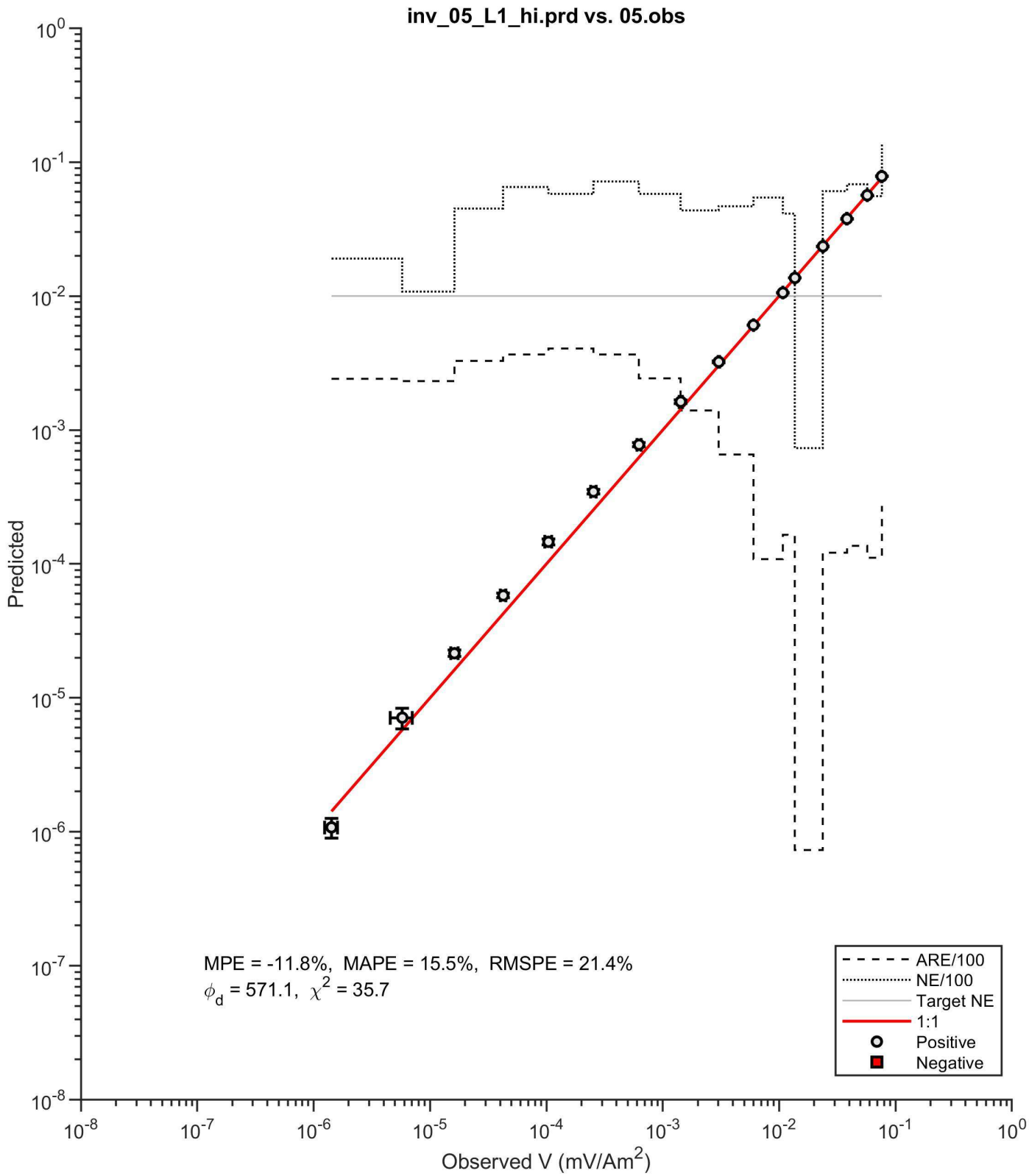
inv_05_L1_hi.prd vs. 05.obs
Predicted
Observed V (mV/Am^2)
10^{0}
10^{-1}
10^{-2}
10^{-3}
10^{-4}
10^{-5}
10^{-6}
10^{-7}
10^{-8}
MPE = -11.8%, MAPE = 15.5%, RMSPE = 21.4%
ϕ_d = 571.1, χ^2 = 35.7
ARE/100
NE/100
Target NE
1:1
Positive
Negative

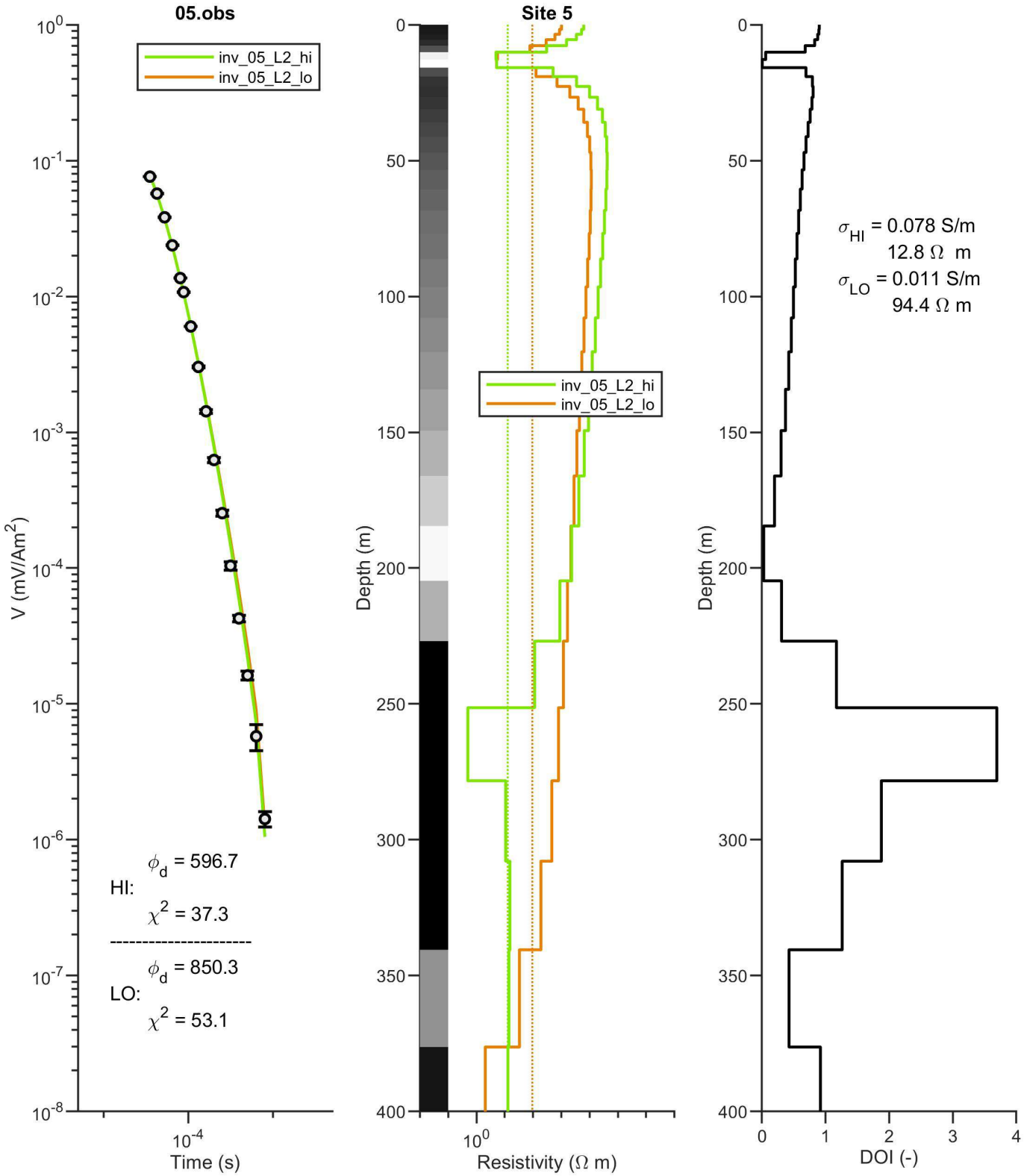
05.obs
inv_05_L2_hi
inv_05_L2_lo
V (mV/Am^2)
Time (s)
ϕ_d = 596.7
HI:
χ^2 = 37.3
ϕ_d = 850.3
LO:
χ^2 = 53.1
Site 5
inv_05_L2_hi
inv_05_L2_lo
Depth (m)
Resistivity (Ω m)
σ_{HI} = 0.078 S/m
12.8 Ω m
σ_{LO} = 0.011 S/m
94.4 Ω m
DOI (-)

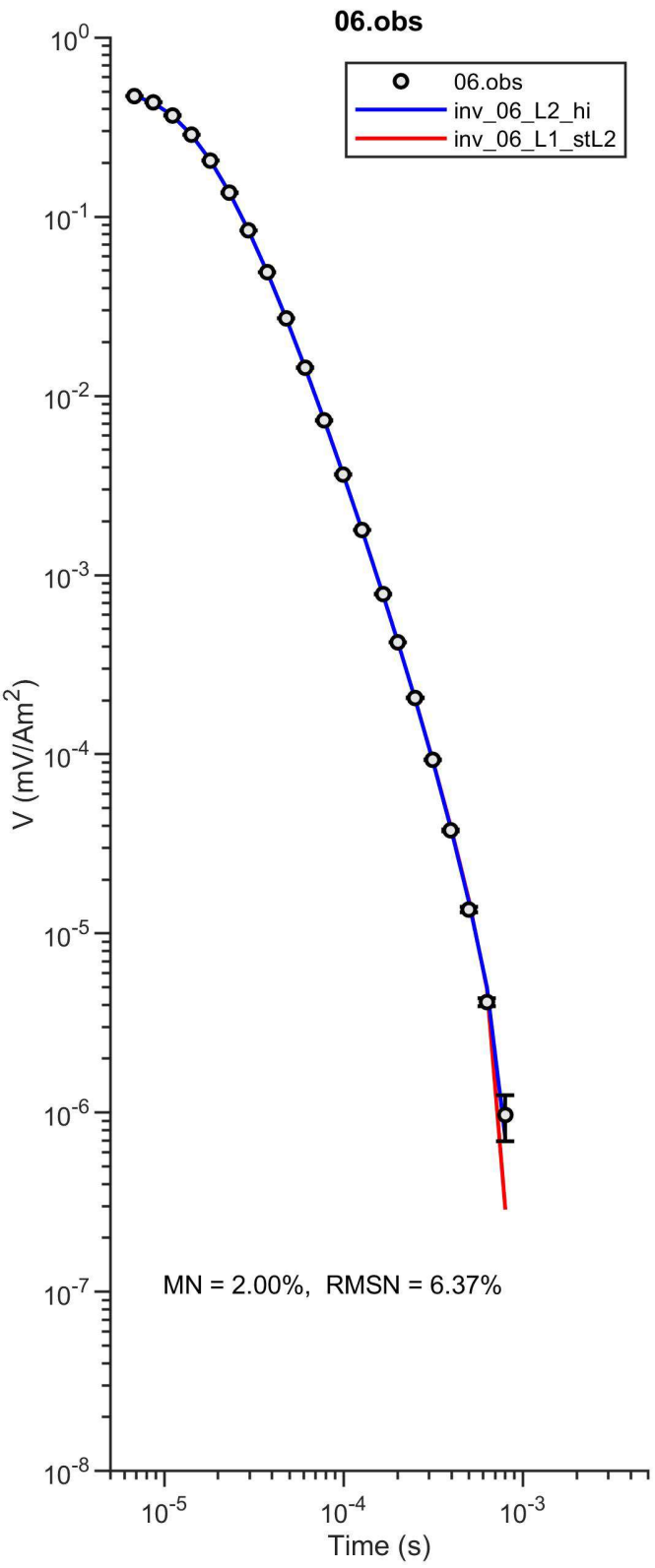
06.obs
06.obs
inv_06_L2_hi
inv_06_L1_stL2
V (mV/Am^2)
Time (s)
MN = 2.00%, RMSN = 6.37%

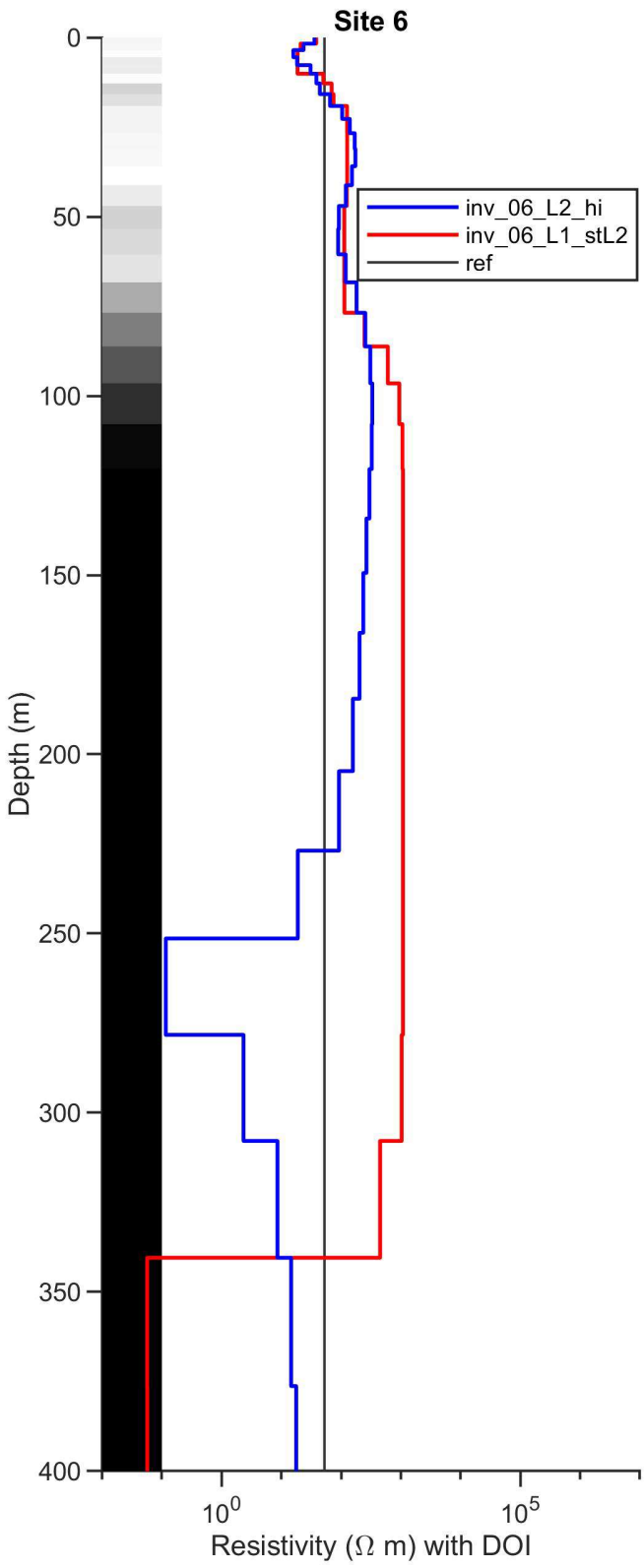
Site 6
inv_06_L2_hi
inv_06_L1_stL2
ref
Depth (m)
Resistivity (Ω m) with DOI

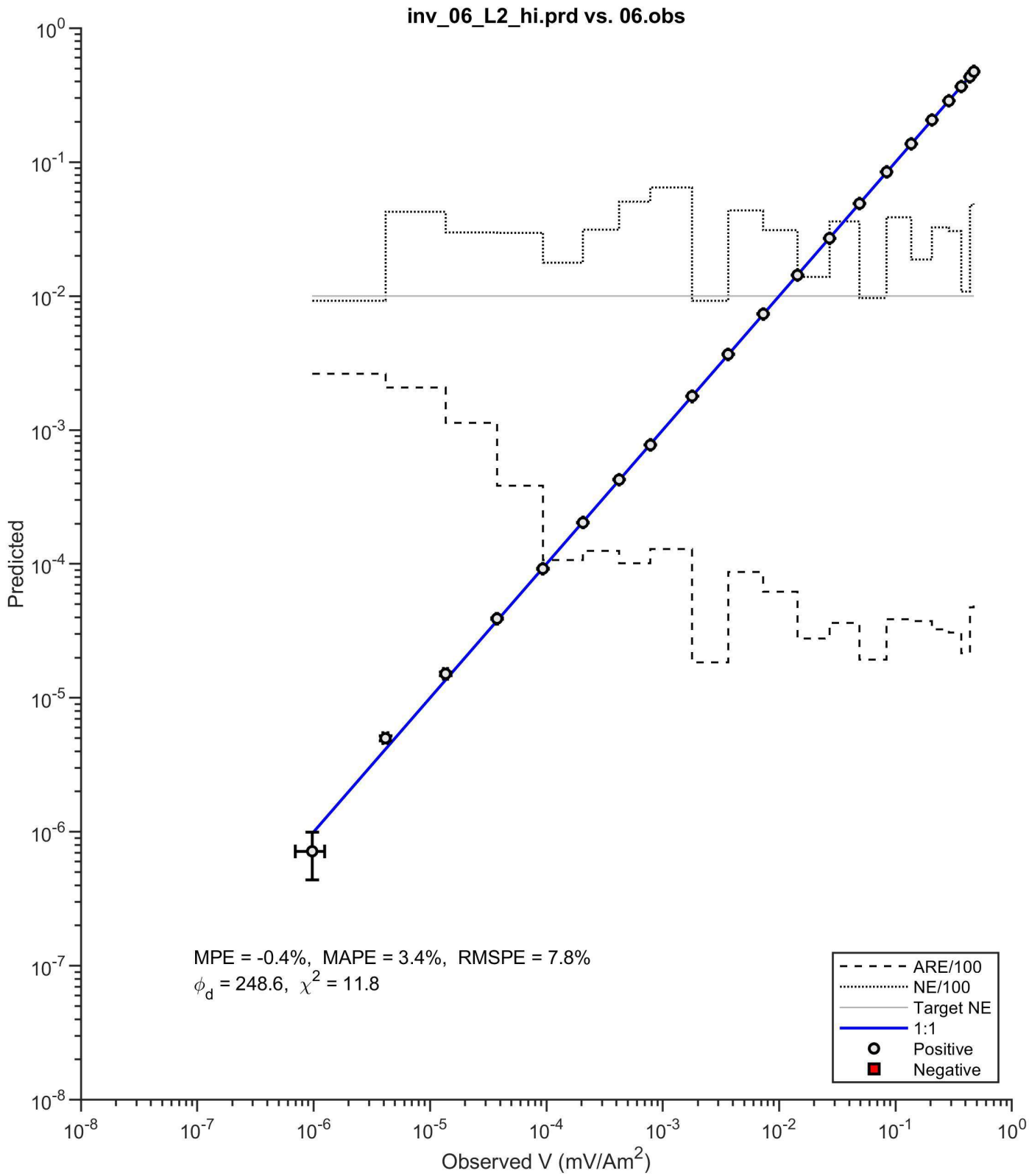
inv_06_L2_hi.prd vs. 06.obs
Predicted
Observed V (mV/Am^2)
MPE = -0.4%, MAPE = 3.4%, RMSPE = 7.8%
ϕ_d = 248.6, χ^2 = 11.8
ARE/100
NE/100
Target NE
1:1
Positive
Negative

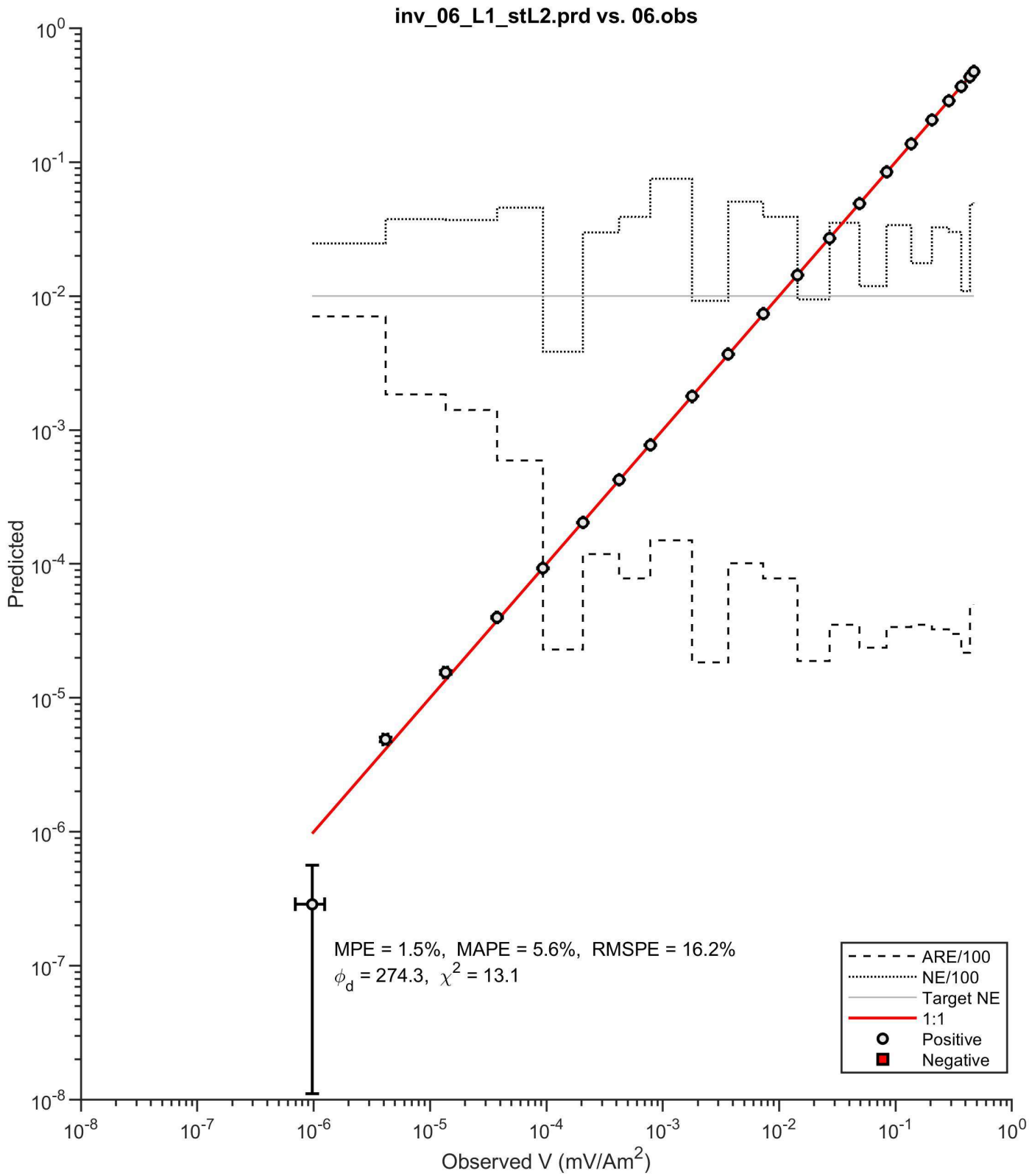
inv_06_L1_stL2.prd vs. 06.obs
Predicted
Observed V (mV/Am^2)
MPE = 1.5%, MAPE = 5.6%, RMSPE = 16.2%
ϕ_d = 274.3, χ^2 = 13.1
ARE/100
NE/100
Target NE
1:1
Positive
Negative

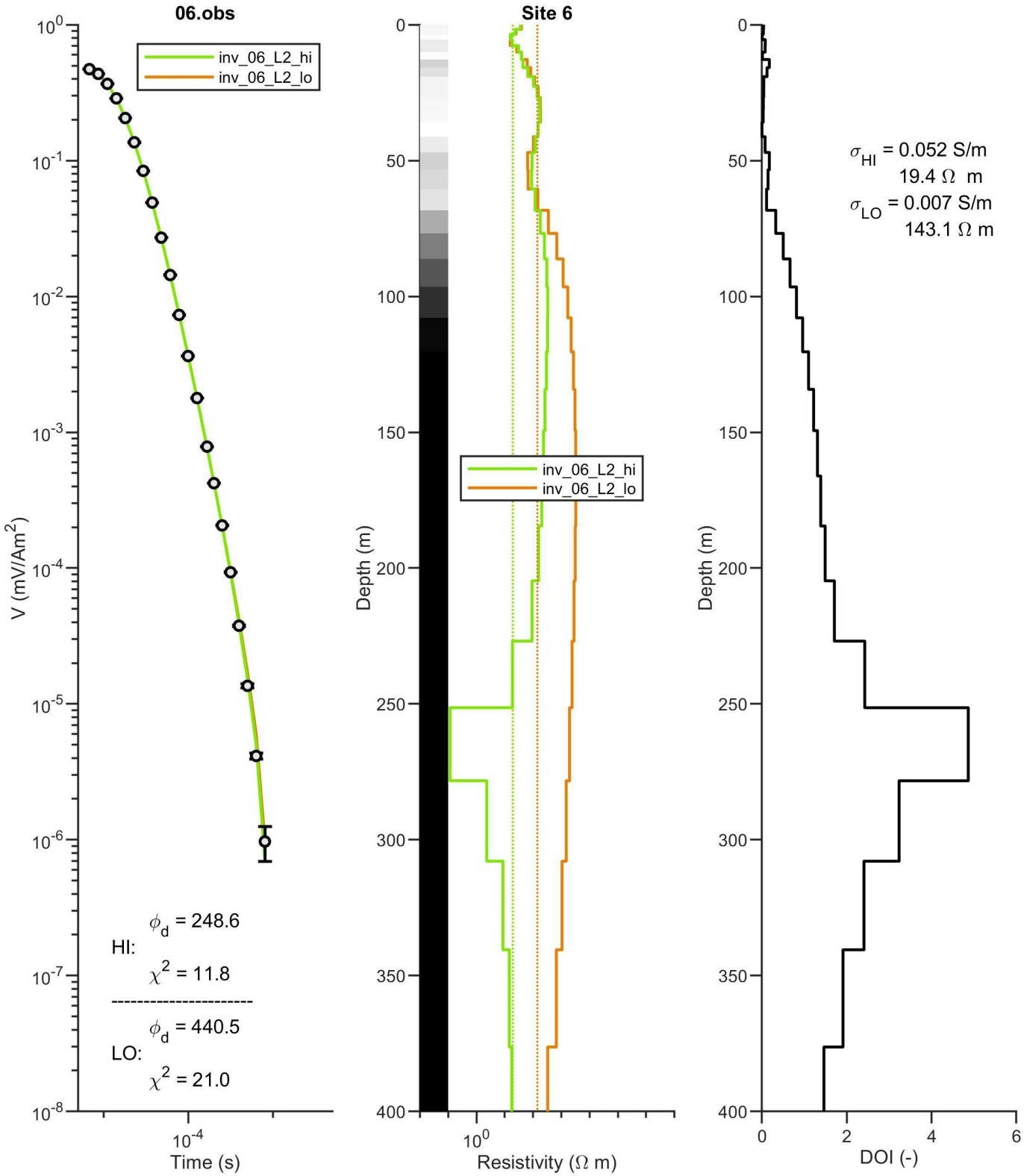
06.obs
inv_06_L2_hi
inv_06_L2_lo
V (mV/Am^2)
Time (s)
ϕ_d = 248.6
HI:
χ^2 = 11.8
ϕ_d = 440.5
LO:
χ^2 = 21.0
Site 6
Depth (m)
Resistivity (Ω m)
σ_{HI} = 0.052 S/m
19.4 Ω m
σ_{LO} = 0.007 S/m
143.1 Ω m
DOI (-)

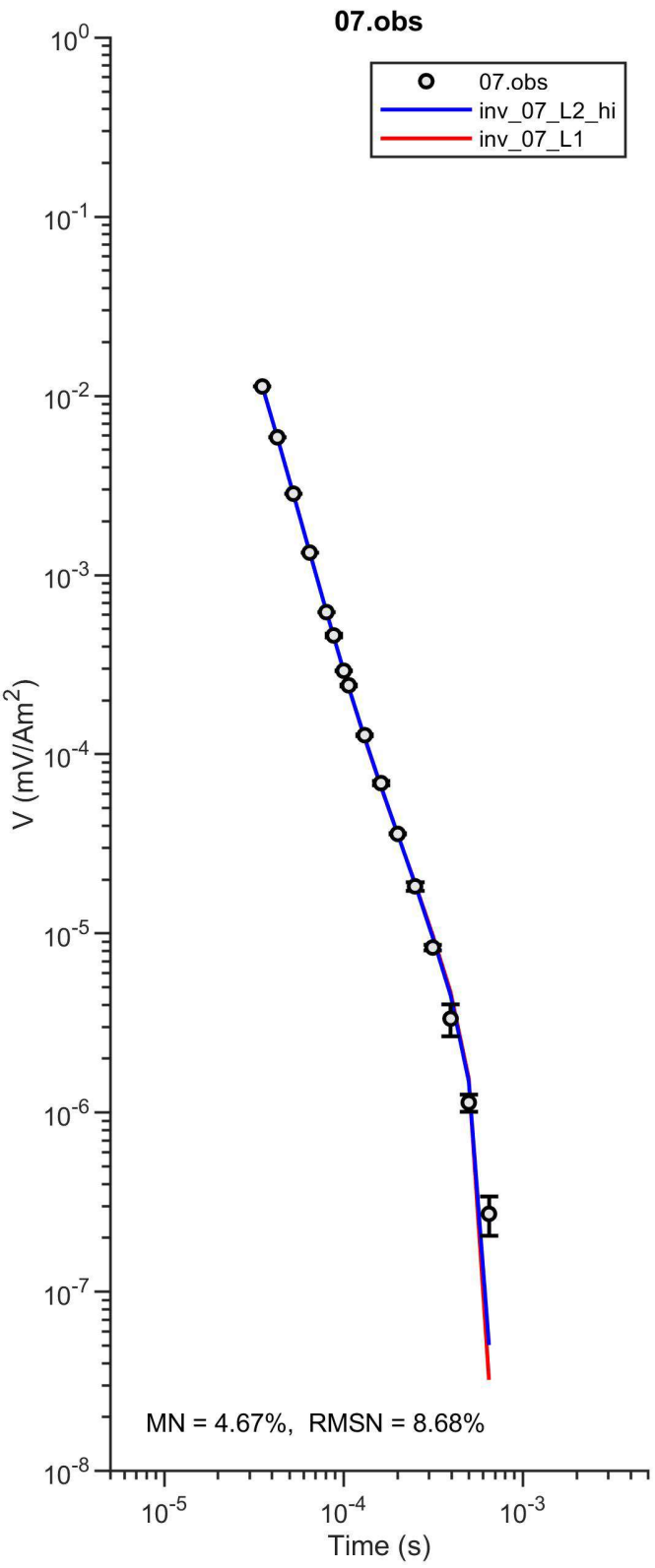
07.obs
07.obs
inv_07_L2_hi
inv_07_L1
V (mV/Am^2)
Time (s)
MN = 4.67%, RMSN = 8.68%

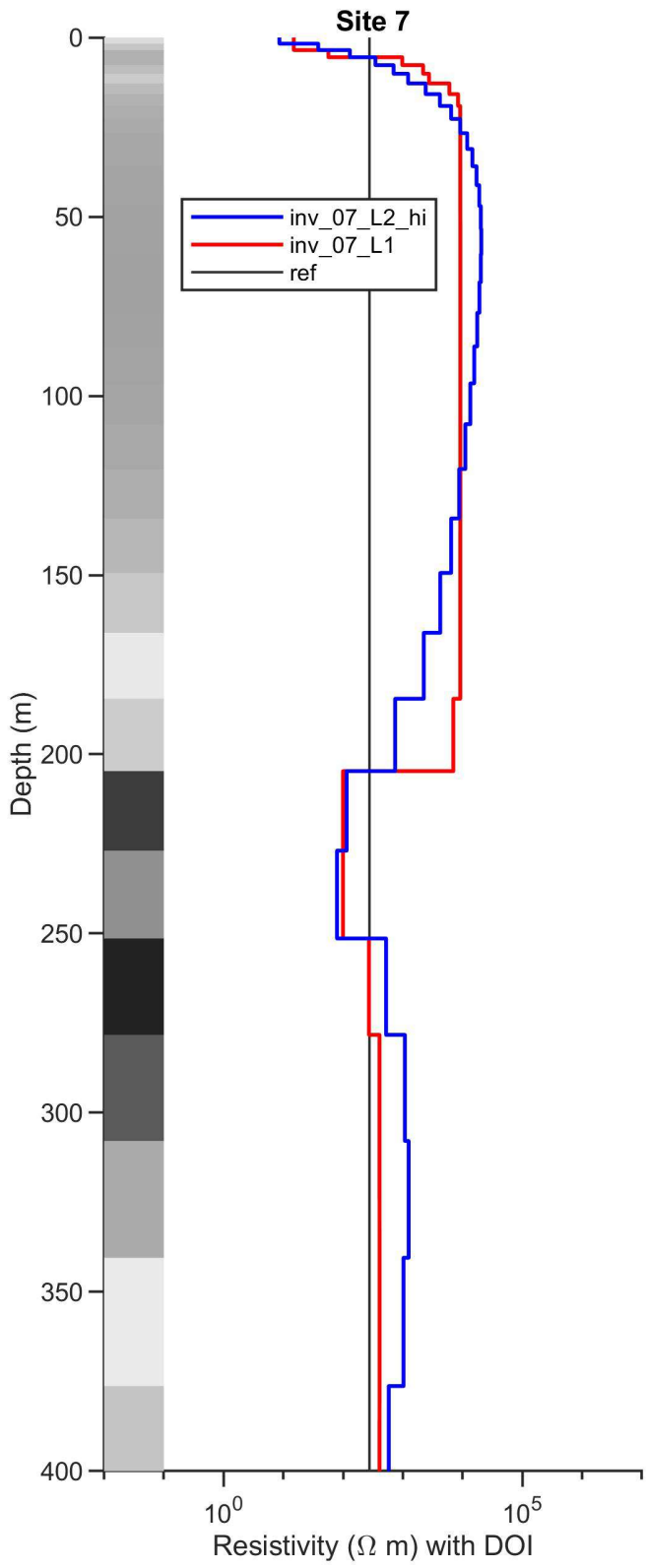
Site 7
inv_07_L2_hi
inv_07_L1
ref
Depth (m)
Resistivity (Ω m) with DOI

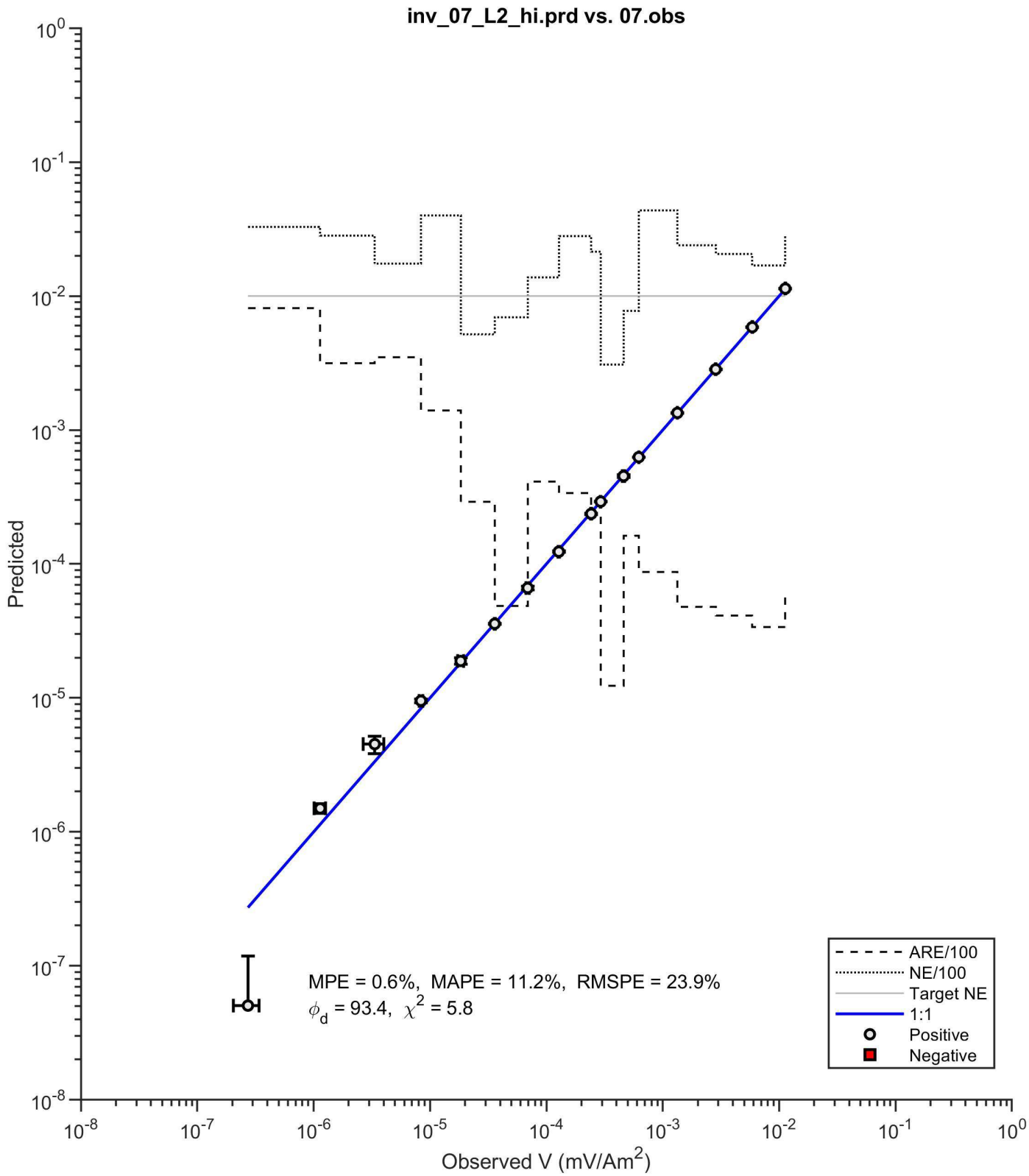
inv_07_L2_hi.prd vs. 07.obs
Predicted
Observed V (mV/Am^2)
10^{0}
10^{-1}
10^{-2}
10^{-3}
10^{-4}
10^{-5}
10^{-6}
10^{-7}
10^{-8}
MPE = 0.6%, MAPE = 11.2%, RMSPE = 23.9%
ϕ_d = 93.4, χ^2 = 5.8
ARE/100
NE/100
Target NE
1:1
Positive
Negative

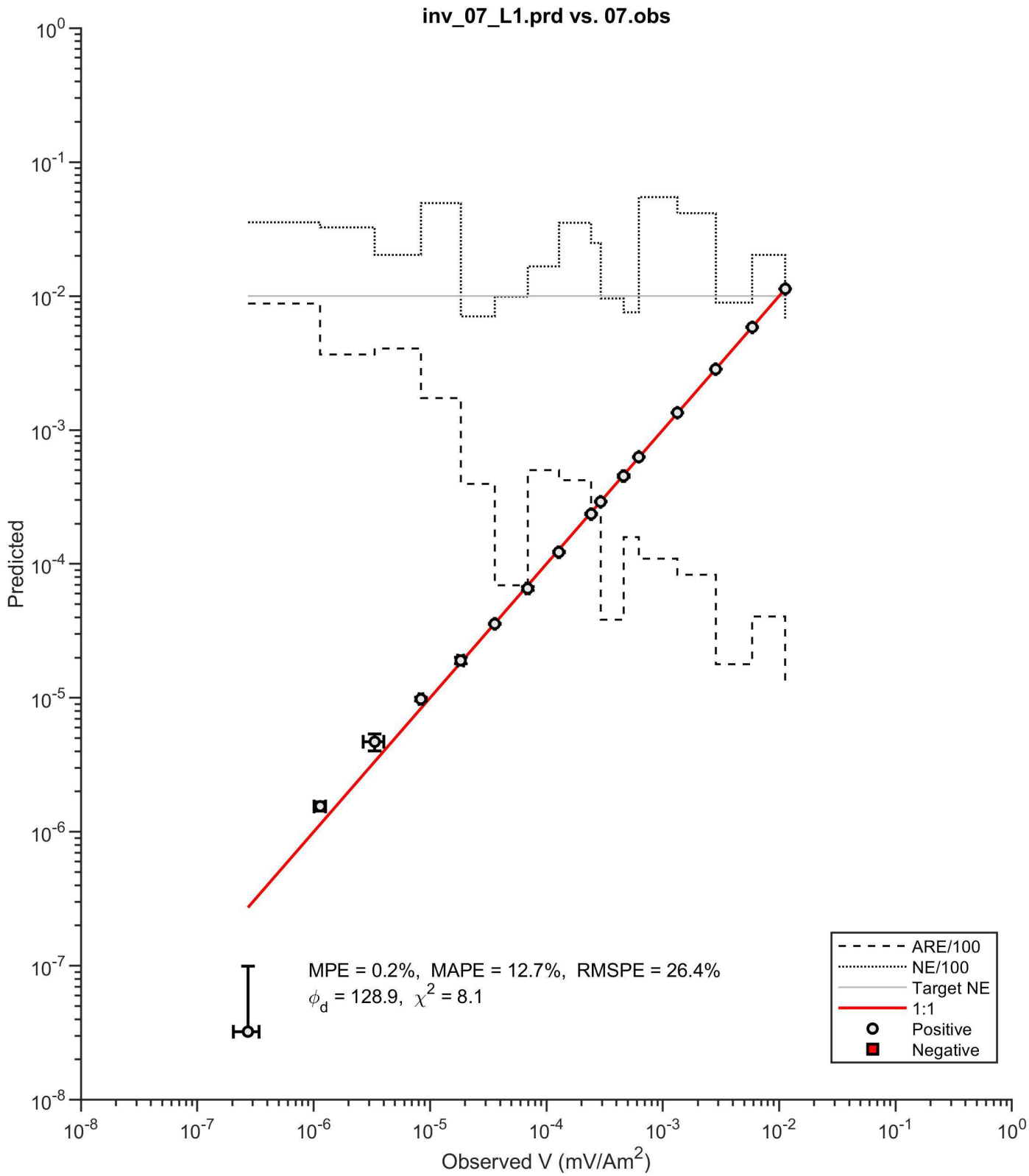
inv_07_L1.prd vs. 07.obs
Predicted
Observed V (mV/Am^2)
10^{0}
10^{-1}
10^{-2}
10^{-3}
10^{-4}
10^{-5}
10^{-6}
10^{-7}
10^{-8}
MPE = 0.2%, MAPE = 12.7%, RMSPE = 26.4%
ϕ_d = 128.9, χ^2 = 8.1
ARE/100
NE/100
Target NE
1:1
Positive
Negative

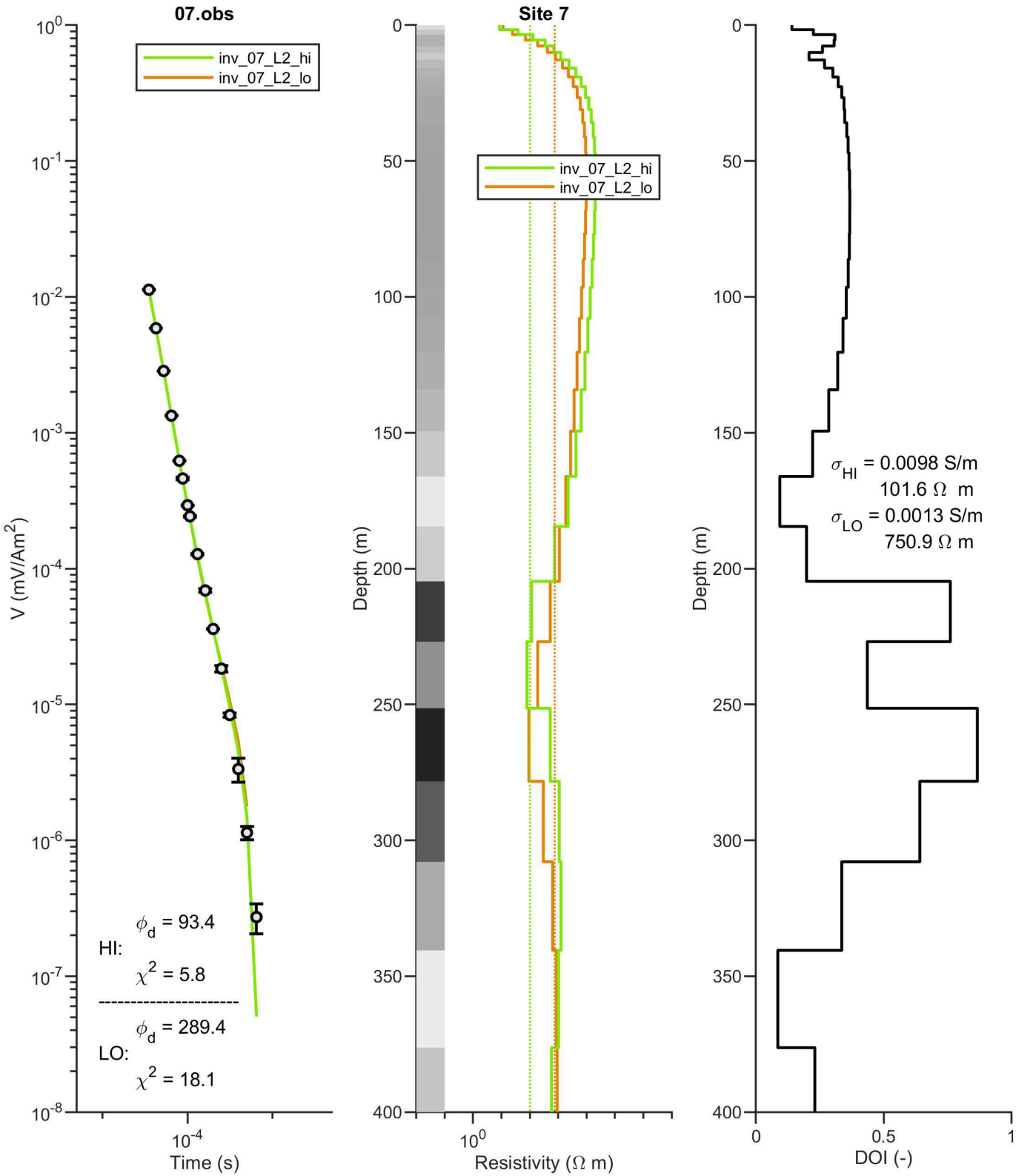
07.obs
inv_07_L2_hi
inv_07_L2_lo
V (mV/Am^2)
Time (s)
ϕ_d = 93.4
HI:
χ^2 = 5.8
ϕ_d = 289.4
LO:
χ^2 = 18.1
Site 7
Depth (m)
Resistivity (Ω m)
σ_{HI} = 0.0098 S/m
101.6 Ω m
σ_{LO} = 0.0013 S/m
750.9 Ω m
DOI (-)

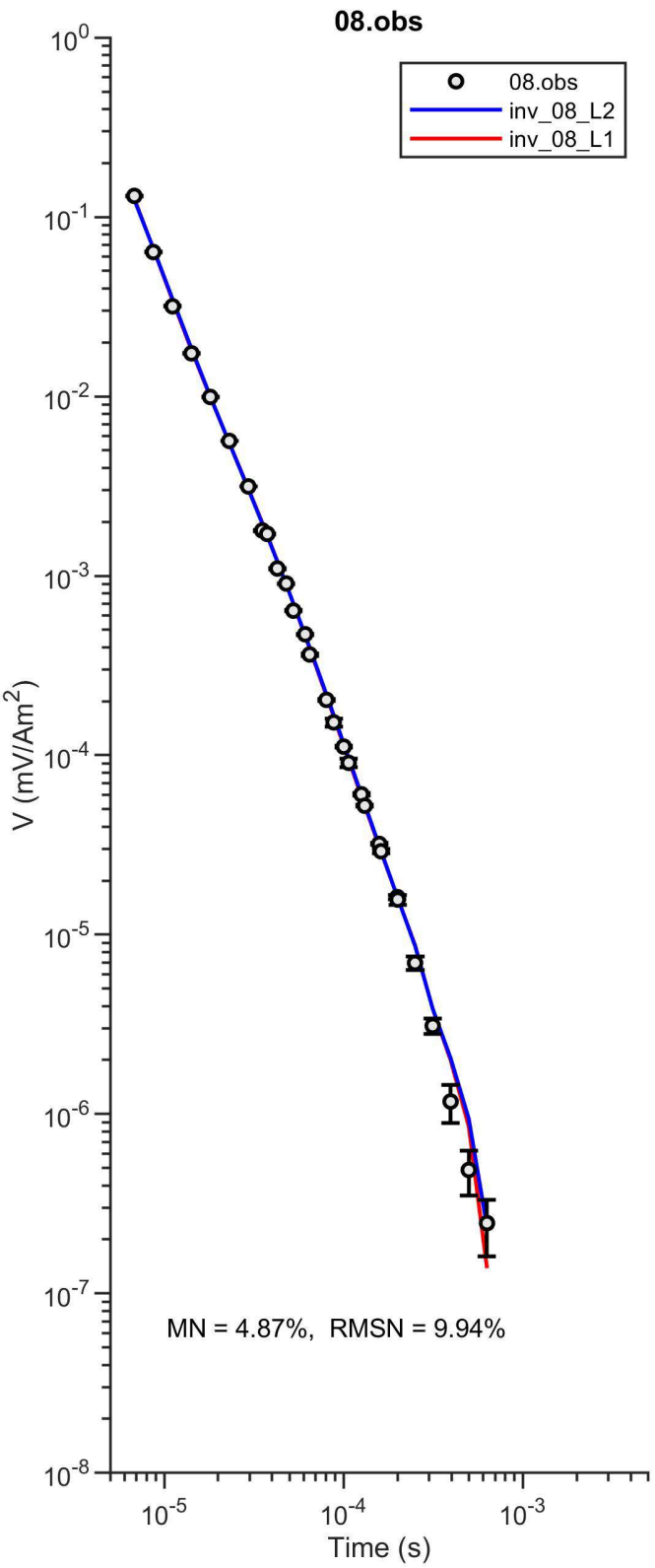
08.obs
08.obs
inv_08_L2
inv_08_L1
V (mV/Am^2)
Time (s)
MN = 4.87%, RMSN = 9.94%

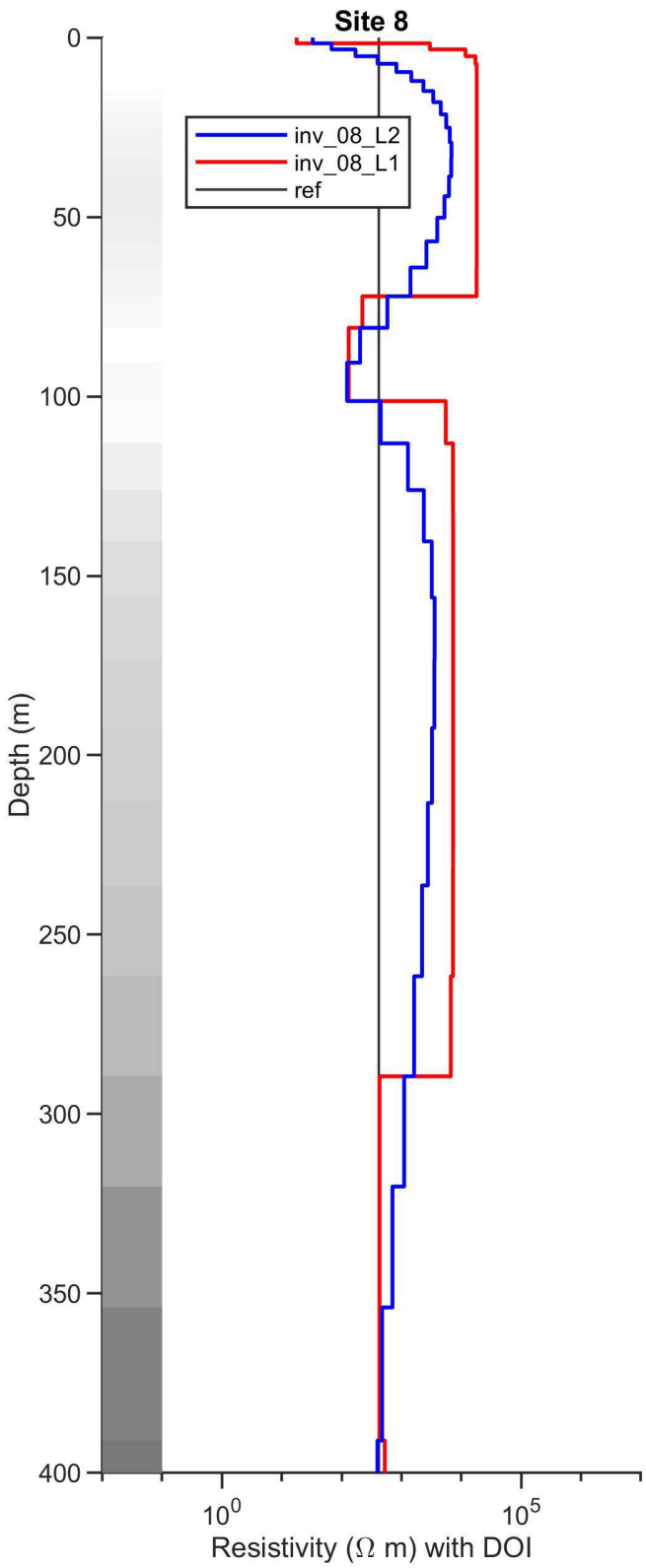
Site 8
inv_08_L2
inv_08_L1
ref
Depth (m)
Resistivity (Ω m) with DOI

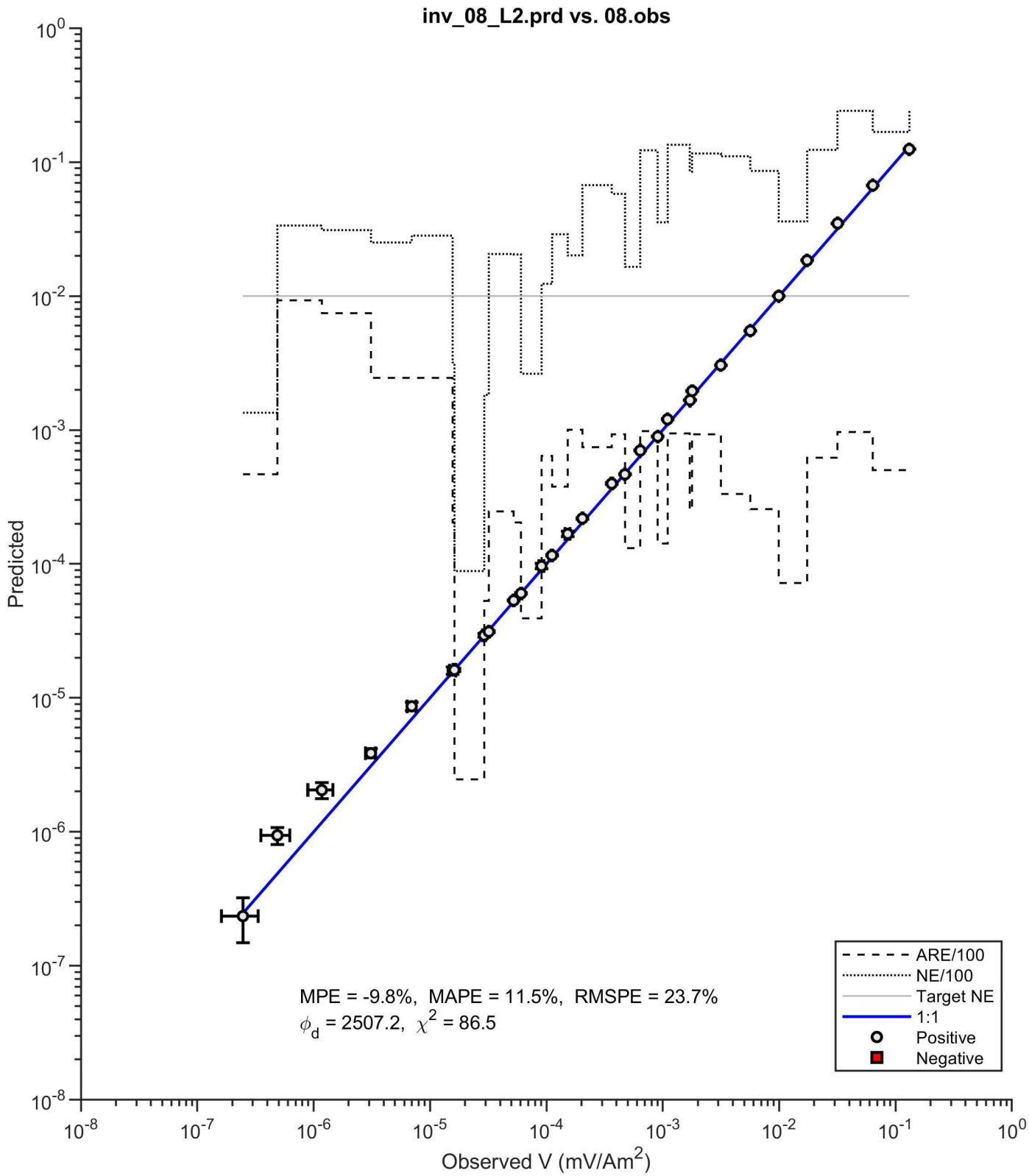
inv_08_L2.prd vs. 08.obs
Predicted
Observed V (mV/Am^2)
10^{0}
10^{-1}
10^{-2}
10^{-3}
10^{-4}
10^{-5}
10^{-6}
10^{-7}
10^{-8}
MPE = -9.8%, MAPE = 11.5%, RMSPE = 23.7%
ϕ_d = 2507.2, χ^2 = 86.5
ARE/100
NE/100
Target NE
1:1
Positive
Negative

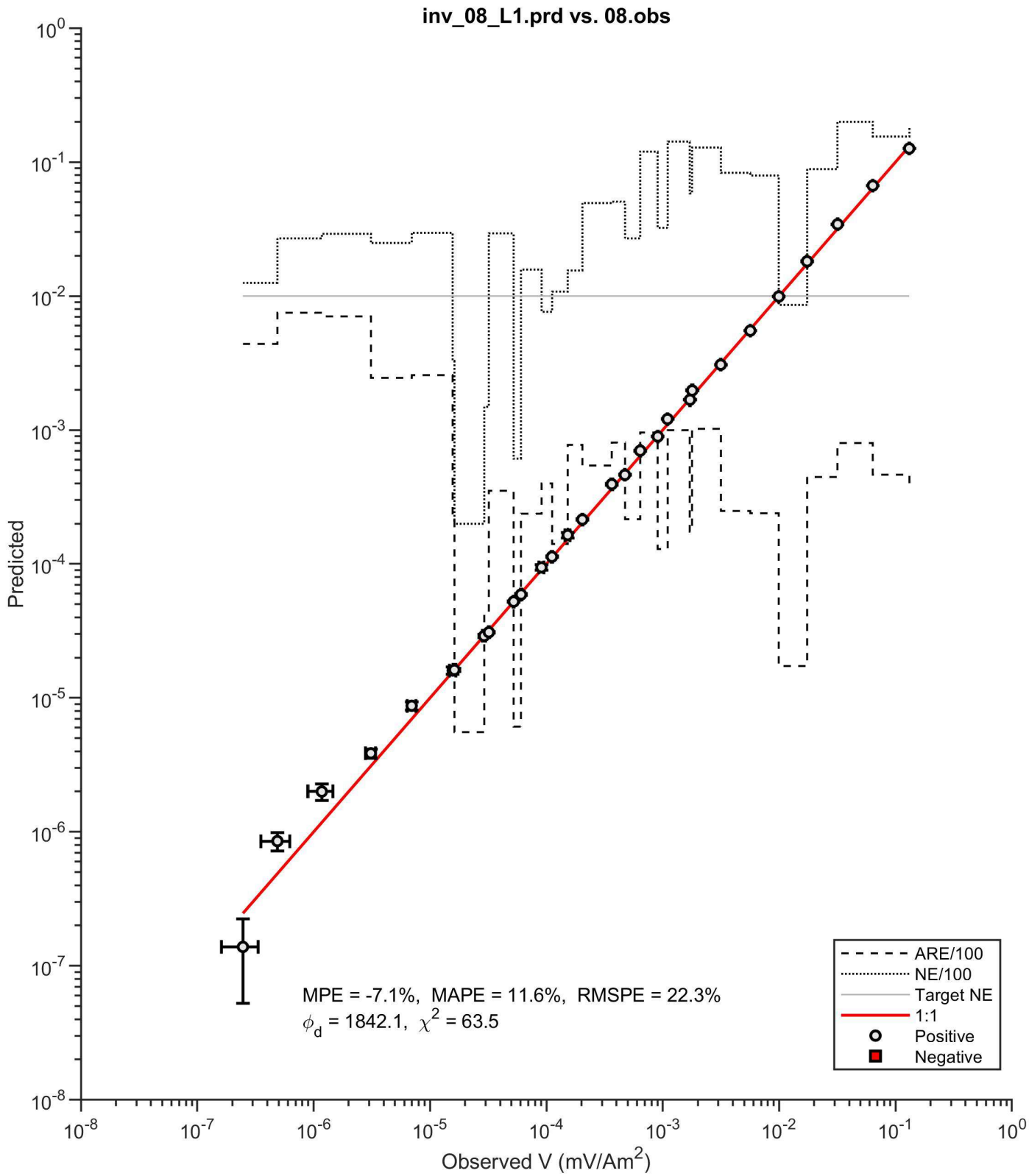
inv_08_L1.prd vs. 08.obs
Predicted
Observed V (mV/Am^2)
10^{0}
10^{-1}
10^{-2}
10^{-3}
10^{-4}
10^{-5}
10^{-6}
10^{-7}
10^{-8}
MPE = -7.1%, MAPE = 11.6%, RMSPE = 22.3%
ϕ_d = 1842.1, χ^2 = 63.5
ARE/100
NE/100
Target NE
1:1
Positive
Negative

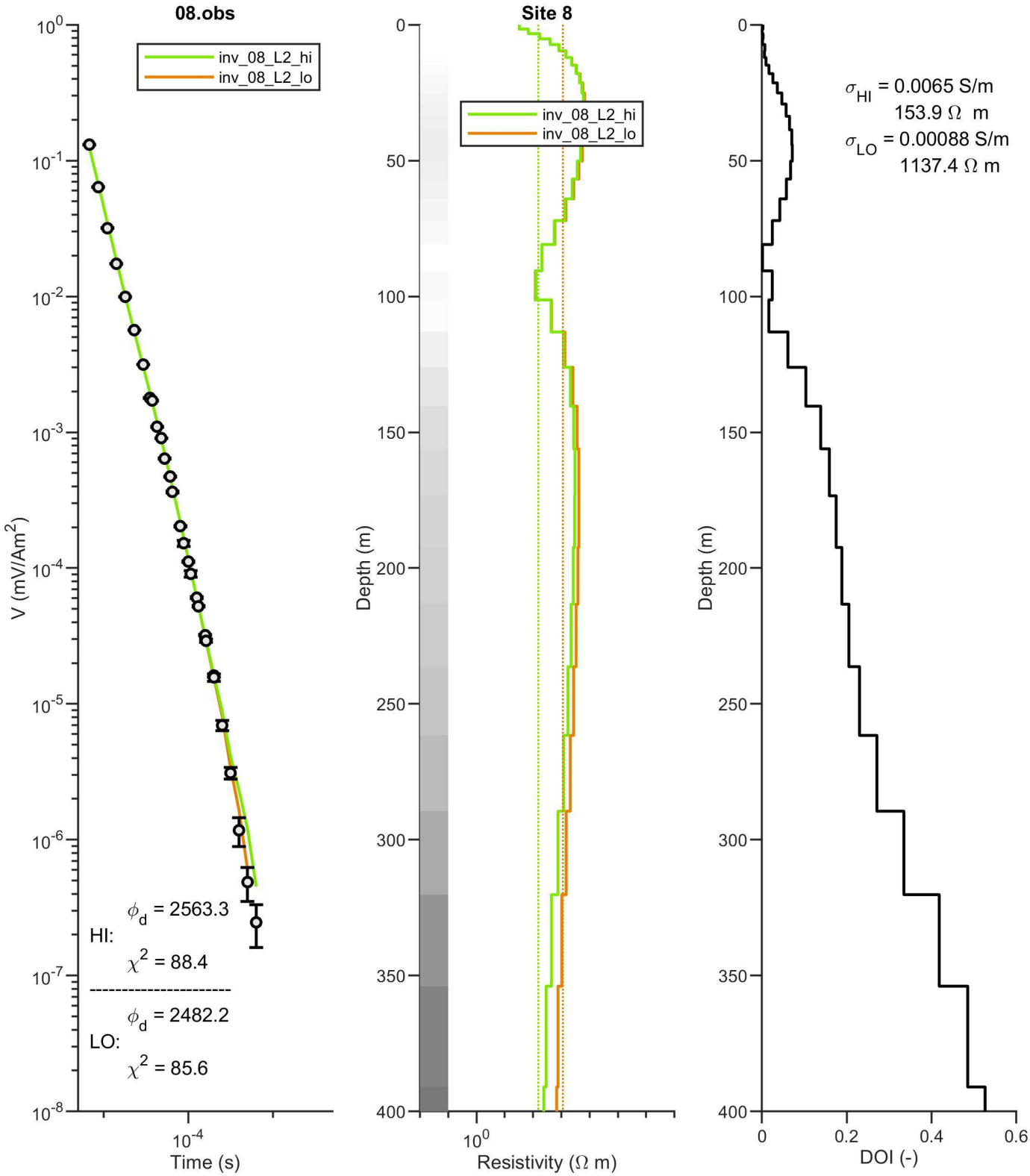
08.obs
inv_08_L2_hi
inv_08_L2_lo
V (mV/Am^2)
Time (s)
ϕ_d = 2563.3
HI:
χ^2 = 88.4
ϕ_d = 2482.2
LO:
χ^2 = 85.6
Site 8
Depth (m)
Resistivity (Ω m)
σ_{HI} = 0.0065 S/m
153.9 Ω m
σ_{LO} = 0.00088 S/m
1137.4 Ω m
DOI (-)

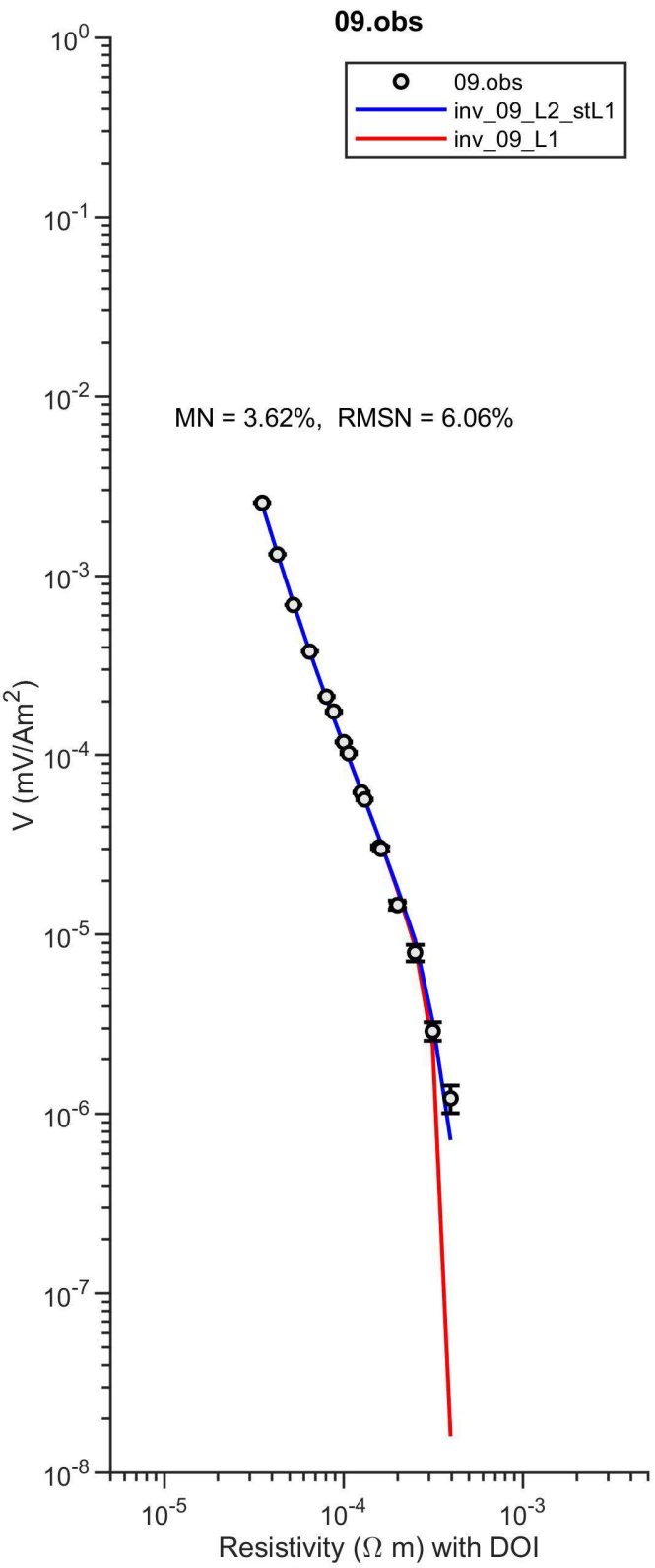
09.obs
09.obs
inv_09_L2_stL1
inv_09_L1
MN = 3.62%, RMSN = 6.06%
V (mV/Am^2)
Resistivity (Ω m) with DOI

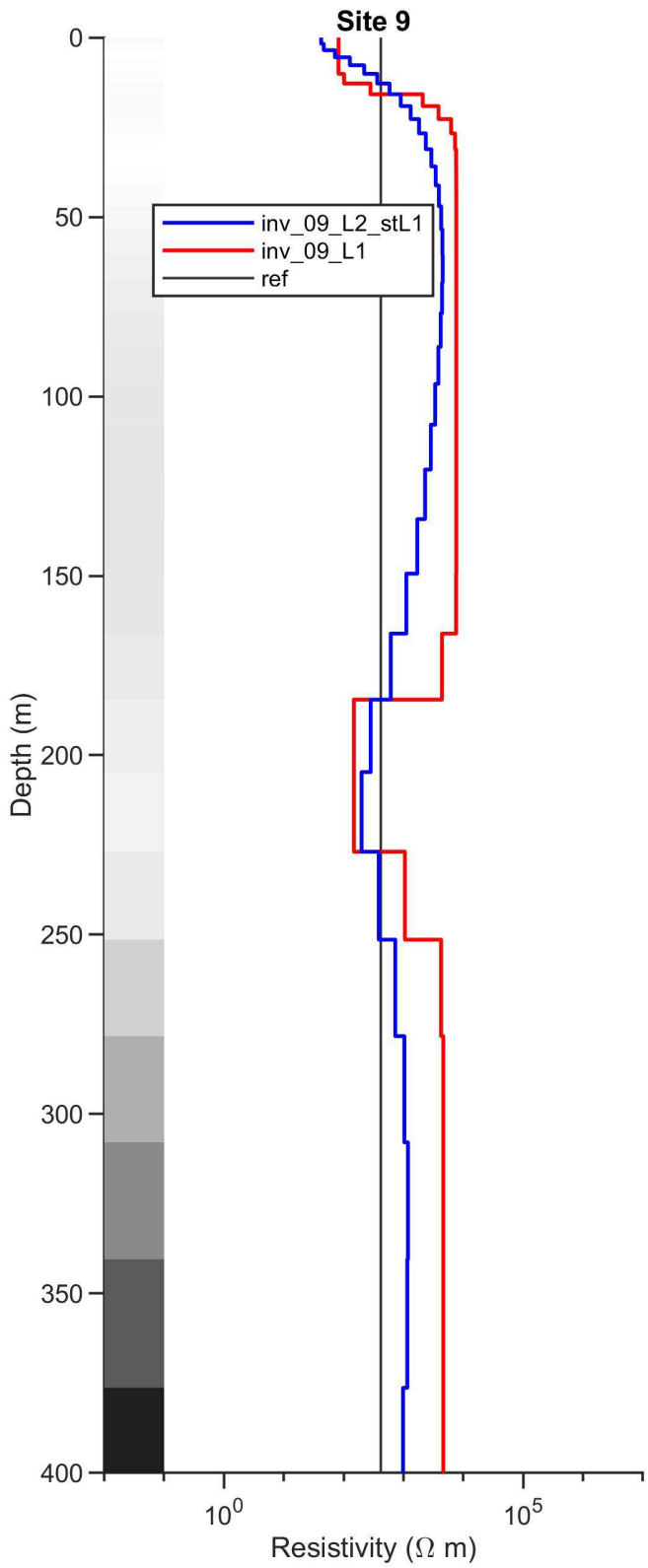
Site 9
inv_09_L2_stL1
inv_09_L1
ref
Depth (m)
Resistivity (Ω m)

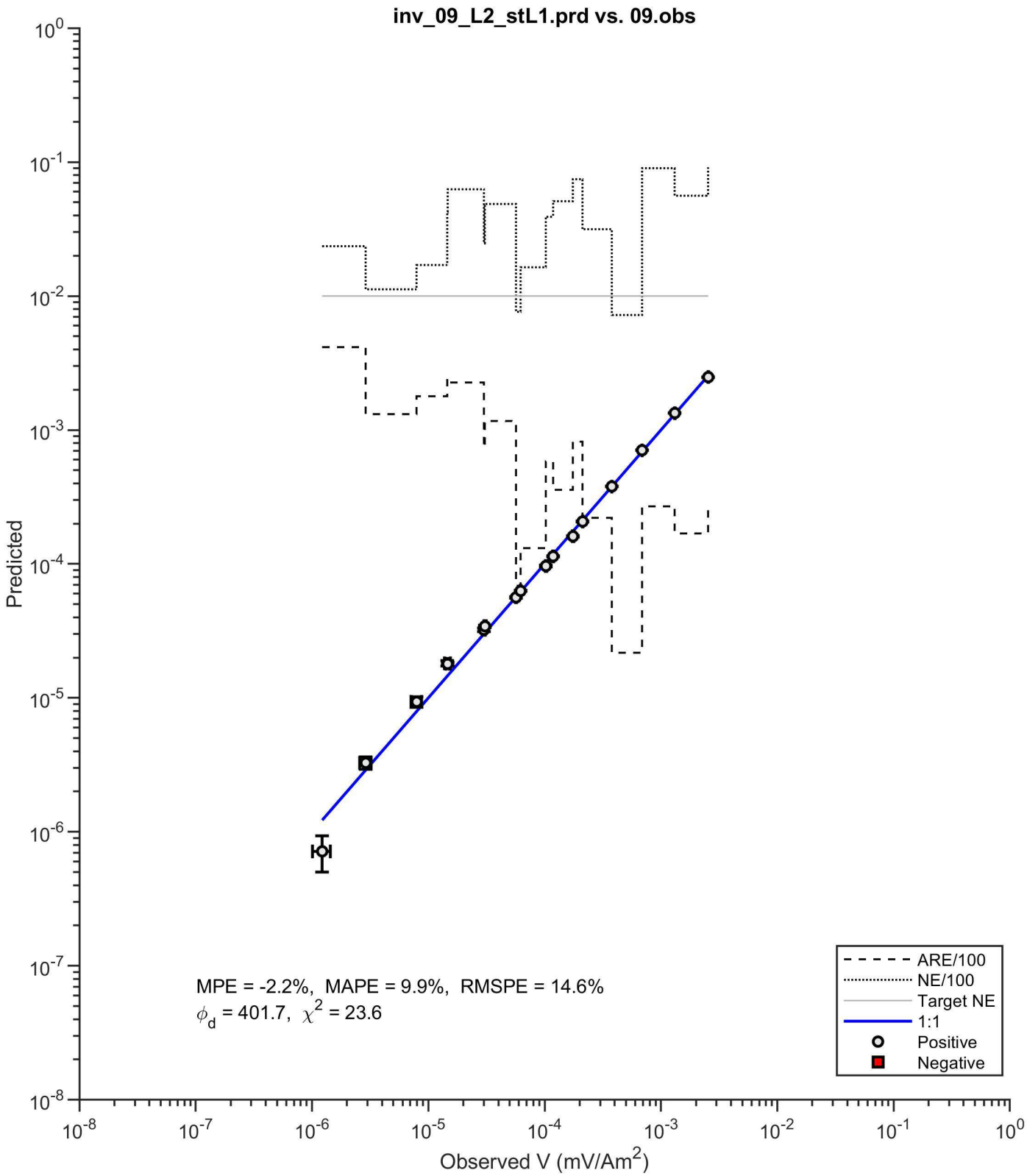
inv_09_L2_stL1.prd vs. 09.obs
Predicted
Observed V (mV/Am^2)
10^{0}
10^{-1}
10^{-2}
10^{-3}
10^{-4}
10^{-5}
10^{-6}
10^{-7}
10^{-8}
MPE = -2.2%, MAPE = 9.9%, RMSPE = 14.6%
ϕ_d = 401.7, χ^2 = 23.6
ARE/100
NE/100
Target NE
1:1
Positive
Negative

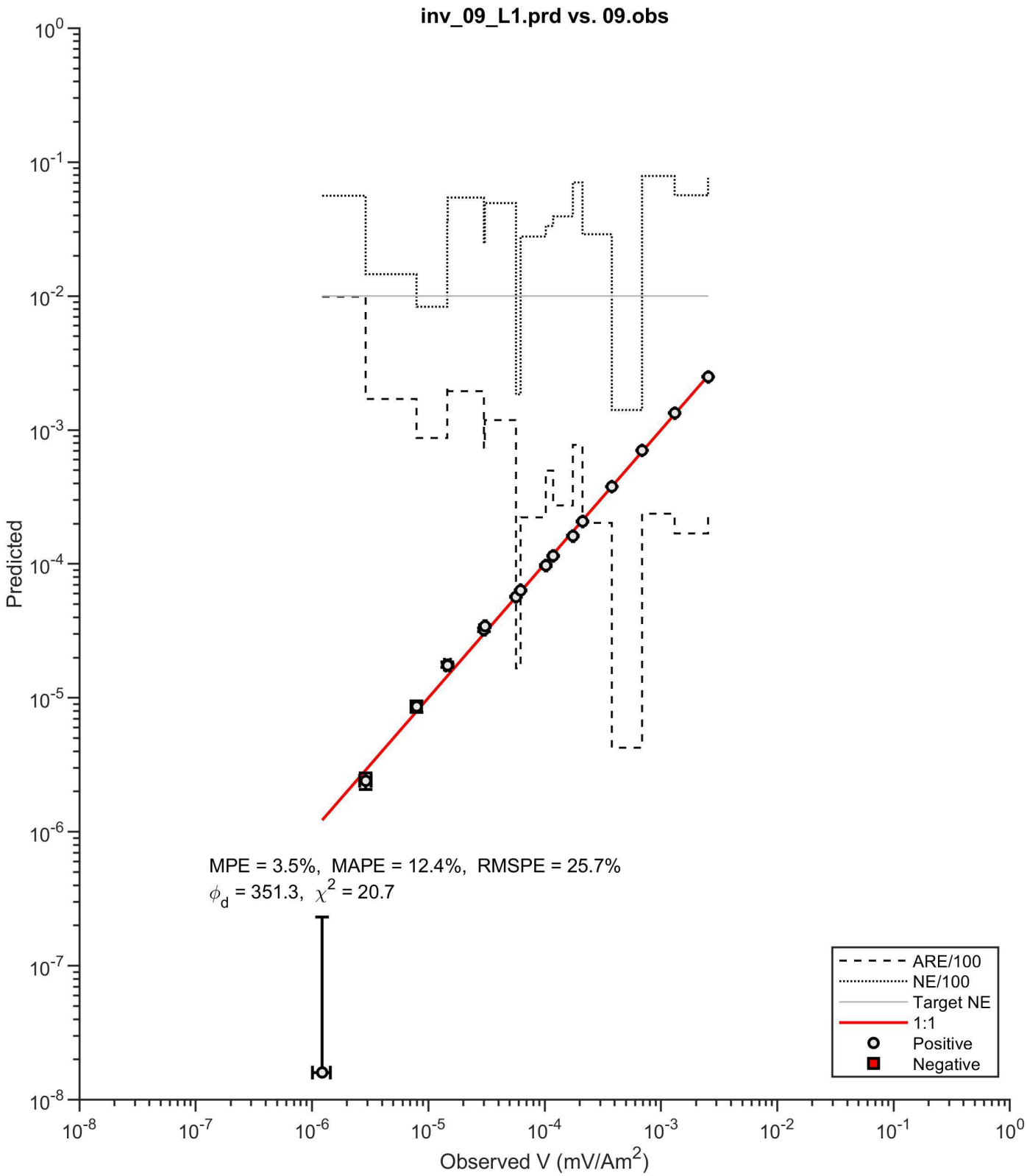
inv_09_L1.prd vs. 09.obs
Predicted
Observed V (mV/Am^2)
10^{0}
10^{-1}
10^{-2}
10^{-3}
10^{-4}
10^{-5}
10^{-6}
10^{-7}
10^{-8}
MPE = 3.5%, MAPE = 12.4%, RMSPE = 25.7%
ϕ_d = 351.3, χ^2 = 20.7
ARE/100
NE/100
Target NE
1:1
Positive
Negative

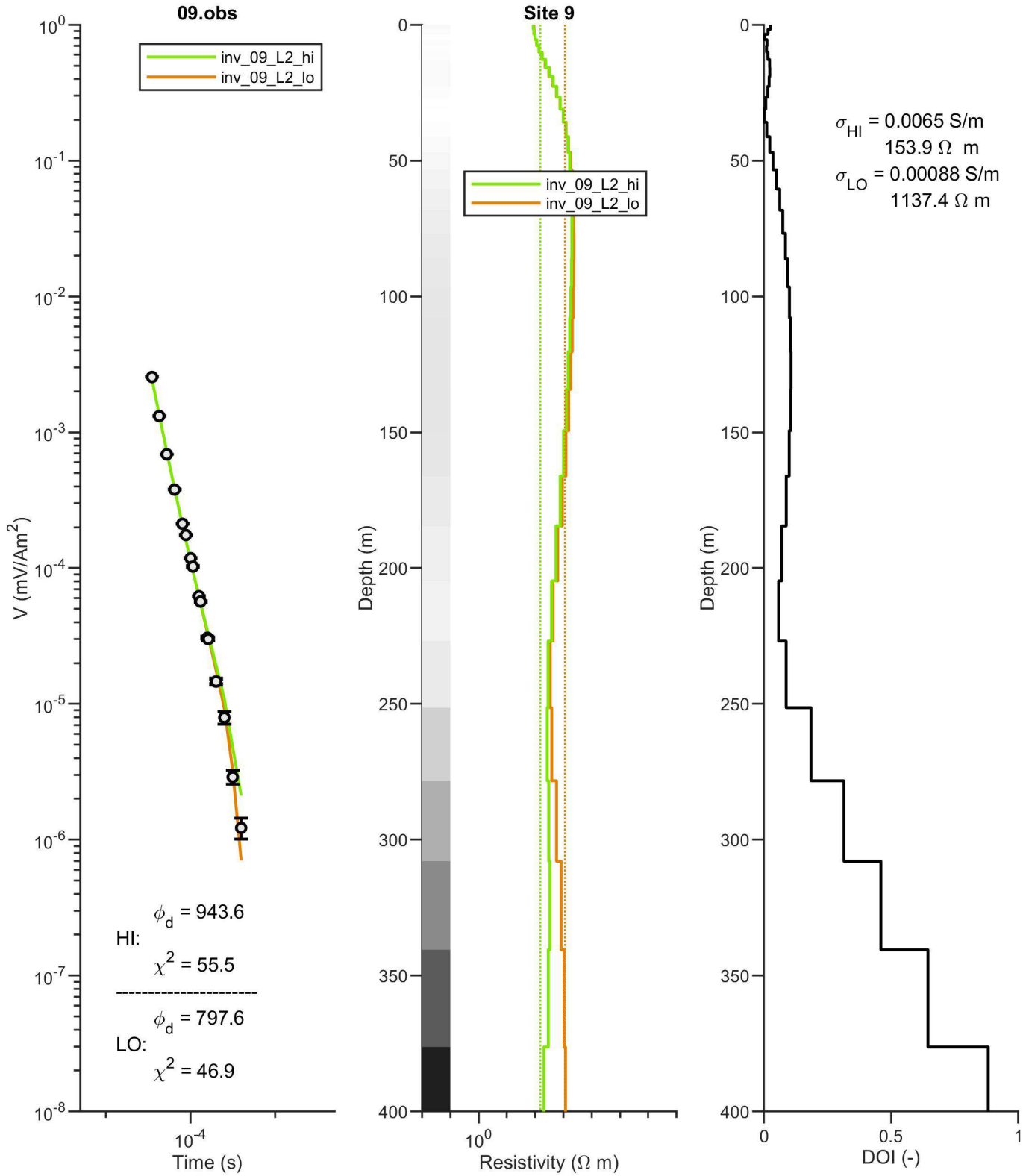
09.obs
inv_09_L2_hi
inv_09_L2_lo
V (mV/Am^2)
Time (s)
ϕ_d = 943.6
HI:
χ^2 = 55.5
ϕ_d = 797.6
LO:
χ^2 = 46.9
Site 9
inv_09_L2_hi
inv_09_L2_lo
Depth (m)
Resistivity (Ω m)
σ_{HI} = 0.0065 S/m
153.9 Ω m
σ_{LO} = 0.00088 S/m
1137.4 Ω m
Depth (m)
DOI (-)

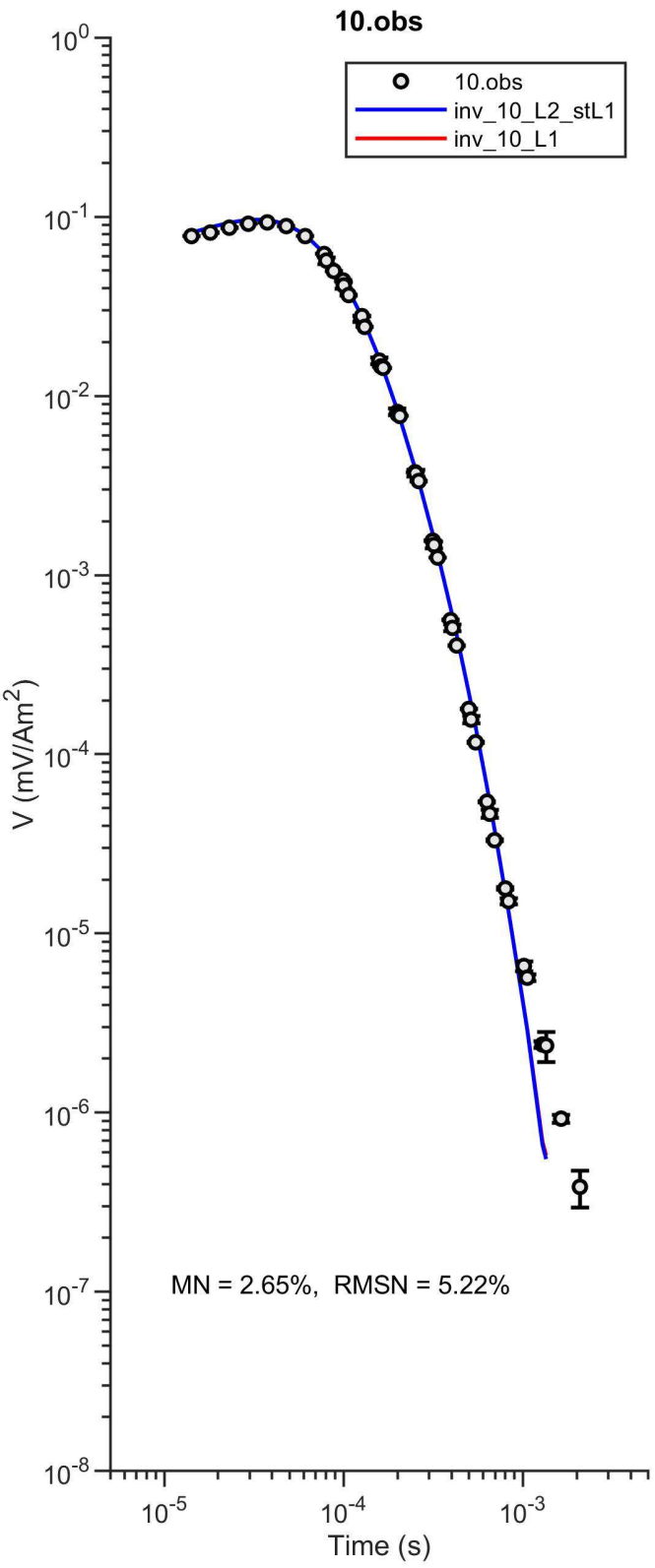
10.obs
10.obs
inv_10_L2_stL1
inv_10_L1
V (mV/Am^2)
Time (s)
MN = 2.65%, RMSN = 5.22%

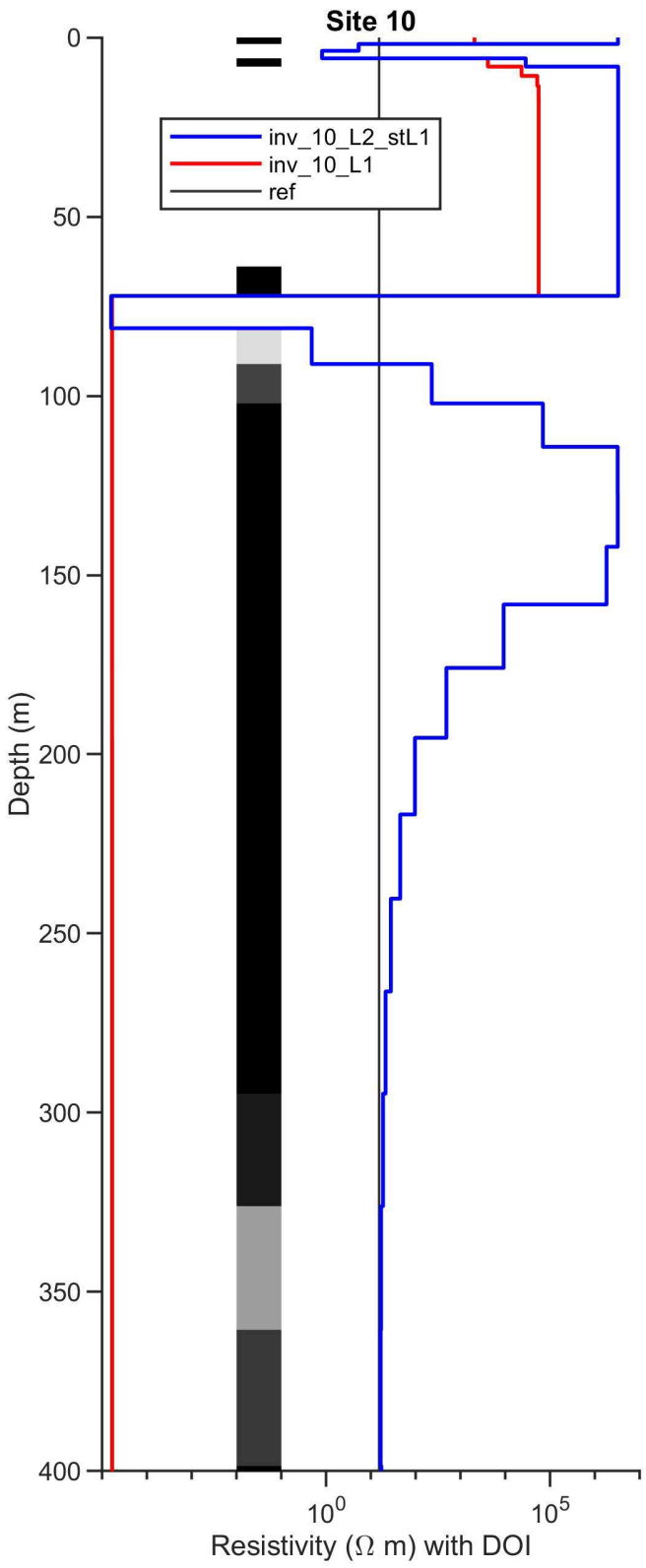
Site 10
inv_10_L2_stL1
inv_10_L1
ref
Depth (m)
Resistivity (Ω m) with DOI

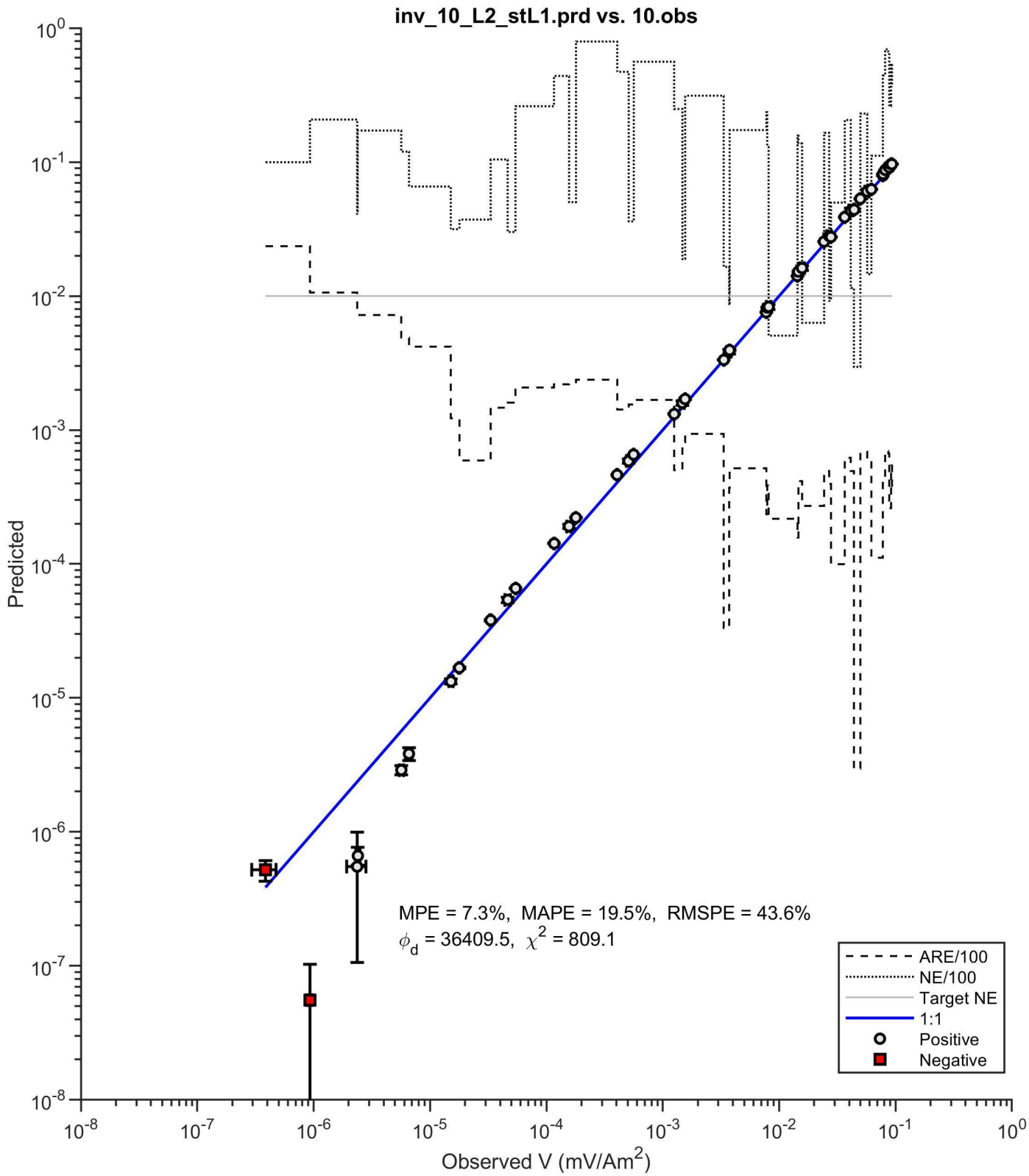
inv_10_L2_stL1.prd vs. 10.obs
Predicted
Observed V (mV/Am^2)
MPE = 7.3%, MAPE = 19.5%, RMSPE = 43.6%
ϕ_d = 36409.5, χ^2 = 809.1
ARE/100
NE/100
Target NE
1:1
Positive
Negative

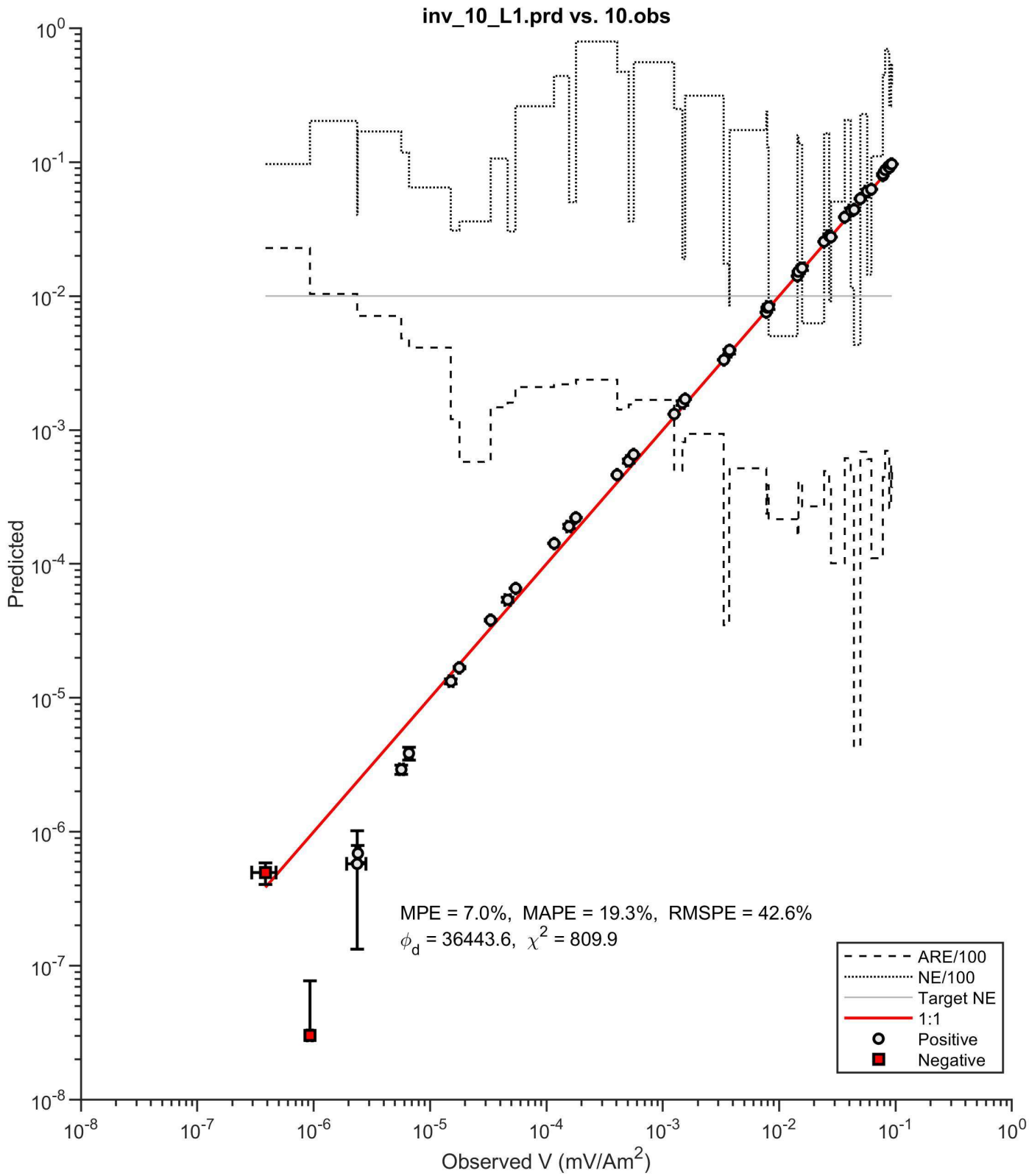
inv_10_L1.prd vs. 10.obs
Predicted
Observed V (mV/Am^2)
MPE = 7.0%, MAPE = 19.3%, RMSPE = 42.6%
ϕ_d = 36443.6, χ^2 = 809.9
ARE/100
NE/100
Target NE
1:1
Positive
Negative

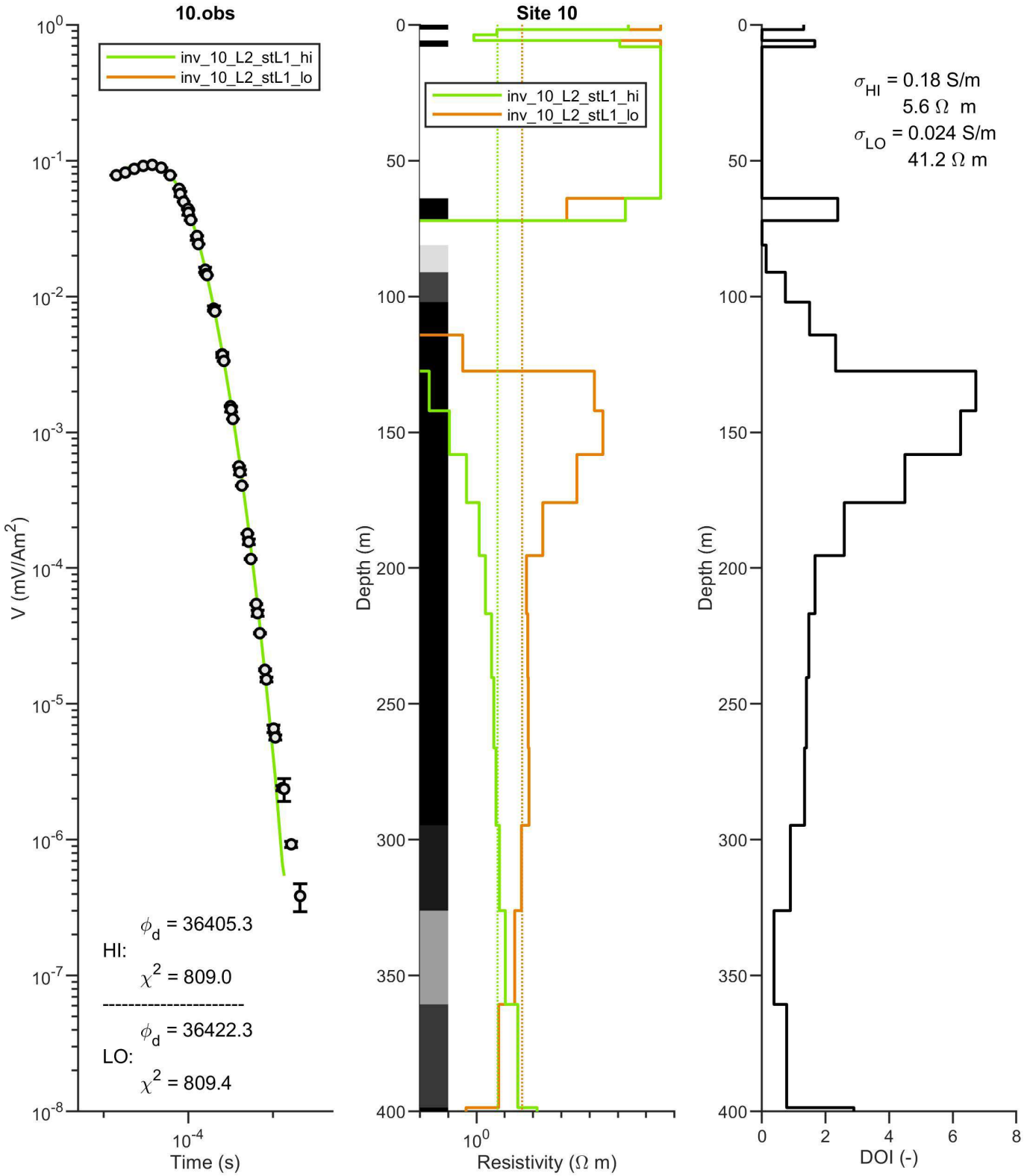
10.obs
inv_10_L2_stL1_hi
inv_10_L2_stL1_lo
V (mV/Am^2)
Time (s)
ϕ_d = 36405.3
HI:
χ^2 = 809.0
ϕ_d = 36422.3
LO:
χ^2 = 809.4
Site 10
inv_10_L2_stL1_hi
inv_10_L2_stL1_lo
Depth (m)
Resistivity (Ω m)
σ_{HI} = 0.18 S/m
5.6 Ω m
σ_{LO} = 0.024 S/m
41.2 Ω m
Depth (m)
DOI (-)

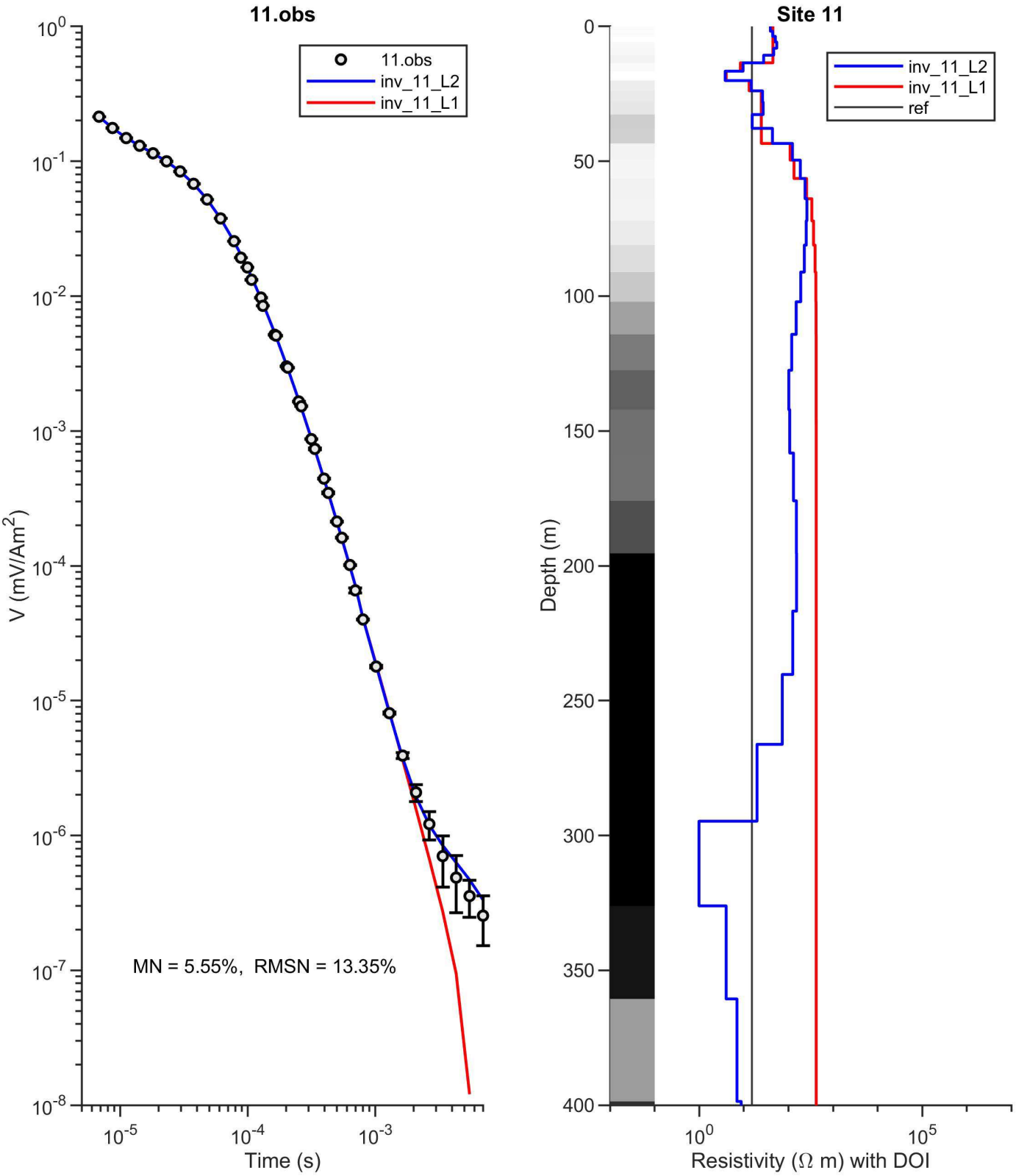
11.obs
11.obs
inv_11_L2
inv_11_L1
V (mV/Am^2)
Time (s)
MN = 5.55%, RMSN = 13.35%
Site 11
inv_11_L2
inv_11_L1
ref
Depth (m)
Resistivity (Ω m) with DOI

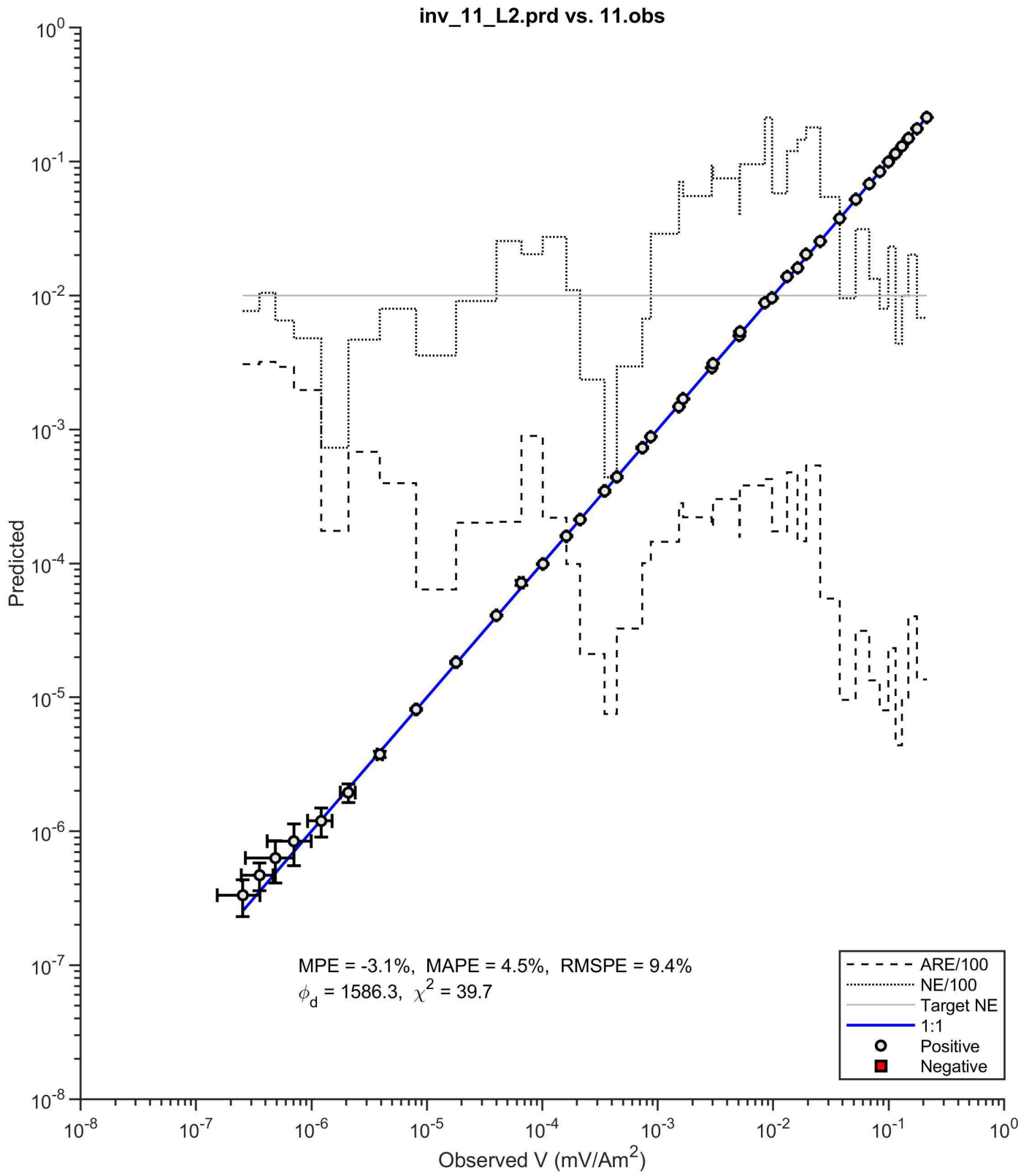
inv_11_L2.prd vs. 11.obs
Predicted
Observed V (mV/Am^2)
MPE = -3.1%, MAPE = 4.5%, RMSPE = 9.4%
ϕ_d = 1586.3, χ^2 = 39.7
ARE/100
NE/100
Target NE
1:1
Positive
Negative

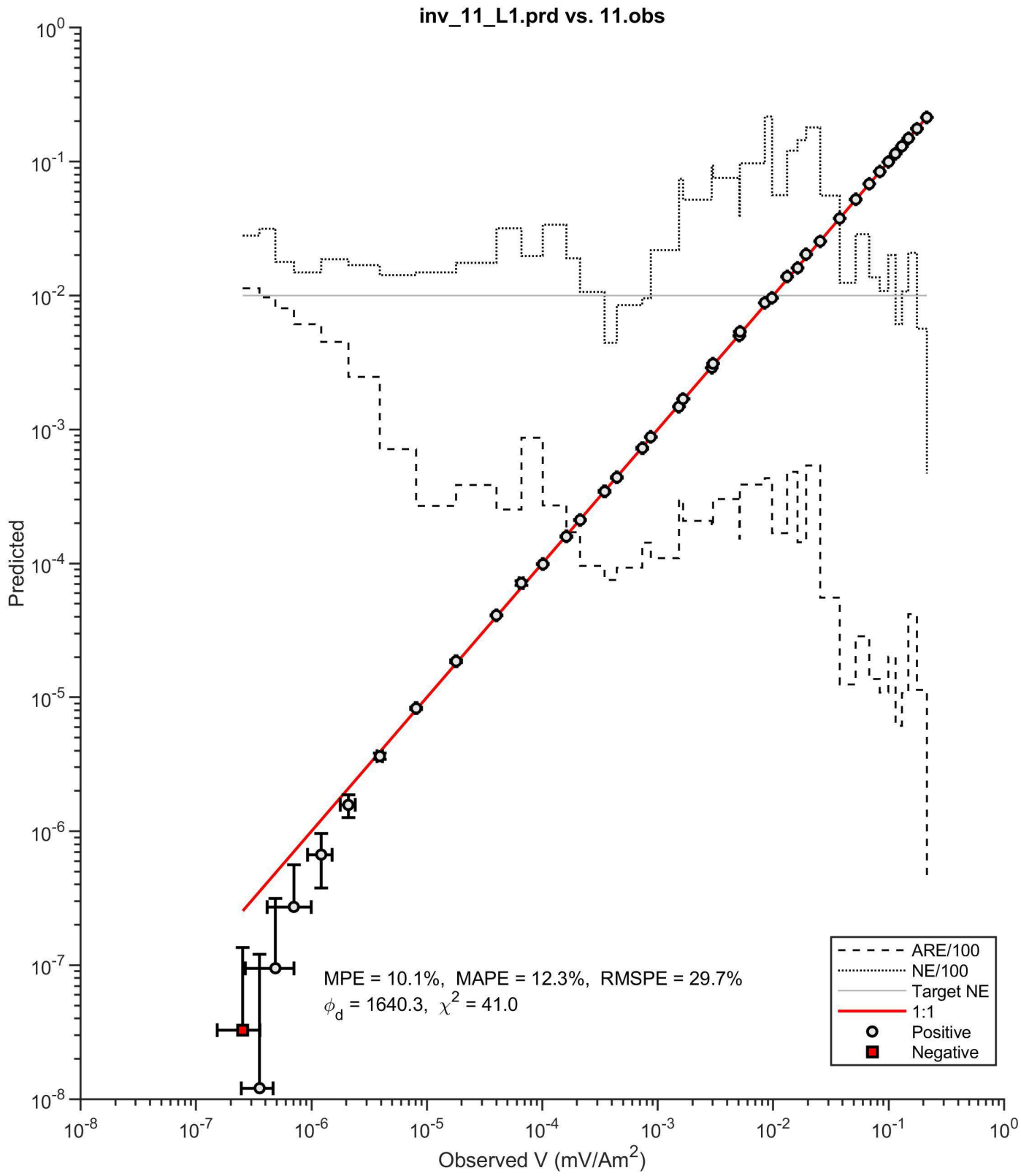
inv_11_L1.prd vs. 11.obs
Predicted
Observed V (mV/Am^2)
MPE = 10.1%, MAPE = 12.3%, RMSPE = 29.7%
ϕ_d = 1640.3, χ^2 = 41.0
ARE/100
NE/100
Target NE
1:1
Positive
Negative

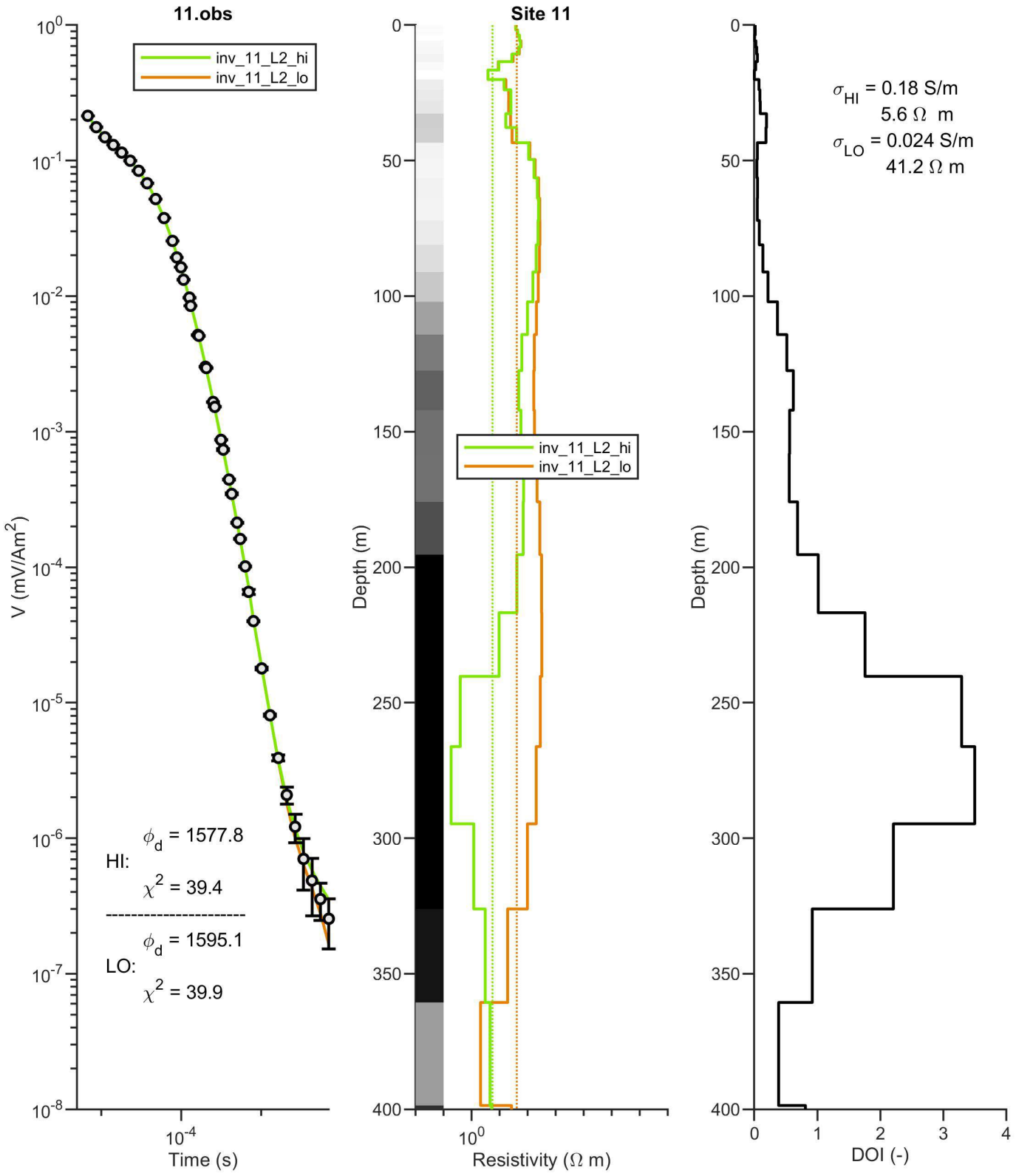
11.obs
inv_11_L2_hi
inv_11_L2_lo
V (mV/Am^2)
Time (s)
ϕ_d = 1577.8
HI:
χ^2 = 39.4
ϕ_d = 1595.1
LO:
χ^2 = 39.9
Site 11
Depth (m)
Resistivity (Ω m)
σ_{HI} = 0.18 S/m
5.6 Ω m
σ_{LO} = 0.024 S/m
41.2 Ω m
DOI (-)

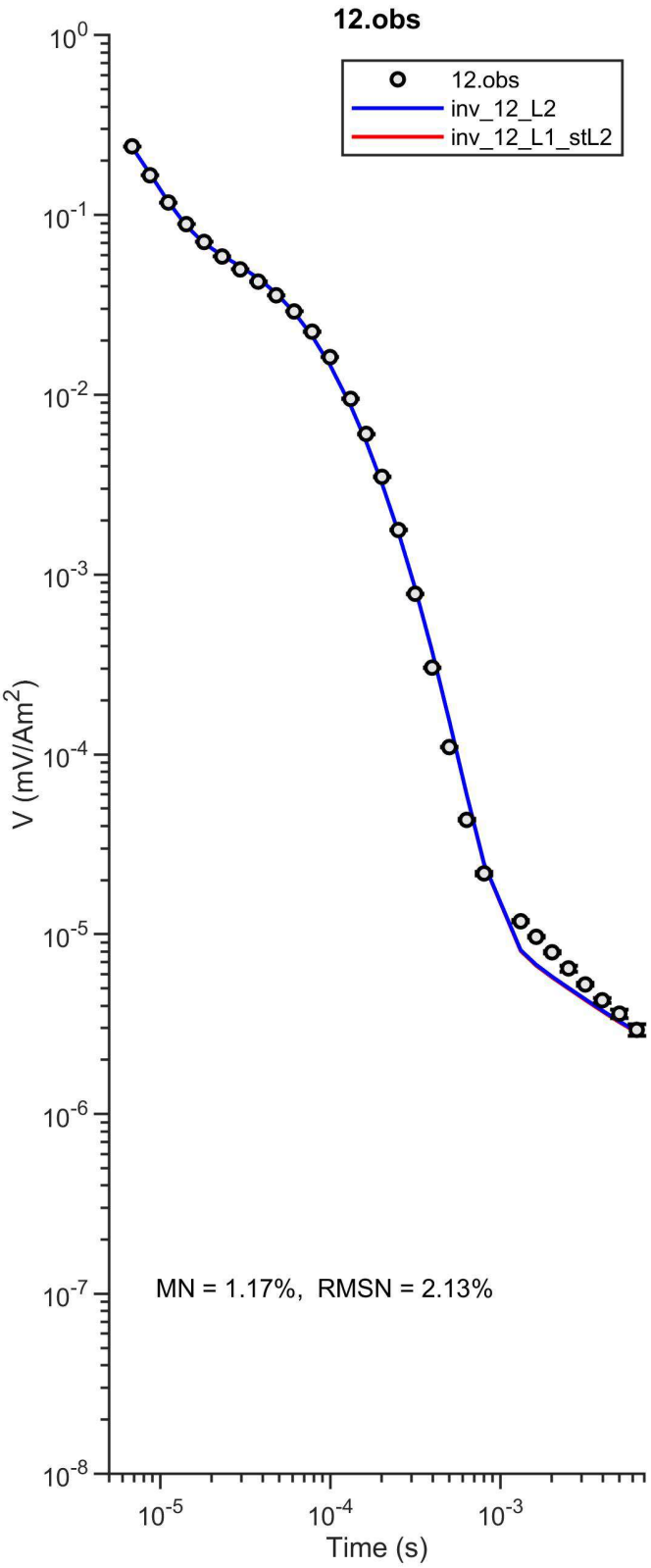
12.obs
12.obs
inv_12_L2
inv_12_L1_stL2
V (mV/Am^2)
Time (s)
MN = 1.17%, RMSN = 2.13%

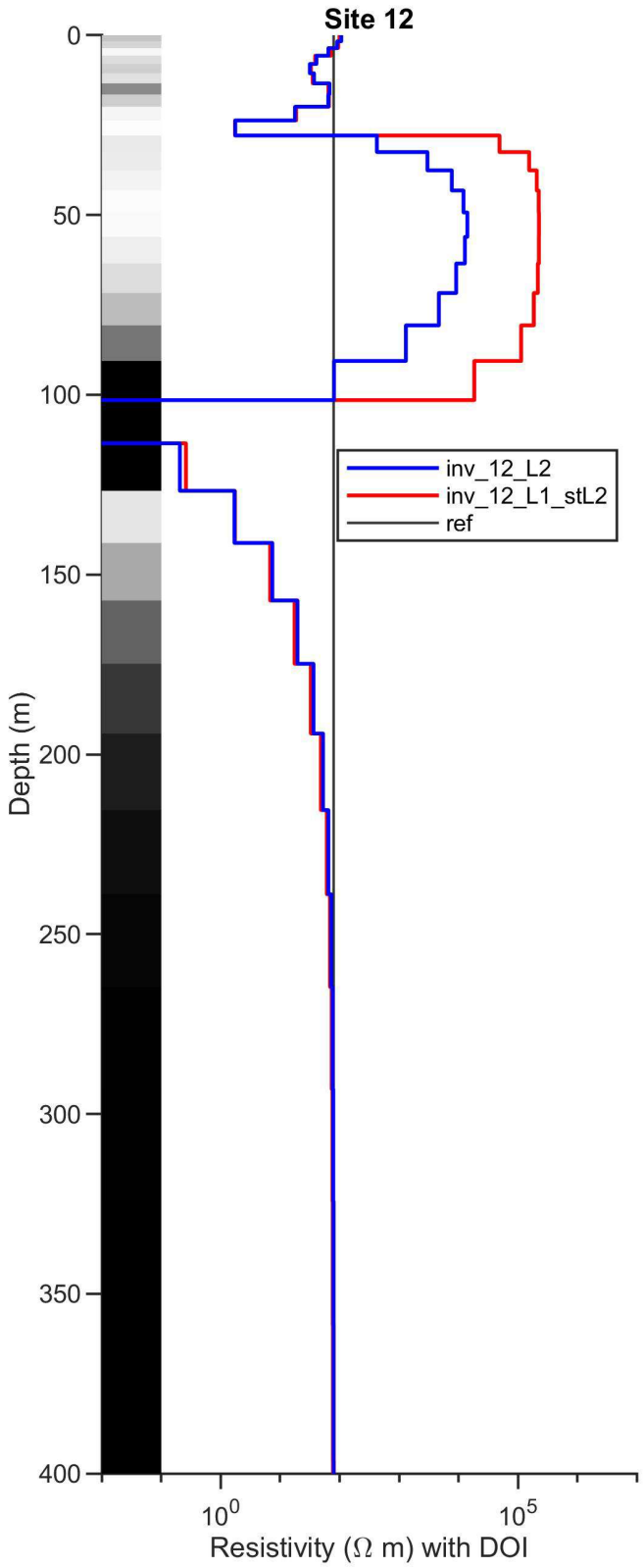
Site 12
inv_12_L2
inv_12_L1_stL2
ref
Depth (m)
Resistivity (Ω m) with DOI

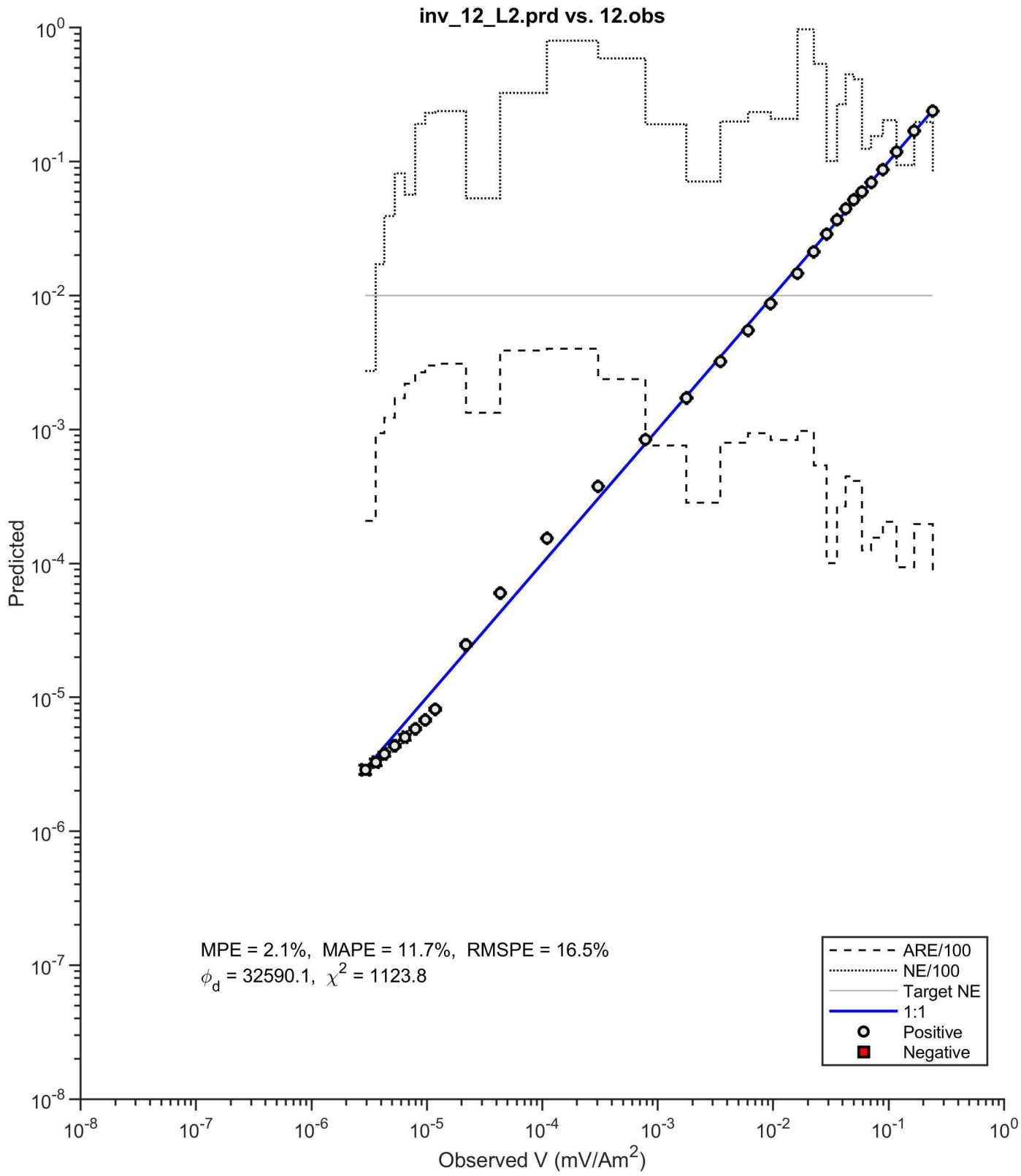
inv_12_L2.prd vs. 12.obs
Predicted
Observed V (mV/Am^2)
10^{0}
10^{-1}
10^{-2}
10^{-3}
10^{-4}
10^{-5}
10^{-6}
10^{-7}
10^{-8}
MPE = 2.1%, MAPE = 11.7%, RMSPE = 16.5%
ϕ_d = 32590.1, χ^2 = 1123.8
ARE/100
NE/100
Target NE
1:1
Positive
Negative

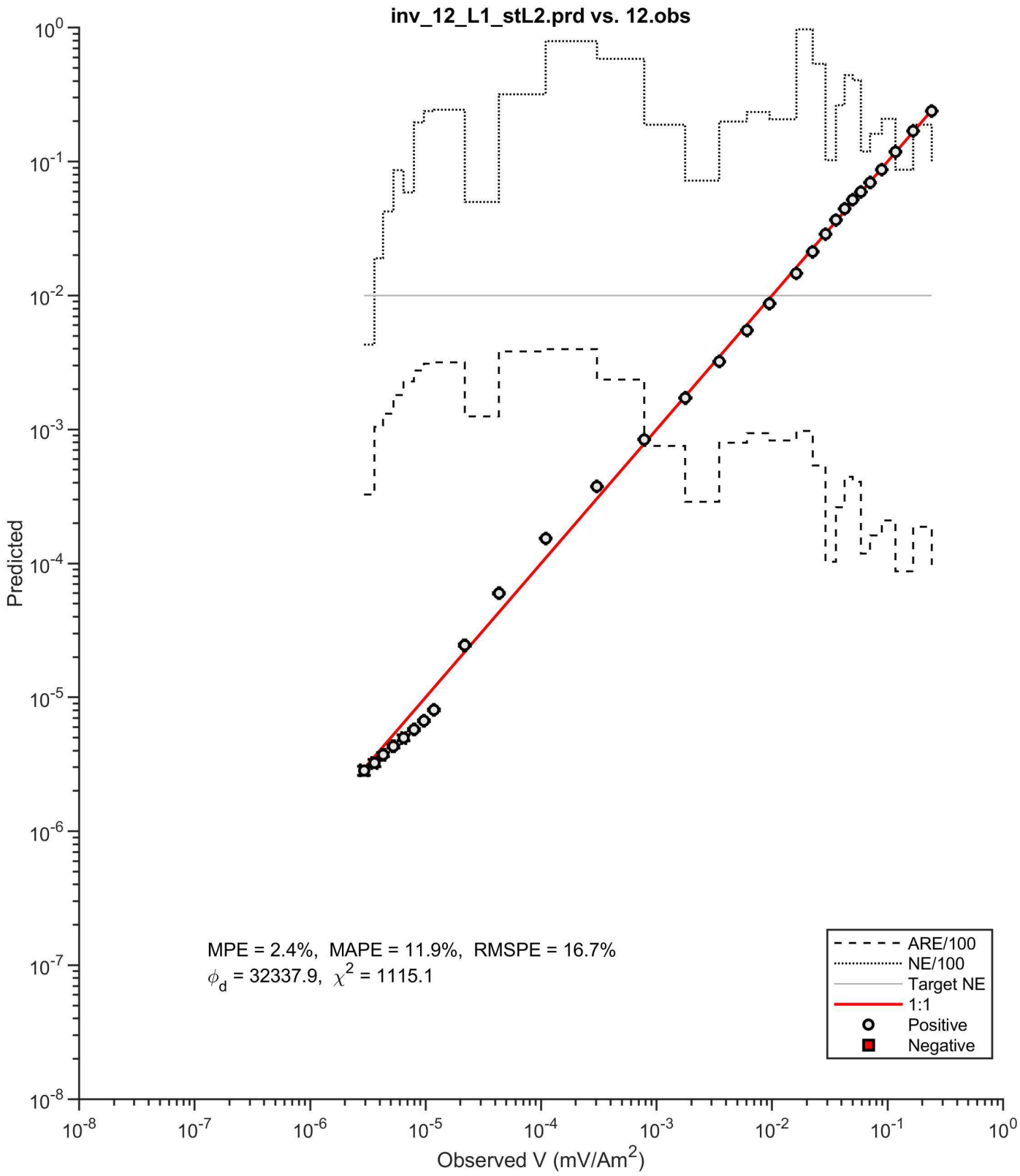
inv_12_L1_stL2.prd vs. 12.obs
Predicted
Observed V (mV/Am^2)
10^{0}
10^{-1}
10^{-2}
10^{-3}
10^{-4}
10^{-5}
10^{-6}
10^{-7}
10^{-8}
MPE = 2.4%, MAPE = 11.9%, RMSPE = 16.7%
ϕ_d = 32337.9, χ^2 = 1115.1
ARE/100
NE/100
Target NE
1:1
Positive
Negative

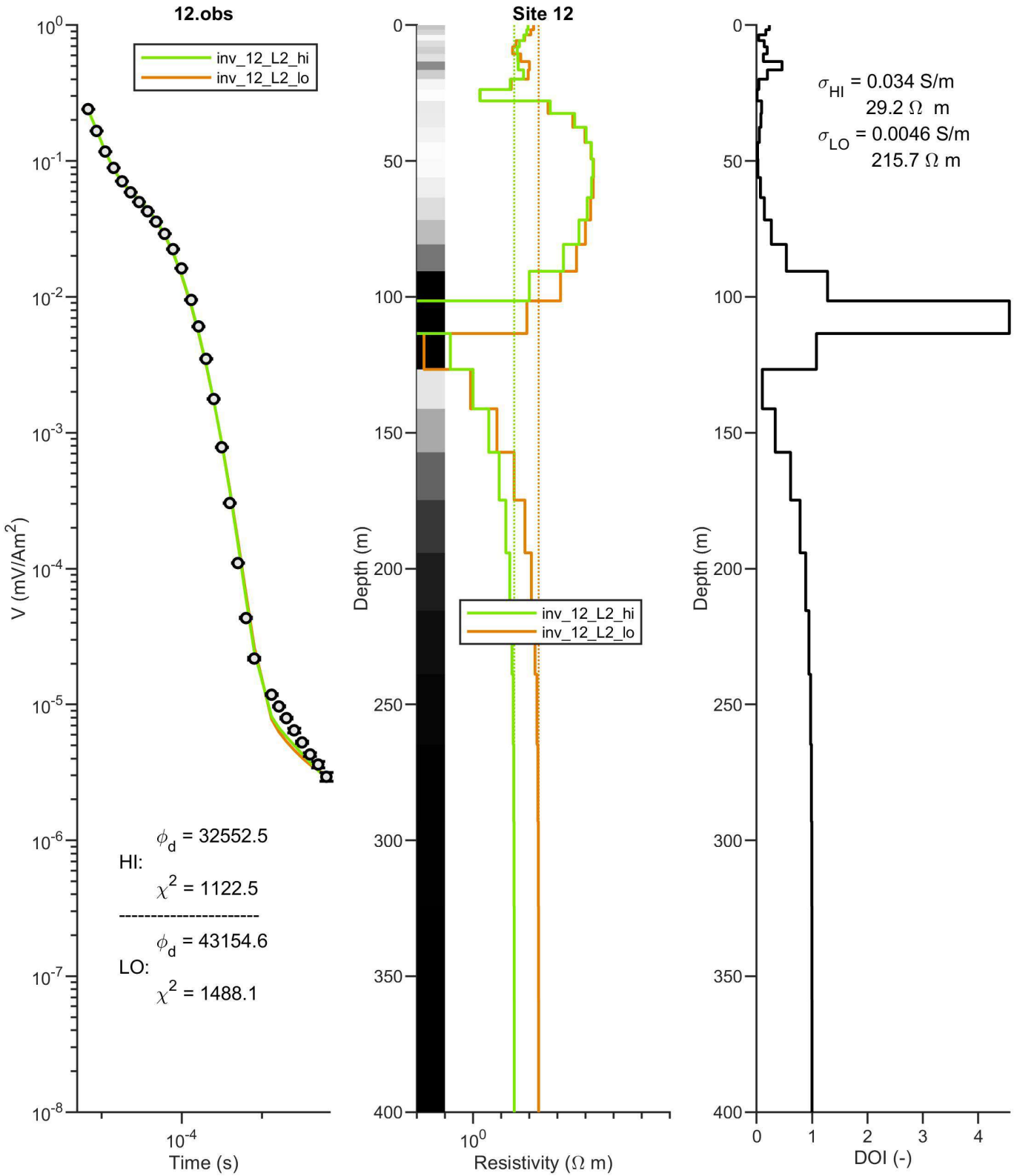
12.obs
inv_12_L2_hi
inv_12_L2_lo
V (mV/Am^2)
Time (s)
ϕ_d = 32552.5
HI:
χ^2 = 1122.5
ϕ_d = 43154.6
LO:
χ^2 = 1488.1
Site 12
Depth (m)
Resistivity (Ω m)
σ_{HI} = 0.034 S/m
29.2 Ω m
σ_{LO} = 0.0046 S/m
215.7 Ω m
DOI (-)

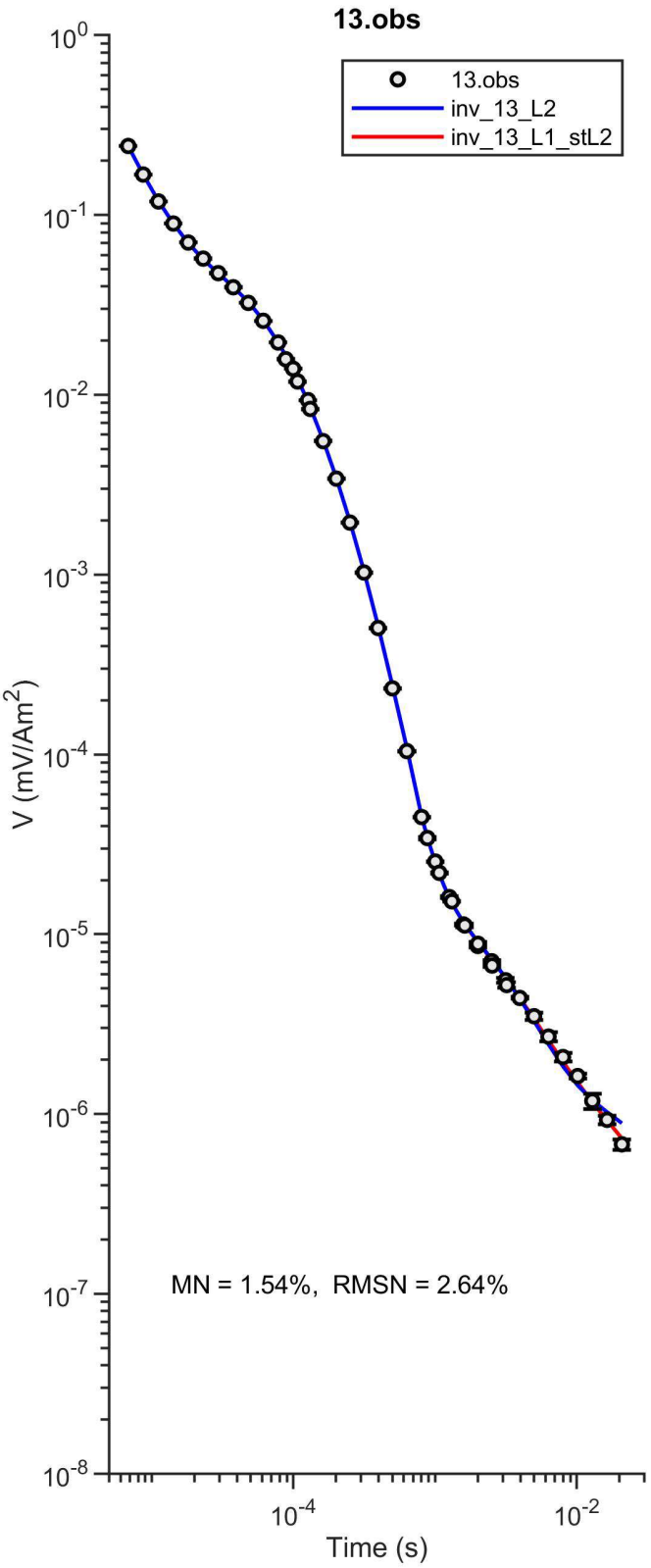
13.obs
13.obs
inv_13_L2
inv_13_L1_stL2
MN = 1.54%, RMSN = 2.64%
V (mV/Am^2)
Time (s)

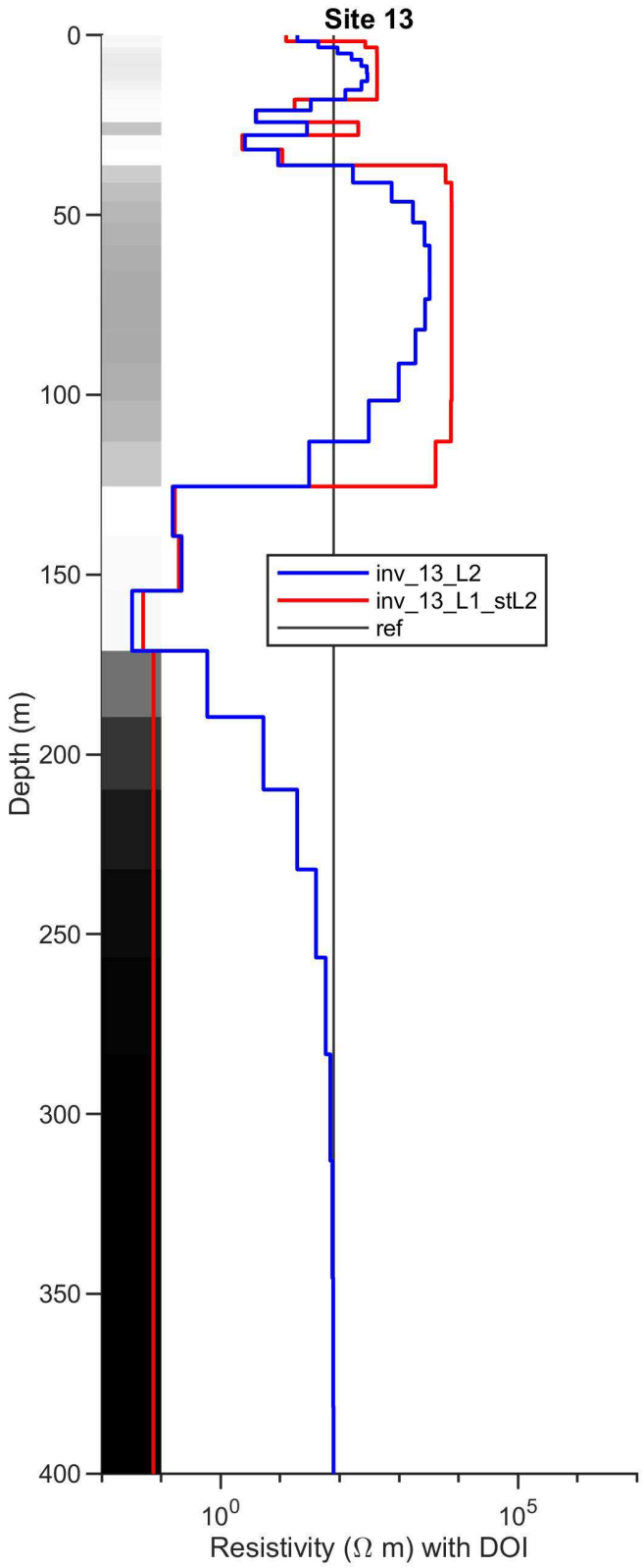
Site 13
inv_13_L2
inv_13_L1_stL2
ref
Depth (m)
Resistivity (Ω m) with DOI

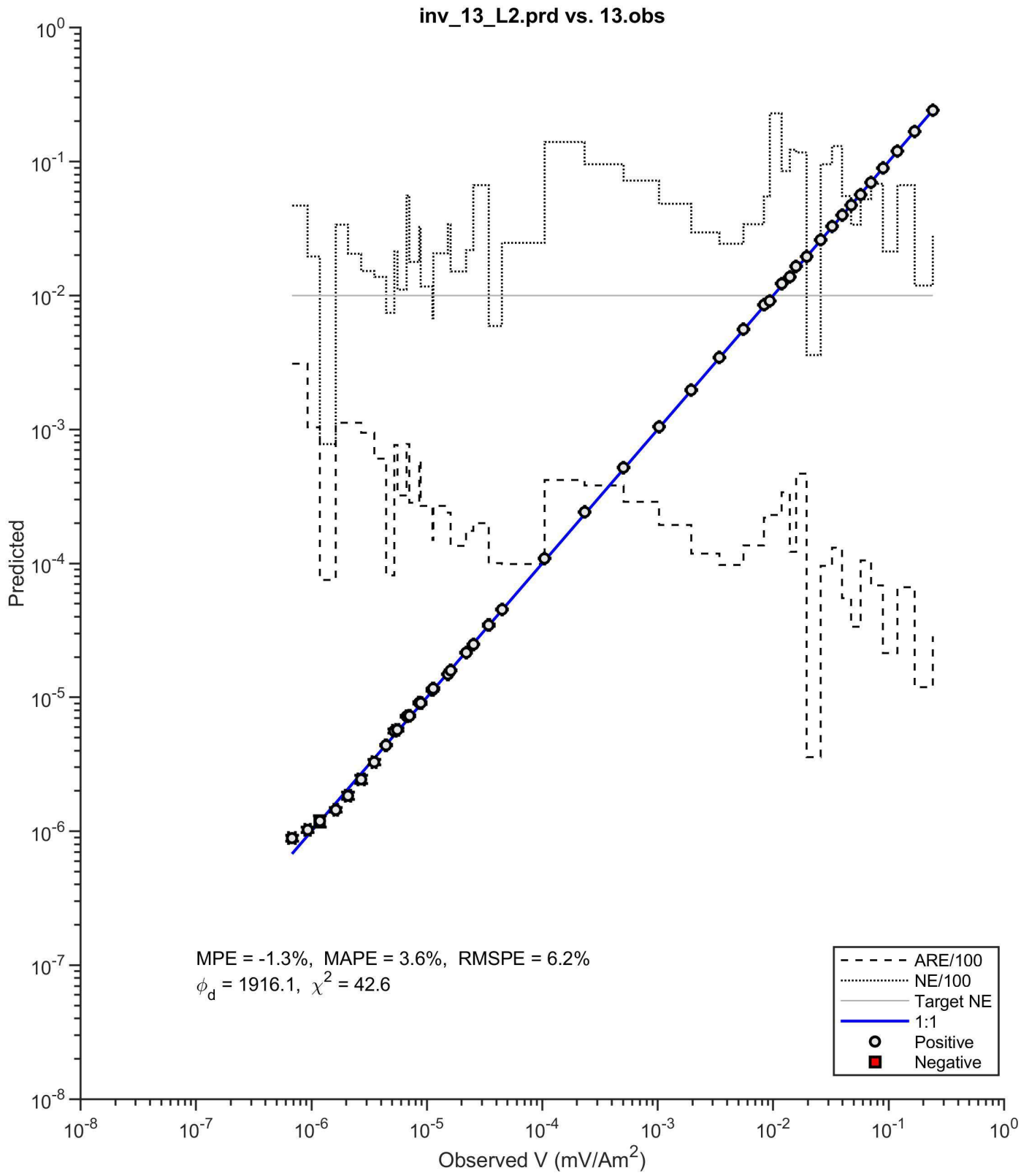
inv_13_L2.prd vs. 13.obs
Predicted
Observed V (mV/Am^2)
10^{0}
10^{-1}
10^{-2}
10^{-3}
10^{-4}
10^{-5}
10^{-6}
10^{-7}
10^{-8}
MPE = -1.3%, MAPE = 3.6%, RMSPE = 6.2%
ϕ_d = 1916.1, χ^2 = 42.6
ARE/100
NE/100
Target NE
1:1
Positive
Negative

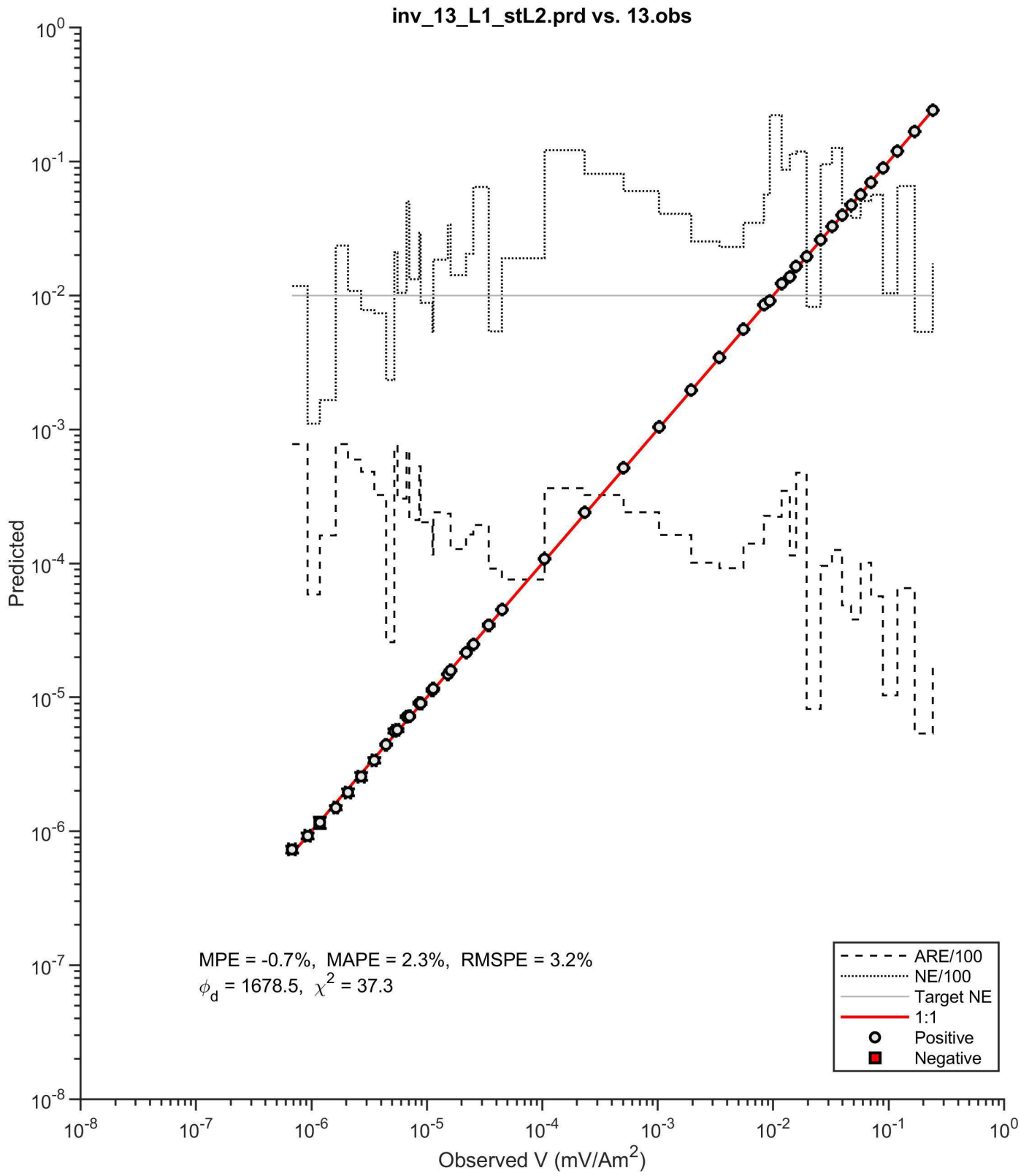
inv_13_L1_stL2.prd vs. 13.obs
Predicted
Observed V (mV/Am^2)
10^{0}
10^{-1}
10^{-2}
10^{-3}
10^{-4}
10^{-5}
10^{-6}
10^{-7}
10^{-8}
MPE = -0.7%, MAPE = 2.3%, RMSPE = 3.2%
ϕ_d = 1678.5, χ^2 = 37.3
ARE/100
NE/100
Target NE
1:1
Positive
Negative

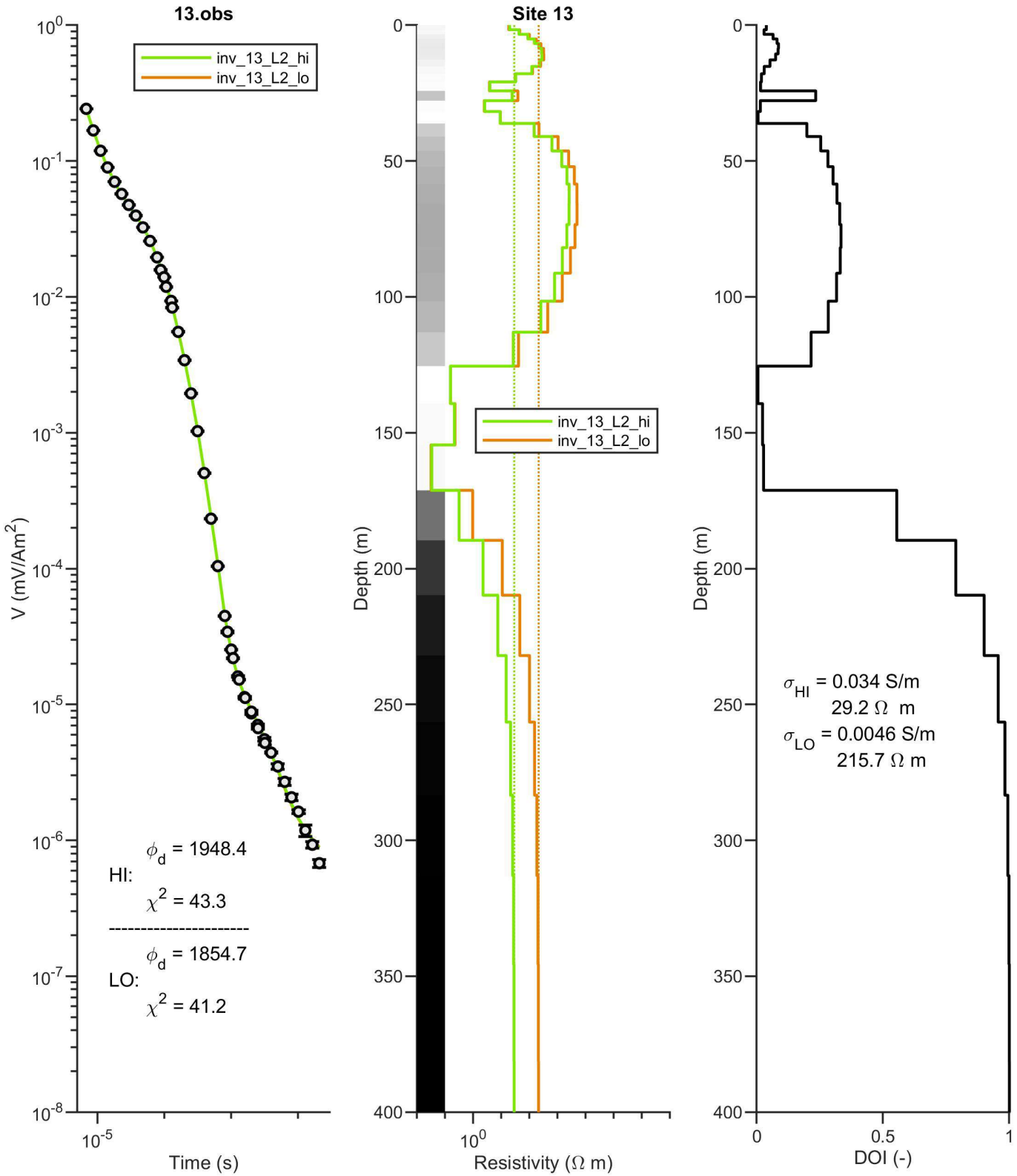
13.obs
inv_13_L2_hi
inv_13_L2_lo
V (mV/Am^2)
Time (s)
ϕ_d = 1948.4
HI:
χ^2 = 43.3
ϕ_d = 1854.7
LO:
χ^2 = 41.2
Site 13
inv_13_L2_hi
inv_13_L2_lo
Depth (m)
Resistivity (Ω m)
σ_{HI} = 0.034 S/m
29.2 Ω m
σ_{LO} = 0.0046 S/m
215.7 Ω m
DOI (-)

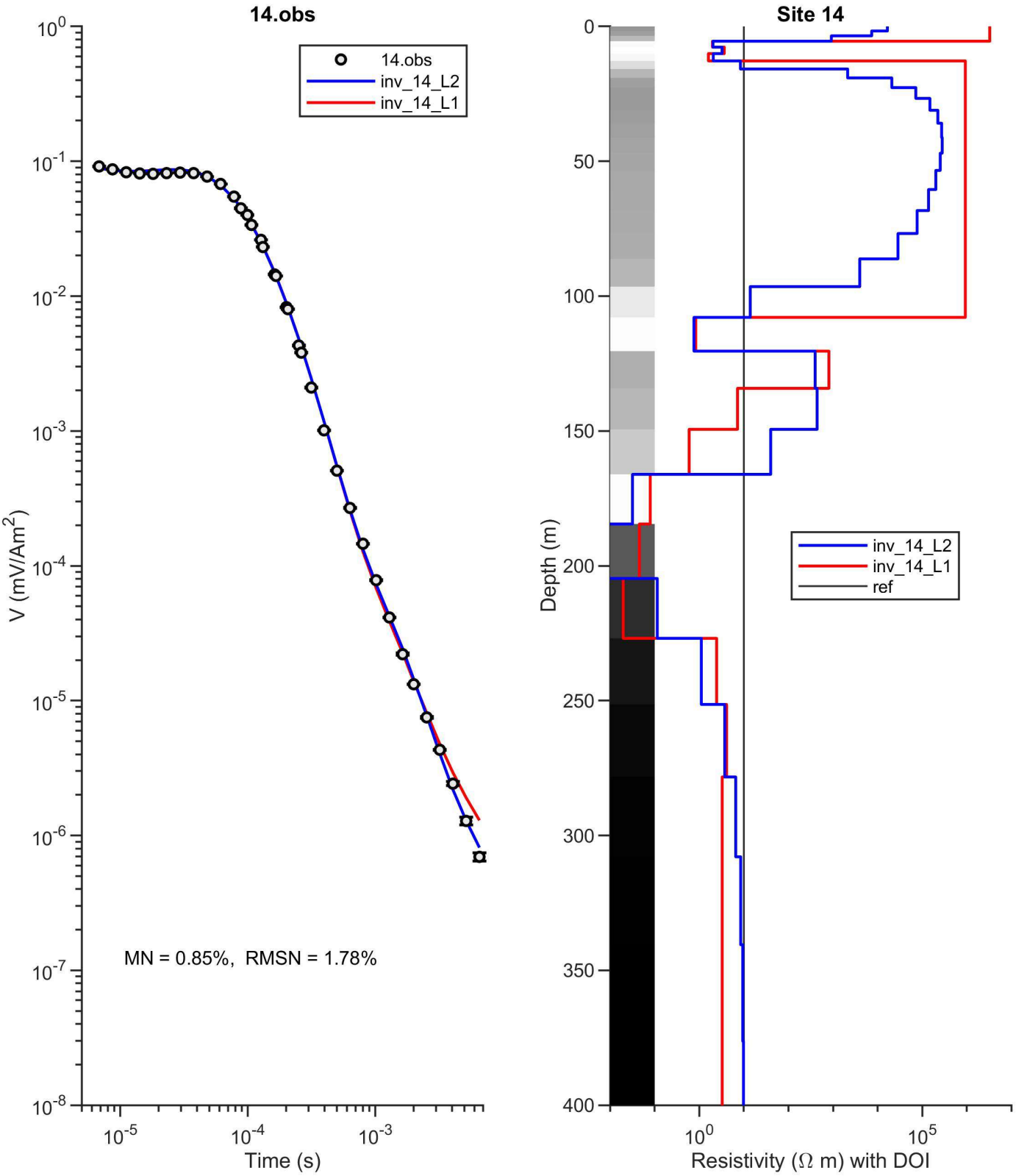
14.obs
14.obs
inv_14_L2
inv_14_L1
V (mV/Am^2)
Time (s)
MN = 0.85%, RMSN = 1.78%
Site 14
inv_14_L2
inv_14_L1
ref
Depth (m)
Resistivity (Ω m) with DOI

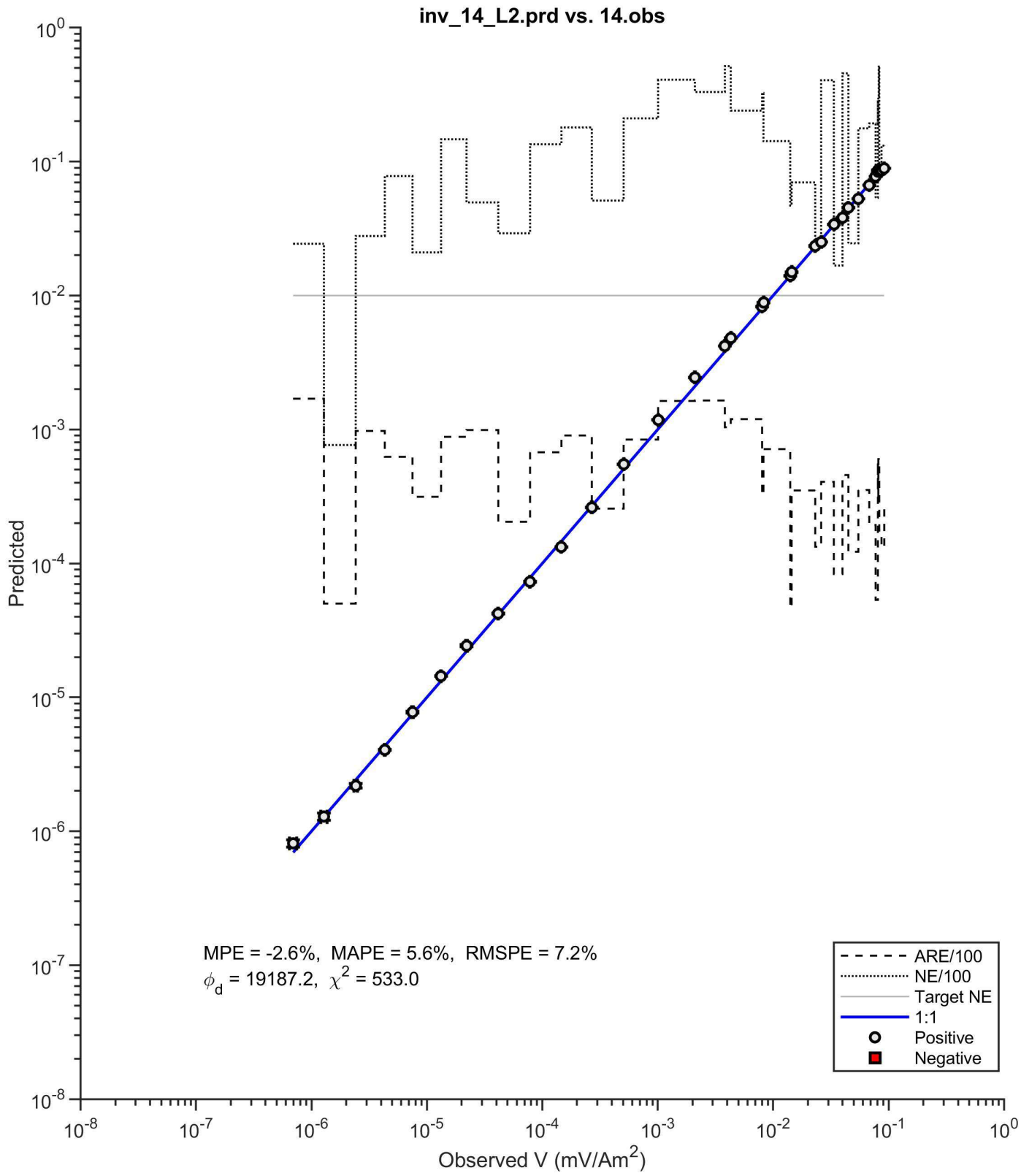
inv_14_L2.prd vs. 14.obs
Predicted
Observed V (mV/Am^2)
10^{0}
10^{-1}
10^{-2}
10^{-3}
10^{-4}
10^{-5}
10^{-6}
10^{-7}
10^{-8}
MPE = -2.6%, MAPE = 5.6%, RMSPE = 7.2%
ϕ_d = 19187.2, χ^2 = 533.0
ARE/100
NE/100
Target NE
1:1
Positive
Negative

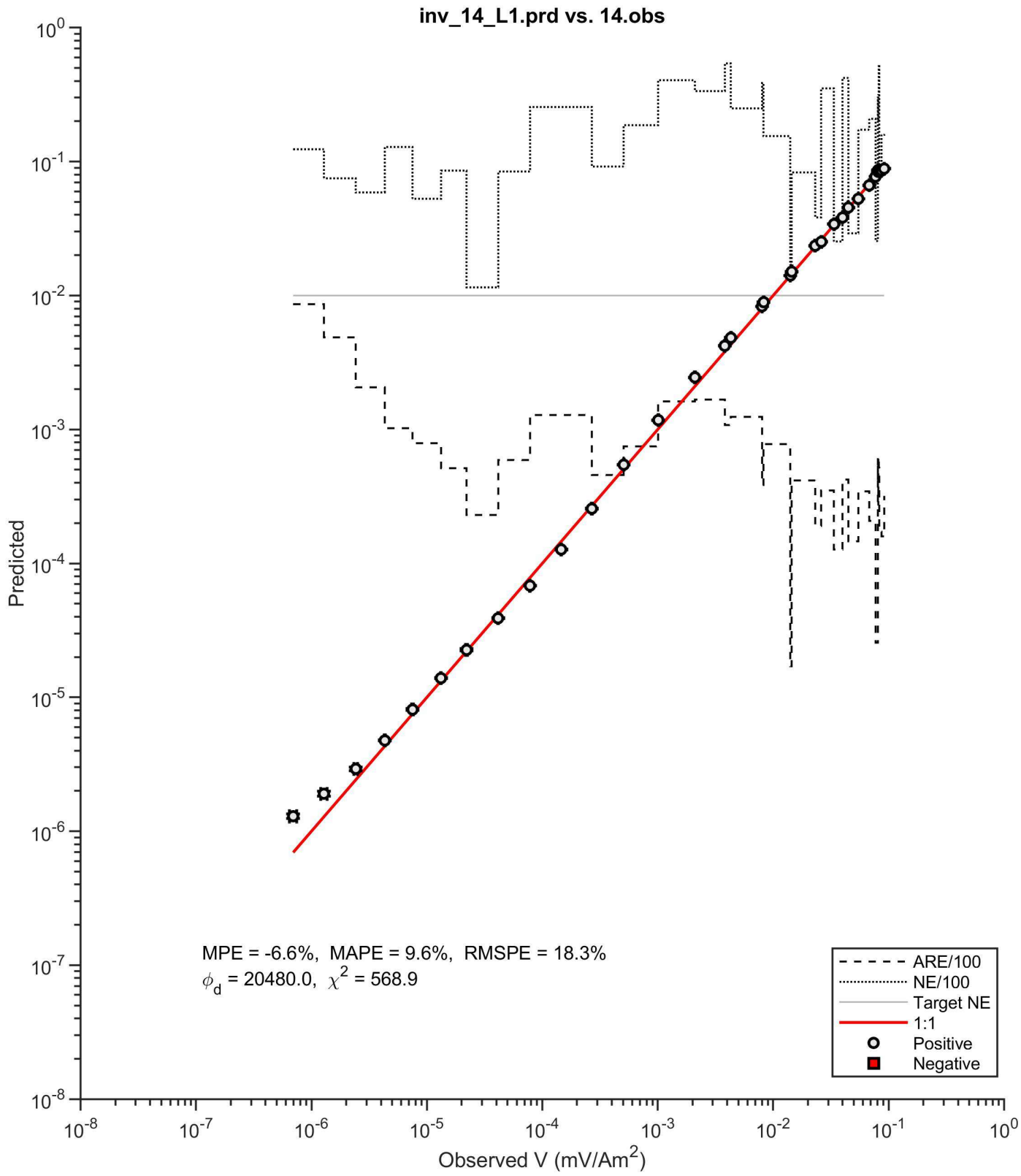
inv_14_L1.prd vs. 14.obs
Predicted
Observed V (mV/Am^2)
MPE = -6.6%, MAPE = 9.6%, RMSPE = 18.3%
ϕ_d = 20480.0, χ^2 = 568.9
ARE/100
NE/100
Target NE
1:1
Positive
Negative

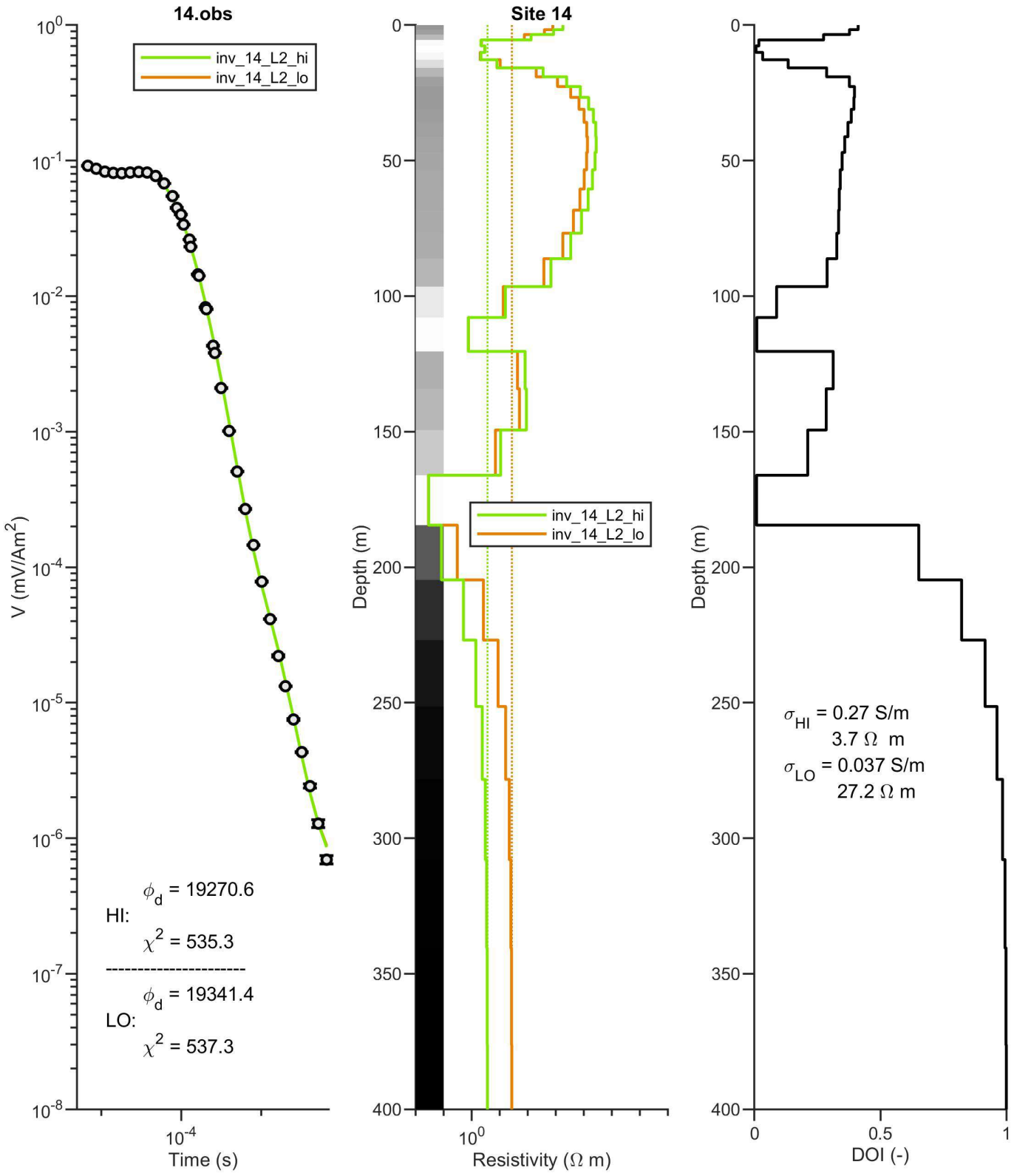
14.obs
inv_14_L2_hi
inv_14_L2_lo
V (mV/Am^2)
Time (s)
ϕ_d = 19270.6
HI:
χ^2 = 535.3
ϕ_d = 19341.4
LO:
χ^2 = 537.3
Site 14
Depth (m)
Resistivity (Ω m)
σ_{HI} = 0.27 S/m
3.7 Ω m
σ_{LO} = 0.037 S/m
27.2 Ω m
DOI (-)

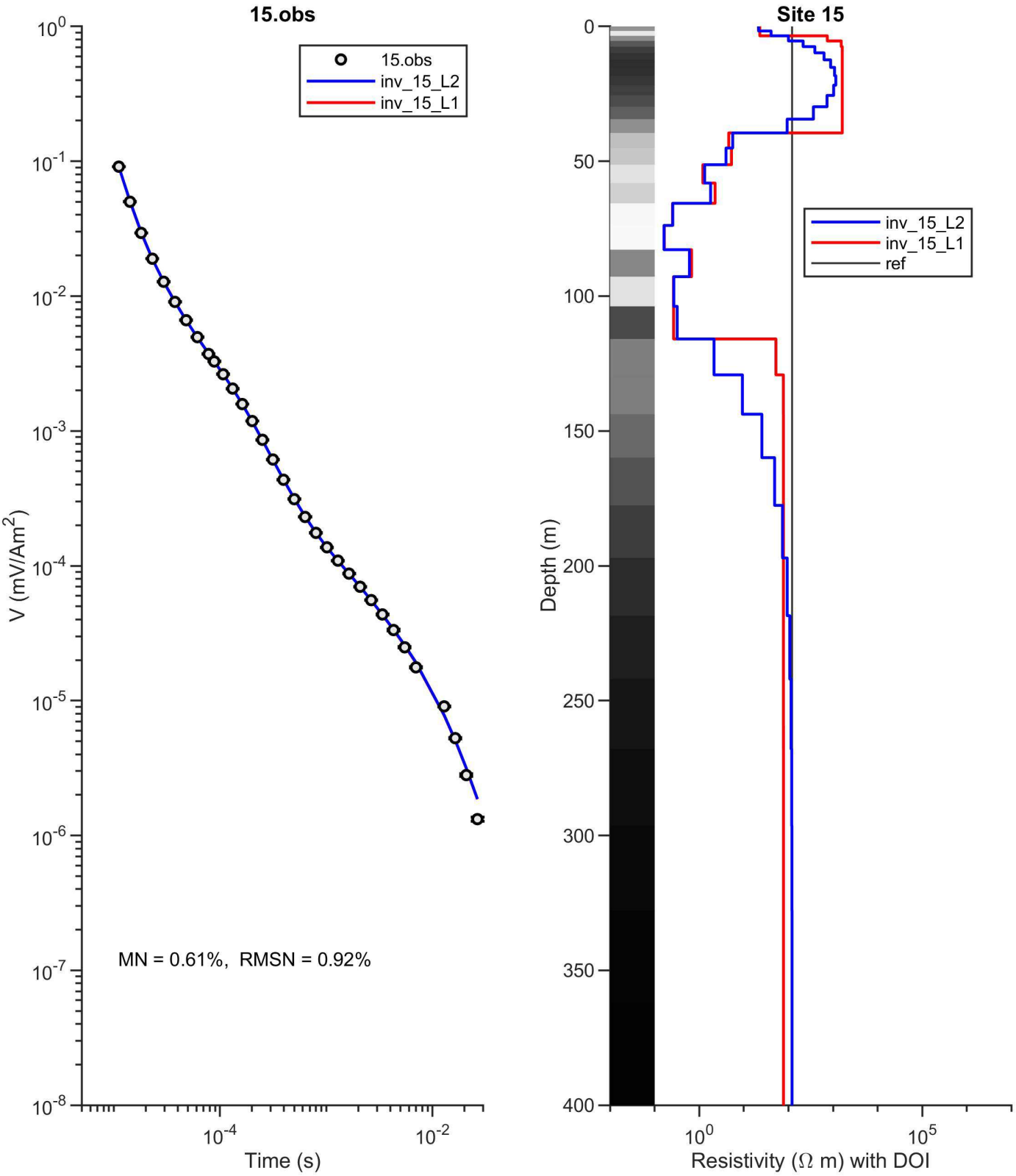
15.obs
15.obs
inv_15_L2
inv_15_L1
V (mV/Am^2)
Time (s)
MN = 0.61%, RMSN = 0.92%
Site 15
inv_15_L2
inv_15_L1
ref
Depth (m)
Resistivity (Ω m) with DOI

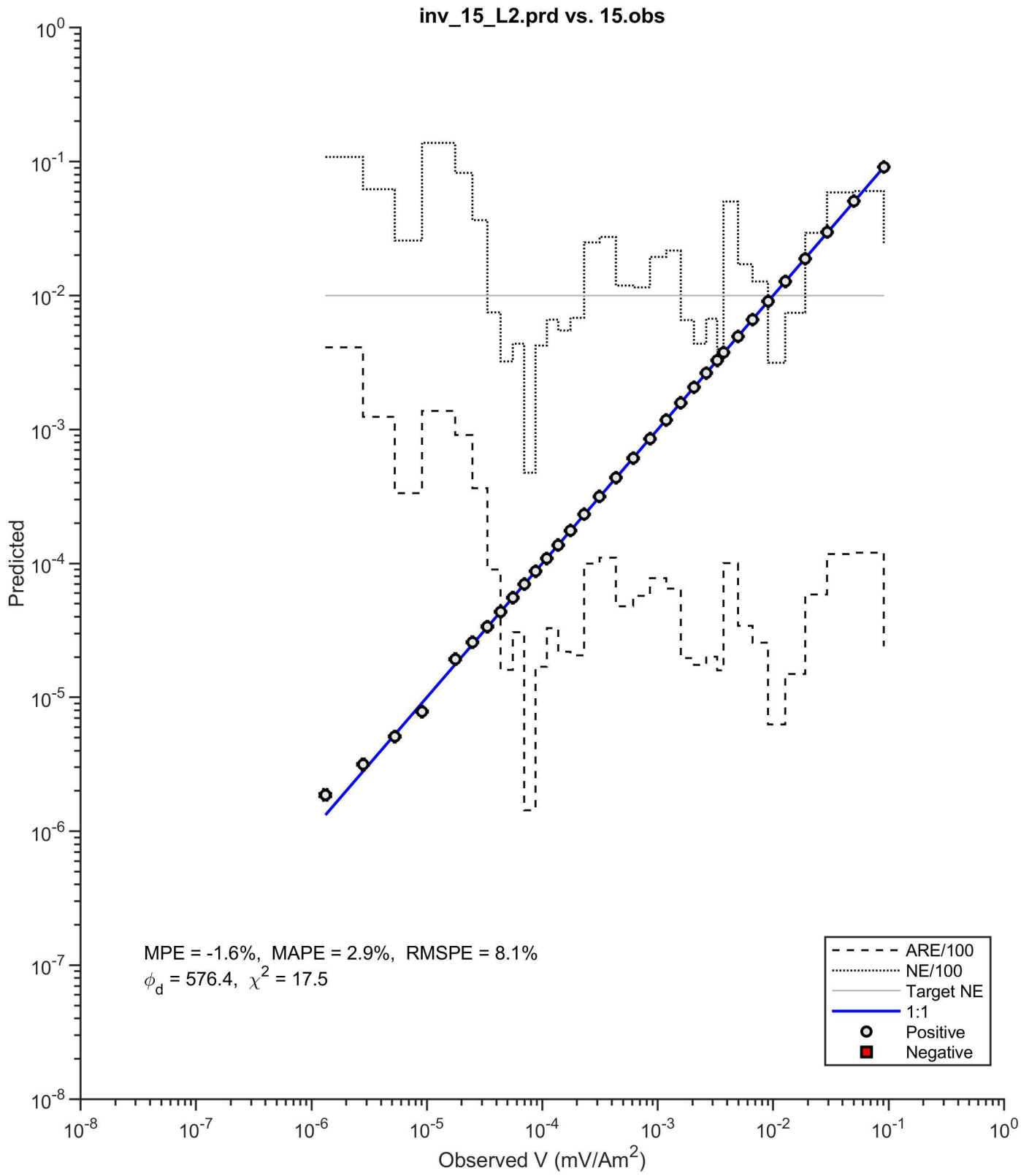
inv_15_L2.prd vs. 15.obs
Predicted
Observed V (mV/Am^2)
10^{0}
10^{-1}
10^{-2}
10^{-3}
10^{-4}
10^{-5}
10^{-6}
10^{-7}
10^{-8}
MPE = -1.6%, MAPE = 2.9%, RMSPE = 8.1%
ϕ_d = 576.4, χ^2 = 17.5
ARE/100
NE/100
Target NE
1:1
Positive
Negative

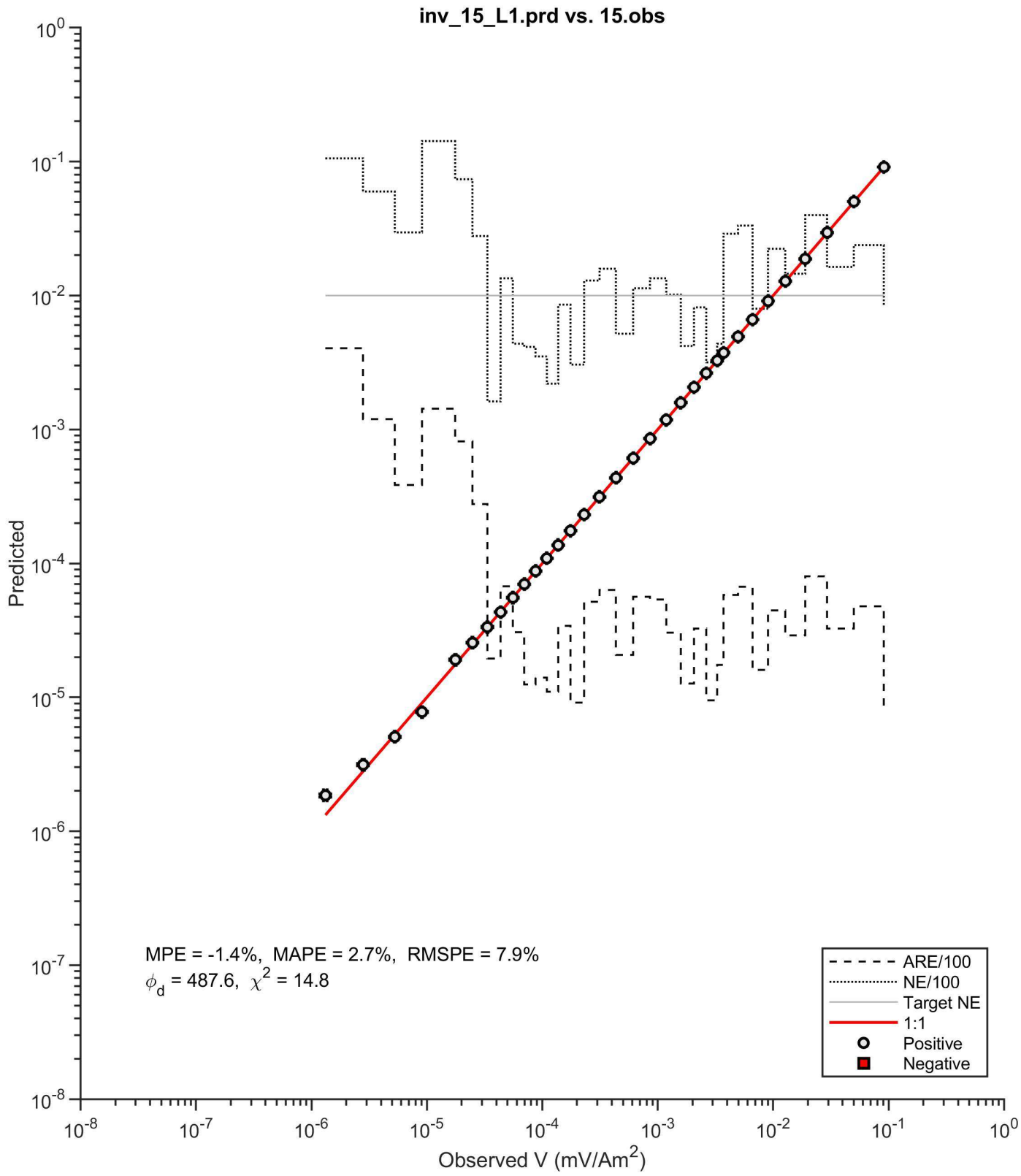
inv_15_L1.prd vs. 15.obs
Predicted
Observed V (mV/Am^2)
MPE = -1.4%, MAPE = 2.7%, RMSPE = 7.9%
ϕ_d = 487.6, χ^2 = 14.8
ARE/100
NE/100
Target NE
1:1
Positive
Negative

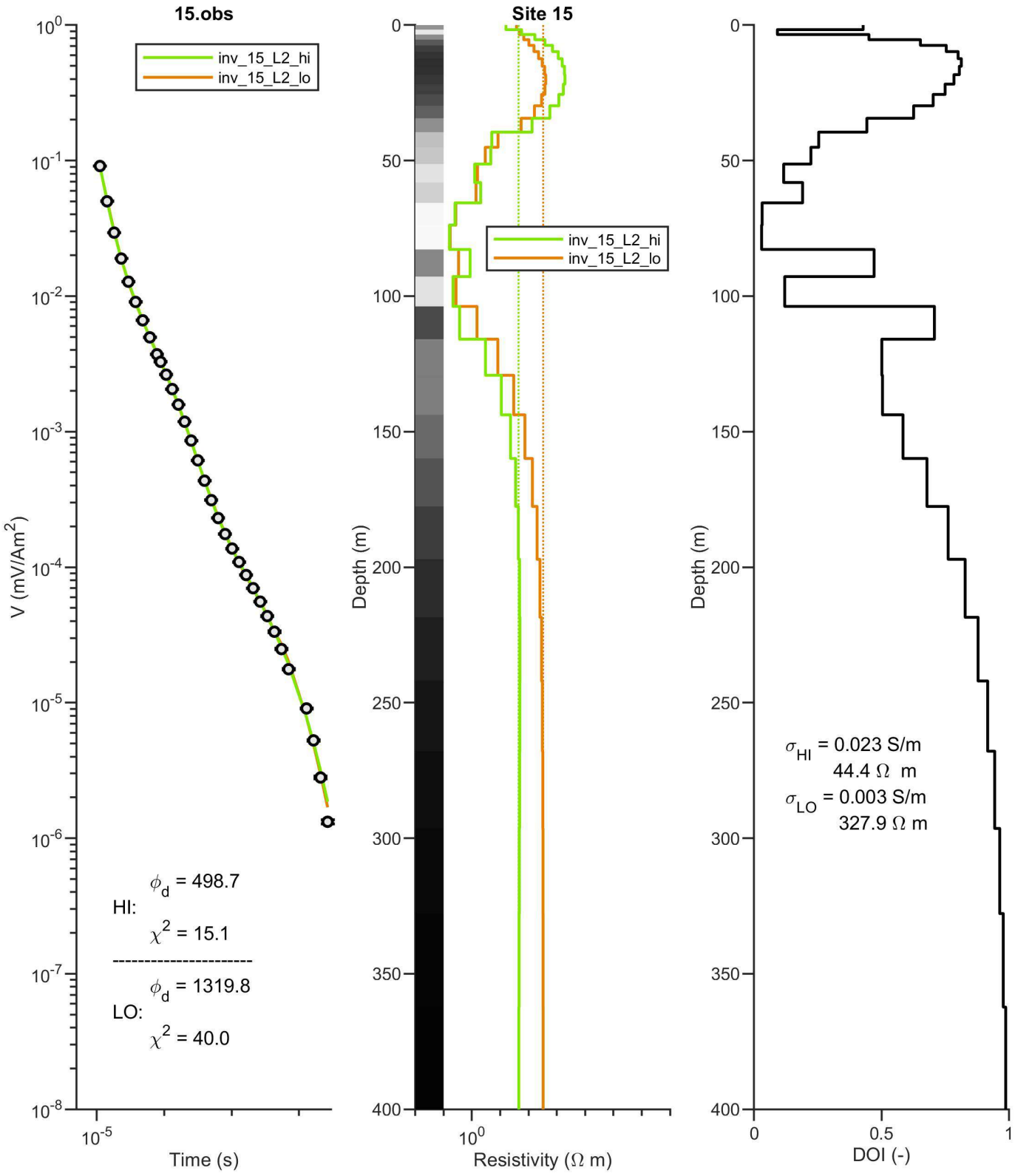
15.obs
inv_15_L2_hi
inv_15_L2_lo
V (mV/Am^2)
Time (s)
ϕ_d = 498.7
HI:
χ^2 = 15.1
ϕ_d = 1319.8
LO:
χ^2 = 40.0
Site 15
inv_15_L2_hi
inv_15_L2_lo
Depth (m)
Resistivity (Ω m)
σ_{HI} = 0.023 S/m
44.4 Ω m
σ_{LO} = 0.003 S/m
327.9 Ω m
DOI (-)

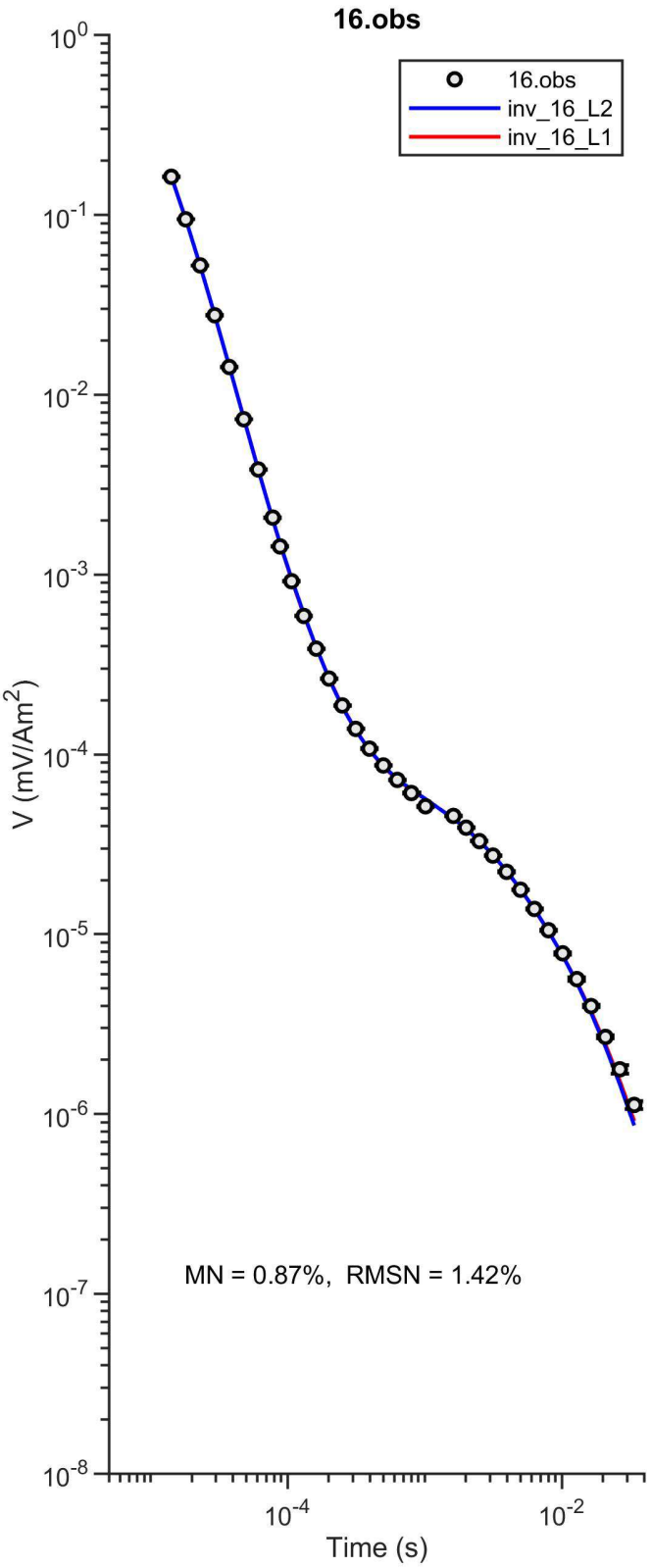
16.obs
16.obs
inv_16_L2
inv_16_L1
V (mV/Am^2)
Time (s)
MN = 0.87%, RMSN = 1.42%

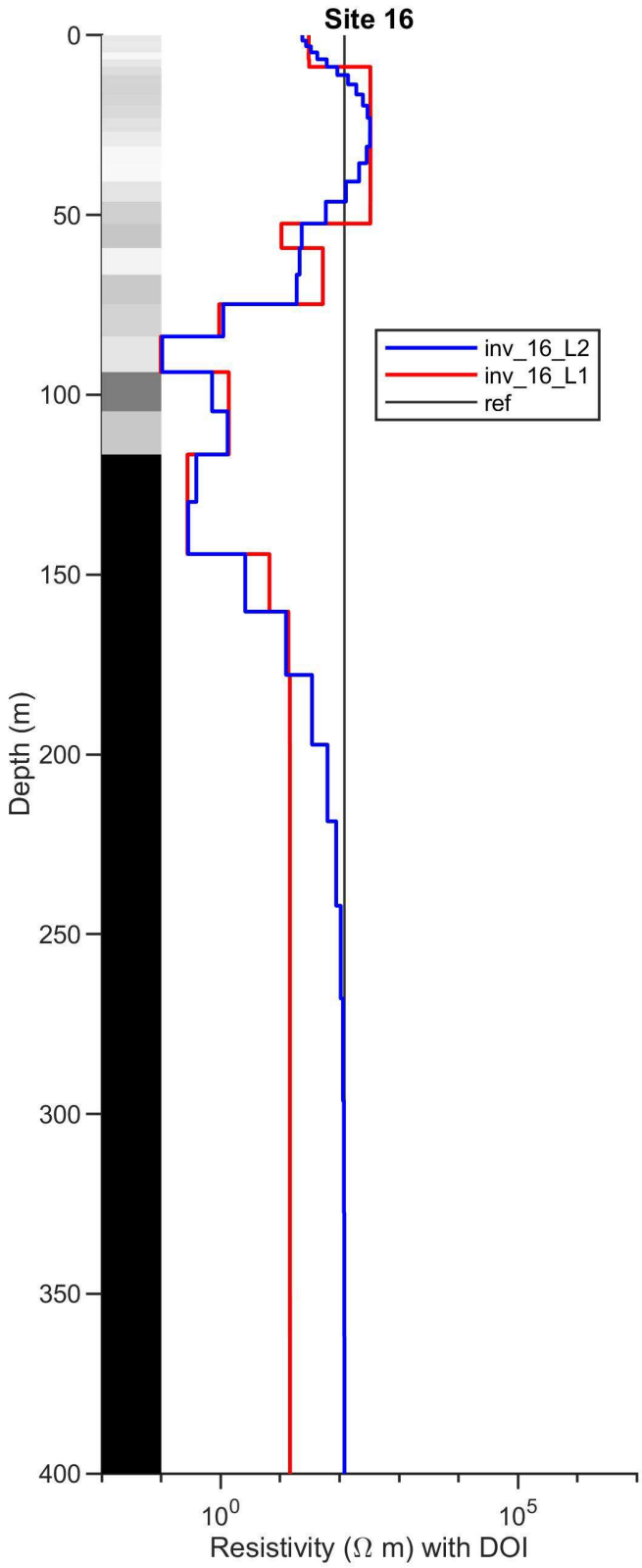
Site 16
inv_16_L2
inv_16_L1
ref
Depth (m)
Resistivity (Ω m) with DOI

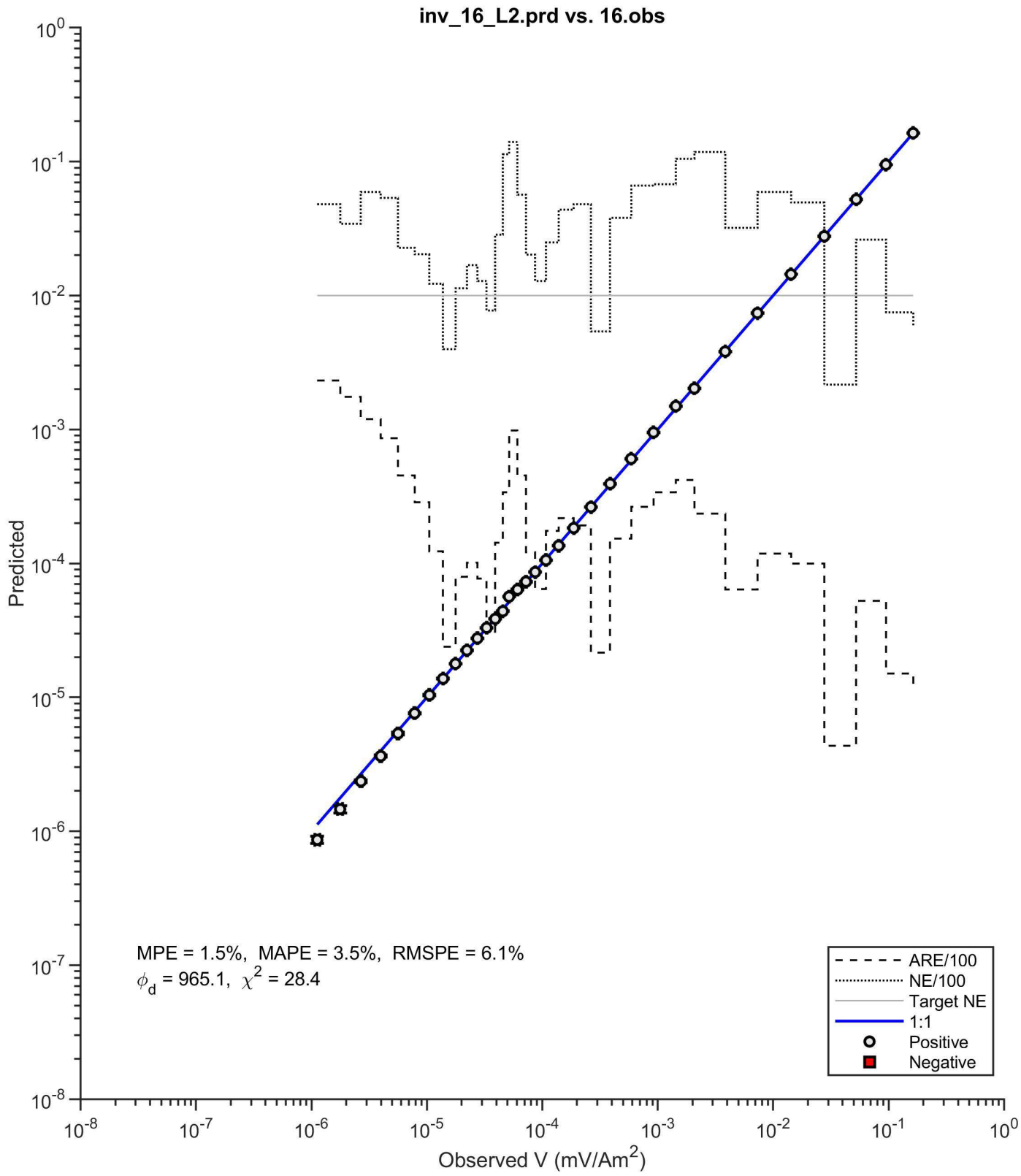
inv_16_L2.prd vs. 16.obs
Predicted
Observed V (mV/Am^2)
MPE = 1.5%, MAPE = 3.5%, RMSPE = 6.1%
ϕ_d = 965.1, χ^2 = 28.4
ARE/100
NE/100
Target NE
1:1
Positive
Negative

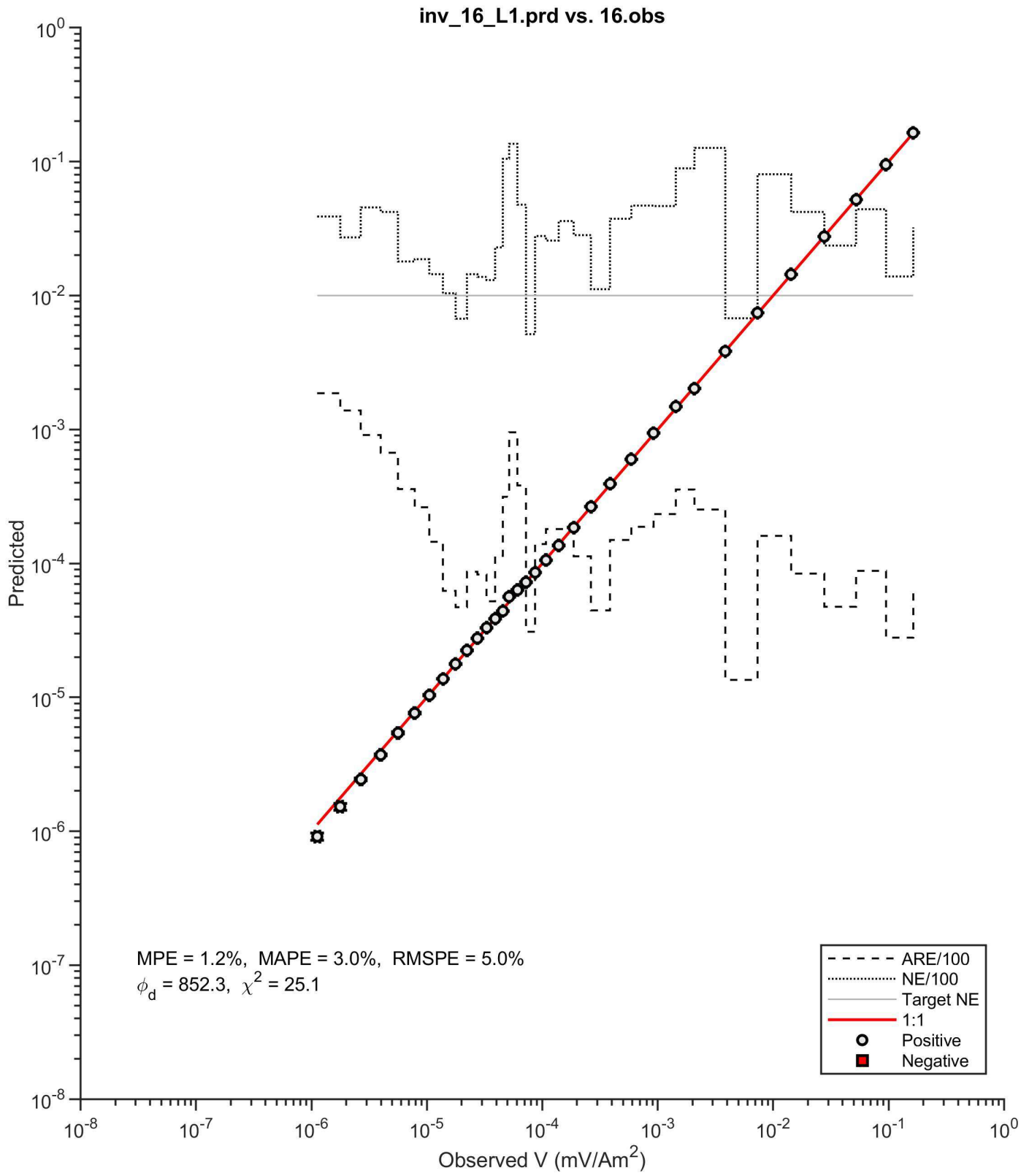
inv_16_L1.prd vs. 16.obs
Predicted
Observed V (mV/Am^2)
10^{0}
10^{-1}
10^{-2}
10^{-3}
10^{-4}
10^{-5}
10^{-6}
10^{-7}
10^{-8}
MPE = 1.2%, MAPE = 3.0%, RMSPE = 5.0%
ϕ_d = 852.3, χ^2 = 25.1
ARE/100
NE/100
Target NE
1:1
Positive
Negative

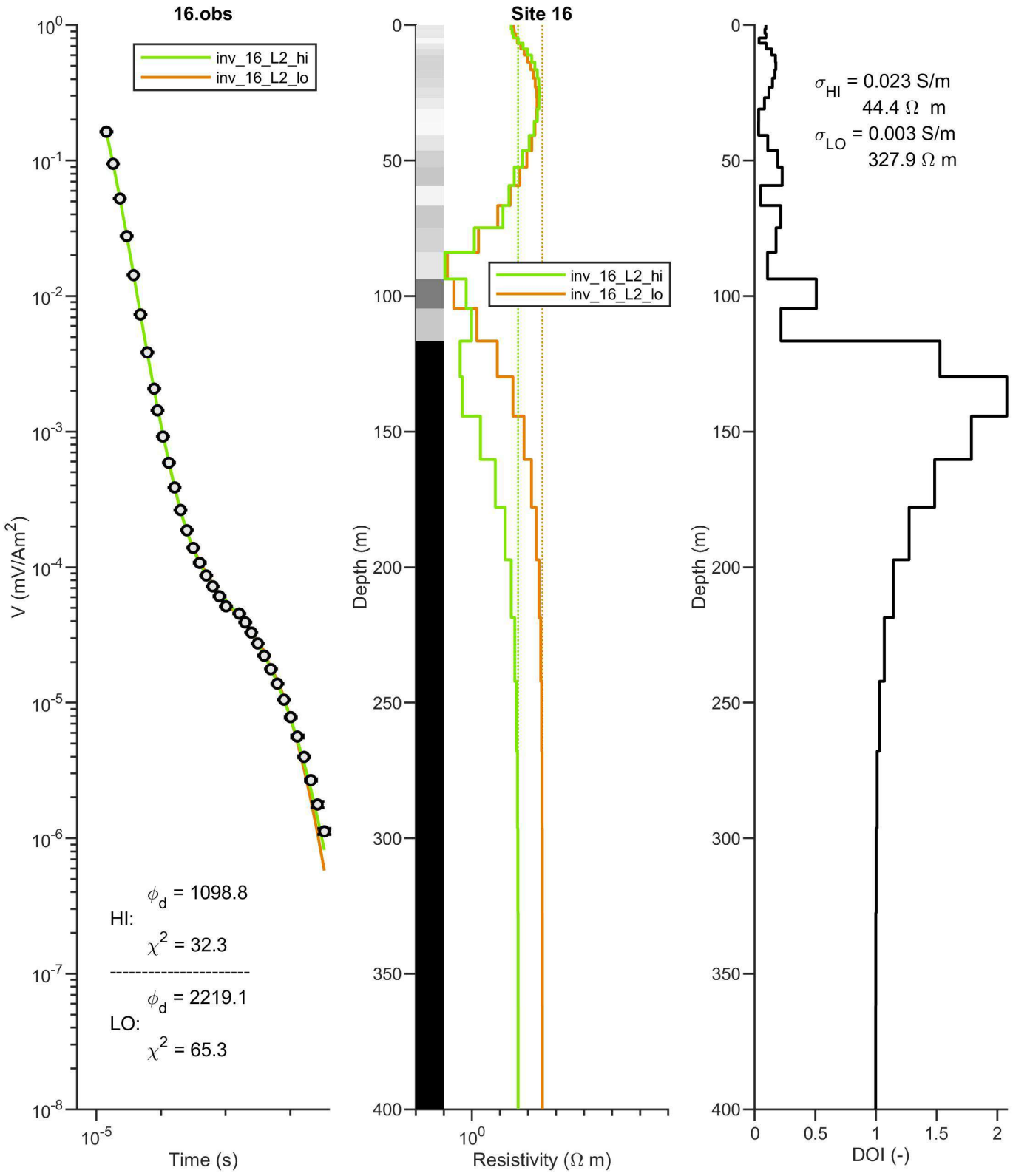
16.obs
inv_16_L2_hi
inv_16_L2_lo
V (mV/Am^2)
Time (s)
ϕ_d = 1098.8
HI:
χ^2 = 32.3
ϕ_d = 2219.1
LO:
χ^2 = 65.3
Site 16
inv_16_L2_hi
inv_16_L2_lo
Depth (m)
Resistivity (Ω m)
σ_{HI} = 0.023 S/m
44.4 Ω m
σ_{LO} = 0.003 S/m
327.9 Ω m
Depth (m)
DOI (-)

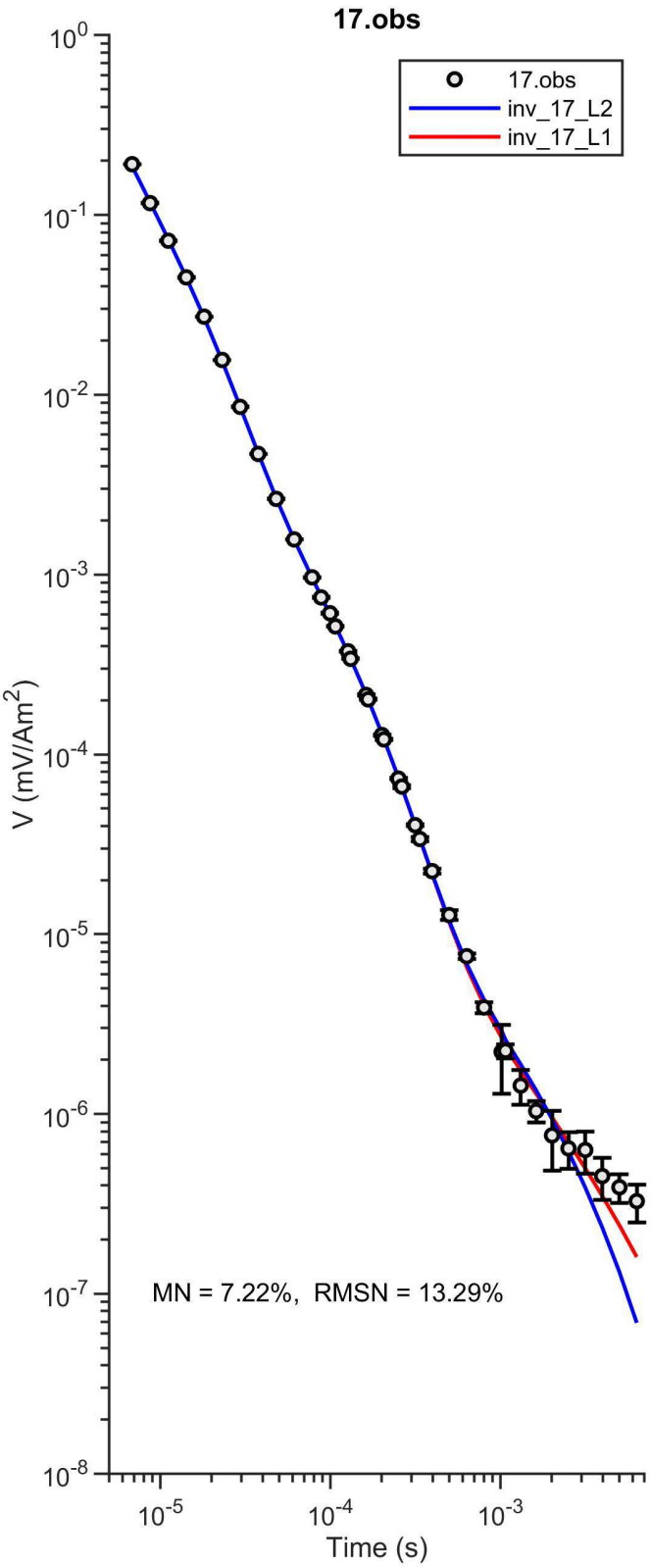
17.obs
17.obs
inv_17_L2
inv_17_L1
V (mV/Am^2)
Time (s)
MN = 7.22%, RMSN = 13.29%

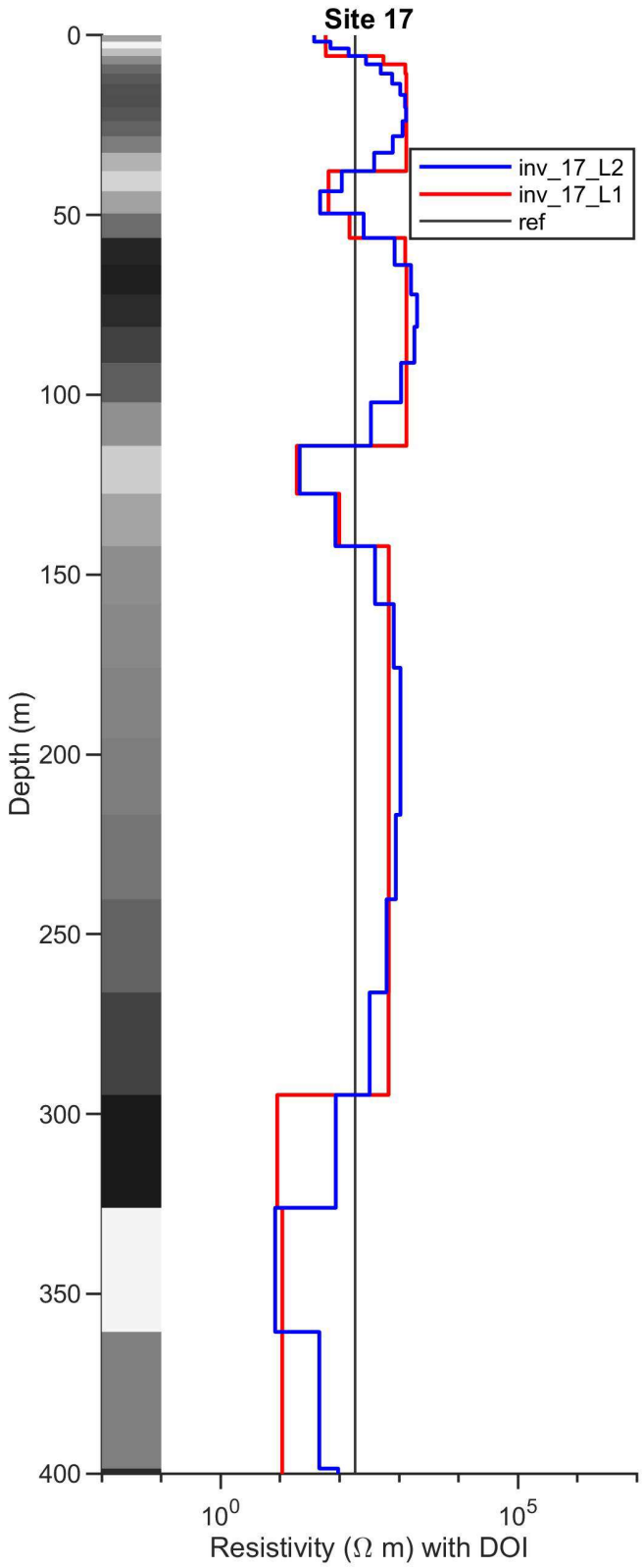
Site 17
inv_17_L2
inv_17_L1
ref
Depth (m)
Resistivity (Ω m) with DOI

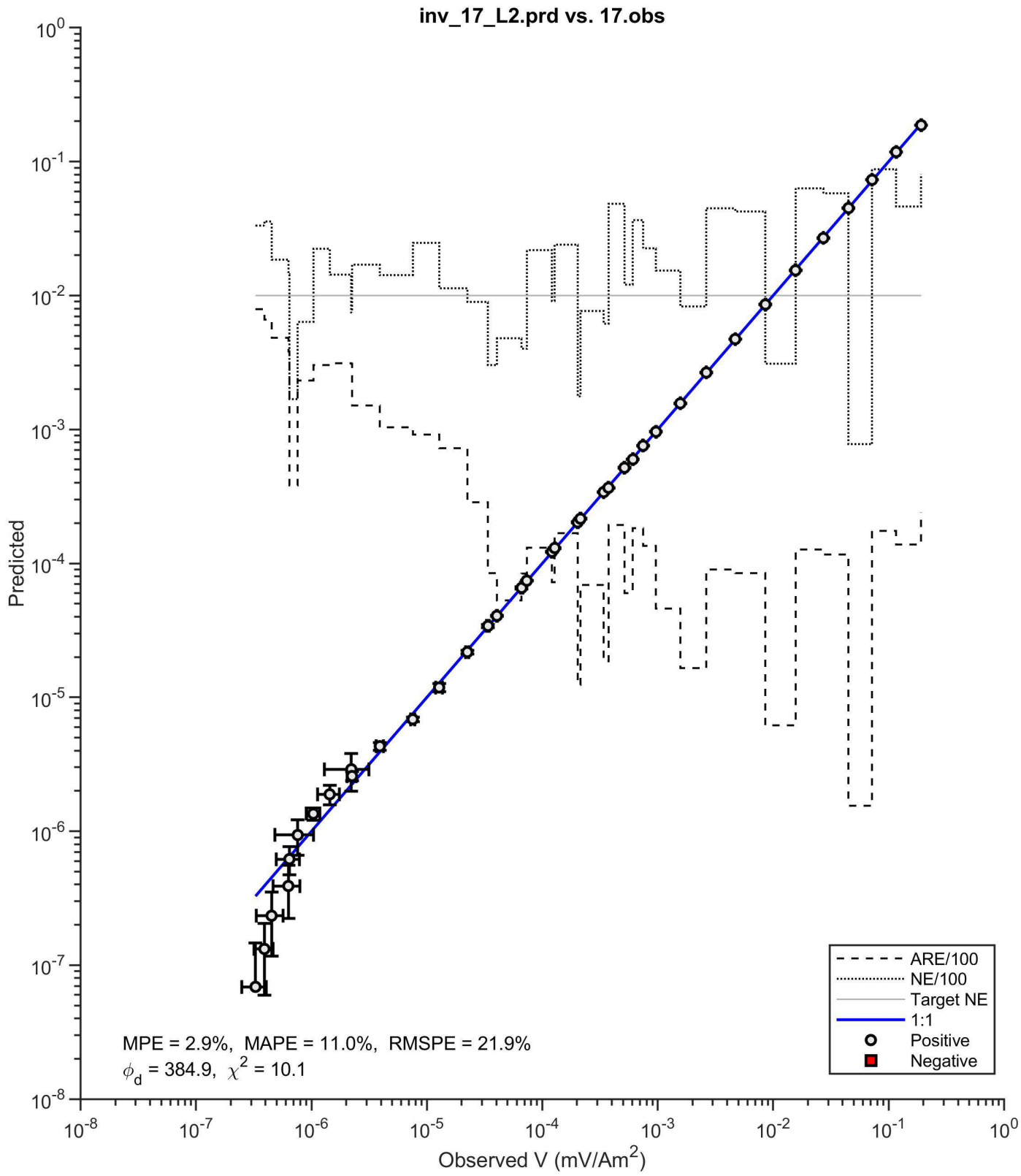
inv_17_L2.prd vs. 17.obs
Predicted
Observed V (mV/Am^2)
10^{0}
10^{-1}
10^{-2}
10^{-3}
10^{-4}
10^{-5}
10^{-6}
10^{-7}
10^{-8}
MPE = 2.9%, MAPE = 11.0%, RMSPE = 21.9%
ϕ_d = 384.9, χ^2 = 10.1
ARE/100
NE/100
Target NE
1:1
Positive
Negative

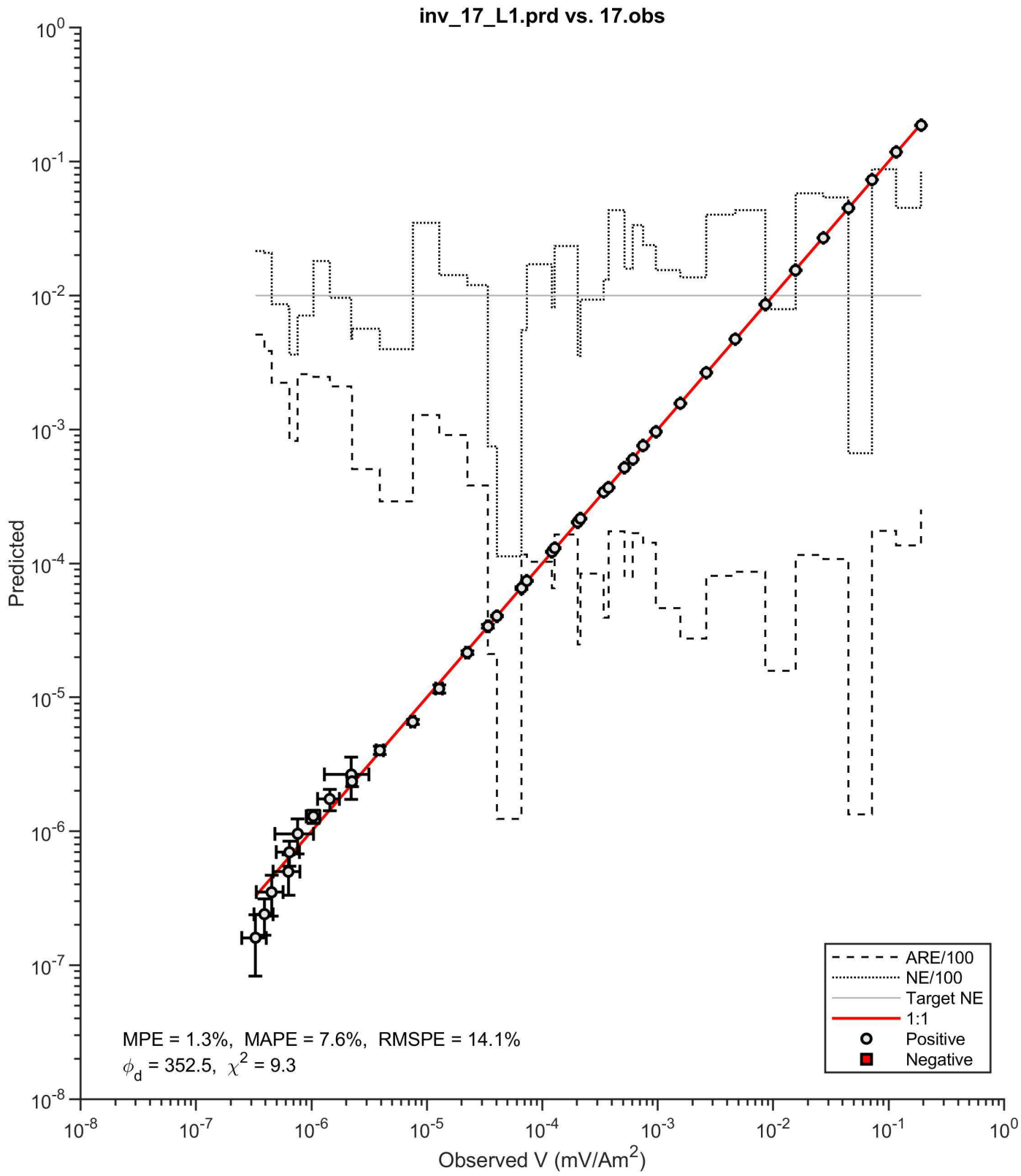
inv_17_L1.prd vs. 17.obs
Predicted
Observed V (mV/Am^2)
10^{0}
10^{-1}
10^{-2}
10^{-3}
10^{-4}
10^{-5}
10^{-6}
10^{-7}
10^{-8}
MPE = 1.3%, MAPE = 7.6%, RMSPE = 14.1%
ϕ_d = 352.5, χ^2 = 9.3
ARE/100
NE/100
Target NE
1:1
Positive
Negative

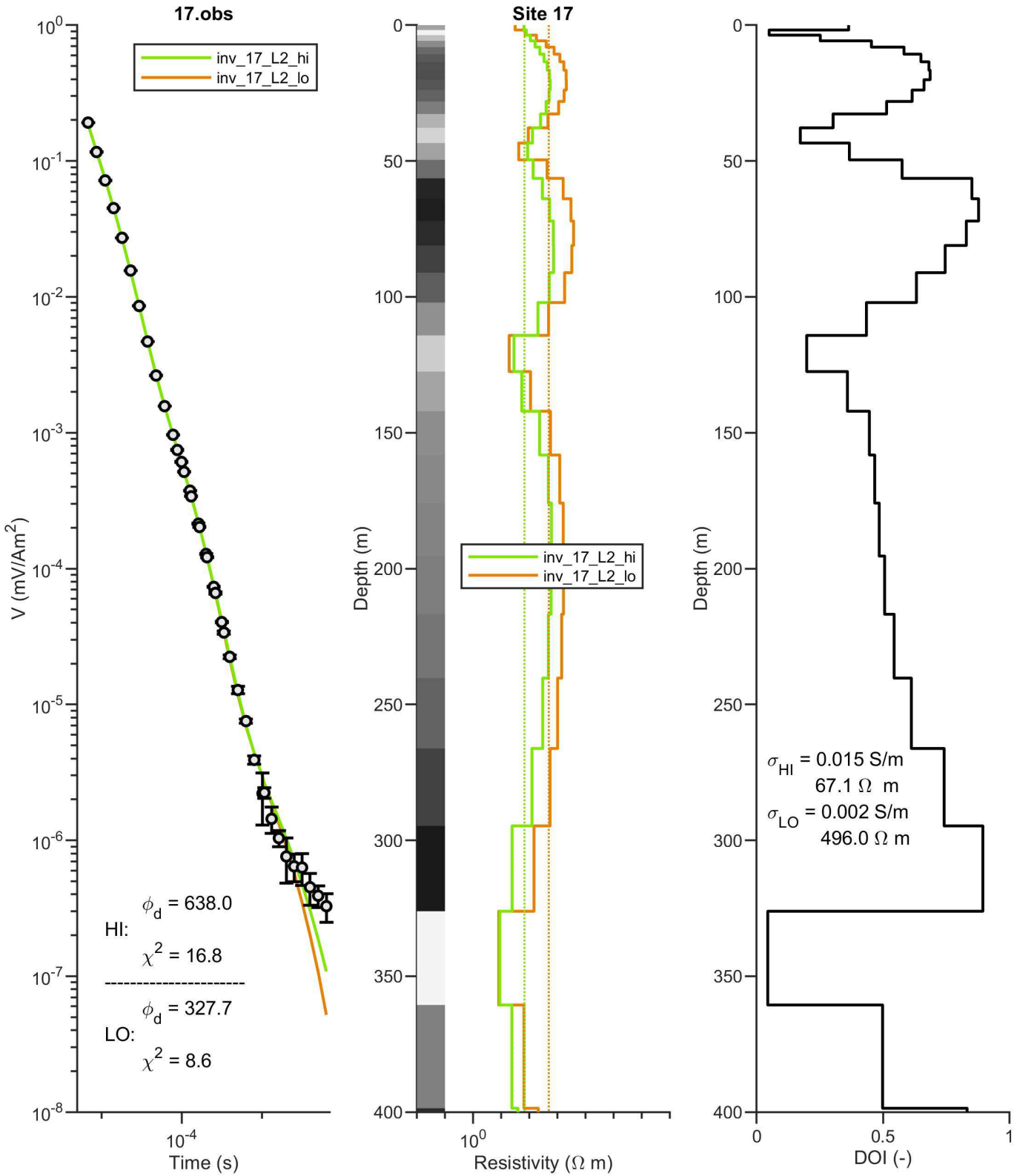
17.obs
inv_17_L2_hi
inv_17_L2_lo
V (mV/Am^2)
Time (s)
ϕ_d = 638.0
HI:
χ^2 = 16.8
ϕ_d = 327.7
LO:
χ^2 = 8.6
Site 17
Depth (m)
Resistivity (Ω m)
DOI (-)
σ_{HI} = 0.015 S/m
67.1 Ω m
σ_{LO} = 0.002 S/m
496.0 Ω m

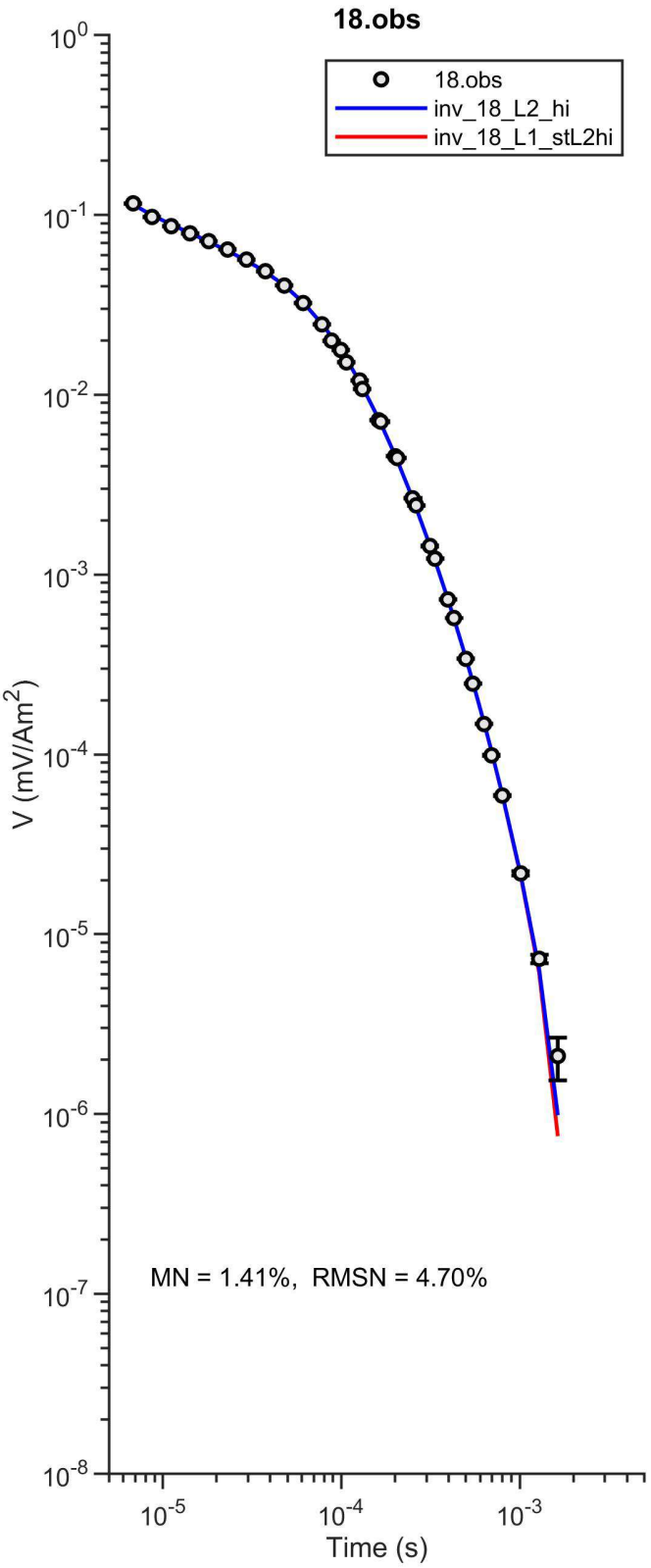
18.obs
18.obs
inv_18_L2_hi
inv_18_L1_stL2hi
V (mV/Am^2)
Time (s)
MN = 1.41%, RMSN = 4.70%

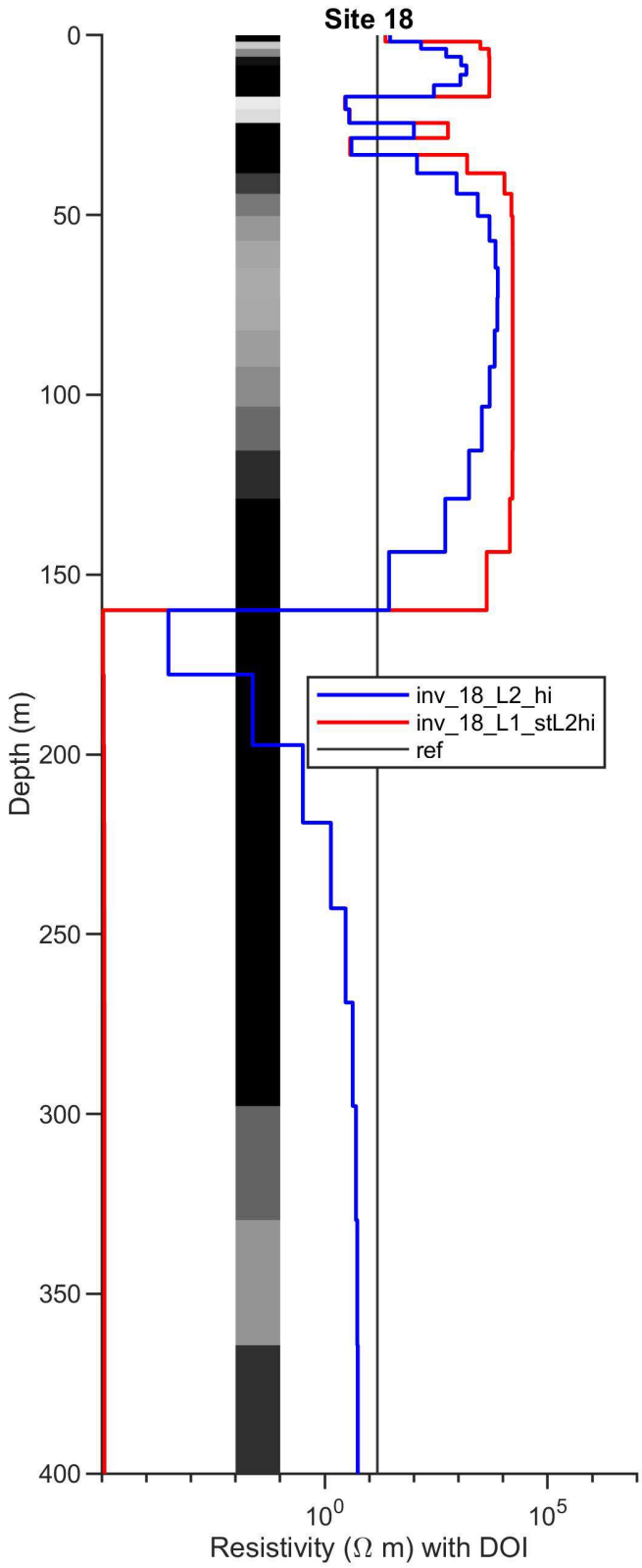
Site 18
inv_18_L2_hi
inv_18_L1_stL2hi
ref
Depth (m)
Resistivity (Ω m) with DOI

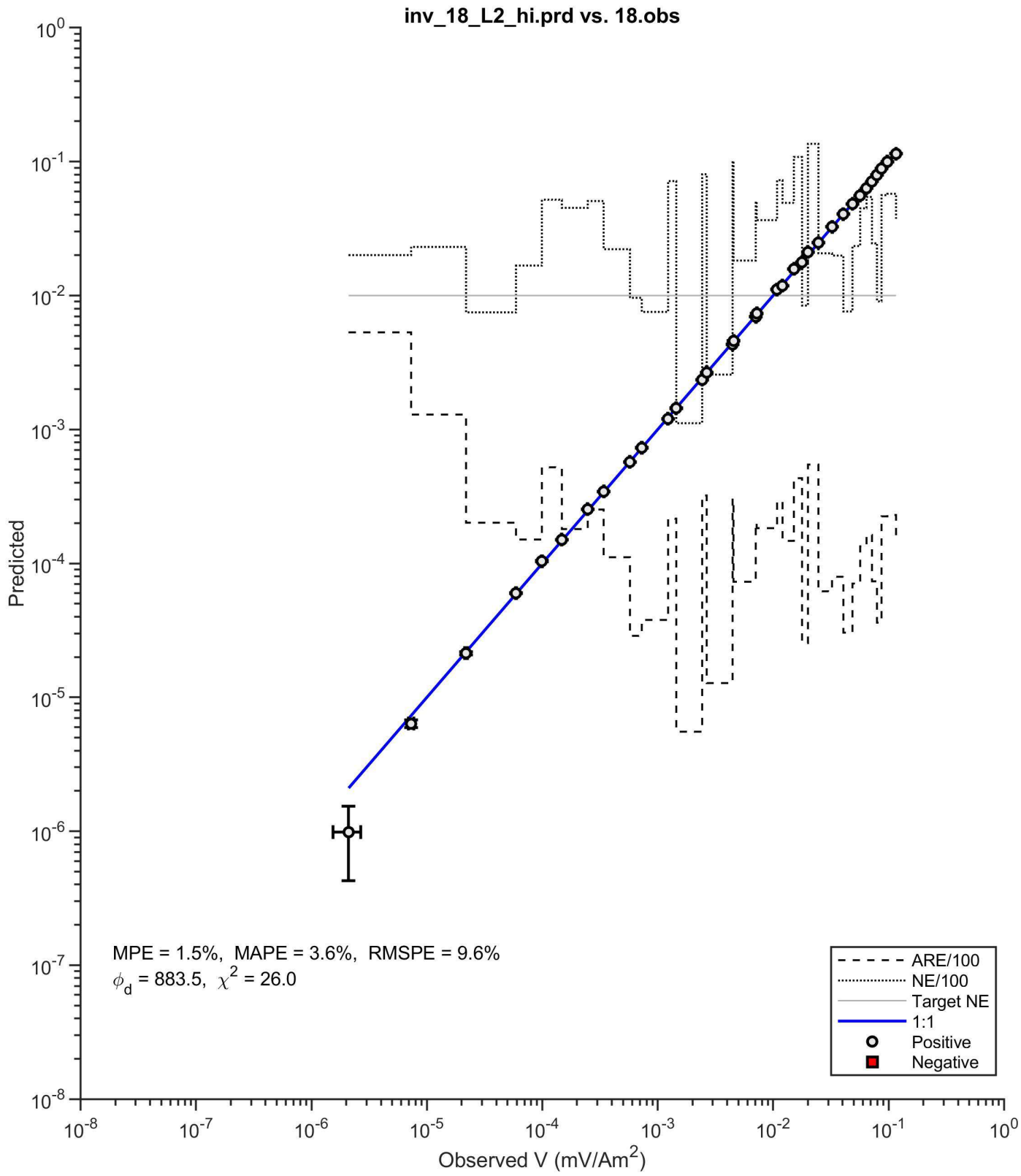
inv_18_L2_hi.prd vs. 18.obs
Predicted
Observed V (mV/Am^2)
10^{0}
10^{-1}
10^{-2}
10^{-3}
10^{-4}
10^{-5}
10^{-6}
10^{-7}
10^{-8}
MPE = 1.5%, MAPE = 3.6%, RMSPE = 9.6%
ϕ_d = 883.5, χ^2 = 26.0
ARE/100
NE/100
Target NE
1:1
Positive
Negative

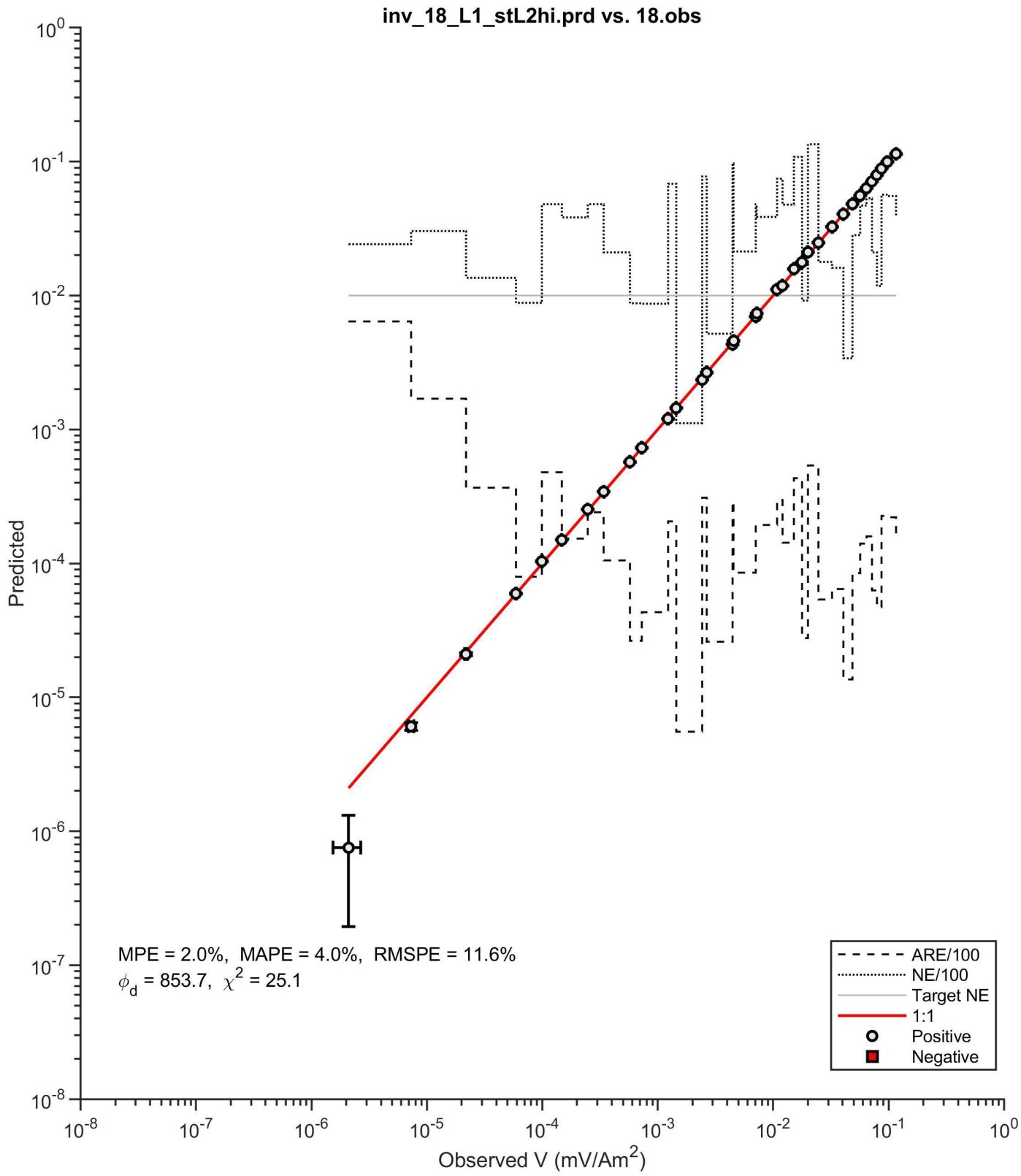
inv_18_L1_stL2hi.prd vs. 18.obs
Predicted
Observed V (mV/Am^2)
10^{0}
10^{-1}
10^{-2}
10^{-3}
10^{-4}
10^{-5}
10^{-6}
10^{-7}
10^{-8}
MPE = 2.0%, MAPE = 4.0%, RMSPE = 11.6%
ϕ_d = 853.7, χ^2 = 25.1
ARE/100
NE/100
Target NE
1:1
Positive
Negative

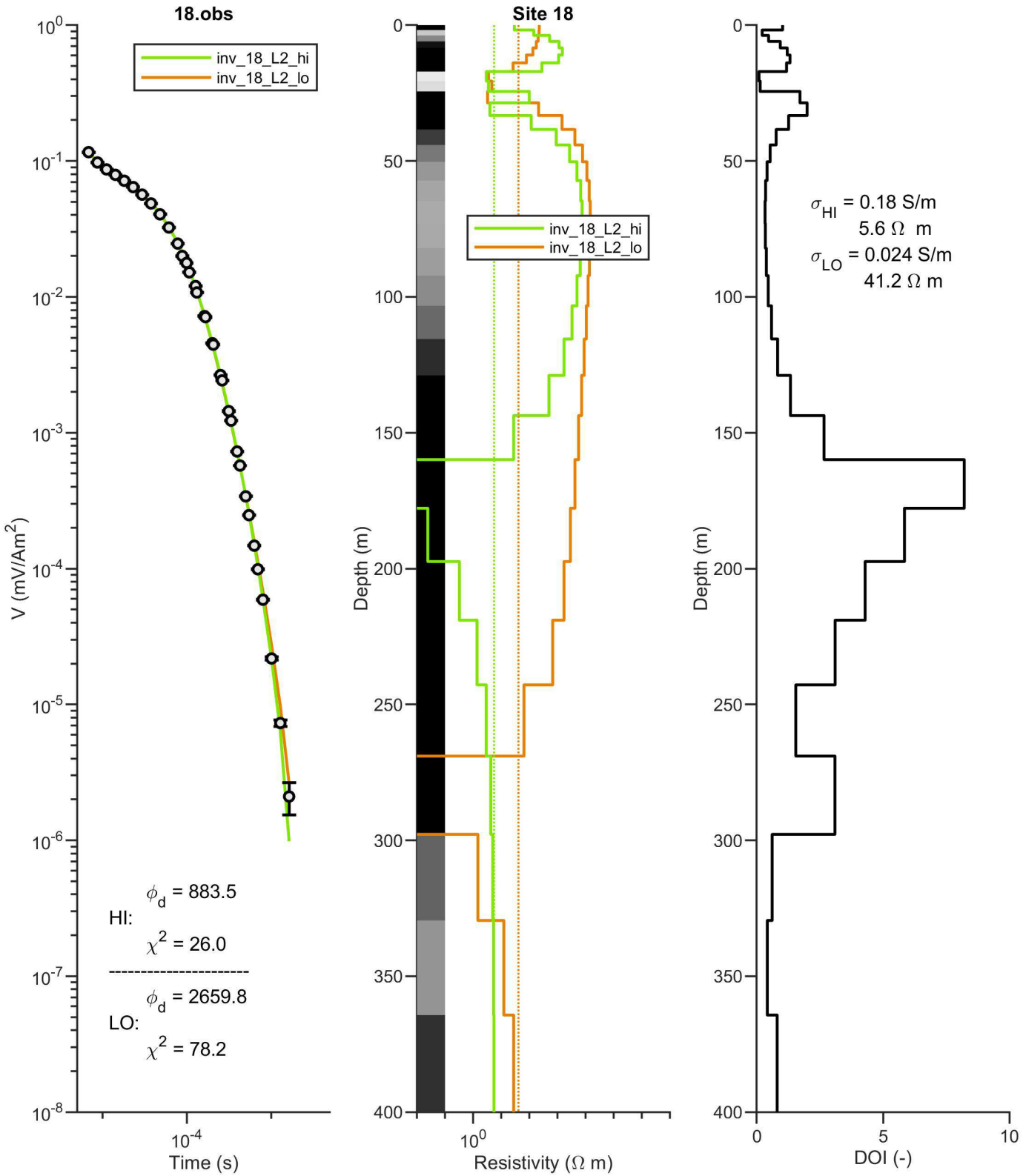
18.obs
inv_18_L2_hi
inv_18_L2_lo
V (mV/Am^2)
Time (s)
ϕ_d = 883.5
HI:
χ^2 = 26.0
ϕ_d = 2659.8
LO:
χ^2 = 78.2
Site 18
inv_18_L2_hi
inv_18_L2_lo
Depth (m)
Resistivity (Ω m)
σ_{HI} = 0.18 S/m
5.6 Ω m
σ_{LO} = 0.024 S/m
41.2 Ω m
DOI (-)

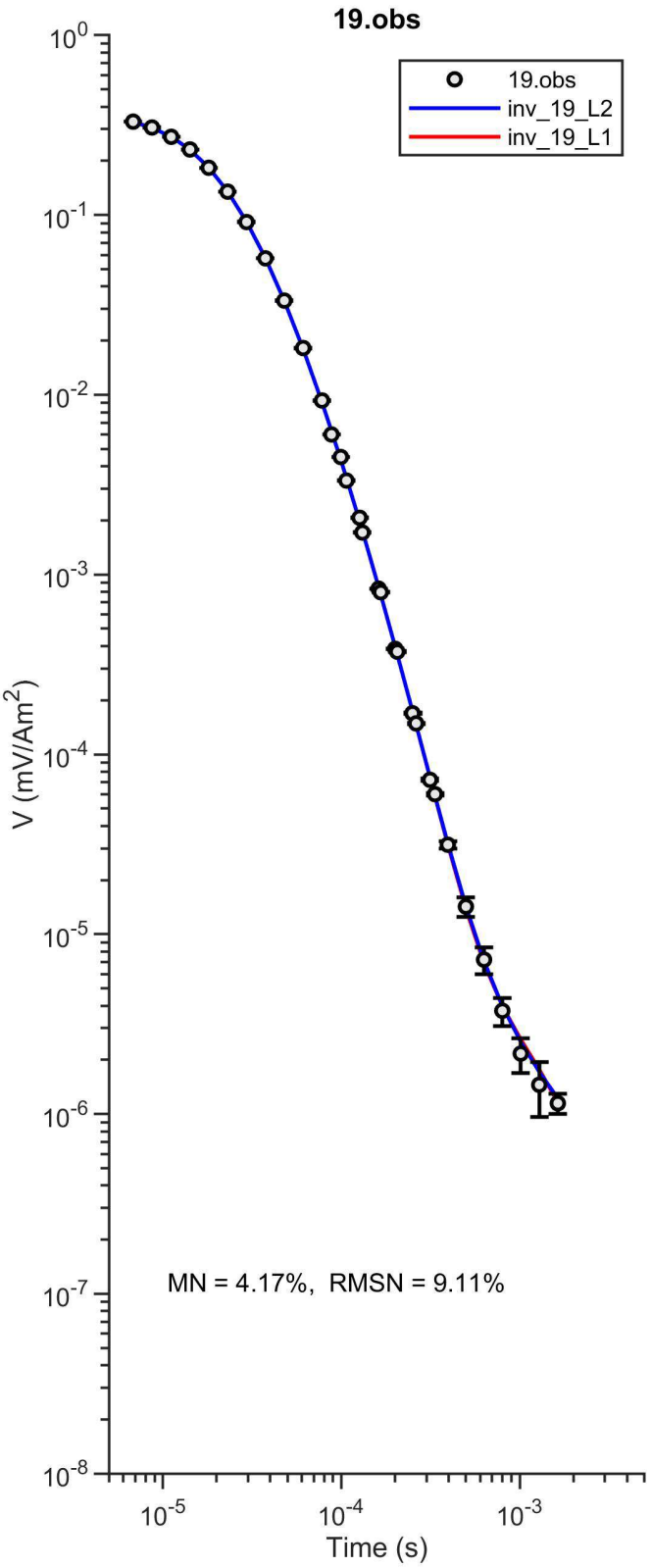
19.obs
19.obs
inv_19_L2
inv_19_L1
V (mV/Am^2)
Time (s)
MN = 4.17%, RMSN = 9.11%

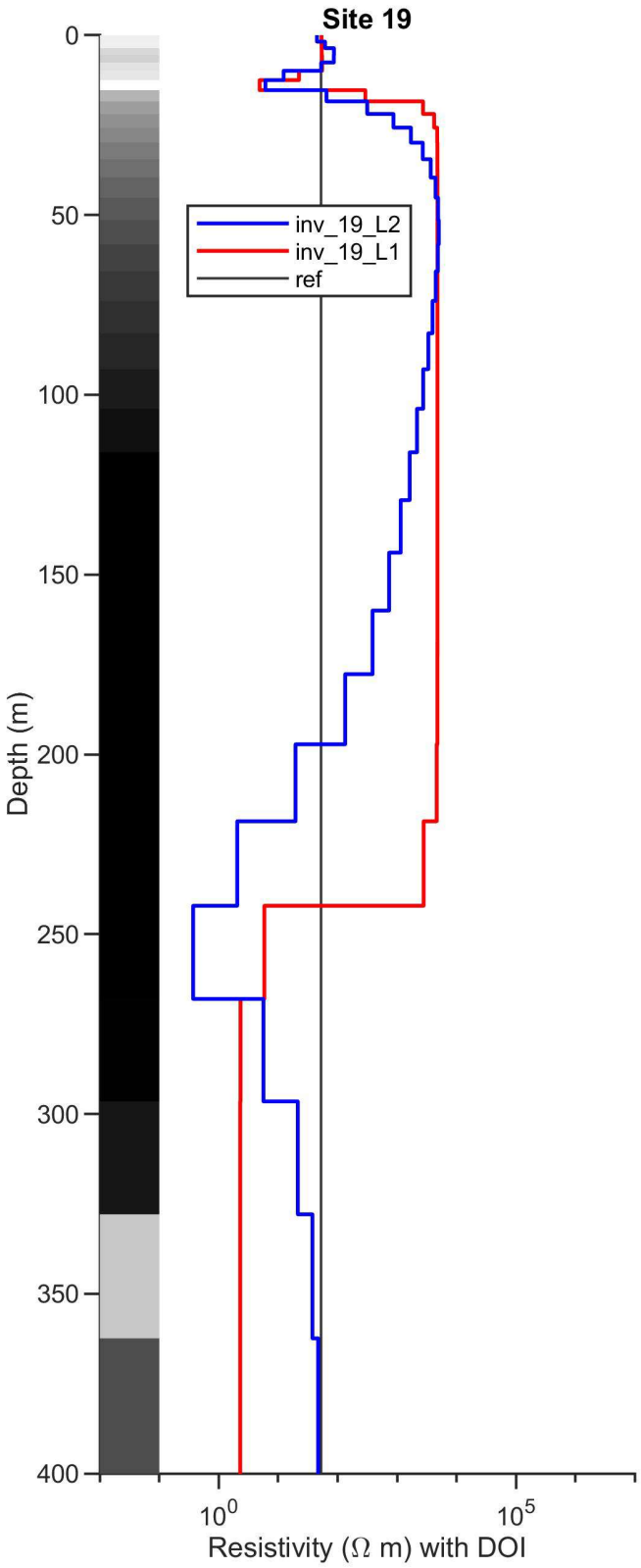
Site 19
inv_19_L2
inv_19_L1
ref
Depth (m)
Resistivity (Ω m) with DOI

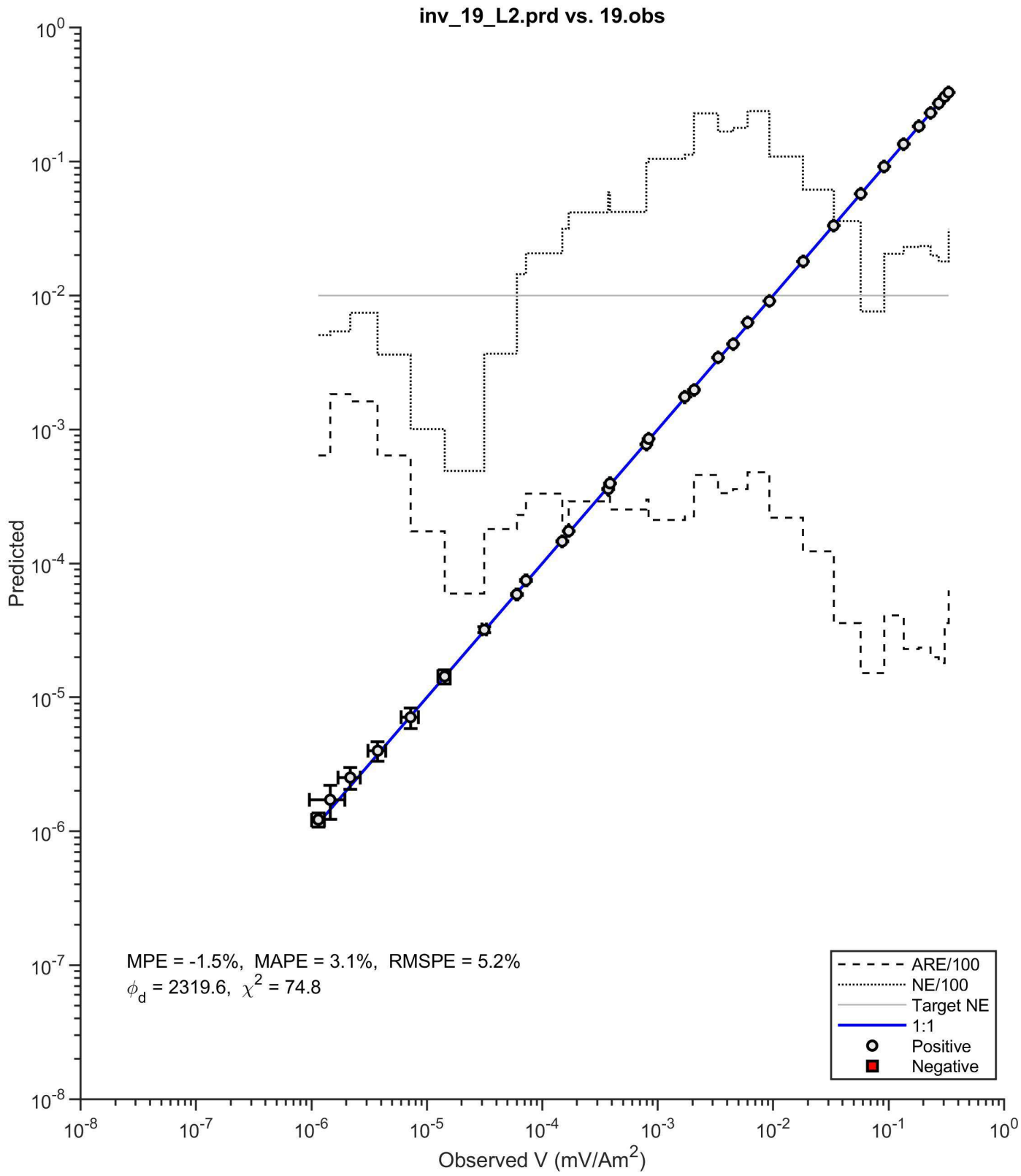
inv_19_L2.prd vs. 19.obs
Predicted
Observed V (mV/Am^2)
10^{0}
10^{-1}
10^{-2}
10^{-3}
10^{-4}
10^{-5}
10^{-6}
10^{-7}
10^{-8}
MPE = -1.5%, MAPE = 3.1%, RMSPE = 5.2%
ϕ_d = 2319.6, χ^2 = 74.8
ARE/100
NE/100
Target NE
1:1
Positive
Negative

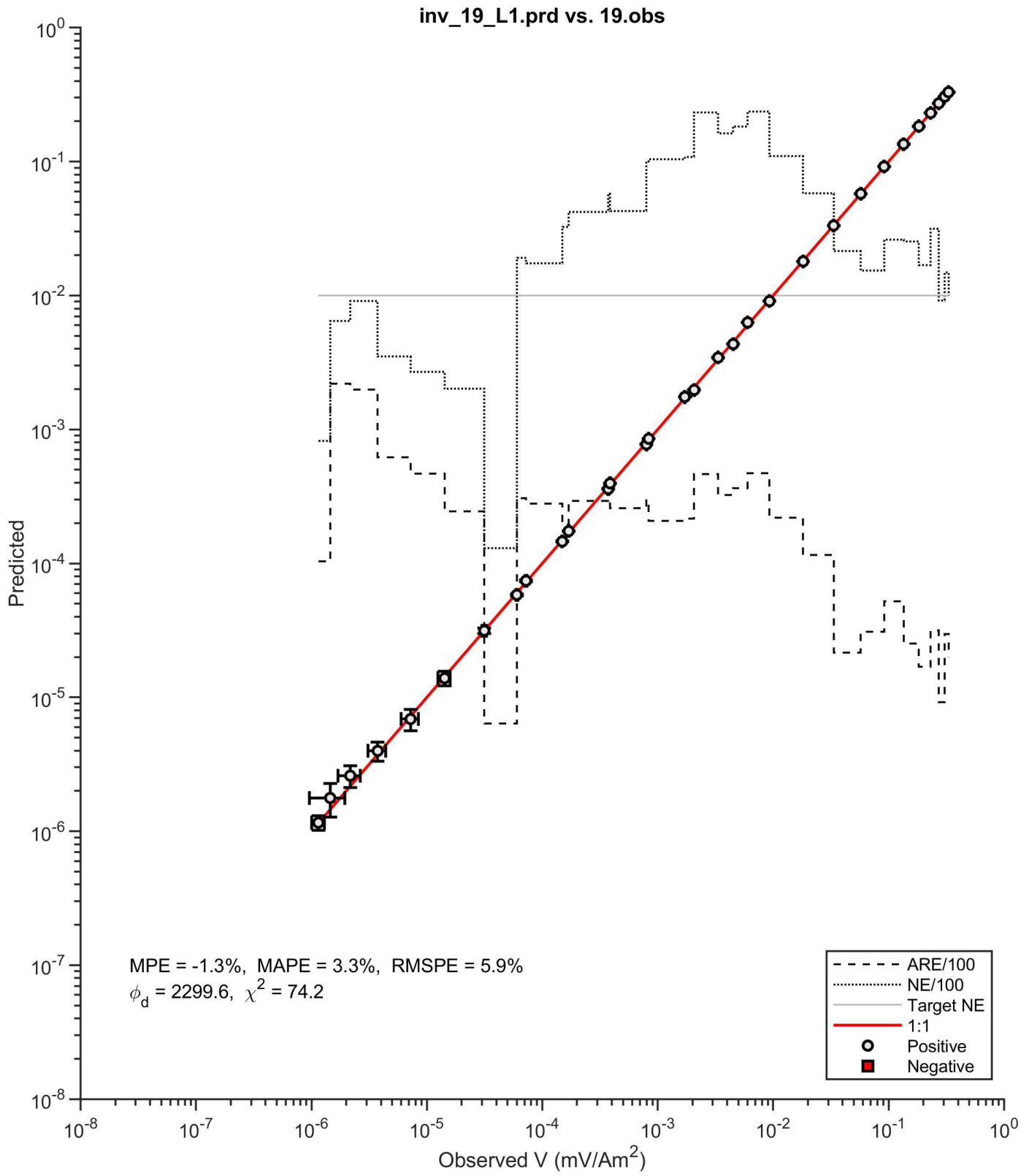
inv_19_L1.prd vs. 19.obs
Predicted
Observed V (mV/Am^2)
10^{0}
10^{-1}
10^{-2}
10^{-3}
10^{-4}
10^{-5}
10^{-6}
10^{-7}
10^{-8}
MPE = -1.3%, MAPE = 3.3%, RMSPE = 5.9%
ϕ_d = 2299.6, χ^2 = 74.2
ARE/100
NE/100
Target NE
1:1
Positive
Negative

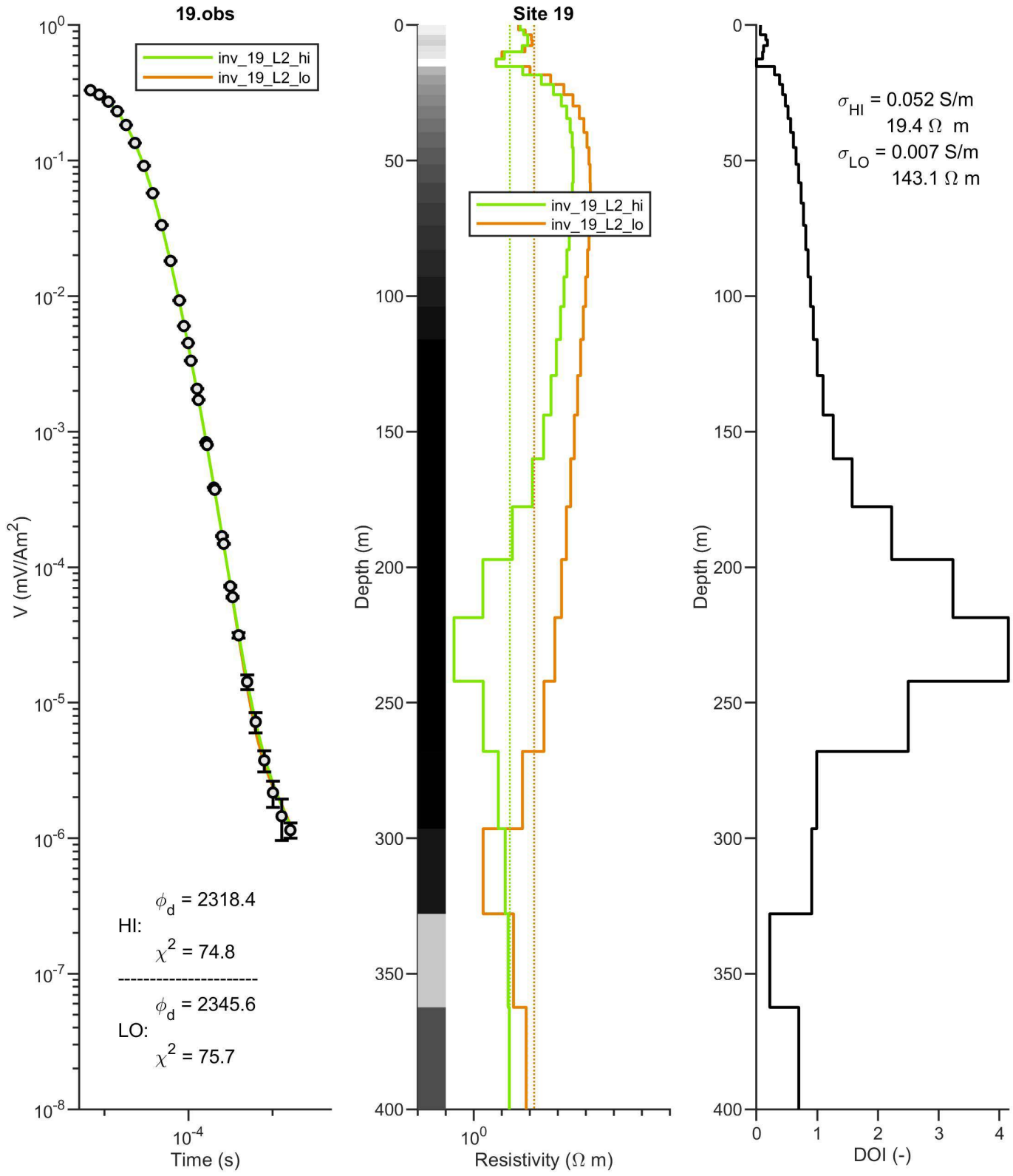
19.obs
inv_19_L2_hi
inv_19_L2_lo
V (mV/Am^2)
Time (s)
ϕ_d = 2318.4
HI:
χ^2 = 74.8
ϕ_d = 2345.6
LO:
χ^2 = 75.7
Site 19
inv_19_L2_hi
inv_19_L2_lo
Depth (m)
Resistivity (Ω m)
σ_{HI} = 0.052 S/m
19.4 Ω m
σ_{LO} = 0.007 S/m
143.1 Ω m
Depth (m)
DOI (-)

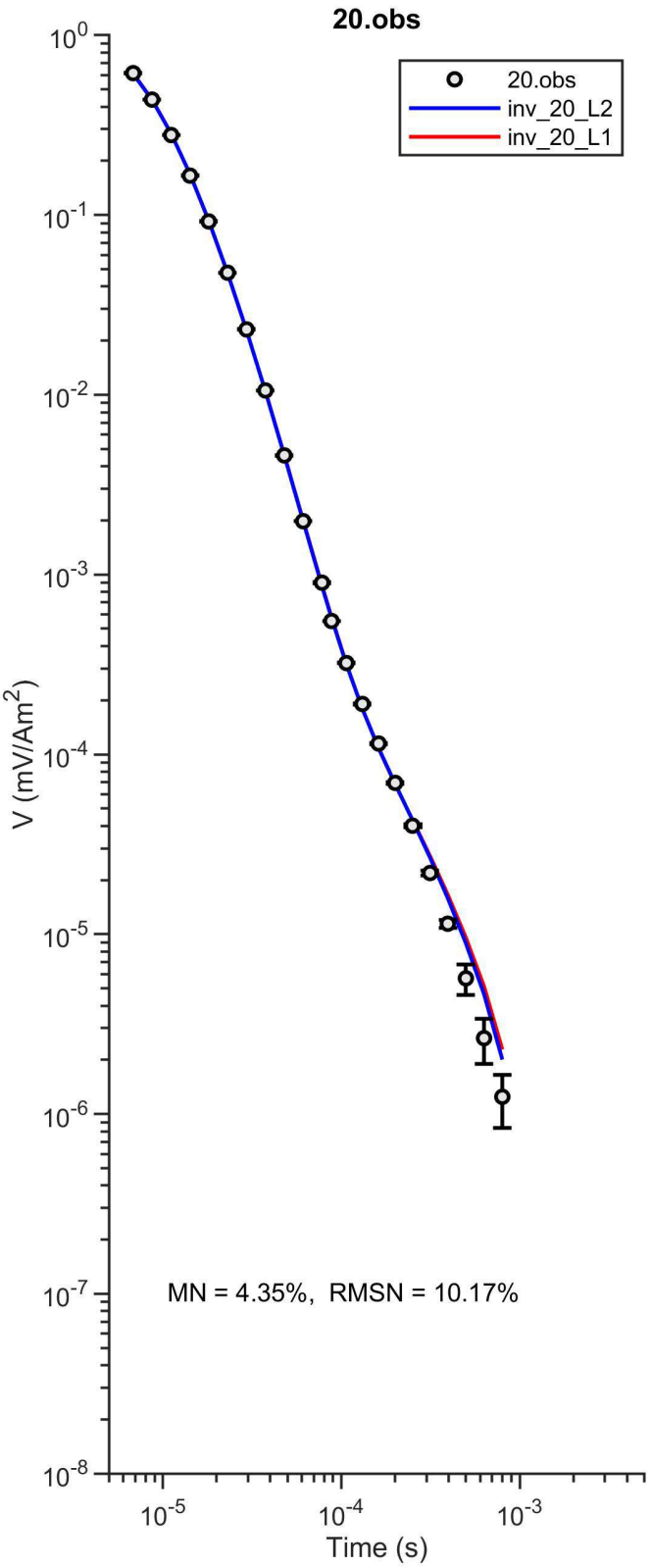
20.obs
20.obs
inv_20_L2
inv_20_L1
V (mV/Am^2)
Time (s)
MN = 4.35%, RMSN = 10.17%

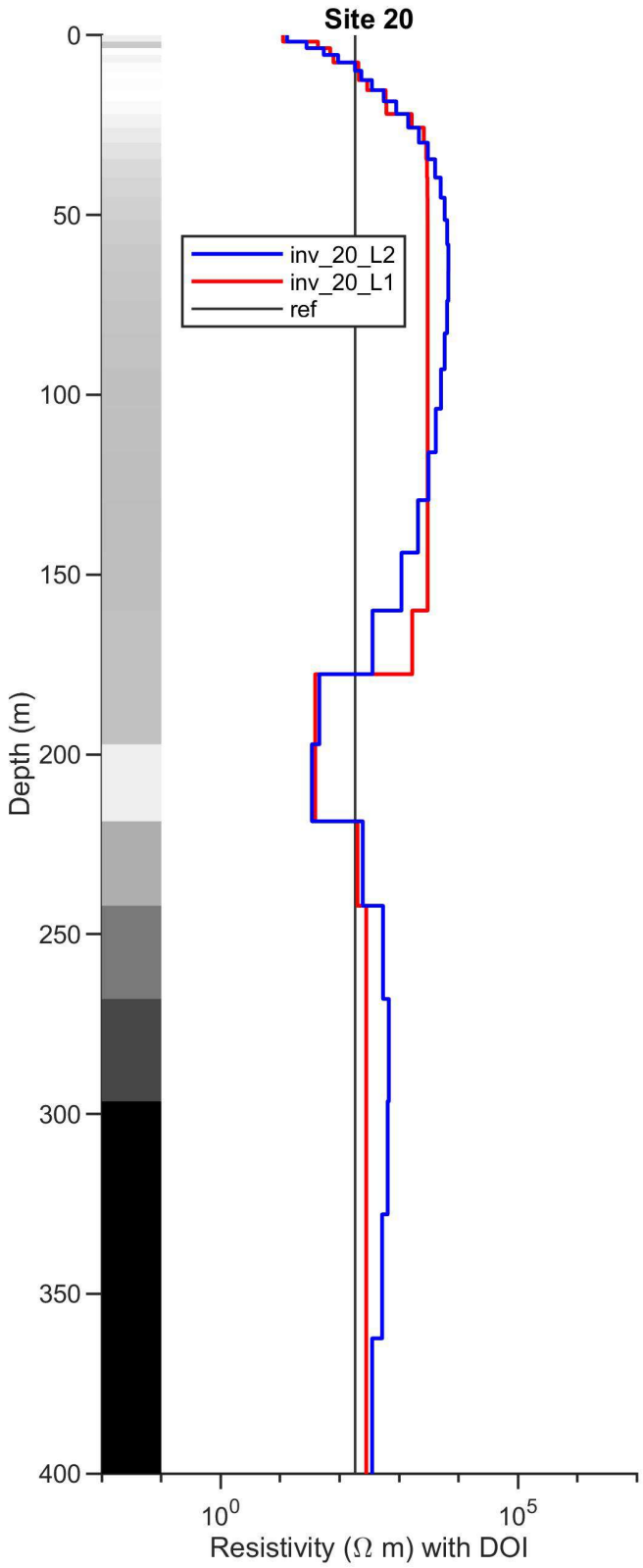
Site 20
inv_20_L2
inv_20_L1
ref
Depth (m)
Resistivity (Ω m) with DOI

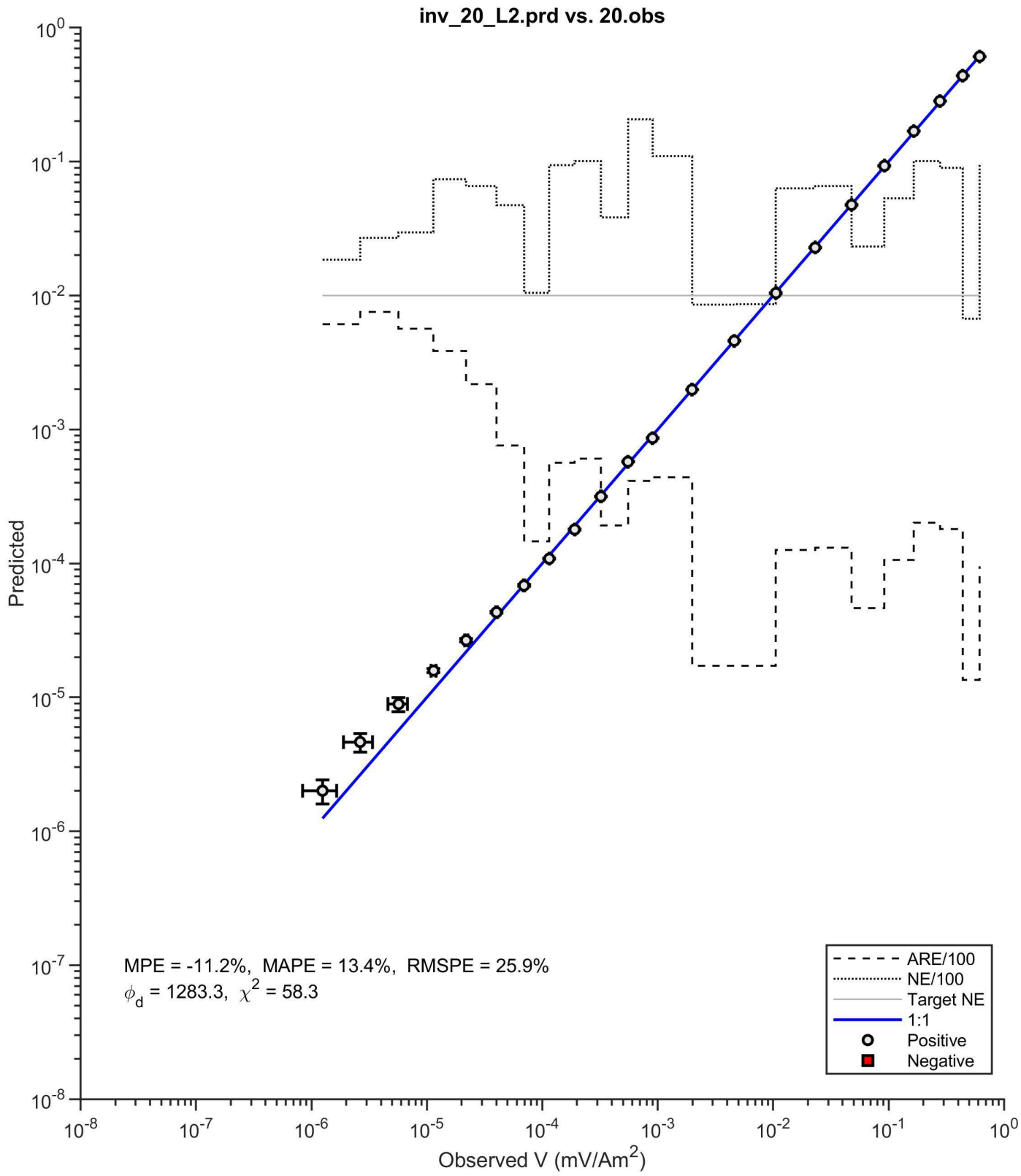
inv_20_L2.prd vs. 20.obs
Predicted
Observed V (mV/Am^2)
MPE = -11.2%, MAPE = 13.4%, RMSPE = 25.9%
ϕ_d = 1283.3, χ^2 = 58.3
ARE/100
NE/100
Target NE
1:1
Positive
Negative

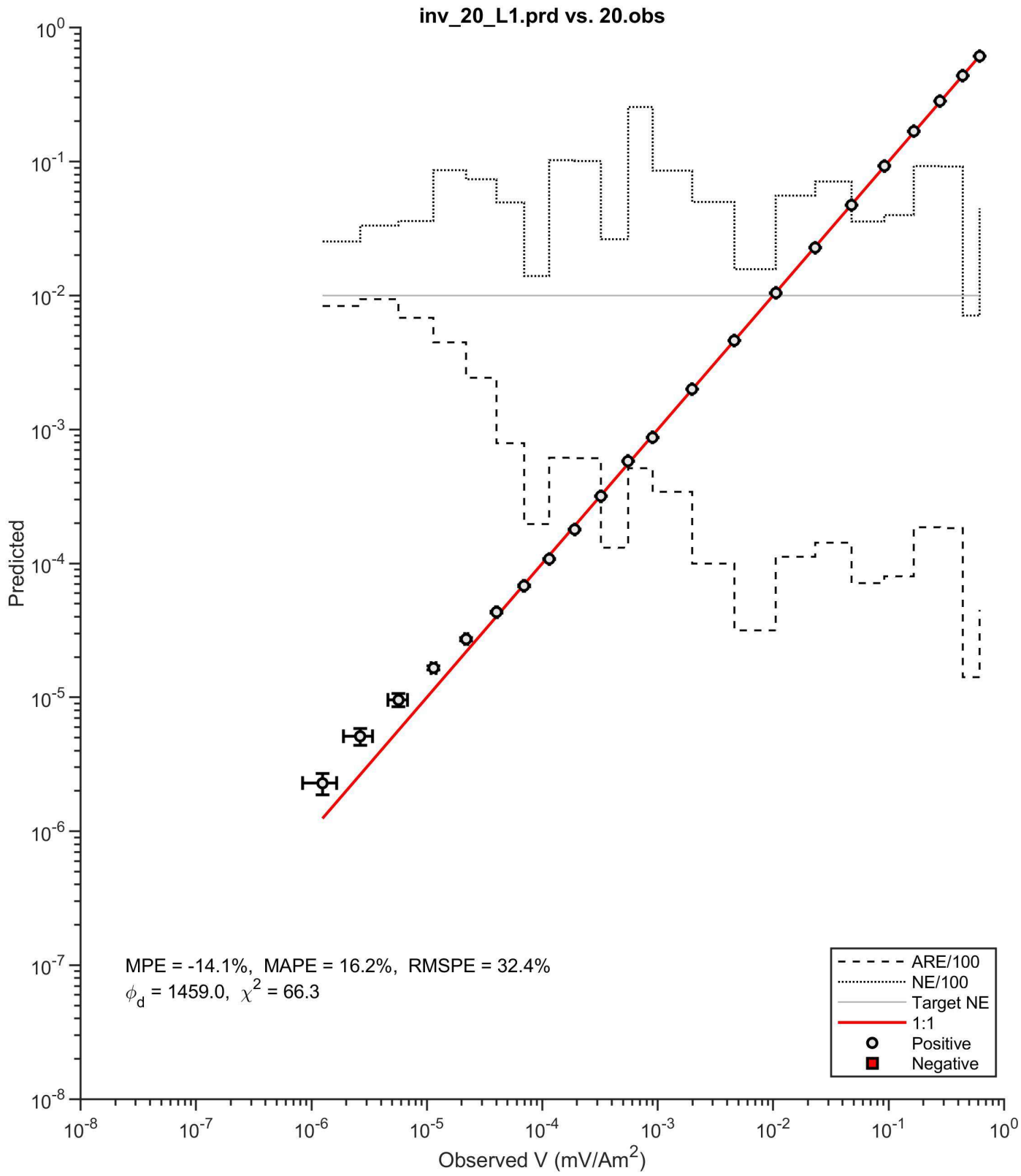
inv_20_L1.prd vs. 20.obs
Predicted
Observed V (mV/Am^2)
MPE = -14.1%, MAPE = 16.2%, RMSPE = 32.4%
ϕ_d = 1459.0, χ^2 = 66.3
ARE/100
NE/100
Target NE
1:1
Positive
Negative

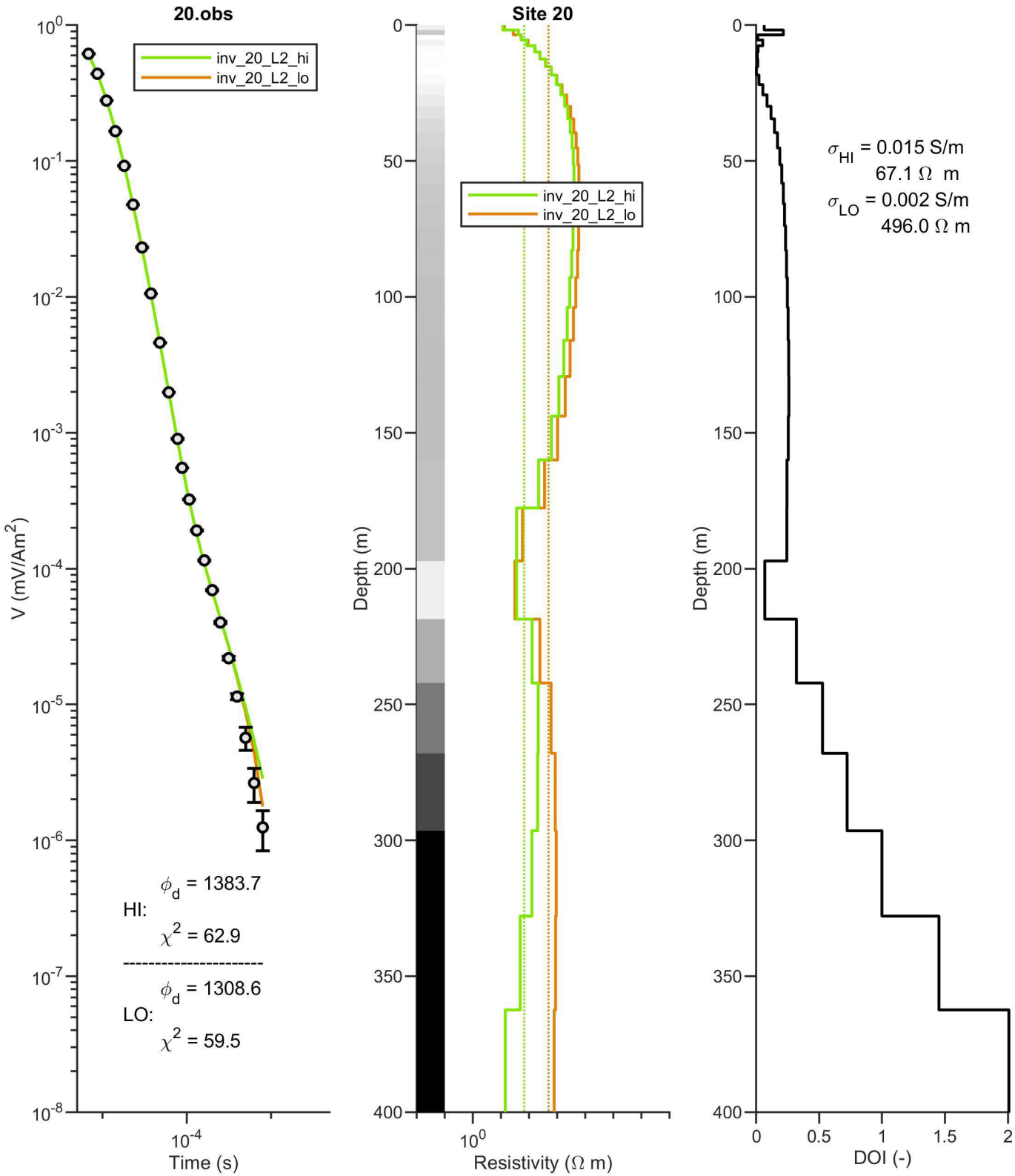
20.obs
inv_20_L2_hi
inv_20_L2_lo
V (mV/Am^2)
Time (s)
ϕ_d = 1383.7
HI:
χ^2 = 62.9
ϕ_d = 1308.6
LO:
χ^2 = 59.5
Site 20
inv_20_L2_hi
inv_20_L2_lo
Depth (m)
Resistivity (Ω m)
σ_{HI} = 0.015 S/m
67.1 Ω m
σ_{LO} = 0.002 S/m
496.0 Ω m
DOI (-)

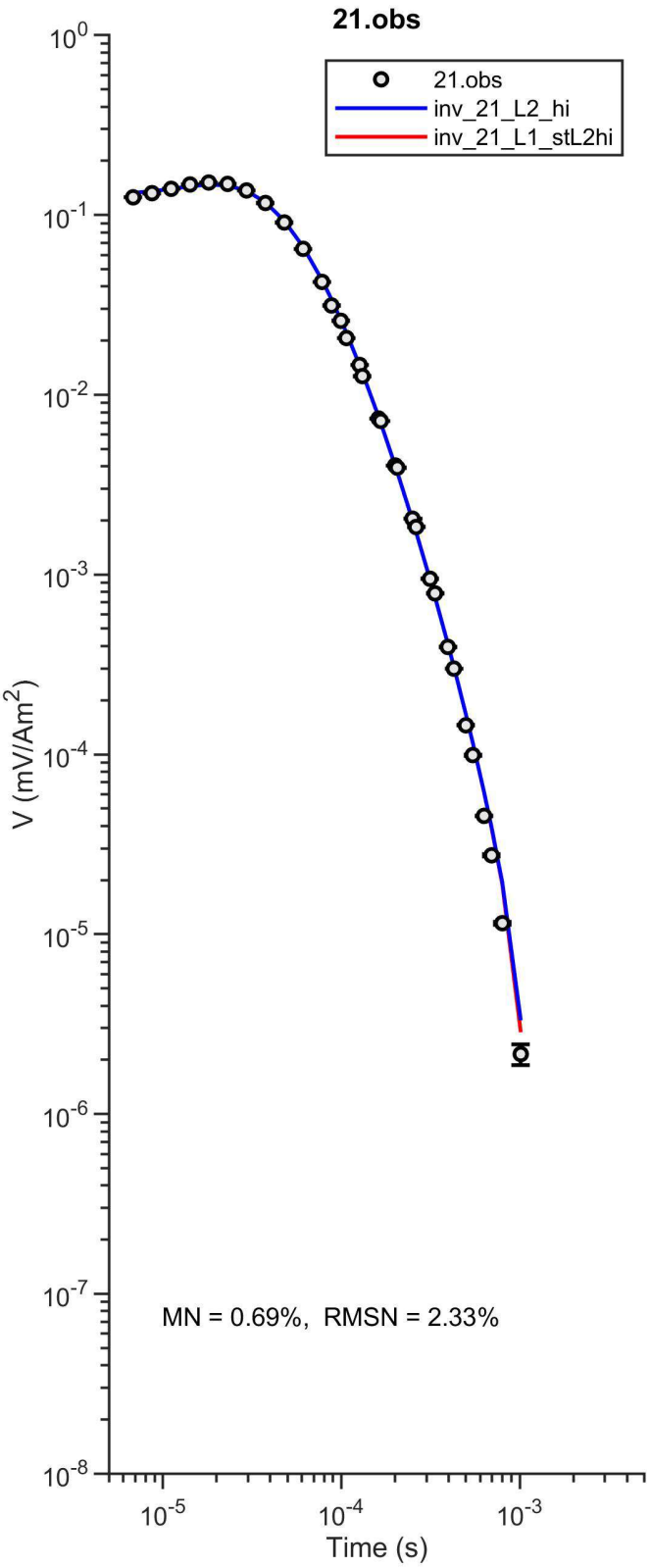
21.obs
21.obs
inv_21_L2_hi
inv_21_L1_stL2hi
V (mV/Am^2)
Time (s)
MN = 0.69%, RMSN = 2.33%

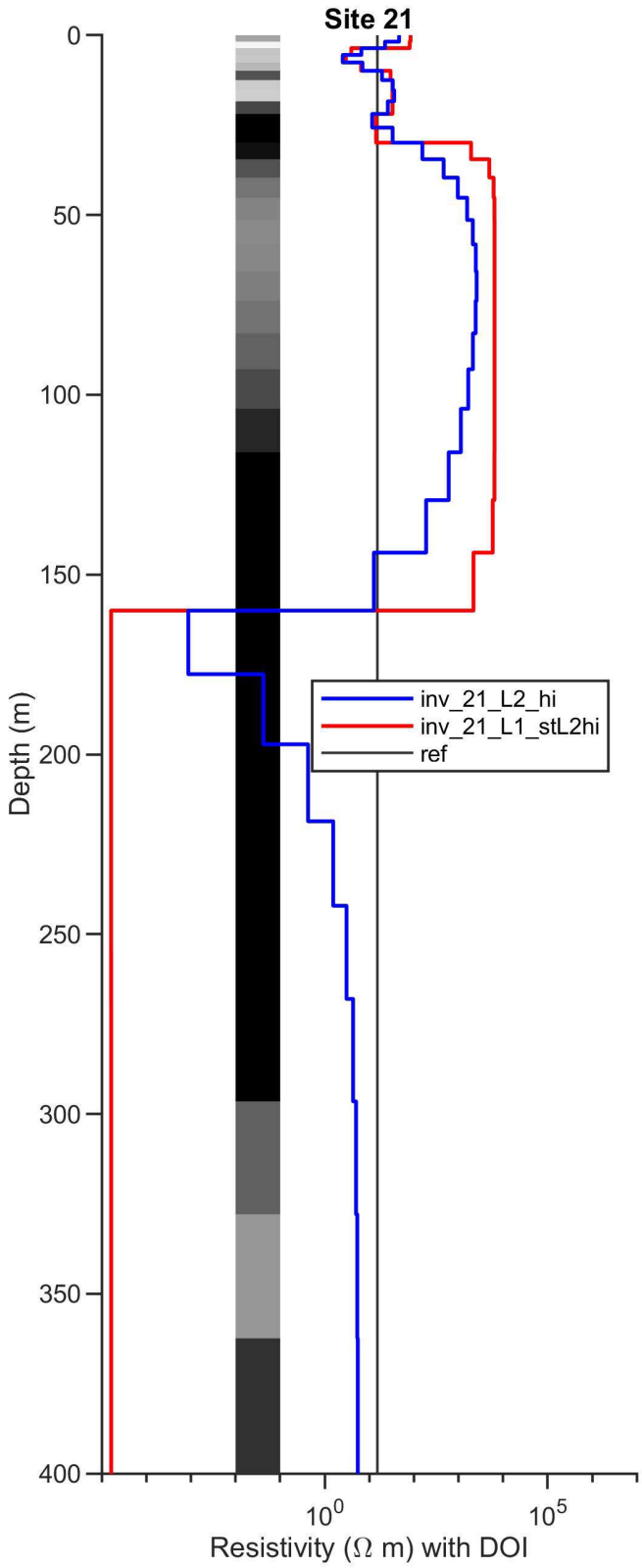
Site 21
Depth (m)
inv_21_L2_hi
inv_21_L1_stL2hi
ref
Resistivity (Ω m) with DOI

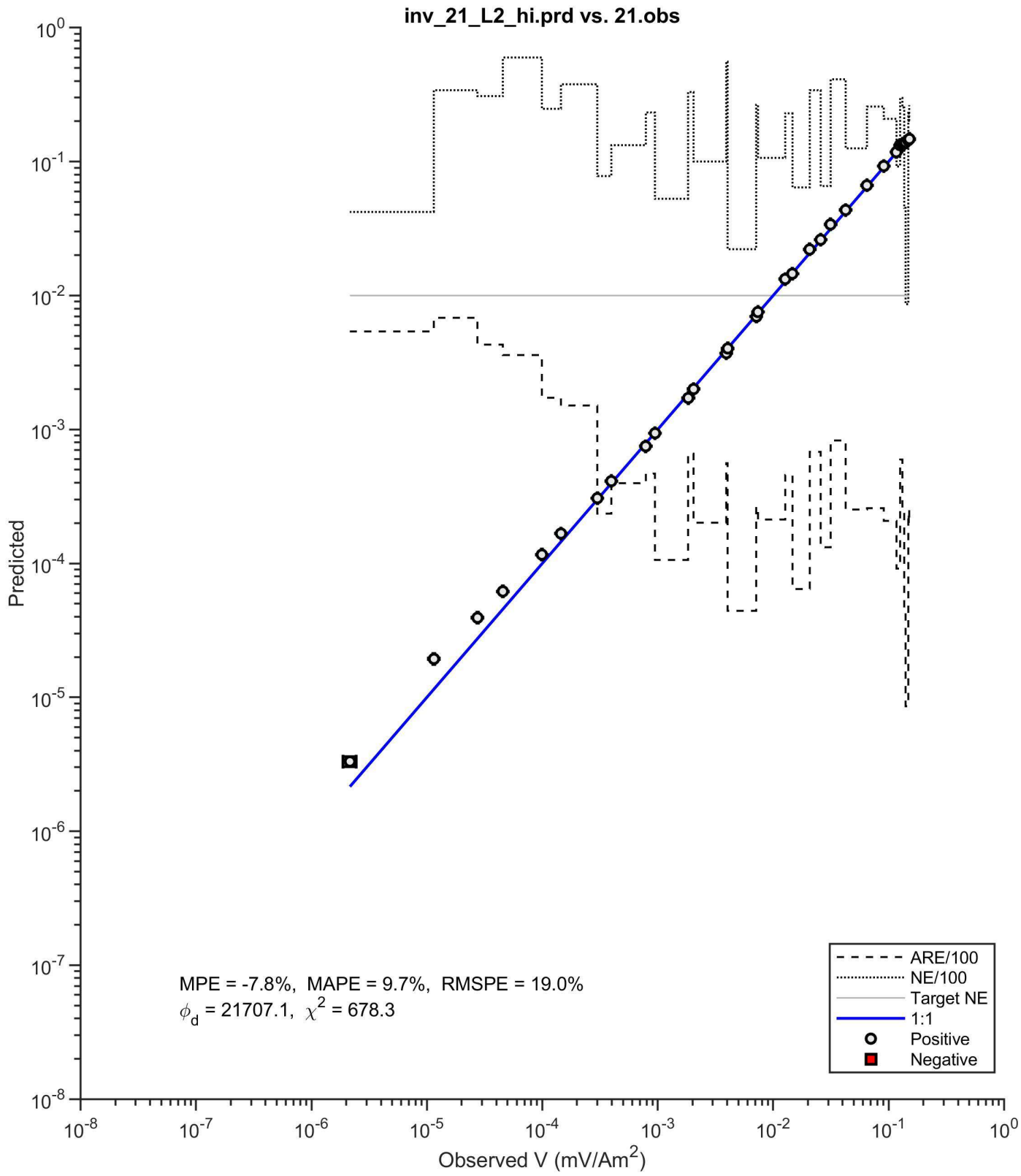
inv_21_L2_hi.prd vs. 21.obs
Predicted
Observed V (mV/Am^2)
10^{0}
10^{-1}
10^{-2}
10^{-3}
10^{-4}
10^{-5}
10^{-6}
10^{-7}
10^{-8}
MPE = -7.8%, MAPE = 9.7%, RMSPE = 19.0%
ϕ_d = 21707.1, χ^2 = 678.3
ARE/100
NE/100
Target NE
1:1
Positive
Negative

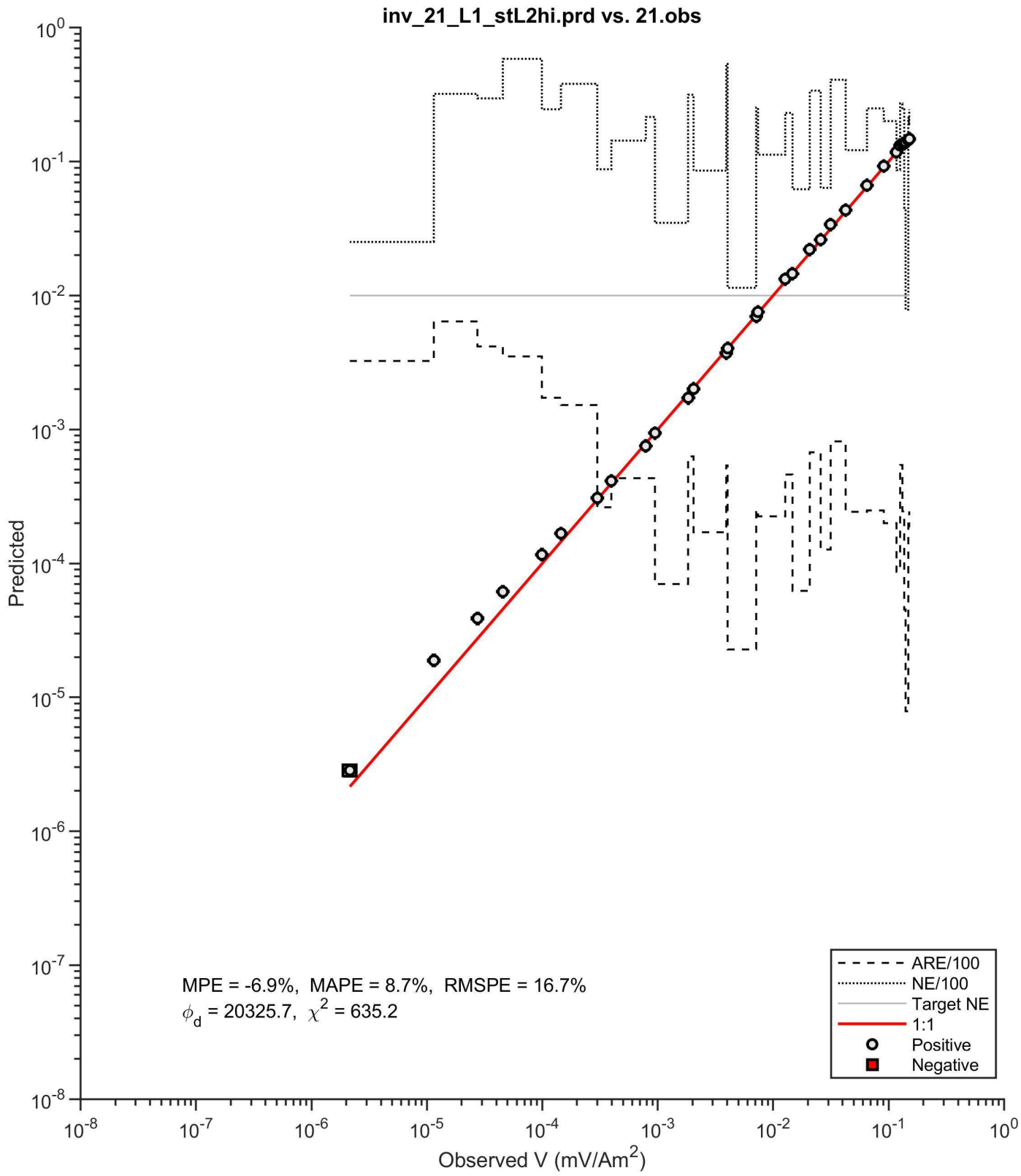
inv_21_L1_stL2hi.prd vs. 21.obs
Predicted
Observed V (mV/Am^2)
MPE = -6.9%, MAPE = 8.7%, RMSPE = 16.7%
ϕ_d = 20325.7, χ^2 = 635.2
ARE/100
NE/100
Target NE
1:1
Positive
Negative

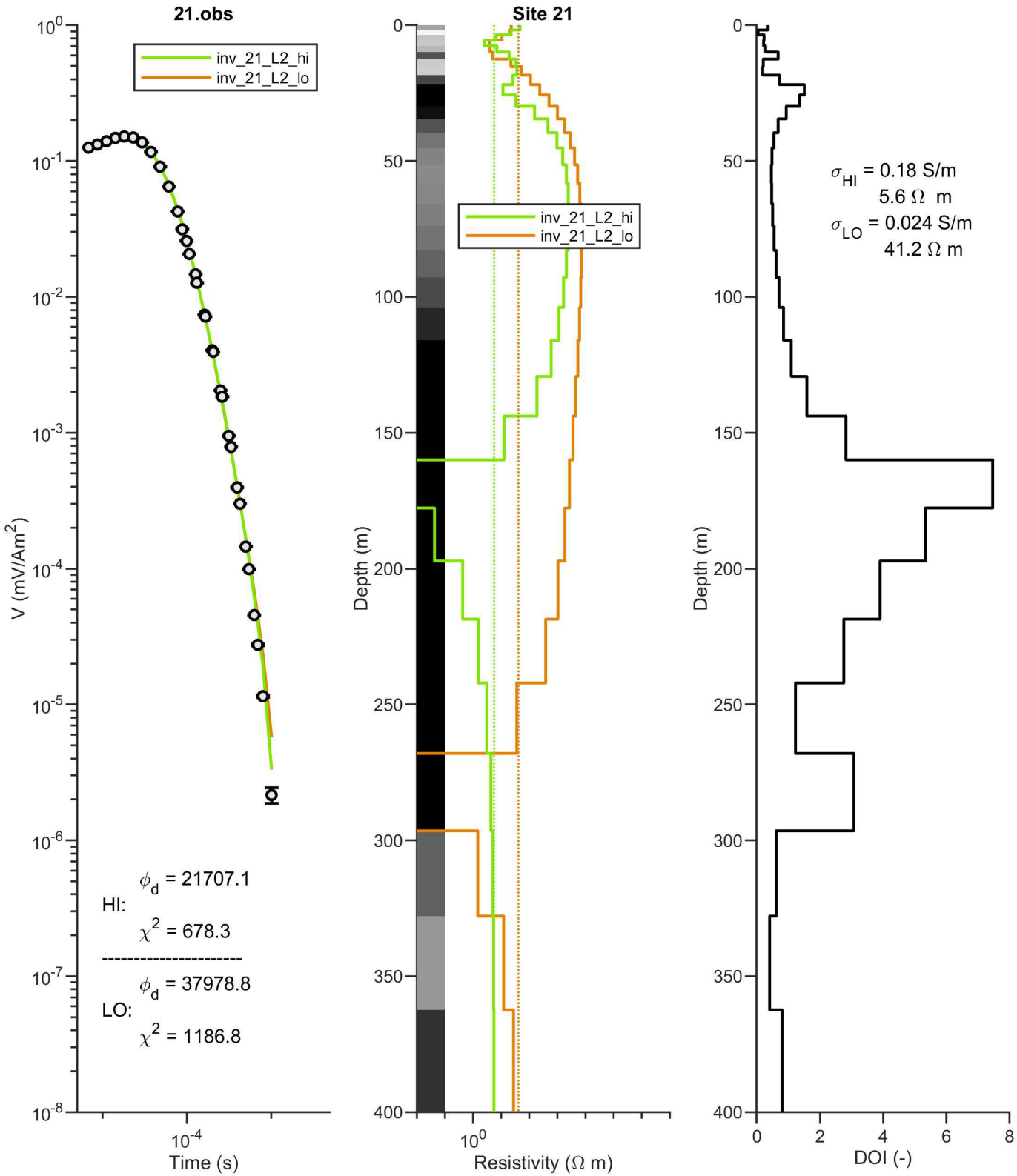
21.obs
inv_21_L2_hi
inv_21_L2_lo
V (mV/Am^2)
Time (s)
ϕ_d = 21707.1
HI:
χ^2 = 678.3
ϕ_d = 37978.8
LO:
χ^2 = 1186.8
Site 21
Depth (m)
Resistivity (Ω m)
σ_{HI} = 0.18 S/m
5.6 Ω m
σ_{LO} = 0.024 S/m
41.2 Ω m
DOI (-)

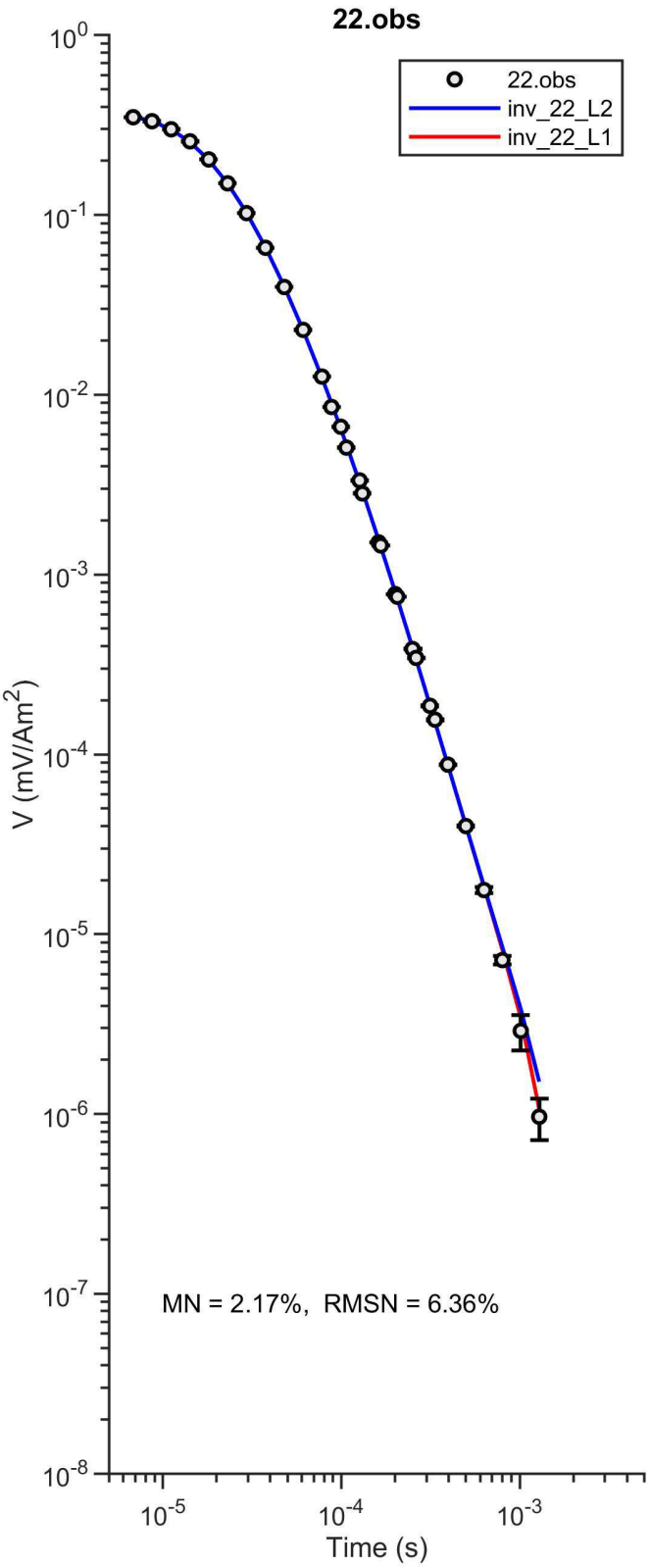
22.obs
22.obs
inv_22_L2
inv_22_L1
V (mV/Am^2)
Time (s)
MN = 2.17%, RMSN = 6.36%

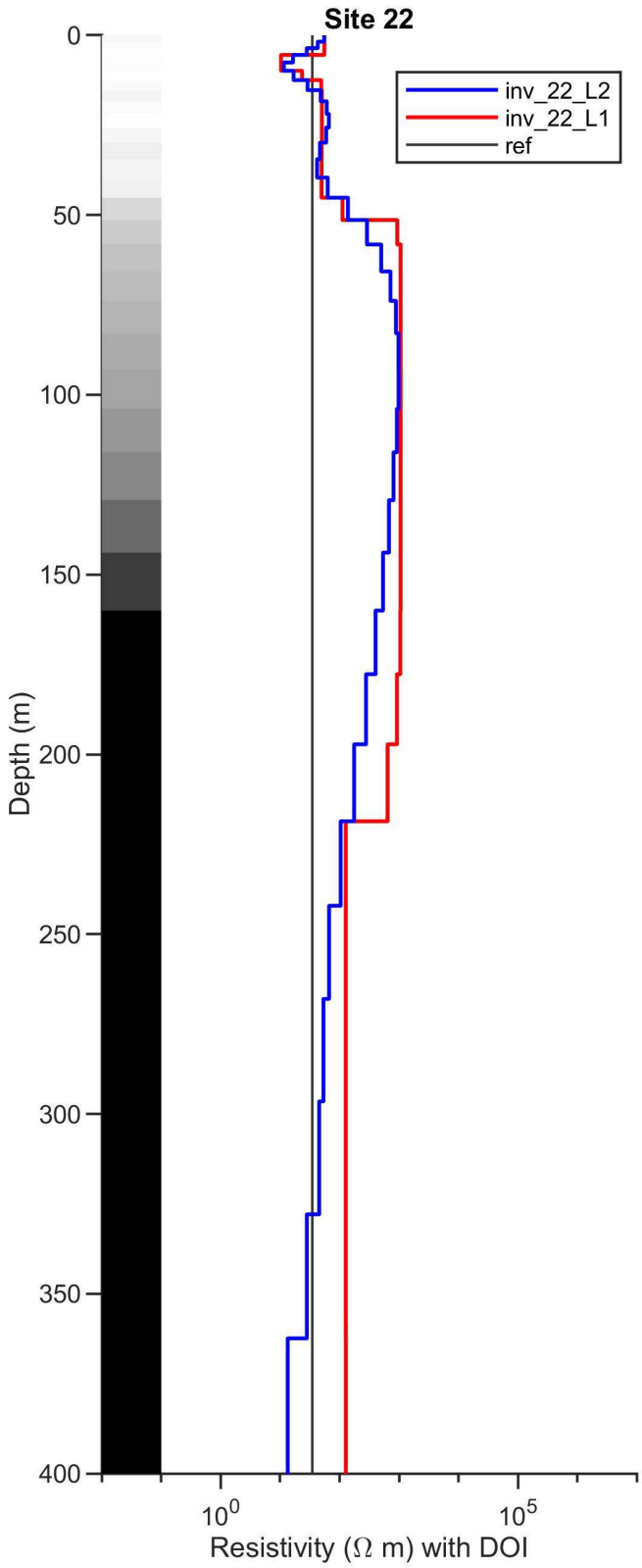
Site 22
inv_22_L2
inv_22_L1
ref
Depth (m)
Resistivity (Ω m) with DOI

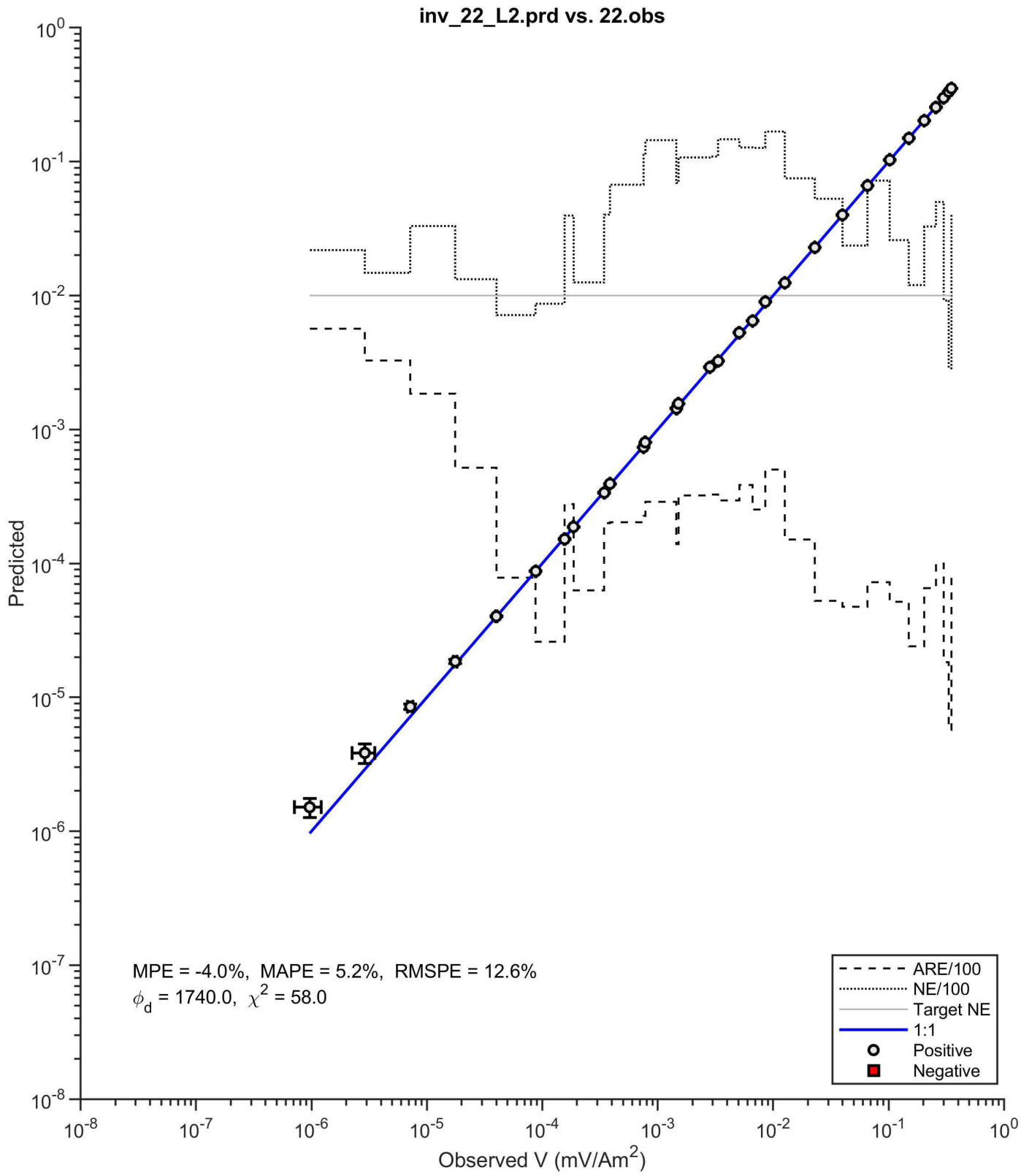
inv_22_L2.prd vs. 22.obs
Predicted
Observed V (mV/Am^2)
10^{0}
10^{-1}
10^{-2}
10^{-3}
10^{-4}
10^{-5}
10^{-6}
10^{-7}
10^{-8}
MPE = -4.0%, MAPE = 5.2%, RMSPE = 12.6%
ϕ_d = 1740.0, χ^2 = 58.0
ARE/100
NE/100
Target NE
1:1
Positive
Negative

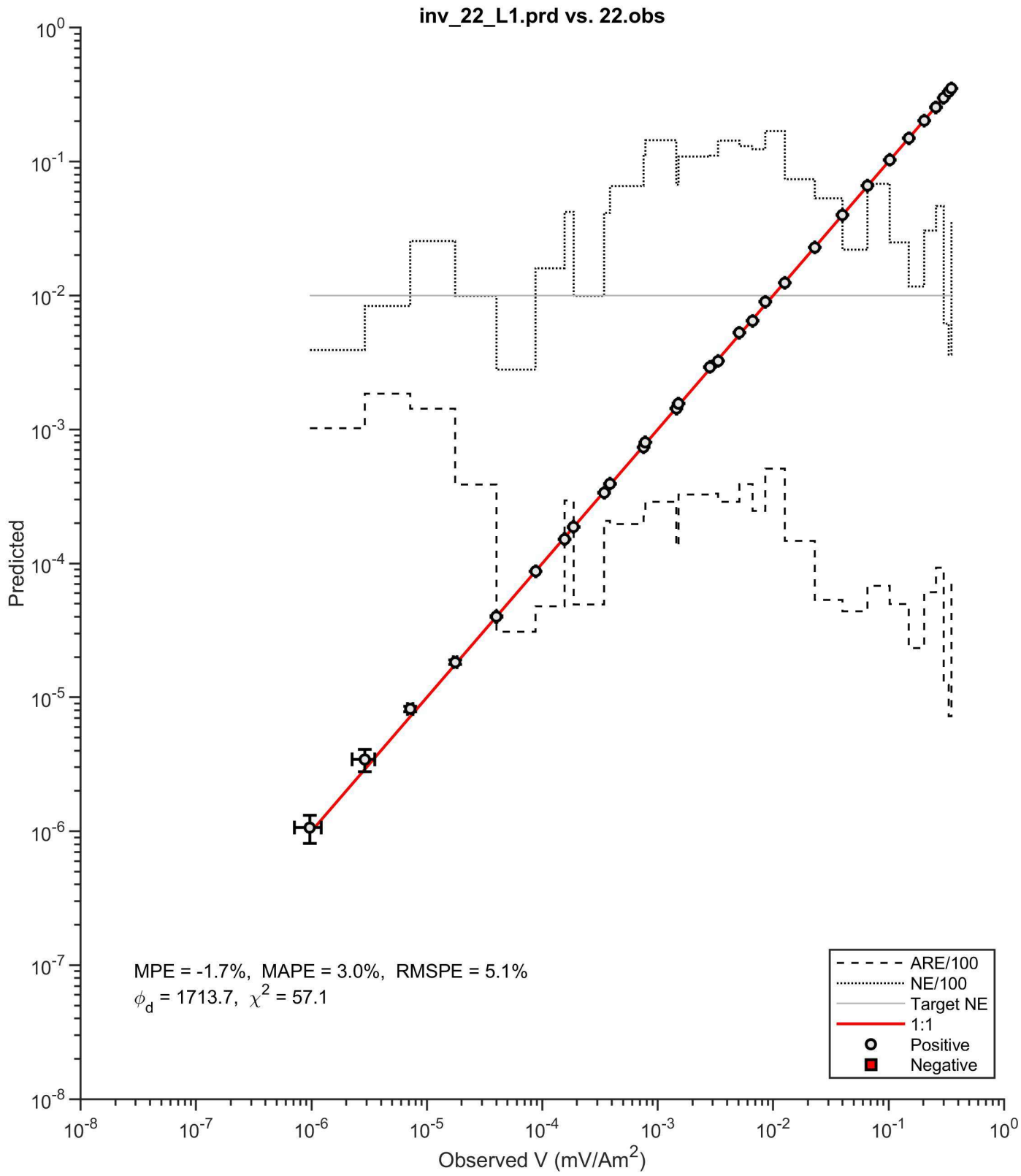
inv_22_L1.prd vs. 22.obs
Predicted
Observed V (mV/Am^2)
MPE = -1.7%, MAPE = 3.0%, RMSPE = 5.1%
ϕ_d = 1713.7, χ^2 = 57.1
ARE/100
NE/100
Target NE
1:1
Positive
Negative

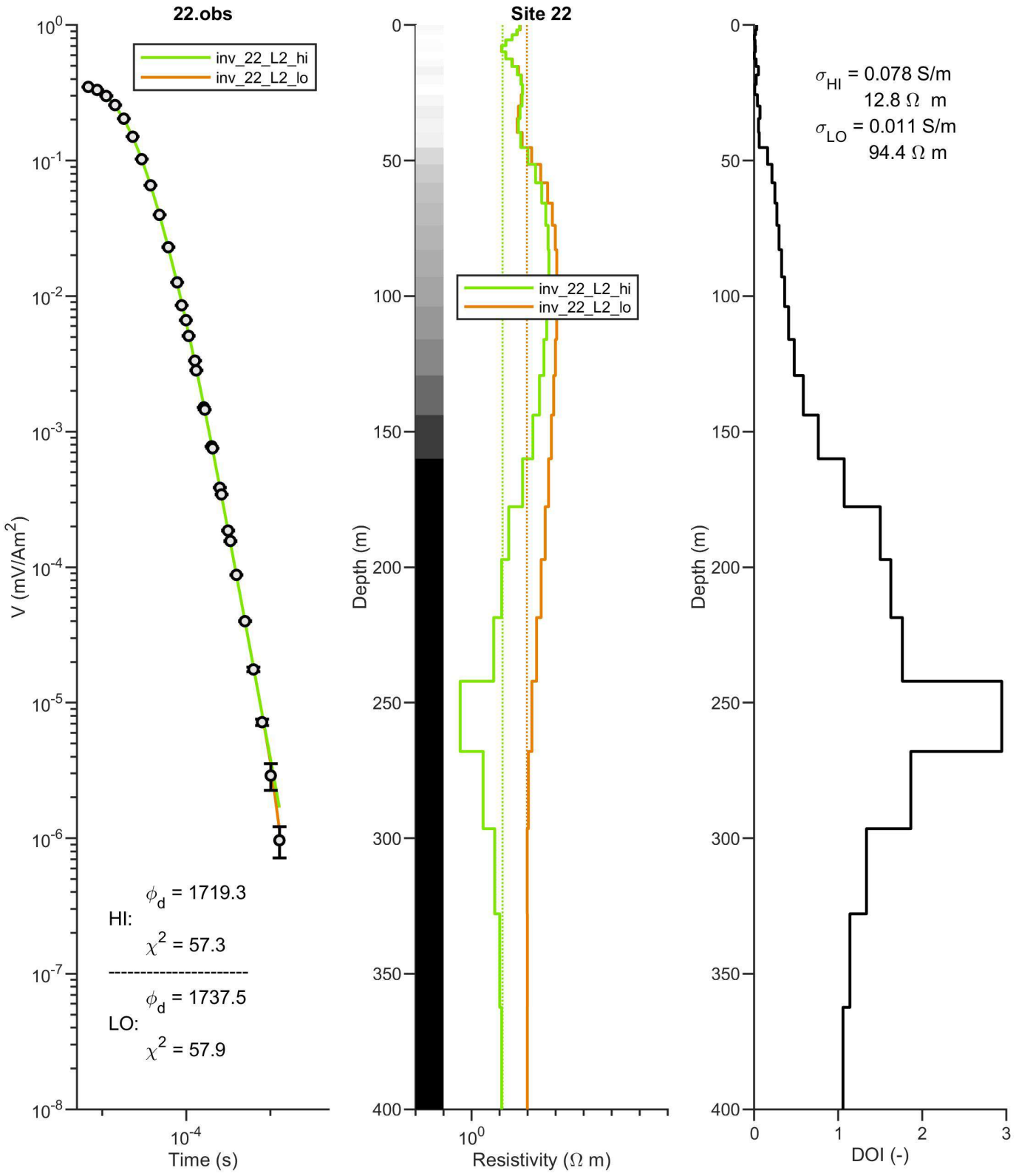
22.obs
inv_22_L2_hi
inv_22_L2_lo
V (mV/Am^2)
Time (s)
ϕ_d = 1719.3
HI:
χ^2 = 57.3
ϕ_d = 1737.5
LO:
χ^2 = 57.9
Site 22
Depth (m)
Resistivity (Ω m)
σ_{HI} = 0.078 S/m
12.8 Ω m
σ_{LO} = 0.011 S/m
94.4 Ω m
DOI (-)